UNIVERSIDADE DE LISBOA

FACULDADE DE CIÊNCIAS

# Out-of-field doses in radiotherapy treatments of paediatric patients

*"Documento Definitivo"*

**Doutoramento em Engenharia Biomédica e Biofísica**

Ana Maria Morais Cravo de Sá

Tese orientada por:

Professor Doutor Pedro Miguel Dinis de Almeida

Doutor José Pedro Miragaia Trancoso Vaz

Documento especialmente elaborado para a obtenção do grau de doutor

2020

UNIVERSIDADE DE LISBOA

FACULDADE DE CIÊNCIAS

Ciências
ULisboa

# Out-of-field doses in radiotherapy treatments of paediatric patients

**Doutoramento em Engenharia Biomédica e Biofísica**

Ana Maria Morais Cravo de Sá

Tese orientada por:

Professor Doutor Pedro Miguel Dinis de Almeida

Doutor José Pedro Miragaia Trancoso Vaz

Júri:

Presidente:

- José Manuel de Nunes Vicente e Rebordão, Investigador Coordenador e Presidente do Departamento de Física, Faculdade Ciências da Universidade de Lisboa

Vogais:

- Doutor Paulo Alexandre Vieira Crespo, Professor Auxiliar, Faculdade Ciências da Universidade de Coimbra
- Doutor João António Miranda dos Santos, Professor Afiliado, Instituto de Ciências Biomédicas Abel Salazar (ICBAS) da Universidade do Porto
- Filomena Imaculada Adriana Nogueira Trindade dos Santos, Diretora do Serviço de Radioterapia do Instituto Português de Oncologia de Lisboa Francisco Gentil, na qualidade de Individualidade de Reconhecida Competência Científica na área
- Doutor José Pedro Miragaia Trancoso Vaz, Investigador Coordenador, Instituto Superior Técnico da Universidade de Lisboa (orientador)
- Doutor Luís Filipe dos Santos Garcia peralta, Professor Associado com Agregação, Faculdade Ciências da Universidade de Lisboa
- Doutora Brígida da Costa Ferreira, Professora Auxiliar, Faculdade Ciências da Universidade de Lisboa

Documento especialmente elaborado para a obtenção do grau de doutor

Este trabalho foi financiado em parte pela bolsa de doutoramento Caixa Geral de Depósitos/IPL-2017

2020

*Aos meus pais,*

*Augusto Sá e Elisabete Cravo Sá*

# ACKNOWLEDGMENTS

First of all, I would like to express my deepest gratitude to my supervisor, Pedro Vaz. His guidance, dedication, toughness and encouragement made this thesis possible. Thank you for standing with me during the good and bad times. A great vote of gratitude goes also to my supervisor, Pedro Almeida. Thank you for your support, dedication and availability.

I express my thankfulness to Centro de Ciências e Tecnologias Nucleares. I am grateful for all the help and companionship provided at the GPSR corridor. I thank Dr. Octávia, for all her kindness and care, Yuriy Romanets, for the help with MCNP, Pedro Teles, Mariana Baptista, for all the precious and essential help and availability, Salvatore Di Maria and Ana Belchior, for the laughs and shared knowledge, Catarina Antunes, for her assertiveness, precious help and kind care.

My appreciation to Instituto de Biofísica e Engenharia Biomédica, namely to Professors Nuno Matela and Alexandre Andrade. I would also like to thank Miguel Pereira and Joana Pereira from Laboratório de Proteção e Segurança Radiológica for providing equipment and expertise, as well as for all the help given, related to the TLD measurements.

Furthermore, I am thankful to the radiotherapy service of Instituto Português de Oncologia de Lisboa Francisco Gentil, for providing the equipment, facilities and expertise necessary for performing the measurements reported in this thesis. Thank you to Tiago Madaleno, Andreia Barateiro and Diana Ferreira.

To my friend, Filipe Pires, thank you for all the amazing moments and for helping me keep sane during all the time we spent in “Sala dos Alunos”.

To my friend, Jorge Borbinha, thank you for helping me with everything I needed and for the laughs, sprints and the VIP room. Together, we have made a way to stand firm and never give up, sometimes with “David da Buraca”.

To my wonderful friend, Carina Marques Coelho, I express my sincere gratitude for our entire journey, accomplished with much sacrifice. Without you, nothing would be possible. You will always be my little star.

To all my friends (you know who you are), thank you for all your support.

To my parents, Elisabete Cravo Sá and Augusto Sá, a deep heartfelt thank you is owed. Not only for continuously inspiring me to grow, but also mainly for allowing me to follow my dreams.

To Inês Pereira thanks for the love and for always knowing how to annoy me.

To Norberto Pereira, my husband, my greatest gratitude for all the help, friendship, love and understanding. Thank you for never letting me give up in the darkest and most difficult moments. Without you, nothing would be possible.

Carolina do Mar, thank you just for existing. You make it all worthwhile.

# RESUMO

Os desenvolvimentos nas tecnologias médicas aumentaram a esperança de vida dos doentes com cancro. Porém, após a realização de radioterapia, o aumento da esperança de vida representa uma preocupação ao nível dos tumores radio-induzidos.

Atualmente utilizam-se técnicas com elevada dose nos volumes alvo, no entanto, administram-se doses indesejadas a tecidos sãos, o que poderá permitir o desenvolvimento de segundos tumores. Assim, a radio-carcinogénese é o efeito secundário mais severo que poderá ser provocado pelas doses fora do campo de irradiação, sendo fundamental a sua avaliação, uma vez que estas apresentam pouca exatidão quando calculadas pelos Sistemas de Planeamento do Tratamento (SPT) comerciais utilizados na prática clínica.

Uma nova abordagem de avaliação das doses fora dos campos de tratamento em radioterapia, destacou-se nos últimos anos enquanto prioridade de investigação em proteção radiológica, especialmente em doentes pediátricos. Esta avaliação compreende desde a comparação entre diferentes técnicas de administração da radiação, a medições realizadas com fantomas físicos e cálculos obtidos através de simulações com base em métodos de Monte Carlo (MC) em combinação com fantomas computacionais.

A Radioterapia Conformacional a Três Dimensões (RTC3D) permite administrar uma dose conformacional ao volume tumoral, enquanto poupa os tecidos sãos circundantes, sendo uma técnica amplamente utilizada nos tratamentos de radioterapia. Com a evolução tecnológica, surgiu a Radioterapia de Intensidade Modelada (RTIM) que utiliza vários pequenos feixes para irradiar o volume tumoral. Adicionalmente à conformação da distribuição de dose ao volume tumoral, alcançada com RTC3D, a intensidade de radiação de cada feixe da RTIM é dividida em pequenos segmentos e modulada através do Colimador Multi-Lâminas (CML), permitindo uma grande diminuição de dose nos Órgãos de Risco (OR) vizinhos. No entando, tem sido debatido a utilização de RTIM, especialmente em doentes pediátricos, uma vez que conduz um “banho” de doses baixas a grandes volumes de tecido são fora dos campos de tratamento.

Este estudo pretende avaliar as doses fora do campo de tratamento, em tumores pediátricos, comparando as técnicas RTC3D e RTIM. Para isso, inicialmente foi detalhadamente modelado e validado um modelo computacional de um Acelerador Linear (LINAC) Varian Clinac 2100 CD, bem como do seu feixe de fotões com energia de 6 MV, assim como os CML Millenium™ com 120 lâminas, pela primeira vez modelado no programa Monte Carlo N – Particle, version 6 (MCNP6). Para a validação do modelo computacional realizaram-se medições de dose, através de curvas de Dose em Profundidade (DP) e Perfis

de Dose (PD), para váras dimensões de campo, dentro e fora dos campos de tratamento, no Varian Clinac 2100 CD do serviço de radioterapia do Instituto Português de Oncologia de Lisboa Francisco Gentil (IPOLFG). Verificou-se uma boa concordância (< 3%) entre os valores de dose medidos e os calculados com MCNP6, tanto para dentro como fora dos campos de tratamento.

Posteriormente adquiriram-se no IPOLFG imagens de Tomografia Computorizada (TC) de um fantoma antropomórfico de 5 anos ATOM® da CIRS e com a ajuda do programa ImageJ criou-se um fantoma pediátrico computacional voxelizado. Obtiveram-se onze volumes de interesse: pele, globos oculares (direito e esquerdo), ossos, volume alvo de planeamento (VAP), medula cervical, tiroide, coração, pulmões (direito e esquerdo) e tecido mole. De seguida o fantoma voxelizado foi implementado no programa computacional MCNP6.

Através das imagens de TC adquiridas do fantoma antropomórfico pediátrico realizaram-se dois planeamentos dosimétricos, um com a técnica RTC3D e outro com a técnica RTIM no software Elicpse da Varian Medical Systems do departamento de física médica do serviço de radioterapia do IPOLFG. Avaliou-se a $D_{min}$, $D_{med}$ e $D_{max}$ para todos os volumes de interesse e para cada uma das técnicas. Para os globos oculares as $D_{min}$, $D_{med}$ e $D_{max}$ foram superiores com a técnica RTIM para todos os volumes, bem como a $D_{max}$ para os pulmões. A técnica RTC3D apresentou valores superiores de $D_{med}$ e $D_{max}$ para a medula cervical, bem como valores de $D_{min}$, $D_{med}$ e $D_{max}$ na tiroide e valores de $D_{max}$ no coração.

Realizaram-se medidas experimentais no LINAC com o fantoma antropomórfico pediátrico e com o auxílio de detetores termoluminescentes (DTL), reproduzindo os planos de tratamento anteriormente criados no sistema de planeamento de tratamento (SPT) Eclipse, para as duas técnicas de tratamento no serviço de radioterapia do IPOLFG. Observaram-se doses nos órgãos fora dos campos de tratamento superiores na técnica RTIM.

No programa MCNP6, adicionou-se de uma forma sem precedente, o modelo computacional do LINAC, com respetivo CML e informação do feixe de fotões com energia de 6 MV, bem como o fantoma voxelizado criado anteriormente. Reproduziu-se os campos de tratamento de ambas as técnicas e as doses fora dos campos de tratamento foram calculadas para todos os órgãos anteriormente segmentados.

Os resultados desta tese mostram que para a técnica RTC3D, as diferenças de doses fora dos campos de tratamento entre as medições com os DTLs e os cálculos com MCNP6 são menores que as diferenças entre as medições de dose com os DTLs e as doses calculadas pelo SPT. Para a técnica de RTIM, as diferenças de doses fora dos campos de tratamento nas medições de dose com os DTLs e cálculos de dose com MCNP6 também são menores que as diferenças de dose medida com os DTLs e as doses calculadas pelo SPT.

Os resultados obtidos parecem indicar que as doses fora dos campos de tratamento são significativamente superiores com a técnica RTIM quando comparado com a RTC3D. As doses medidas pelos DTLs para as diferentes técnicas apresentam para o globo ocular direito valores de 593 mGy para a técnica RTC3D e 13040.6 mGy para a técnica RTIM. A medula cervical apresenta doses de 180.9 mGy com RTC3D e 182.3 mGy com a técnica RTIM. Para a tiroide obtiveram-se doses de 69.7 mGy com RTC3D e 79.4 mGy com RTIM. Para o pulmão direito, mediram-se dose de 28 mGy para RTC3D e 37.4 mGy para RTIM.

Adicionalmente, as doses fora dos campos de tratamento podem ser muito submestimadas pelo SPT e as doses avaliadas neste trabalho podem presumivelmente conduzir ao desenvolvimento de segundos tumores. A decisão do tipo e modalidade de tratamento deverá sempre ser realizada pelos médicos radioncologistas, considerando toda a informaçãoo clínica relevante sobre o doente.

Este trabalho encontra-se dividido em oito grandes capítulos. O primeiro capítulo introduz a temática das doses fora dos campos de tratamento em doentes pediátricos, menciona aspetos técnicos das técnicas de tratamento RTC3D e RTIM, bem como os objetivos da tese, metodologia adotada e estrutura da tese. O segundo capítulo refere os princípios teóricos da proteçãoo radiológica e dosimetria na radioterapia, nomeadamente a classificação da radiação, unidades e quantidades de dosimetria externa para radioterapia, interações de fotões e eletrões com a matéria e radio-proteção em radioterapia. O terceiro capítulo aborda os aspetos físicos da radioterapia conformacional e do planeamento do tratamento, descrevendo o LINAC, bem como o planeamento do tratamento em radioterapia. O capítulo quatro, refere os aspetos mais gerais de simulações por métodos de MC, a sua aplicação na radioterapia, bem como o programa computacional MCNP6. A segunda parte do capítulo quatro refere os fantomas físicos e computacionais mais utilizados para o cálculo de doses nos órgãos, bem como a utilização dos métodos de MC nos fantomas computacionais. O quinto capítulo apresenta a modelação e a validação do LINAC, do feixe de fotões de 6 MV e respetivos CMLs. O sexto capítulo apresenta a criação de um fantoma voxelizado a partir das imagens de TC de um fantoma antropomórfico pediátrico. O sétimo capítulo avalia as doses fora dos campos de tratamento com as duas diferentes técnicas de tratamento para os diferentes órgãos do fantoma pediátrico. Por fim, o capítulo oito apresenta as principais conclusões da tese e sugere trabalho futuro.

Os resultados nesta tese demonstram uma poderosa combinação de (1) medições dosimétricas em ambiente clínico, (2) uma modelação detalhada de um LINAC, feixe de tratamento e respetivo CML, (3) simulação de doses num fantoma pediátrico em órgãos fora dos campos de tratamento, (4) criação de um fantoma pediátrico computacional voxelizado

e (5) doses fora dos campos de tratamento com duas técnicas de tratamento. Tudo isto poderá ter um impacto nas áreas da proteção radiológica e dosimetria, nomeadamente na administração de tratamentos pediátricos nos serviços de radioterapia nacionais e internacionais.

**Palavras-chave:** Radioterapia; Doses Fora dos Campos de Tratamento; Tumores Pediátricos; Simulações Monte Carlo; Fantoma de Voxel Computacionais.

# ABSTRACT

Out-of-field doses are delivery to healthy tissues, which may allow the development of second tumours. Its evaluation with MC methods is essential since these doses are inaccurate when calculated by TPSs. The use of IMRT has been discussed, especially in paediatric patients, as it leads to a "bath" of low doses to large volumes of out-of-field tissue.

This study aims to evaluate out-of-field doses in paediatric tumours by comparing 3DCRT and IMRT techniques. Thus, a computer model of a LINAC, as well as its 6 MV energy photon beam, and MLC, were initially modelled and validated in MCNP6. Subsequently, CT images of a paediatric anthropomorphic phantom were acquired in IPOLFG and with the ImageJ program; a voxelized paediatric computational phantom was created. Two dosimetric plans were performed, one with the 3DCRT technique and the other with the IMRT technique.

Experimental measurements were carried out in LINAC with the paediatric anthropomorphic phantom and with TLDs reproducing the treatment plans previously created in TPS.

In the MCNP6 program, the model of the LINAC was added in an unprecedented way, with its MLC and the 6 MV energy photon beam, as well as the previously created voxelized phantom and the out-of-field doses for all organs were calculated for both techniques.

The results have shown that out-of-field doses can be seriously underestimated with TPSs. The out-of-field doses are higher when using the IMRT technique (right eye = 13040.6 mGy), compared to the 3DCRT technique (right eye = 593 mGy).

This thesis demonstrates a powerful combination of (1) dosimetric measurements in a clinical environment, (2) modelling of a LINAC, treatment beam and MLC, (3) out-of-field organ doses in a paediatric phantom, (4) creation of a voxelized paediatric phantom. This could have an impact in radiological protection and dosimetry in radiotherapy services.

**Key-words:** Radiotherapy; Out-of-field Doses; Paediatric Tumours; Monte Carlo Simulations; Computational Voxel Phantoms.

# LIST OF PUBLICATIONS

Papers in International Scientific Journals with Referees:

- Cravo Sá A, Barateiro A, Bednarz B, Borges C, Pereira J, Baptista M, et al. Assessment of out-of-field doses in radiotherapy treatments of paediatric patients using Monte Carlo methods and measurements. Phys Medica 2020;71:53–61. doi:10.1016/j.ejmp.2020.02.008.

Oral Communications in Scientific Conferences:

- Sá, AC., Barateiro, A., Bednarz, B., Borges, J., Pereira J., Baptista, M., Pereira, M., Zarza-Moreno, M., Almeida, P., Vaz, P., Madaleno, T., Romanets Y. (2019). Monte Carlo Assessment of Out-of-Field Doses in Radiotherapy Treatments of Paediatric Patients. Book of abstracts 3rd International Conference on Dosimetry and its Applications.
- Sá, AC., Barateiro, A., Bednarz, B., Borges, J., Pereira J., Baptista, M., Pereira, M., Zarza-Moreno, M., Almeida, P., Vaz, P., Madaleno, T., Romanets Y. (2019). Out-of-Field Doses in Radiotherapy Treatments of Paediatric Patients. ART National Congress, November 2019 held in Lisbon.
- Sá, AC., Barateiro, A., Bednarz, B., Borges, J., Pereira J., Baptista, M., Pereira, M., Zarza-Moreno, M., Almeida, P., Vaz, P., Madaleno, T., Romanets Y. (2019). Out-of-field doses in radiotherapy treatments of paediatric patients: A Monte Carlo model, Thematic Strand Radiopharmaceutical Sciences and Health Physics, IST, November 2019.
- Sá, AC., Barateiro, A., Bednarz, B., Borges, J., Pereira J., Baptista, M., Pereira, M., Zarza-Moreno, M., Almeida, P., Vaz, P., Madaleno, T., Romanets Y. (2018). Monte Carlo Validation of 6MV Varian 2100 CD Linear Accelerator, PhD Conference of the Physics Department, Faculty of Sciences of the University of Lisbon.

Poster Communications in Scientific Conferences:

- Sá, AC., P. Vaz, P. Almeida, M. Zarza-Moreno (2015). Evaluation of out-of-field doses in paediatric patients undergoing radiotherapy: A literature review, book of

abstracts do Workshop Lowdose – PT 2015, IST, IPATIMUP, FCM/UNL, FFUL and INSA, in Centro de Ciências e Tecnologias Nucleares, 2015.

- Sá, AC., P. Vaz, P. Almeida, M. Zarza-Moreno (2015). Evaluation of Out-of-field Doses in Paediatric Patients Undergoing Radiotherapy: Comparison of 3DCRT and IMRT Techniques – A Ph.D. Project, 7$^{th}$ Workshop on Biomedical Engeneering, held in Instituto Biofísica e Engenharia Biomédica, FCUL 2015.

# TABLE OF CONTENTS

**ACKNOWLEDGMENTS** ..... **I**

**RESUMO** ..... **III**

**ABSTRACT** ..... **VII**

**LIST OF PUBLICATIONS** ..... **VIII**

**TABLE OF CONTENTS** ..... **X**

**LIST OF TABLES** ..... **XVII**

**LIST OF FIGURES** ..... **XVIII**

**LIST OF ABBREVIATIONS** ..... **XXI**

**SECTION I - INTRODUCTION** ..... **1**

**CHAPTER 1 – BACKGROUND AND MOTIVATION** ..... **1**

1.1. INTRODUCTION ..... 1

1.2. PAEDIATRIC CANCER ..... 2

1.3. 3D CONFORMAL RADIOTHERAPY ..... 5

1.4. INTENSITY-MODULATED RADIATION THERAPY ..... 6

1.5. UNWANTED DOSES IN RADIOTHERAPY ..... 8

1.6. OBJECTIVES, METHODOLOGY ANS STRUCTURE OF THE PHD THESIS ..... 8

**SECTION II – THEORETICAL PRINCIPLES** ..... **10**

**CHAPTER 2 – RADIATION PROTECTION AND DOSIMETRY IN RADIOTHERAPY** ..... **10**

2.1. CLASSIFICATION OF RADIATION ..... 10

2.2. UNITS AND QUANTITIES OF EXTERNAL DOSIMETRY RELEVANT FOR RADIOTHERAPY ..... 11

2.2.1. Exposure ..... 11

2.2.2. Fluence ..... 11

2.2.3. Kinectic Energy Released Per Unit Of Mass (KERMA) ..... 11

2.2.4. Absorbed Dose ..... 12

2.2.5. Equivalent Dose ..... 12

2.2.6. Effective dose ..... 13

2.3. INTERACTION OF PHOTONS WITH MATTER ..... 13

2.3.1. Photoelectric Effect ..... 14
2.3.2. Compton Scattering ..... 15
2.3.3. Pair Production ..... 16
2.4. INTERACTION OF ELECTRONS WITH MATTER ..... 17
2.5. RADIATION PROTECTION IN RADIOTHERAPY ..... 17
2.5.1. Radiation Protection Principles ..... 18
2.5.1.1. The Justification ..... 18
2.5.1.2. The Optimization ..... 20
2.5.1.3. Dose Limitation ..... 21
2.5.2. Radiation Health Effects ..... 21
2.5.2.1. Stochastic Effects ..... 22
2.5.2.1.1. Cancer ..... 22
2.5.2.1.2. Chromosome Mutations ..... 23
2.5.2.2. Deterministic Effects ..... 23
2.5.2.2.1. Cardiovascular Injury ..... 24
2.5.2.2.2. Cataracts ..... 24
2.5.2.2.3. Fetus Abnormality ..... 24
2.5.3. Out-of-field doses ..... 25
2.5.4. Radio-Induced Tumours in Paediatric Patients ..... 27
2.5.4.1. Carcinogenic Risk of 3DCRT and IMRT Techniques ..... 30
**CHAPTER 3 – CONFORMAL RADIOTHERAPY PHYSICS, TREATMENT PLANNING AND CLINICAL ASPECTS ..... 32**
3.1. MEDICAL LINEAR ACCELERATOR ..... 32
3.1.1. LINAC Components ..... 33
3.1.1.1. Injection System ..... 34
3.1.1.2. RF Power Generation System ..... 35
3.1.1.3. Accelerating Wave Guide ..... 35
3.1.1.4. Auxiliary System ..... 35
3.1.1.5. Beam Transport System ..... 35
3.1.1.6. Beam Collimation and Beam Monitoring System ..... 36

3.1.2. Treatment head ..... 36
3.1.2.1. X-ray Production Target ..... 36
3.1.2.2. Flattening Filter (FF) ..... 37
3.1.2.3. Primary Collimators ..... 37
3.1.2.4. Secondary Collimators ..... 38
3.1.2.5. Multi-Leaf Collimators (MLC) ..... 38
3.1.2.6. Ionization Chambers ..... 38
3.1.3. Beam Production ..... 39
3.1.3.1. Photon Beam ..... 39
3.1.3.2. Electron Beam ..... 40
3.1.4. Dosimetric Parameters and Measurements ..... 40
3.1.4.1. Ionization Chambers ..... 41
3.1.4.2. Water Phantoms ..... 42
3.1.4.3. Percentage Depth Dose ..... 42
3.1.4.4. Dose Profile ..... 44
3.2. RADIOTHERAPY TREATMENT PLANNING ..... 44
3.2.1. Prescription, Registration and Documentation in Radiotherapy ..... 46
3.2.1.1. ICRU Report 29 ..... 46
3.2.1.2. ICRU Report 50 and ICRU Report 62 ..... 46
3.2.1.3. ICRU Report 71 ..... 48
3.2.1.4. ICRU Report 83 ..... 48
3.2.1.5. Volumes Definition in Radiotherapy ..... 48
3.2.2. Dose Calculation Limitations in Commercial TPS ..... 52
3.2.2.1. Dose Measurements versus Calculations, Models and Algorithms ..... 52
3.2.2.2. From 2D to 3D and to Increasingly Complex Radiotherapy Techniques ..... 53
3.2.2.3. TPS Accuracy, Commissioning and Quality Control ..... 54
3.2.3. 3DCRT Dosimetric Treatment Planning ..... 55
3.2.4. IMRT Dosimetric Treatment Planning ..... 56
**CHAPTER 4 – MONTE CARLO SIMULATION METHODS AND ANTHROPOMORPHIC VOXEL PHANTOMS ..... 61**

4.1. MONTE CARLO SIMULATION METHODS IN PARTICLE TRANSPORT ..... 61
4.1.1. General Concepts ..... 61
4.1.1.1. Pseudo Random Number Generators ..... 62
4.1.2. Application of Monte Carlo Methods in Radiotherapy ..... 62
4.1.2.1. Simulation of Out-of-Field Doses in Radiotherapy ..... 64
4.1.2.2. The MCNP Computer Program ..... 65
4.1.2.2.1. Input File Structure ..... 66
4.1.2.2.2. Cell and Surface Cards ..... 66
4.1.2.2.3. Data Cards ..... 67
4.1.2.2.4. Calculation of the Absorbed Dose with MCNP ..... 69
4.1.2.2.5. Variance Reduction ..... 69
4.1.2.2.6. Relative Error and Figure Of Merit (FOM) ..... 71
4.2. HUMAN PHANTOMS ..... 71
4.2.1. Physical Phantoms ..... 72
4.2.1.1. Anthropomorphic Phantoms ..... 72
4.2.2. Anthropomorphic Computational Phantoms ..... 74
4.2.2.1. Mathematical or Stylized Phantoms ..... 75
4.2.2.2. Anthropomorfic Voxel Phantoms ..... 77
4.2.2.2.1. Existing Anthropomorphic Voxel Phantoms ..... 78
4.2.2.2.2. Paediatric Voxel Phantoms ..... 80
4.2.2.2.3. ICRP Reference Voxel Phantoms ..... 81
4.2.2.2.4. Voxel Phantoms Construction ..... 83
4.2.2.2.5. Drawbacks and Limitations of Voxel Models ..... 83
4.2.2.3. BREP Computational Phantoms ..... 84
4.2.3. Monte Carlo Methods and Computational Phantoms ..... 88
**SECTION III – METHODS AND RESULTS ..... 90**
**CHAPTER 5 – OUT-OF-FIELD AND IN-FIELD MODELING AND VALIDATION OF 6 MV LINAC ..... 90**
5.1. MOTIVATION ..... 90
5.2. CLINICAL MEASUREMENTS ..... 91
5.2.1. Millenium™ 120-leaf MLC ..... 91

5.2.2. Measurements of the Beam Profiles and PDD Curves using a Clinac Varian 2100 CD Operated at 6 MV ..... 93
5.3. MC MODELLING AND SIMULATIONS ..... 95
5.3.1. Innovative Model of the LINAC Components Coupled to the 120-leaf MLC ..... 95
5.3.1.1. MCNP Modeling of the Water Phantom ..... 97
5.3.1.2. MCNP6 MC Simulations of the Transmission and DLS ..... 98
5.3.1.3. MCNP6 MC Simulations of the Full Model (LINAC coupled to MLC) ..... 99
5.4. RESULTS ..... 99
5.4.1. Preliminary Results of the LINAC Head Geometry Assessment ..... 99
5.4.2. Millennium$^{tm}$ 120-leaf MLC Validation ..... 101
5.4.3. Varian Clinac 2100 CD Head Operated at 6 MV Validation ..... 102
5.4.3.1. Comparison of PDD Curves ..... 103
5.4.3.2. Comparison of Dose Profile Curves ..... 105
5.5. DISCUSSION ..... 110
5.5.1. Electron Beam Modeling ..... 110
5.5.2. Modeling of the Millenium™ 120-leaf MLC ..... 111
5.5.3. Modeling of the Varian Clinac 2100 CD ..... 111
5.6. CONCLUSIONS ..... 112
**CHAPTER 6 – DEVELOPMENT AND IMPLEMENTATION OF A PAEDIATRIC COMPUTATIONAL PHANTOM ..... 114**
6.1. MOTIVATION ..... 114
6.2. MATERIALS AND METHODS ..... 114
6.2.1. Acquisition of CT images of a Paediatric Phantom ..... 114
6.2.2. Development and Implementation of the Paediatric Voxel Phantom ..... 117
6.3. RESULTS ..... 124
6.3.1. Paediatric Phantom CT Images ..... 124
6.3.2. Paediatric Voxel Phantom ..... 124
6.4. DISCUSSION ..... 129
6.5. CONCLUSIONS ..... 131
**CHAPTER 7 – ASSESSMENT OF OUT-OF-FIELD DOSES IN PAEDIATRIC PATIENTS ..... 132**

7.1. MOTIVATION ..... 132
7.2. MATERIALS AND METHODS ..... 133
7.2.1. Treatment Planning ..... 133
7.2.1.1. Definition of the Origin of Dosimetric Planning ..... 133
7.2.1.2. Volumes of Interest Segmentation ..... 134
7.2.1.2.1. External Contouring ..... 134
7.2.1.2.2. PTV Definition ..... 134
7.2.1.2.3. OAR ..... 135
7.2.1.3. 3DCRT Planning ..... 136
7.2.1.3.1. Fields ..... 136
7.2.1.3.2. Dose Distribution Assessment ..... 139
7.2.1.3.3. Dose Distribution Optimization ..... 142
7.2.1.4. IMRT Planning ..... 143
7.2.1.4.1. Fields ..... 143
7.2.1.4.2. Dose Objectives ..... 144
7.2.1.4.3. Dose Distribution Assessment ..... 144
7.2.1.4.4. Dose Distribution Optimization ..... 147
7.2.2. TLD Measurements Using a Paediatric Phantom ..... 147
7.2.3. MCNP6 Monte Carlo Simulations of Out-of-Field Doses ..... 150
7.3. RESULTS ..... 152
7.3.1. TPS Dose Calculation ..... 152
7.3.2. Out-of-Field Doses in Paediatric Phantom Measurements with TLDs – Physical Paediatric Phantom ..... 155
7.3.3. Out-of-Field Doses in Paediatric Phantom Calculations With MCNP – Computational Paediatric Phantom ..... 158
7.3.4. Comparison Between TLD Measurements, TPS ans MCNP Calculations ..... 161
7.4. DISCUSSION ..... 170
7.4.1. Uncertainties of TLDs Measurements, TPS and MCNP6 Calculations ..... 171
7.4.2. Tps Dose Calculations ..... 172
7.4.3. TLD Measurements ..... 174

7.4.4. Comparison Between TLD Measurements, TPS and MC Calculations ..... 174
7.5. CONCLUSIONS ..... 176
**SECTION IV – CONCLUSIONS ..... 177**
**CHAPTER 8 – CONCLUSIONS AND FUTURE WORK ..... 177**
8.1. SUMMARY AND CONCLUSIONS ..... 178
8.1.1. Out-of-Field and In-Field Validation of the Computational Model of the LINAC Head for a 6 MV Photon Beam ..... 178
8.1.2. Paediatric Computational Voxel Phantom ..... 179
8.1.3. Out-of-Field Doses Assessment ..... 179
8.2. FUTURE WORK ..... 180
**REFERENCES ..... 182**

# LIST OF TABLES

TABLE 1 - TYPES OF TALLIES AVAILABLE IN MCNP6 ..... 68
TABLE 2 - CHARACTERISTICS OF ATOM® PHANTOMS. ..... 74
TABLE 3 - MAIN CHARACTERISTICS OF ADULT FEMALE AND MALE REFERENCE COMPUTATIONAL PHANTOMS... 82
TABLE 4 - IN-FIELD AND OUT-OF-FIELD GEOMETRY. ..... 95
TABLE 5 - DESCRIPTION OF THE PHANTOM COLOURS. ..... 129
TABLE 6 - 3DCRT PLANNING DOSE PARAMETERS. ..... 138
TABLE 7 - MLC LEAF POSITIONS. ..... 138
TABLE 8 - NORMAL TISSUE TOLERANCE FOR STANDARD FRACTIONATION. ..... 142
TABLE 9 - IMRT PLANNING DOSE PARAMETERS. ..... 143
TABLE 10 - OPTIMIZATION OBJECTIVES FOR INVERSE PLANNING. ..... 144
TABLE 11 - TLDS PLACEMENT IN DIFFERENT SECTIONS AND LOCATION NUMBERS OF THE PHANTOM. ..... 148
TABLE 12 - ORGAN CHARACTERISTICS ASSESSED IN PHANTOM. ..... 149
TABLE 13 - VOLUMES OF INTEREST DOSES CALCULATED BY TPS FOR 3DCRT AND IMRT. ..... 152
TABLE 14 – OUT-OF-FIELD ORGAN DOSES MEASURED BY TLDS FOR 3DCRT AND IMRT TREATMENTS. ..... 155
TABLE 15 - OUT-OF-FIELD ORGAN DOSES CALCULATED BY MCNP6 FOR 3DCRT AND IMRT TECHNIQUES.. 158

# LIST OF FIGURES


FIGURE 1 – INCIDENCE AND MORTALITY RATES PER TUMOUR TYPE WORLDWIDE IN 2018, BOTH SEXES, AGES 0-19 . ..... 2
FIGURE 2 – ESTIMATION BETWEEN 2015-2030 OF INCIDENT GLOBAL PAEDIATRIC CASES. ..... 4
FIGURE 3 - DIFFERENCES BETWEEN 3DCRT AND IMRT. ..... 7
FIGURE 4 - MAIN PHOTON INTERACTIONS WITH MATTER . ..... 14
FIGURE 5 - PHOTOELECTRIC EFFECT . ..... 15
FIGURE 6 – COMPTON SCATTERING. ..... 15
FIGURE 7 – NUCLEAR PAIR PRODUCTION. ..... 16
FIGURE 8 - BIOLOGICAL EFFECTS OF IONIZING RADIATION ..... 22
FIGURE 9 – COMPARISON OF A 3DCRT AND IMRT PLAN . ..... 25
FIGURE 10 - SCHEME OF A MEDICAL LINAC. ..... 33
FIGURE 11 - SCHEME OF A X-RAY BEAM PATH (A) AND VARIAN LINAC HEAD (B) ..... 37
FIGURE 12 – SCHEME OF A LINAC MLC . ..... 38
FIGURE 13 – SCHEME OF AN ELECTRON BEAM PATH . ..... 40
FIGURE 14 – PTW IONIZATION CHAMBER SEMIFLEX TYPE 31010 ..... 42
FIGURE 15 – PTW WATER PHANTOM MP3-M. ..... 42
FIGURE 16 – PDD SCHEME. ..... 43
FIGURE 17 – DIFFERENT PHOTON AND ELECTRON BEAM PDDS. ..... 43
FIGURE 18 – DOSE PROFILES FOR AN 18 MV X-RAY BEAM OF DIFERENTE DIMENSIONS. ..... 44
FIGURE 19 - DIFFERENCES BETWEEN 2D AND 3DCRT DOSE DISTRIBUTIONS. ..... 45
FIGURE 20 - DIFFERENT VOLUMES DEFINED BY ICRU: LEFT - ICRU REPORT 29, MIDDLE - ICRU REPORT 50, RIGHT - ICRU REPORT 62 ..... 49
FIGURE 21 - EXAMPLE OF DIFFERENT TISSUE ORGANIZATION STRUCTURES. (A) SERIAL ORGAN (B) PARALLEL ORGAN (C) SERIAL-PARALLEL ORGAN (D) COMBINATION OF SERIAL AND PARALLEL ORGAN . ..... 51
FIGURE 22 - TONGUE-AND-GROOVE EFFECT. ..... 57
FIGURE 23 - MLC MOVEMENT RESTRICTIONS. (A) MINIMUM GAP DISTANCE; (B) NO INTERDIGITATION LEAF MOTION; (C) MAXIMUM DISTANCE PAST MIDLINE . ..... 58
FIGURE 24 - PROBLEM COMPLEXITY AND TIME TO SOLUTION FOR MC AND ANALYTIC/DETERMINISTIC METHODS ..... 63
FIGURE 25 - MCNP INPUT FILE STRUCTURE. ..... 66
FIGURE 26 - REPRESENTATION OF THE ENERGY DEPOSITED BY THE MCNP TALLY *F8. ..... 69
FIGURE 27 - FEMALE AND MALE VERSIONS OF ALDERSON RADIATION THERAPY PHANTOM . ..... 73
FIGURE 28 - ATOM® PHANTOMS ..... 73
FIGURE 29 - EVOLUTION OF HUMAN COMPUTATIONAL PHANTOMS ..... 75
FIGURE 30 - ADULT STYLIZED MIRD-5 PHANTOMS. ..... 76
FIGURE 31 - REX AND REGINA PHANTOMS ..... 78

FIGURE 32 - UF SERIES B OF PAEDIATRIC COMPUTATIONAL PHANTOMS..... 81
FIGURE 33 - UF PHANTOM FAMILY..... 85
FIGURE 34 - FASH AND MASH PHANTOMS . ..... 86
FIGURE 35 - MESH PHANTOMS . ..... 87
FIGURE 36 - MLC GEOMETRY USED TO CALCULATE THE TRANSMISSION. ..... 93
FIGURE 37 - SCHEMATIC REPRESENTATION OF IN AND OUT-OF-FIELD VALIDATION PERFORMING MEASUREMENTS IN A WATER PHANTOM. ..... 94
FIGURE 38 - MCNP6 MODEL OF VARIAN CLINAC 2100 CD HEAD WITH MAIN COMPONENTES AND SECONDARY SHIELDING. ..... 96
FIGURE 39 - MCNP6 WATER PHANTOM MODEL WITH SOME POSITIONS OF THE IONIZING CHAMBER FOR PDDS. ..... 97
FIGURE 40 - MCNP6 WATER PHANTOM MODEL WITH SOME POSITIONS OF THE IONIZING CHAMBER FOR DOSE PROFILES. ..... 98
FIGURE 41 - ENERGY DEPOSITION CALCULATED USING A MESH TALLY TYPE 3 PLOT . ..... 100
FIGURE 42 - AVERAGE PHOTON AND ELECTRON FLUX AS A FUNCTION OF DEPTH IN THE WATER PHANTOM, NORMALIZED TO THE NUMBER OF GENERATED/SOURCE PARTICLES. ..... 101
FIGURE 43 - MEASUREMENTS AND MCNP SIMULATIONS OF THE DLS FOR 0.5, 1, 5, 10 AND 20 MM GAP SIZES. ..... 102
FIGURE 44 - BEAM PROFILE MEASUREMENT OBTAINED BY PTW™ MEPHYSTO SOFTWARE. ..... 103
FIGURE 45 - IN-FIELD COMPARISON OF MEASURED AND CALCULATED PDDS FOR A 5 X 5 $CM^2$ FIELD. ..... 104
FIGURE 46 - IN-FIELD COMPARISON OF MEASURED AND CALCULATED PDDS FOR A 10 X 10 $CM^2$ FIELD. ..... 105
FIGURE 47 - IN-FIELD COMPARISON OF MEASURED AND CALCULATED DOSE PROFILES FOR A 10 X 10 $CM^2$ FIELD ..... 106
FIGURE 48 - IN-FIELD COMPARISON OF MEASURED AND CALCULATED DOSE PROFILES FOR A 30 X 30 $CM^2$ FIELD. ..... 107
FIGURE 49 - OUT-OF-FIELD COMPARISON OF MEASURED AND CALCULATED DOSE FOR A 5 X 5 CM2 FIELD.... 108
FIGURE 50 - OUT-OF-FIELD COMPARISON OF MEASURED AND CALCULATED DOSE FOR A 10 X 10 $CM^2$ FIELD. 109
FIGURE 51 - 5 YEARS OLD ATOM 705-D ANTHROPOMORFIC PHANTOM FROM CIRS. ..... 115
FIGURE 52 - COMPUTED TOMOGRAPHY SCANNER WITH PAEDIATRIC PHANTOM IN SUPINE POSITION INSIDE THE GANTRY. ..... 116
FIGURE 53 - WHOLE BODY DEFINITION IN A THORACIC AXIAL SLICE. ..... 117
FIGURE 54 - SKIN DEFINITION IN A THORACIC AXIAL SLICE. ..... 118
FIGURE 55 - REMOVAL OF SKIN IN A THORACIC AXIAL SLICE. ..... 118
FIGURE 56 - LUNGS DEFINITION IN A THORACIC AXIAL SLICE. ..... 119
FIGURE 57 - REMOVAL OF LUNGS IN A THORACIC AXIAL SLICE. ..... 119
FIGURE 58 - BONES DEFINITION IN A HEAD AXIAL SLICE. ..... 120
FIGURE 59 - REMOVAL OF BONES IN A THORACIC AXIAL SLICE. ..... 120
FIGURE 60 - THORACIC AXIAL SLICE AFTER REMOVING ALL STRUCTURES. ..... 121
FIGURE 61 - THORACIC AXIAL SLICE OF THE VOXEL PHANTOM. ..... 122

FIGURE 62 - VOXELIZED PHANTOM IN IMAGEJ 3D VOLUME VIEWER. LEFT: FRONT VIEW RIGHT: LATERAL VIEW. ..... 123
FIGURE 63 - REFERENCE SLICE WITH RADIOPAQUE MARKERS. ..... 124
FIGURE 64 - AXIAL VIEW OF THE VOXELIZED PHANTOM IN IMAGEJ SOFTWARE. ..... 125
FIGURE 65 - SAGITTAL VIEW OF THE VOXELIZED PHANTOM IN IMAGEJ SOFTWARE. ..... 125
FIGURE 66 - CORONAL VIEW OF THE VOXELIZED PHANTOM IN IMAGEJ SOFTWARE. ..... 126
FIGURE 67 - AXIAL VIEW OF THE VOXEL PHANTOM IMPLEMENTED IN MCNP6. ..... 126
FIGURE 68 - SAGITTAL VIEW OF THE VOXEL PHANTOM IMPLEMENTED IN MCNP6. ..... 127
FIGURE 69 – CORONAL VIEW OF THE VOXEL PHANTOM IMPLEMENTED IN MCNP6. ..... 128
FIGURE 70 – ORIGIN DEFINITION. ..... 133
FIGURE 71 – PTV DEFINITON.. ..... 135
FIGURE 72 – AXIAL SLICE OF THE PHANTOM.. ..... 136
FIGURE 73 – VOLUMETRIC RECONSTRUCTION OF THE SEGMENTED VOLUMES. ..... 137
FIGURE 74 – FIELD ARRANGEMENT FOR 3DCRT PLAN. ..... 139
FIGURE 75 – ASSESSMENT OF 95% OF PRESCRIBED DOSE IN PTV. ..... 140
FIGURE 76 – DVH OF THE 3DCRT PLAN. A: OVERVIEW OF THE DVH; B: DETAIL OF THE OAR. ..... 141
FIGURE 77 – IMRT FIELD ARRANGEMENT. ..... 143
FIGURE 78 – DVH OF THE IMRT PLAN. A: OVERVIEW OF THE DVH; B: DETAIL OF THE OAR. ..... 146
FIGURE 79 – EXAMPLE OF TLDS PLACEMENT IN THE PHANTOM. ..... 147
FIGURE 80 – DOSES CALCULATED BY THE TPS FOR ALL STRUCTURES.. ..... 154
FIGURE 81 – OUT-OF-FIELD MEAN ORGAN DOSES MEASURED BY TLDS FOR THE 3DCRT AND IMRT TECHNIQUES. ..... 157
FIGURE 82 – OUT-OF-FIELD ORGAN DOSES CALCULATED BY MC SIMULATIONS USING MCNP6. ..... 160
FIGURE 83 – COMPARISON OF DOSE DISTRIBUTIONS BETWEEN THE 3DCRT AND IMRT TECHNIQUES UP TO A MINIMUM DOSE OF 500 MGY ..... 162
FIGURE 84 – COMPARISON OF DOSE DISTRIBUTIONS BETWEEN 3DCRT AND IMRT TECHNIQUES UP TO A MINIMUM DOSE OF 10000 MGY ..... 164
FIGURE 85 – COMPARISON BETWEEN DOSES OUTSIDE THE TREATMENT FIELDS OBTAINED BY TPS VS TLD FOR 3DCRT. ..... 166
FIGURE 86 – COMPARISON BETWEEN DOSES OUTSIDE THE TREATMENT FIELDS OBTAINED BY MCNP6 VS TLD FOR 3DCRT. ..... 167
FIGURE 87 – COMPARISON BETWEEN DOSES OUTSIDE THE TREATMENT FIELDS OBTAINED BY TPS VS TLD FOR IMRT. ..... 168
FIGURE 88 – COMPARISON BETWEEN DOSES OUTSIDE THE TREATMENT FIELDS OBTAINED BY MCNP6 VS TLD FOR IMRT. ..... 169

# LIST OF ABBREVIATIONS

| | |
|---|---|
| 3DCRT | Three Dimensional Conformal Radiation Therapy |
| AAA | Analytical Anisotropic Algorithm |
| AAPM | American Association of Physicists in Medicine |
| ALARA | As Low As Reasonable Achievable |
| ARPANSA | Australian Radiation Protection and Nuclear Safety Agency |
| BEIR | Biological Effects of Ionizing Radiation |
| $C^2TN$ | Centro de Ciência e Tecnologias Nucleares |
| CBCT | Cone Beam Computed Tomography |
| CI | Conformity Index |
| CT | Computed Tomography |
| CTV | Clinical Target Volume |
| DSL | Dosimetric Leaf Separation |
| dMLC | Dynamic Multi-Leaf Collimator |
| DVH | Dose Volume Histogram |
| ESTRO | European Society for Radiotherapy and Oncology |
| EUD | Equivalent Uniform Dose |
| FCUL | Faculdade de Ciências da Universidade de Lisboa |
| FF | Flattening Filter |
| FWHM | Full Width at Half Maximum |
| GTV | Gross Tumour Volume |

| | |
|---|---|
| HI | Homogeneity Index |
| IAEA | International Atomic Energy Agency |
| ICRU | International Commission on Radiation Units and Measurements |
| ICRP | International Commission on Radiological Protection |
| IGRT | Image-Guided Radiotherapy |
| IMRT | Intensity Modulated Radiation Therapy |
| IPOLFG | Instituto Português de Oncologia de Lisboa Francisco Gentil, E.P.E. |
| KERMA | Kinetic Energy Released Per Unit of Mass |
| LINAC | Linear Accelerator |
| MC | Monte Carlo |
| MCNP | Monte Carlo N-Particle |
| MCNPX | Monte Carlo N-Particle Extended |
| MIRD | Medical Internal Radiation Dose |
| MLC | Multi-Leaf Collimator |
| MRI | Magnetic Resonance Imaging |
| NCRP | National Council on Radiation Protection & Measurements |
| NIST | National Institute of Standards and Technology |
| NTCP | Normal Tissue Complication Probability |
| OAR | Organs at Risk |
| PET | Positron Emission Tomography |
| PDD | Percentage Depth Dose |
| PMMA | Polymethylmethacrylate |

| | |
|---|---|
| PRV | Planning Organ at Risk Volume |
| PTV | Planning Target Volume |
| RF | Radiofrequency |
| sMLC | Static Multi-leaf Collimator |
| SAR | Scatter-air Ratio |
| SDEF | Source Definition |
| TAR | Tissue-to-air Ratio |
| TCP | Tumour Control Probability |
| TPS | Treatment Planning System |
| UNSCEAR | United Nations Scientific Committee on the Effects of Atomic Radiation |
| VMAT | Volumetric Modulated Arc Therapy |
| WWG | Weight Window Generator |

# SECTION I - INTRODUCTION

# CHAPTER 1 – BACKGROUND AND MOTIVATION

## 1.1. INTRODUCTION

Radiotherapy is a form of cancer treatment that uses ionizing radiation to deliver a prescribed radiation dose to the target volume, while minimizing the dose received in the organs at risk (OAR) and healthy tissues [1,2].

Intensity-modulated radiation therapy (IMRT) is a powerful and sophisticated technique often preferred to three dimensional conformal radiation therapy (3DCRT) because it allows to deliver lower doses to the OAR and to obtain better target dose conformity and dose homogeneity [3]. However, when IMRT is used, healthy tissues are exposed to higher low dose values, which may increase the risk of occurrence of radiation-induced second malignancies [3–5]; this increase of risk is particularly important to be considered and must be evaluated in radiation therapy treatments of paediatric patients. These low doses in the healthy tissues are often referred to as out-of-field doses and are essentially due to scattered radiation within the patient's body and to scattered radiation in the head of the linear accelerator (LINAC) used in radiotherapy [1]. The assessment of the out-of-field doses with a detailed modelling and simulation of a LINAC and Mega voltage (MV) beams, can be performed using Monte Carlo (MC) methods [1,6], that offer as well an accurate methodology to simulate human organs and tissues, represented by sophisticated anthropomorphic computational phantoms.

Dose assessment in patients undergoing radiotherapy is performed within the treatment field, as well as in the OAR closest to the target volume and treatment planning systems (TPS) do not adequately calculate the dose a few centimetres from the penumbra [3,4]. Therefore, it is mandatory to evaluate the dose outside the treatment field, performing physical phantom measurements, MC simulations and using information obtained from the TPS. Therefore, out-of-field doses are a cause of clinical concern in the development of secondary malignant neoplasms, particularly in paediatric patients. A second tumour is defined as a histologically distinct tumour that

develops after the first malignant tumours. Radiation-induced tumours can be the price of success if the primary tumours is cured, or at least controlled [5]. There is consensus within the scientific community that the increasing use of the IMRT technique might presumably lead to the development of second cancers [7,8].

### 1.2. PAEDIATRIC CANCER

In the last 30 years the incidence of paediatric tumours has increased by about 0.5% in children and 1% in adolescents and it was found that between 1991 and 2010 this incidence gradually increased [9]. In the last decade, incidence rates have remained stable [9,10], but mortality rates have continuously decreased [10]. In the last three decades with new treatments tailored to paediatric patients, including surgery, radiotherapy and chemotherapy, there was an improvement in survival [10] of 2.7% for patients under 19, compared to 1.4% for adults [10]. The peak incidence of paediatric tumours occurs at ages between 1 and 5 years old and later between 15 and 20 years old [10]. In developed countries, more than half of cancer patients receive radiotherapy at some stage of their treatment [11].

Figure 1 shows that leukaemia represent the most frequent type of tumour in children, however, the most frequent tumours treated with radiotherapy are brain and central nervous system tumours [10,12]. Tumours of the central nervous system represent 30% of all paediatric tumours [13] and their treatment requires radiotherapy in over 50% of cases [2,14]

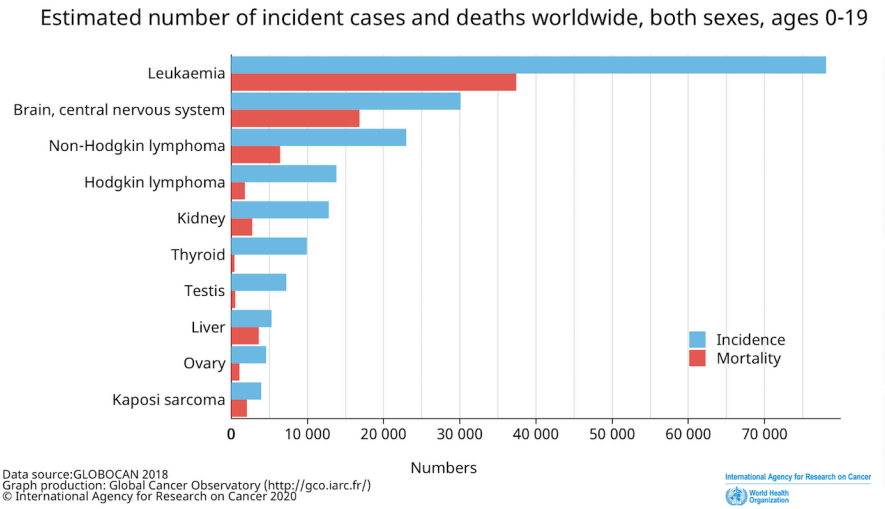


**Figure 1 –** Incidence and mortality rates per tumour type worldwide in 2018, both sexes, ages 0-19 (adapted from [12]).

Paediatric patients´ irradiation is extremely challenging, mainly because each tissue in the irradiated volume is potentially at risk for toxicity and tolerance doses are often lower, when compared to adults [5,10]. This is because at a younger age cells are more sensitive to radiation during the period of cell proliferation [5,8,15,16]. For example, in children, no more than 18 Gy can be administered to bone tissues because they are in the growth phase, whereas in adults this will not be a concern [10]. Additionally, doses of more than 5-10 Gy in the ovaries or testicles can lead to infertility. Another example is irradiation of the pituitary gland with doses above 20 Gy, which may result in a reduction in hormone production [10]. When assessing late side effects of radiation to the healthy structures of the brain it is found that they are particularly sensitive to the total dose, dose per fraction and volume of the radiated brain [13]. Thus, radiotherapy treatment of paediatric patients requires an increased concern about side effects, which can become very detrimental for the patient's quality of life [17].

Through epidemiological studies, there is scientific evidence that low organ doses, namely 30 to 90 mSv, result in an increased cancer risk [18]. The lifetime attributable risk (LAR) to a single small dose of radiation at a certain age is higher for children, however, decreases with age [19], although children have a longer lifetime risk of developing radio-induced tumours when compared to adults. The LAR is the probability of developing a tumour due to exposure to ionizing radiation in an individual representative of the population [20]. The latency period of a radiation induced tumour can be 30 to 40 years after radiation treatment. It is estimated that the cumulative risk is about 2 to 11% during a follow-up period of 25 years. After about 10 years, the risk may stabilize for some types of tumours such as non-Hodgkin's lymphoma and acute nonlymphocytic leukaemia, however, for other types of tumours it may increase to more than 20 years after treatment [21]. Through data from the Committee on the Biological Effects of Ionizing Radiation (BEIR) [22] and the United Nations Scientific Committee on the Effects of Atomic Radiation (UNSCEAR) [23], the International Commission on Radiological Protection (ICRP) estimated that the lifetime risk of death from cancer for the working population is 0.08/Sv for high-dose radiation and 0.04/Sv for low-dose radiation. For young people the values are 0.1/Sv for high-dose radiation and 0.5/Sv for low-dose radiation [24].

During the last decade, significant improvements have been made in the treatment of this type of tumours, resulting in a higher survival of patients [13], and currently, approximately 74% of children diagnosed with central nervous system tumours will

have a 5-year survival [25]. On the other hand, as shown in Figure 2, it is estimated that there will be 6.7 million cases of paediatric tumours worldwide between 2015 and 2030 [26].

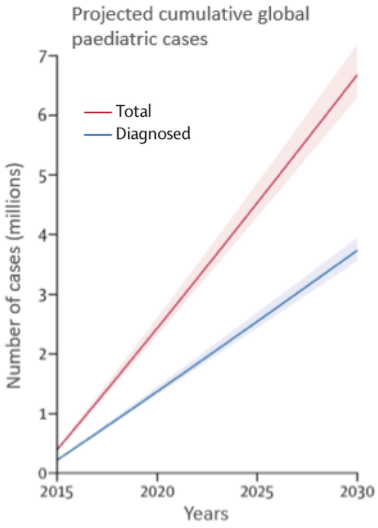


**Figure 2 –** Estimation between 2015-2030 of incident global paediatric cases (adapted from [26]). Shaded zones represent 95% of the confidence interval.

According to the literature more than 70% of paediatric cancer patients will be long-term survivors [4], which makes it more likely that side effects of previous treatments will occur.

Meduloblastoma and low-grade glioma are the two most common solid tumours in childhood, with a survival rate between 60-85% [10,13]. Despite improvements in therapeutic approaches, brain radiotherapy results in inflammation, angiogenesis and cell death, causing damage to white and grey matter. Thus, children who undergo radiotherapy of the central nervous system often present long-term decrease and disorders in cognitive functions, such as attention, working memory, processing speed, learning, and verbal and visuoespacial abilities [13]. Moreover, a growing number of individuals who survived a tumour in their childhood develop neurological deficits, depression, anxiety, headaches, dizziness and decreased social behaviour during adulthood, negatively affecting their quality of life [13].

## 1.3. 3D CONFORMAL RADIOTHERAPY

Three-Dimensional Conformal Radiotherapy (3DCRT) was introduced in the early 1960s and is an extension of conformal radiotherapy with the inclusion of 3D treatment planning [27]. The main aim of 3DCRT is to administer a high conformal dose to the target volume, while minimizing the dose in healthy tissues [27,28]. This goal can only be achieved if there are imaging resources, such as conventional X-ray imaging, computed tomography, magnetic resonance imaging and positron emission tomography, so that it is possible to accurately define and delineate the target volume and the organs at risk [27]. In addition, for treatment planning, an accurate and reproducible positioning system should also be used so that the requisites for 3DCRT are accomplished.

The most common modality of radiation administration for paediatric tumours is 3DCRT, in which the treatment beams are modified and beam apertures moulded with Multi-Leaf Collimators (MLC) or blocks to the target volume [13,29]. The 3DCRT can be divided into two different types/classes, one applying only a geometric conformation of the treatment fields, while the other also models the intensity of the fluency in the geometrically conformed field [30].

In 3DCRT, the dose distribution is conformed in such a way that the high dose region is in the target volume. In neighbouring healthy tissues, the dose should be kept below the tissue tolerance limits. Each type of tissue has its own radiation tolerance dose and when this is exceeded, side effects are expected [31]. In radiotherapy it is assumed that when there is a dose reduction in healthy tissue, the dose given to the target volume can be increased [31]. An increase in dose to the target volume will translate into a higher tumour control probability, while a decrease in dose to healthy tissue will allow a decrease in side effects, i.e. a lower probability of complications in healthy tissue [31]. However, there is a problem, i.e. the depth dose profile of a photon beam is described by an exponentially decreasing function of the depth. This implies that the dose is usually higher near the surface than at the depth location of the tumour [31]. To improve this situation, more than one treatment beam is often used. In the region of overlapping beams, there is a higher dose delivered. If the beams are adapted three-dimensionally to the planning target volume (PTV), then the overlap region should include PTV [31]. However, this is not the case when there are simple beam configurations and the organ at risk is close to the target volume. Therefore, more complex beam configurations will be required to achieve an acceptable dose distribution and a better conformation of the dose distribution to the tumour volume. An

important step in 3DCRT was the introduction of irregular fields performed with blocks. Cerrobend blocks proved to be time consuming and expensive and MLC were developed [27]. MLCs are devices that adapt the treatment beam to the shape of the target volume and consist of two banks of opposite leafs that collimate the beam and can move independently from each other [27].

After what we have said it is logical to expect that the conformation of the dose distributions can be increased by using beams individually adapted to the shape of the tumour. However, there are cases, especially with concave and mobile target volumes, where conventional planning and treatment techniques fail.

### 1.4. INTENSITY-MODULATED RADIATION THERAPY

Recent irradiation techniques, such as Intensity-Modulated Radiation Therapy (IMRT), were developed to be able to avoid healthy tissue areas such as healthy brain tissue, allowing the reduction of neurocognitive side effects induced by irradiation when treating brain tumours [13]. Compared to 3DCRT, IMRT uses several beams of modulated intensity, which allows to obtain dose distributions more homogenous and highly conformed to the tumour volumes, whilst sparing the surrounding healthy tissues [28,32–35] and reducing deterministic effects [36].

IMRT is a advanced method of 3DCRT [30,37]. Although 3DCRT facilitates a dose increase in target volumes and/or a lower dose in healthy tissues [38], IMRT can still lead to an improvement in treatment. IMRT uses a sophisticated radiation beam administration to improve the conformation of the dose distribution around the tumour volume. This is achieved by varying the intensities of the beam within a field, as opposed to the uniform intensity beam used in 3DCRT [37] , as can be seen in Figure 3. This variation in intensity can only be obtained through the movement of MLCs. The IMRT combines patterns of non-uniform intensity in each irradiation field to obtain a uniform dose at the target volume [38]. The beam intensity is modified depending on whether the tumour or a healthy tissue is in its path. For this reason the beam is divided into multiple segments, which are the essence of IMRT, i.e. in a treatment session, IMRT allows to treat only a portion of the PTV at a given time [28]. When a given segment of the beam reaches a healthy tissue, its intensity is lower than the intensity of a segment that reaches the tumour, allowing complex dose distributions [38]. In IMRT, the fluency of the particles in the radiation beam is varied, which allows a greater conformation to the tumour and the creation of concave isodose profiles.

Specifically, it is not only the shape of the controlled beam, but the combinations of opening and closing of the MLC that model the intensity [39]. For this reason, IMRT provides a significant improvement in dose delivery compared to conventional treatments. It also provides an unprecedented ability to dynamically vary the conformed dose to the tumour shape from different angles and to spare normal tissues and organs at risk that may be potentially damaged during treatment [39,40]. Figure 3 shows the differences between the two techniques.

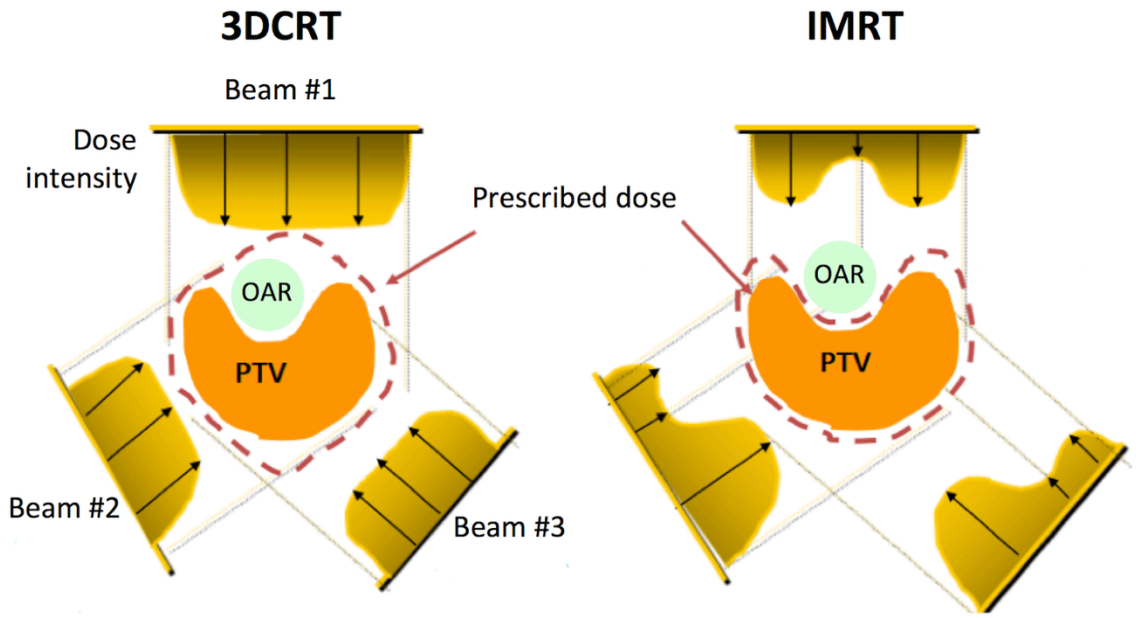


**Figure 3 -** Differences between 3DCRT and IMRT.

Of all the possible ways to administer IMRT, the use of MLC in LINACs is the most common form [37]. MLCs can be used both in static mode - Step and Shoot (sMLC) and dynamic mode - Sliding Window (dMLC) [41]. Both techniques require a computational control of the MLC, but differ in the fact that during irradiation, in the dMLC technique the leafs are in continuous movement, while in the sMLC technique a sequence of multiple fields is used, each with a fixed shape and its own predetermined radiation dose [37]. In the latter, after administering the dose of the first subfield the beam is ceased, the form of MLC is modified and the beam is switched back on to administer the second subfield, and so on [37,40].

The disadvantage of the IMRT technique is that it has a large number of monitor units (MU) compared to 3DCRT due to the movement of the MLC during irradiation [41].

More details about IMRT technique are provided in section 3.2.4.

## 1.5. UNWANTED DOSES IN RADIOTHERAPY

With the new treatment techniques, such as IMRT, it is possible to achieve high conformation in the PTV, with lower unwanted doses delivered to the healthy tissues in the patient's body [4,29,42–46]. These doses are called out-of-field doses and are due to the linear accelerator gantry leakage radiation, the scattered radiation from collimation devices and beam modifiers and the scattered radiation inside the patient's body [16,32,34,43,44,47–49]. One of the major sources of the leakage and scattered radiation in the head of the equipment is due to the presence of the flattening filter (FF) and it has been demonstrated that without the use of this filter, there is a reduction of the leakage radiation of 58% at one meter from the treatment fields. Since IMRT can be planned and administered without the FF, then peripheral doses can be significantly reduced, decreasing the incidence of second tumours [32].

For most clinical situations, it is assumed that organs distant from the target volume receive a small dose and are not accounted for as part of the treatment planning of patients undergoing radiotherapy [7], because such dose is significantly lower compared to the prescribed dose for the target volume [48]. However, it is known that low doses, between 50 mGy [50] and 100 mGy [51] outside the treated volume, increase the radiological risk of developing second tumours [7,15,43,50].

## 1.6. OBJECTIVES, METHODOLOGY ANS STRUCTURE OF THE PHD THESIS

In this thesis out-of-field doses in radiotherapy treatments of paediatric patients undergoing brain irradiation are evaluated and assessed.

The main objective of this study is to compare the doses outside the treatment field with the IMRT and 3DCRT techniques, for paediatric tumours. The methodology used combines:

- Dosimetric measurements performed in clinical settings at a reference oncology hospital in Portugal - Instituto Português de Oncologia de Lisboa Francisco Gentil, E.P.E. (IPOLFG) using appropriate radiation detection equipment (ionization chambers, dosimeters) and a physical paediatric phantom.
- Modelling and simulation, using MC methods with anthropomorphic voxel phantoms. A MC computer program (MCNP) representative of the state-of-the-

art in particle transport simulation is used to assess organ doses, particle fluencies and other relevant dosimetric quantities.

- Dosimetric results obtained using Treatment Planning Systems routinely in radiotherapy treatments.

The study and reported results include the:

- Development and implementation, for the first time, of a model of the Millenium™ 120-leaf MLC coupled to the Varian 2100 CD Clinac head.
- Validation, for the first time, of the 6 MV in-field and out-of-field beam of Varian 2100 CD Clinac head, using measurements and MC calculations.
- Creation of an anthropomorphic voxel phantom from a physical paediatric phantom, using computed tomography images.

The document is organized in 4 main sections with 8 chapters as follows:

- Section 1 presents the first chapter describing the background and motivation. In this chapter an introduction is made to the problem of the study and the concepts of the study are briefly presented as well as the structure and objectives of the thesis.
- Section 2 presents the theoretical principles of the thesis divided between chapters 2, 3 and 4. In Chapter 2 the concepts of radiation protection and dosimetry in radiotherapy are addressed. In Chapter 3 notions about conformal radiotherapy physics, treatment planning and clinical aspects are presented. In chapter 4 concepts related to MC methods and human phantoms are discussed.
- Section 3 highlights the methods and results of the thesis divided into 5, 6 and 7 chapters. Chapter 5 presents the out-of-field and in-field validation of 6 MV LINAC. Chapter 6 describes the creation of the paediatric computational phantom. In Chapter 7 the assessment of out-of-field doses in paediatric patients is presented.
- Section 4 outlines in Chapter 8 the conclusions of the research and the future work.

# SECTION II – THEORETICAL PRINCIPLES

# CHAPTER 2 – RADIATION PROTECTION AND DOSIMETRY IN RADIOTHERAPY

The use of ionizing radiation for medical applications represents more than 99.9% of the per capita dose from anthropogenic sources [52]. In 1980, it was estimated that 1.7 billion clinical procedures using ionizing radiation were performed worldwide whereas in 2007 this number was of almost 4 billion [53]. Globally, the benefits of using ionizing radiation in medicine largely outweigh the losses [54]. The main areas in medicine using ionizing radiation are radiotherapy, radiology, nuclear medicine an interventional procedures [55].

## 2.1. CLASSIFICATION OF RADIATION

With respect to its interaction with matter, radiation can be classified into two main categories: ionizing radiation and non-ionizing, depending on whether it may cause, or not, the ionization of atoms or molecules. Ionizing radiation can directly or indirectly ionize matter.

Directly ionizing radiation includes charged particles ($\alpha$ particles, heavy ions, protons and electrons) that deposit their energy in a material mainly through inelastic Coulomb interactions. Indirectly ionizing radiation comprises neutral particles (photons and neutrons) that deposit their energy in the material through two steps process [56]:

1. A charged particle is released in the material due to an interaction induced by the neutral particle;
2. The released particle deposit energy in the material through Coulomb interactions.

In radiotherapy, both directly and indirectly ionization radiations are used to treat cancer patients.

## 2.2. UNITS AND QUANTITIES OF EXTERNAL DOSIMETRY RELEVANT FOR RADIOTHERAPY

The medical use of ionizing radiation requires accurate dose measurements [56]. During radiation treatments, the prescribed dose should be delivered to the PTV, increasing the tumour control probability and decreasing the normal tissue complication probability. Different quantities and units should be considered throughout this process, including exposure, fluence, kinetic energy released in material (kerma) and absorbed dose.

### 2.2.1. EXPOSURE

The exposure, $X$, can be defined as the quotient between $\Delta Q$ and $\Delta m_{air}$, where $\Delta Q$ is the amount of charge produced by ionization induced by a photon radiation field inside a volume of air of mass, $\Delta m_{air}$,

$$X = \frac{\Delta Q}{\Delta m_{air}} \quad (2.1)$$

The unit used to quantify exposure is the roentgen (R). One R represents a charge of $2.58 \times 10^{-4}$ C created in a kilogram of air [56,57]. Exposure can only be used to quantify the intensity of a photon radiation field (and the ionizations it causes) in air.

### 2.2.2. FLUENCE

Fluence, $\Phi$, is given by the quotient of $dN$ by $da$, where $dN$ is the number of photons incident on a sphere and $da$ is cross-sectional area of the sphere [58]

$$\Phi = \frac{dN}{da} \quad (2.2)$$

The fluence, $\Phi$, is expressed in $m^{-2}$ [58].

### 2.2.3. KINECTIC ENERGY RELEASED PER UNIT OF MASS (KERMA)

KERMA, K, is the quotient of $dE_{tr}$ by $\mathrm{dm}$, where $dE_{tr}$ is the mean sum of the initial kinetic energies of all charged particles liberated by uncharged ionizing radiation per unit of mass and $\mathrm{dm}$ is the mass of the material [56,58],

$$K = \frac{dE_{tr}}{dm} \quad (2.3)$$

and it is expressed in J.kg$^{-1}$ (S.I.) units or using the special unit Gray (Gy). The values of KERMA and absorbed dose are approximately the same in the case of low-energy photons. For example, if a 50 keV photon interacts in a small tumour volume, the electron range in the tissue is 40 μm and can be ignored and limited to the target volume, because the energy transferred in collision is locally absorbed by the material [59].

For high-energy photons, i.e. for energy photons higher than 1 MeV, the KERMA value is higher than the absorbed dose values, since x-rays and some highly energetic electrons leak the target volume before depositing their energy [56,59]. The air mass used to measure Kerma is the same as that used to measure radiation dose. The Kerma, K, as two components: the collision kerma, $Kcol$ and the radiative kerma, $Krad$ [56].

$$K = Krad + Kcol \quad (2.4)$$

For photons, the radiative kerma, $Krad$, defines the initial kinetic energy of the secondary particles, due to bremsstrahlung. The collision kerma, $Kcol$, is the result of Coulomb force interactions with electrons in material and is equal to the absorbed dose, when charge particles equilibrium occurs [56].

### 2.2.4. Absorbed Dose

The absorbed dose, *D*, is the energy deposited by the particle's constituent of the radiation field per unit mass of the material they cross and is defined as:

$$D = \frac{\Delta E_{ab}}{\Delta m} \quad (2.5)$$

where $\Delta E_{ab}$ is the deposited energy and $\Delta m$ is the mass of material. The absorbed dose, *D*, is expressed in J.kg$^{-1}$ (S.I.) units or Gy [56,58,59].

### 2.2.5. Equivalent Dose

The equivalent dose ($H_T$) is the dose absorbed by the tissue or organ, $T$, weighted according to type and quality of radiation, $R$, defined by:

$$H_{T,R} = w_R \times D_{T,R} \quad (\text{Eq. } 2.6)$$

where $D_{T,R}$ is the average absorbed dose to the tissue or organ, $T$, and $w_R$ is the weighting factor of the type of radiation. The unit of measurement for the equivalent dose J.kg$^{-1}$ and its special designation is Sievert (Sv) [60].

### 2.2.6. EFFECTIVE DOSE

Effective dose, $E$, is the sum of the equivalent weighted doses in all tissues and organs of the body, resulting from internal and external irradiation, which is defined by:

$$E = \sum_T w_T \times H_T = \sum_T w_T \times \sum_R w_R \times D_{T,R} \quad \text{(Eq.2.7)}$$

where $D_{T,R}$ is the mean absorbed dose to the tissue or organ, $T$, as a result of radiation $R$, $w_R$ is the weighting factor for the type of radiation and $w_T$ is the tissue or organ weighting factor, $T$. The unit of measurement for the equivalent dose is J.kg$^{-1}$ and its special designation is Sievert (Sv) [60].

## 2.3. INTERACTION OF PHOTONS WITH MATTER

As described previously, photons ionize matter indirectly and transmit their energy to electrons, which deposit afterwards most of their energy in the material [59]. An x-ray photon can interact with matter in several different ways: photoelectric effect, Compton scattering, electronic pair production, nuclear pair production, Rayleigh scattering and photonuclear reactions [2,56,59].

The forms of interaction of photons with matter which are of clinical importance for radiation treatments are the Compton scattering, photoelectric effect and pair production [2], as can been seen in Figure 4. The probability of each type of interaction of photons with matter is dependent on the atomic number, Z, of the material and on the photon energy. For a material with a Z=7, i.e. an atomic number equivalent to tissue and for a monoenergetic photon beam, the photoelectric effect is the dominant interaction for energies below 30 keV. From 30 keV the dominant interaction is the Compton effect until close to 24 MeV. From 24 MeV the pair production becomes the dominant interaction [2]. These interactions are the most important for radiotherapy because they are the most predominant, considering the therapeutic energies used as well as the atomic number of human tissues The most important interaction for

radiation therapy is the Compton scattering, because this effect is dominant at therapeutic energies [59].

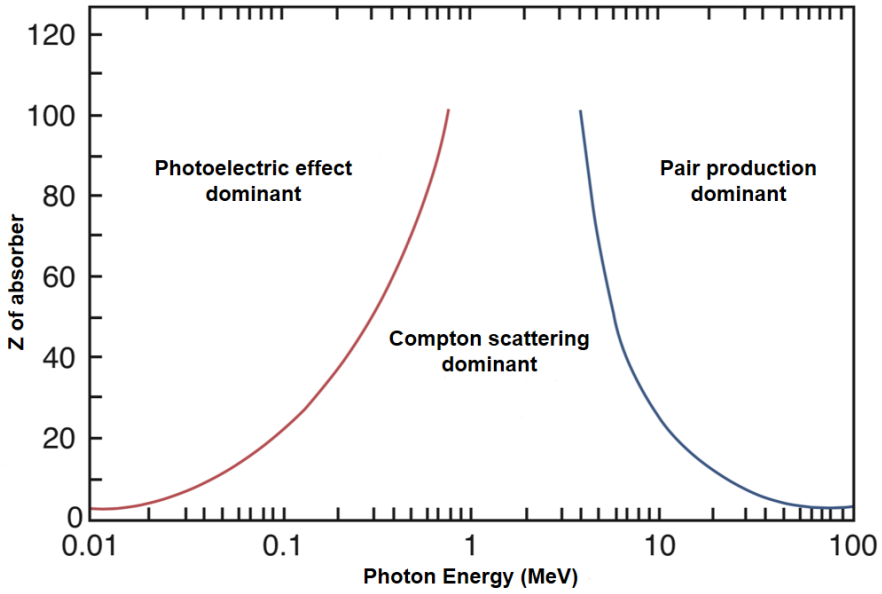


**Figure 4 -** Main photon interactions with matter (adapted from [2]).

The photoelectric effect is dominant at lower energies and at higher Z elements, Compton scattering predominates at intermediate energies and pair production is the main type of interaction at higher energies [58,59]. Generally, Compton scattering decreases as the energy of the incident photon increase and is features low sensitivity with the Z of the element [2,57].

### 2.3.1. PHOTOELECTRIC EFFECT

Currently, for radiotherapy, the photoelectric effect has only an historical importance, because this effect is dominant at low photon energies [57,58], because orthvoltage and superficial therapies use lower photon energies. Currently this effect is predominant when using the image during treatments because energy is used in the order of keV. In photoelectric effect, almost all the energy of the incident photon is transmitted to an orbital electron and afterwards the photon is absorbed. The orbital electron is ejected from the atom with kinetic energy equal to the energy of the incoming photon minus its binding energy [2,57]. The energy of the electron is absorbed in the material where this process happens [57]. The re-distribution of the

orbital electrons following the ejection of the electron, leads to the release of characteristic x-rays and Auger electrons [2,56,59], as detailed in Figure 5.

The neutral atom turns out to be a positively charged ion after the removal of the electron, with a gap in an inner shell that needs to be filled. The atom becomes stable again, by filling the gap with a close, less tightly bound electron more distant from the nucleus and an Auger electron or characteristic x-rays is emitted [2].

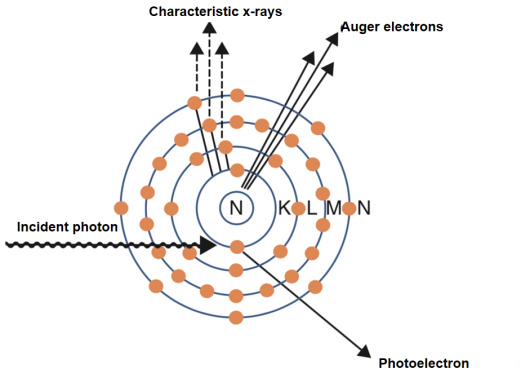


**Figure 5 -** Photoelectric effect (adapted from [2]).

### 2.3.2. COMPTON SCATTERING

In Compton scattering, the incident photon interacts with a electron and some of its energy is transferred to the electron; the photon is deflected at some angle relative to its initial direction and carries the remaining energy is transmitted to another photon [2,56–58], as shown in Figure 6

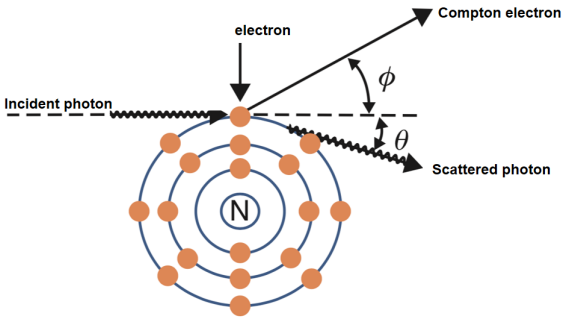


**Figure 6 –** Compton scattering (adapted from [2]).

According to the direction of the incident photon, the Compton electron is limited to angles between 0º and 90º, however, the scattered photon can be scattered at any angle with the direction of the incident photon. The angles decrease with the increase of the incident photon energy and when the energy of the incident photon is low, the scattered photons are scattered with an almost isotropic distribution [2,56].

### 2.3.3. Pair Production

Nuclear pair production and electronic pair production are often referred to as pair production. In the nuclear pair production process, the incident photon interacts in the proximity of the nucleus and its energy is converted into the creation of an electron-positron pair. At the end of the deceleration the positron annihilates with the orbital electron to create two photons of 511 keV [2,56–59], as can be seen in Figure 7.

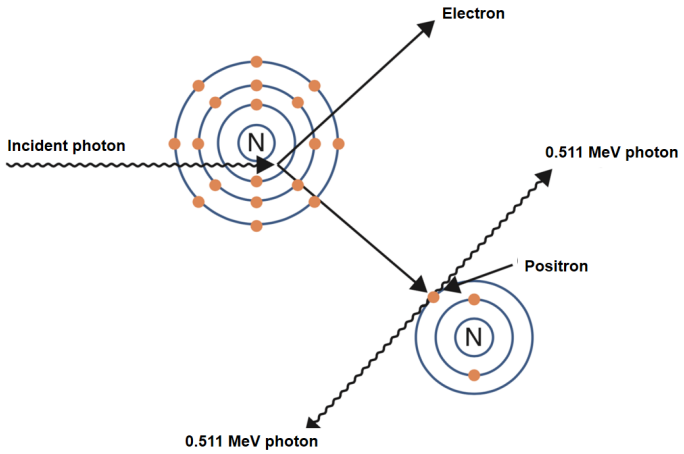


**Figure 7 –** Nuclear pair production (adapted from [2]).

The energy of the incident photon should be at least 1.022 MeV to give origin to pair production [58,59]. When the incident photon interacts with an orbital electron, electronic pair production or triplet production occurs. Though, this process is much less likely than nuclear pair production and the minimum energy of the incident photon is 2.044 MeV. At the end of the process, the incident photon disappears and the original orbital electron and the electron-positron pair are released [56]. Nuclear pair production and electronic pair production are often referred to as pair production.

## 2.4. INTERACTION OF ELECTRONS WITH MATTER

When an electron hits a certain material, several interactions can occur which can be classified into two different types, namely elastic and inelastic interactions. In the elastic interactions no kinetic energy is lost and in inelastic interactions some part of the kinetic energy is transformed into some other form of energy [2]. There are four different situations [2,57,61]: (i) Elastic collisions can occur with the nucleus and result in scattering of the electron. The amount of scattering that occurs depends on the atomic number of the nucleus, i.e. the greater the atomic number, the greater the scattering. (ii) Elastic collisions with the orbital electrons that also lead to the scattering of the incident electron, but there is no energy transfer. In radiotherapy these collisions are important in the attenuation of the beam due to the scattering electrons. This causes changes in dose distributions, especially in situations where there is the junction of media with different atomic numbers, such as bone and muscle. (iii) Inelastic collisions with the orbital electrons lead to a loss of energy from the incident electron to the orbital electron. When the energy is sufficient for the electron to pass to the higher energy level, it is called excitation. The space that has lost the electron is quickly filled by another orbital electron that releases a photon. This photon can generate characteristic x-rays. When enough energy is transferred to an orbital electron, it can leave the atom, leaving it ionized. This electron can cause more ionizations, until it loses its energy: (iv) Inelastic collisions with the nucleus that results in the production of “braking radiation” or bremsstrahlung. The incident electron is deflected from its initial path and loses a portion of its kinetic energy in the form of bremsstrahlung [61].

## 2.5. RADIATION PROTECTION IN RADIOTHERAPY

Medical exposures to ionizing radiation occur in various fields, including in radiodiagnostic, interventional procedures, nuclear medicine and radiotherapy [55,60]. From the moment radiotherapy is adopted as adequate treatment, the radiation protection of the patient, requires an optimal balance between delivering a high dose to the tumour target volume, minimizing the dose to the OAR and avoiding unnecessary exposure of healthy tissues [62,63].

### 2.5.1. RADIATION PROTECTION PRINCIPLES

According to ICRP publication 105, about protection of patients in radiation therapy, there are three fundamental principles of the system of radiation protection: justification of dose, optimization of dose amounts and dose limitation [64]. From these, the principle of justification and the principle of optimization are source-related and applied in therapeutic, diagnostic and interventional procedures. The principle of dose limitation is individual-related because it depends on the dose to which the individual has been exposed in the past. This principle concerns planned exposure scenarios, other than medical exposure of patients and must not exceed the suitable restrictions recommended by the ICRP [60,63–65].

We shall now describe in more detail each one of these principles.

#### 2.5.1.1. The Justification

The justification principle states that for therapeutic purposes, ionizing radiation should be used only when its use produces greater benefit when compared to techniques and procedures not using it [55,58,60,62]. This principle can be reassessed whenever new information or new technology becomes accessible [60].

Exposure of patients to ionizing radiation requires a more detailed analysis and implementation of the justification process, because the fundamental purpose of medical exposures is to bring a greater benefit than harm to the patient [60]

Therefore three levels of justification must be considered [55]:

- Level 1: Know whether the appropriate use of radiation in a clinical context is justified and that such use does more good than harm;
- Level 2: Know whether a certain procedure is justified with a specific objective, to assess whether the potential health improvement due to treatment is greater than the risk of exposure to ionizing radiation. National and international professional entities and/or health or radiological protection authorities must be involved in this level of justification, as the benefits go beyond the direct health benefits for patients only, they include the benefits of their families and society. Likewise, even though a patient receives the highest dose exposures during a treatment using radiation, one must also consider the staff and public exposures, as well as the risk of accidental exposures. Decisions concerning this level of justification may depend on socio-economic conditions, or even the

availability of equipment and trained staff. They may also change over time as new techniques and technologies emerge;

- Level 3: At this level, in addition to the need to justify the general procedure (e.g. the use of radiotherapy), it is also necessary to justify a procedure to an individual patient, under certain situations. For example, a new diagnostic exam could be included at this level, considering that the information from the old exam is already obsolete. Justifications can be provided with prior definition of patient categories as well as their criteria for referral to more complex radiological procedures.

In the particular case of radiotherapy, the International Atomic Energy Agency (IAEA), point to two levels of justification [65,66]:

- Level 1: Exposure to ionized radiation must be justified for both new and existing procedures. The involvement of professional societies must be ensured and they are considered central to this judgement.
- Level 2: Each procedure shall be subject to a new justification, on a case-by-case basis, by the physician responsible for the prescribing the dose.

The decision to undergo radiotherapy is based on a professional judgment of the benefit it brings to the patient's health. The benefit will be the therapeutic outcome, including the direct health benefits to the patient, as well as the societal impact, resulting from medical exposure. Damage caused by absorbed doses to normal tissues is an unavoidable part of a justified procedure. Thus, each procedure must be carefully analysed [66]. The decision to perform a radiotherapy treatment shall be taken by the radiation oncologist responsible for the treatment. The radiation oncologist needs to [65]: (1) Study the appropriate use of imaging and therapeutic procedures, including their advantages and disadvantages, as well as the total dose and side effects; (2) Guarantee that the procedure is medically necessary; (3) Provide advice to the patient (or guardian) on the potential injuries associated with treatment; (4) Getting the informed consent of the patient (or guardian).

The justification process shall consider the efficacy, harm and benefits of using alternative treatments such as surgery or chemotherapy, alone or in combination with radiotherapy [66]. This choice should be influenced by patient preference, staff expertise, availability of alternative treatments and adequate resources [65].

There are exceptional cases that need further justification, namely medical exposure of pregnant patients, as there is literature suggesting that the embryo or fetus is more

sensitive to ionizing radiation than adults. Similarly, radiation therapy for patients under the age of 18 requires a higher level of justification [65]. This is essentially due to the susceptibility of the paediatric individuals to ionizing radiation and the concern about the development of radio-induced tumours, considering that they have a longer life expectancy, during which the side effects of such exposure may manifest themselves. Paediatric radiotherapy is best performed in institutions with oncologic experience of children, linked to paediatric oncology groups that use internationally approved treatment protocols [65].

#### 2.5.1.2. The Optimization

The optimization process applies to all situations that have been considered justified and concerns all exposure situations: existing exposure situations, emergency exposure situations and planned exposure situations [60].

The optimization principle mentions that the number of people exposed, the probability of exposure and the magnitude of individual doses caused by ionizing radiation should be kept as low as reasonably achievable (ALARA), considering social and economic factors should be considered [55,58,60,62,65,67]. To optimize the doses of patients in radiotherapy it is necessary to separate the dose delivery to the target volume and the dose administered in the rest of the patient. The dose at target volume should be high enough to ensure effective treatment. However, to achieve this, optimization of tissue protection outside the target volume involves maintaining doses to these tissues ALARA, in order to decrease the likelihood of serious complications in normal tissues [55,65]. Optimization of protection for medical exposure additionally also involves the prevention of accidents in radiation therapy [63].

Optimization is an iterative process that encompasses [60]: (i) Assessment of the exposure situation; (ii) Definition of a fitting value for dose limitation or reference level; (iii) Selection of the possible protection options; (iv) Definition of the best option under the current circumstances; (v) Application of the chosen option.

The optimization of the protection is related to the management of the radiation dose to the patient considering the clinical objective. The optimization is performed at two levels [55]: (1) In the creation, selection and construction of equipment and facilities and (2) During daily work procedures.

#### 2.5.1.3. Dose Limitation

The general dose limitation principle stipulates that the dose to any individual in planned conditions should not exceed the recommended values [55,60]. These values are defined in order to avoid deterministic radiation dose effects and to decrease stochastic radiation dose effects to an acceptable level [58], i.e., to a level that does not cause harm to the individual. The dose limitation does not apply in the case of medical exposures if it is considered that there is a total benefit to the individual under treatment from exposure to ionizing radiation [55,62]. Thus, the use of dose limits may unnecessarily decrease the dose given on medical settings, reducing the effectiveness of treatments, ultimately inhibiting the achievement of an optimal treatment [55].

### 2.5.2. RADIATION HEALTH EFFECTS

In radiological protection, the effects of ionizing radiation are divided into stochastic effects and deterministic effects[1] [68], as can be seen in Figure 8. Stochastic effects involve the non-lethal modification of somatic or germ cell genetic material of the exposed individual. They are characterized by a probabilistic relationship, that is, the probability for the effect to occur (but not its severity) depends on the dose of ionizing radiation. Deterministic effects or tissue effects result from exposure to ionizing radiation which, above a certain dose threshold causes cellular damage or death, impairing the function of the irradiated tissue or organ [55].

[1] "Deterministic effects" are also referred to as "tissues reactions" according to the latest ICRP recommendations

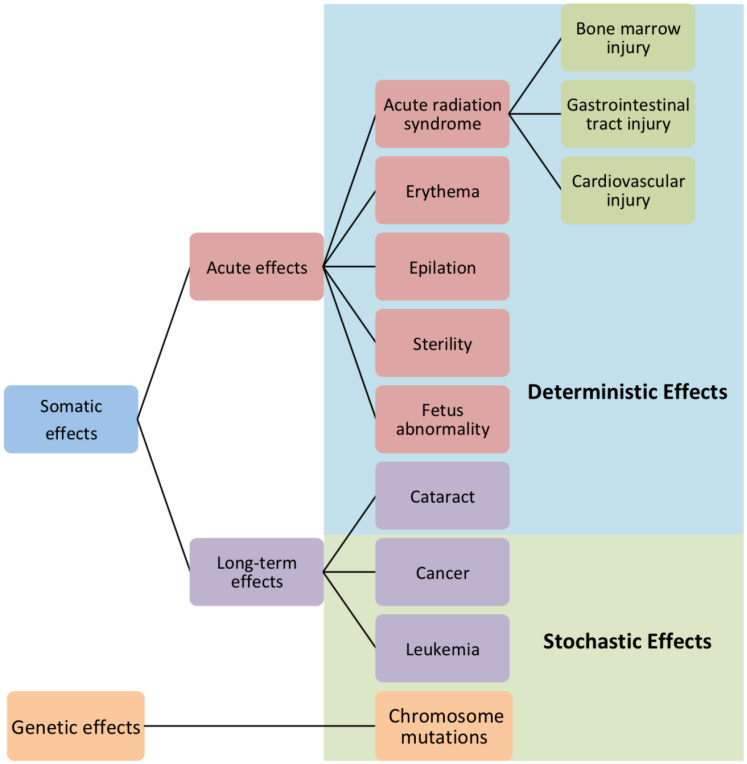


**Figure 8 -** Biological effects of ionizing radiation (adapted from [55]).

#### 2.5.2.1. Stochastic Effects

Stochastic effects occur without threshold dose; the effect probability of these effects increases with dose and the severity of the effect is not related to the magnitude of the exposure to ionizing radiation [55,58,60]. These effects may manifest several decades after the exposure [58]. The most common stochastic effect is cancer, namely leukaemia's and solid tumours. Hereditary effects are less common [55].

##### *2.5.2.1.1. Cancer*

Ionizing radiation is known to cause cancer but is a relatively weak carcinogen. Data from Hiroshima and Nagasaki atomic bombs survivors indicate that only 4.9% of the 17.448 solid tumours are attributed to bombs [69].

Radiation does not cause cancer in different tissues to the same degree. Tissues such as the lungs and breast have a high sensitivity to radiation, while the kidney and bladder have lower sensitivity. Radio-induced tumours are characterised by a latent period between exposure to ionizing radiation and the onset of cancer. The minimum

latency period varies from a few years for non-chronic lymphocytic leukaemia, about 5 years for sarcomas and thyroid tumours and 10 or more years for most other tissues [55]. One study suggested that the latency period for radio-induced leukaemia reaches its peak between 7 to 12 years, while solid tumours require a period longer than 10 years [70], except in sarcomas where the period may be shorter than 10 years [43].

After a total body dose, the risk of developing a tumour is approximately 10% per Gy and the risk of a fatal tumour is approximately half of that [55]. Radio-induced tumours become statistically significant at doses of 150 mSv and above [53]. At lower doses, the risk is difficult to determine, mainly because there is a high incidence of tumours due to other causes [55].

#### *2.5.2.1.2. Chromosome Mutations*

Experiments with fruit flies showed that x-rays are a mutagenic agent and the exposure to ionizing radiation was of great concern. Subsequently, numerous studies with humans involving the progeny of atomic bomb survivors as well as children with paediatric tumours who were treated with radiotherapy, showed no increase in the variety of hereditary effects studied. Additionally, human studies to assess the effects of exposure to ionizing radiation before conception showed no increase in tumours or other anomalies in the offspring [71].

### 2.5.2.2. Deterministic Effects

Deterministic effects or tissue reactions are essentially due to cell death and include, among others, necrosis, ulceration and skin burns. These effects are characterised by a threshold dose, below which no effect is visible and above which the severity of the effect increases with the dose [55,60].

Acute effects can occur minutes, hours, days or even a few weeks after exposure to ionizing radiation. Sub acute effects occur after a few months and finally, the late effects can occur from months to years after exposure. Chronic changes or late effects are often due to fibrosis and/or narrowing or obstruction of small blood vessels, causing tissue necrosis [55].

In radiotherapy the highest doses are delivered to internal organs and therefore its effects are often difficult to evaluate clinically. In that sense they are quite different from the most common deterministic effects of diagnostic and interventional radiology

(erythema, depilation and necrosis with ulceration). However, they also vary with the amount of dose received, its fractionation, the time elapsed since exposure, as well as the volume of irradiated tissue [72].

#### *2.5.2.2.1. Cardiovascular Injury*

Several studies report that after radiotherapy there is a high risk of cardiovascular disease due to the high doses received by the heart or neck. Recent studies show evidence of an increased risk of cardiovascular disease among the atomic bomb survivors, starting at doses of around 0.5 Gy [73,74].

#### *2.5.2.2.2. Cataracts*

For many decades it has been known that after exposure of the eye lenses to high radiation doses (> 2 Gy), led to the development of cataracts (opacity of the eye lens). This indicates that in radiotherapy, fractionated doses over weeks that exceed several Gy can cause cataracts to the patients, a few years after treatment [75]. This type of cataracts caused by exposure to radiation differs from cataracts that appear due to age, because they initially appear at the back of the lens and the irradiation of the lens may form an opaque layer on the anterior area of the lens [58]. The state-of the-art of the scientific knowledge currently indicates that cataracts can be detected after exposure to doses as low as 0.5 Gy [75]; as opposed to the longstanding assumption of a threshold of about 2 Gy for cataracts induced following exposure to gamma or beta radiation [58].

#### *2.5.2.2.3. Fetus Abnormality*

It is known that the risks of fetus abnormality are higher at the beginning of pregnancy, where the formation of the organs begins. Between 8 and 15 weeks of gestation, doses of about 1 Gy in the central nervous system of the fetus result in a high probability of mental retardation. Between 16 and 25 weeks of gestation the risk becomes lower and after this period the risk ceases to exist. On the other hand, there is no evidence that doses below 100-200 mGy cause fetal malformations in humans or even in animals. The risk of developing radio-induced tumours will be further detailed in section 2.4.4.1., particularly in paediatric patients.

### 2.5.3. OUT-OF-FIELD DOSES

It became important to evaluate treatment dose delivery techniques, such as IMRT, since the total number of MU used is often higher than the number of MU required for the treatment of equivalent cases using 3DCRT, with a higher dose in healthy tissue [16,21,29,33,34,40,43,45,76]. Recently, the scientific community has discussed whether the risk of developing second tumours is associated with the increasing use of IMRT [47] in clinical practice, since it involves the delivery of doses to large volumes of tissue outside the treatment field [14,21,32,35,44,45], as detailed in Figure 9.

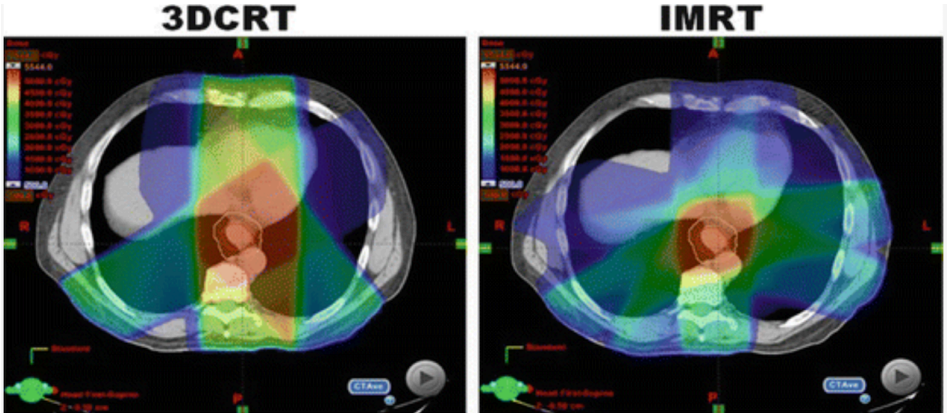


**Figure 9 –** Comparison of a 3DCRT and IMRT plan (adapted from [77]).

Figure 9 shows lower doses in esophageal treatment planning, as well as greater dose conformation to the target volume with IMRT compared to 3DCRT planning.

Ruben et al., in 2011, compared 3DCRT with IMRT, concluding that the out-of-field doses with IMRT increases i) for smaller field dimensions and ii) when there is an increase of the MU or of the distance from the field edge, or iii) when the depth of the measurement decreases [33]. The same authors concluded that the IMRT yields a higher total dose of scattered radiation in the patient than the 3DCRT [33]. Additionally, in another study, other authors found that the IMRT increases the dose throughout the patient's body, when compared with 3DCRT, and may presumably double the incidence of solid tumours in long-term survivors [32].

Sharma et al. [78,79], as well as Klein et al. [80], analysed the doses according to the distance for IMRT treatments with 6MV and 18 MV. Both verified that the 6 MV beams cause higher doses at shorter distances from the treatment field. On the other hand the

18 MV beams showed higher doses at greater distance due to greater radiation leakage [78–80]. Verellen and Vanhavere estimated the equivalent dose of a 6 MV beam as 1.2 x $10^{-2}$ mili-Sievert per monitor unit (mSv/UM) and 1.6 x $10^{-2}$ mSv/UM for 3DCRT and IMRT, respectively [81]. A study developed by Mazonakis et al. showed that for a 6 MV photon beam the dose from scattered radiation can range from 2.6 to 4.4 cGy per treatment, depending on the patient [82].

Although the components of scatter radiation have been investigated for 3DCRT, there is little similar information for IMRT [33]. The results of one study showed that the effective dose and risk of developing cancer is eight times higher with IMRT when compared to conventional radiotherapy [81]. Further studies will be needed to understand the effects of IMRT on the risk of developing second tumours [14,83]. In addition to the new/emerging methods of radiotherapy involve a large number of treatment verification images are associated and these are known to contribute between 5% and 20% of the total dose to organs outside the treatment fields [14].

The scattered radiation inside the patient is the main contributor of dose near the treatment field edge [80], namely for distances of less than 20 cm [76], while the leakage radiation (from the LINAC head) seems to provide the most significant contribution to the absorbed doses at greater distances from the treatment field edge [80] (e.g. more than 20 cm) [76]. Diallo et al. evaluated 115 second tumours and found that 106 tumours occurred at distances between 2.5 and 5 cm outside the irradiated volume and only 9 tumours at distances higher than 20 cm outside the limits of the treatment field [84]. One study showed that in 115 paediatric patients diagnosed with secondary tumours after undergoing radiotherapy, 22% of these tumours were located less than 5 cm from the initial tumour volume and some were located up to 1m away [32].

For IMRT treatments with 6 MV beams, the scattered radiation is essentially due to radiation leakage from the linear accelerator head, as well as to internal patient scattering [46]. For higher than 6 MV energy beams, neutrons are generated by photonuclear reactions [43], but has been shown that neutron doses do not significantly increase the risk of carcinogenesis for IMRT with an 18 MV beam compared to a 6 MV beam [43]. Other authors mention that when IMRT is delivered with energies above 10 MV [32], or even 8 MV [35] neutrons are produced in the head of the equipment. Neutrons can yield significant contribution to the total dose, causing unwanted biological effects such as radio-induced tumours [32,35]. In 2006, Sharma et al. found

that dynamic fields require between 2 and 14 more MU than static fields, to achieve the same dose at the isocenter, obtaining higher peripheral doses for dynamic fields [43].

In the study conducted by Followill et al. on out-of-field doses for IMRT with 6 MV, 18 MV and 25 MV, the authors obtained the equivalent doses, per cGy, of 80 μSv, 6.5 μSv and 10 μSv, respectively. The corresponding neutron doses were 0.0 μSv, 46 μSv and 76 μSv [43]. Using the recommended risk values of NCRP for fatal radiation induced cancers, the researchers calculated the risk of developing tumours between a minimum of 0.4% for 6MV beams and 24.4% for 25 MV beams [43]. The presence of a MLC could influence the peripheral dose, when positioned at the edge of the field. For 6 MV and 18 MV beams, the configuration of the MLC's leafs led to a reduction in peripheral dose of 6% to 50% when compared to fully retracted MLC's [43].

In the work developed by Chibani and Ma, in 2003, cited by Taylor and Kron [43], the code Monte Carlo N-Particle eXtended (MCNPX) was applied to evaluate the resulting dose of nuclear particles (neutrons, protons and alpha particles), originated by the photons interactions. Neutrons were found to contribute more than 75% to the total dose. The equivalent dose due to neutrons, 50 cm away from the treatment field, yields a probability of developing secondary tumours of 1.1%, 1.1% and 2.0%, in a 70 Gy administration by a Siemens linear accelerator with 18 MV, a Varian 15 MV linear accelerator and a Varian 18 MV linear accelerator, respectively [43].

As described in the literature, the dose due to photons decreases considerably with increasing distance from the target organ, while the dose due to neutrons is homogeneously distributed in the organs [85]. However, the contribution of neutrons to the induction of second tumours is more dominant in organs more distant from the target volume and organs near the tumour are predominantly affected by the dose due to photons [85,86].

### 2.5.4. Radio-Induced Tumours in Paediatric Patients

Children are considered to be a factor of 10 times more sensitive to radiation than adults, and therefore radiation-induced tumours in paediatric patients are of great concern [14]. This is presumably due to increased susceptibility of normal tissues to the mutagenic effects of radiation at younger ages, increased cell proliferation in children and genetic susceptibility related to some primary tumours [10]. Radiation-induced tumours may develop in organs contained within the treatment fields, for example, in

high-dose regions, or even in organs distant from the treatment fields exposed to lower radiation doses [14].

According to National Council on Radiation Protection and Measurements (NCRP) report 116, the intestine, lung and stomach are the most common sites for the development of second tumours after exposure to radiation [14,87]. However, thyroid is known to have a low tolerance to radiation, especially in children [14,29]. An increased incidence of thyroid cancer has been reported after exposure to an average dose of 0.05Gy in children and young adults [14].

Side effects caused by radiotherapy may manifest immediately after treatment and others may occur after a latency period [21,49]. However, life expectancy after radiotherapy is a topic of concern due to the long-term effects of radiation, particularly radio-induced tumours [13,14,25,29,43,49,76,85], especially in paediatric patients [10,13,14,21,25,29,32,43,46,49]. It has been shown that even 30 to 40 years after the initial treatment of radiotherapy, survivors maintain an increased risk of developing a second tumour [21].

It has been discussed that the cumulative incidence of secondary tumours may be higher than 20% of all patients undergoing radiotherapy [16]. The incidence of these secondary tumours depends on the dose distribution administered, the size of the irradiated volume, the dose, the dose rate, among other factors specific to patients [16].

The risk of developing a radiation-induced lifetime tumour is calculated to be about 5%/Sv, where 1 Sv is the exposure radiation equivalent to about 1 Gy of the absorbed dose. This risk is linear with doses from 10 to 50 mSv up to about 3 Sv [87]. The risk is often reduced to a factor of 2 when there is fractional exposure [10]. Clinical studies performed on tens of thousands of survivors of paediatric tumours seems to indicate that there is a linear dose-response relationship for almost all types of second tumours. The most common second tumours such as sarcoma, breast tumours and thyroid tumours were found most frequently in the irradiation field [10]. Some second tumours appear more than 10 cm from the treatment target, where the dose is mainly due to leakage and scattered radiation from the head of the equipment and to scattered radiation in the patient. This dose corresponds to about 3% of the dose delivered to the tumour, namely about 2 Gy [10]. Since the risk of developing second tumours is higher in high-dose regions, consequently most second tumours appear in or very close to the treated volume [10].

There are numerous methods of assessing the risk of developing second tumours described in the literature [10]. One of them is the absolute risk that is the number of individuals who will develop a second tumour per 10.000 individuals exposed per year or over their lifetime [10,51]. Calculating this value is complex, because at long follow-up intervals the absolute population risk to develop a tumour is high, reducing the relative risk associated with treatment during childhood. For example, the risk of a 60-year-old individual to develop a tumour is almost 5%. Epidemiologists usually express the risk of developing a second tumour in terms of relative risk [10,51]. The relative risk is the ratio of the risk for an exposed individual and the risk of the unexposed population to ionizing radiation. The relative risk can be calculated for specific factors, such as for radiotherapy alone or even for chemotherapy. The terms excess relative risk excess absolute risk are defined by subtracting 1 from the relative risk or subtracting the risk of the general population from the absolute risk [10,51].

Another common method to assess the risk of inducing second tumours is the cumulative incidence, i.e. the frequency of exposed individuals developing a second tumour in a given period. This must incorporate a number of clinical factors that cannot be separated, such as when assessing the relative risk [10].

The use of studies of paediatric patients undergoing radiation therapy to estimate the biological effects of low doses on tissues raises a number of questions [51]. Radiation therapy exposures to high ionizing radiation are for only one part of the body and for cancer patients, resulting in a different risk when compared to individuals exposed to a uniform dose throughout the body. Cancer patients have different tissue radiosensitivity compared to healthy individuals [51]. However, these studies are valuable and will be more important in the next decade because they provide a unique opportunity to assess the following issues [51]: (i) Effects of different types of radiation; (ii) Risks of specific tumours; (iii) Effects of potential risk modifiers such as age, gender and fractionation of exposure; (iv) Possibility of genetic susceptibility to induce tumours; (v) Assessment of secondary tumours induced by out-of-field doses, namely for paediatric patients.

In paediatric patients, the risk of developing secondary tumours in the first 25 years after initial radiotherapy treatment may reach 25% [46] and after diagnosis may be 12% [51]. The risk of developing a paediatric tumour or leukaemia after exposure at pregnancy is practically the same as for children [88]. For doses of 10 mGy or less the relative risk is 1.4. Although this value is high, the total individual risk after 10 mGy is about 0.3 to 0.4%, since the incidence of paediatric tumours is about 0.2 to 0.3% [55]

#### 2.5.4.1. Carcinogenic Risk of 3DCRT and IMRT Techniques

Recently, the scientific community has discussed whether the risk of developing second tumours is associated with an increased use of IMRT in clinical practice, because the IMRT administers doses to large volumes of tissue outside of the treatment field [40]. This happens because there are smaller treatment fields, which implies that there are more beams, increasing the low dose caused by fall-off outside the treatment fields [10]. Thus, the risks of radiotherapy treatments with the application of modern techniques have not yet been determined and are not evident for many years, due to their long latency period when referring to the induction of solid tumours [89]. Thus, further studies will be necessary to understand the effects of IMRT on the risk of developing second neoplasms [89].

Radio-carcinogenesis is the most severe side effect that can be caused by doses outside the treatment field [43] and its evaluation is fundamental [76]. The probability of inducing a tumour is dose dependent, and for a dose of 0.1 Gy, the average LAR of cancer mortality is 0.76% for women and 0.51% for men [43]. It is also observed that the risk of developing second tumours varies for different linear accelerators, for example, for IMRT with 6 MV in Varian and Siemens accelerators the risk of developing second tumours is 2.9% and 3.7%, respectively [43]. As for the risk for different radiotherapy techniques, when comparing the carcinogenic risk between 3DCRT and IMRT it is found that IMRT presents a higher risk [8], namely, about 0.5% for 3DCRT and 1% for IMRT [43].

Nowadays, image-guided radiotherapy (IGRT) has been increasingly used to verify the positioning of the patient and the treatment beams [14]. With the daily use of portal imaging or MV Cone Beam Computed Tomography (CBCT), exposures of up to 100 mGy/day are possible. This may increase the risk of developing second tumours, especially in young patients [14]. The Childhood Cancer Survivor Study reported that the cumulative incidence of all tumours, 30 years after diagnosis, was 20.5% and showed to be higher for patients undergoing radiotherapy [14].

The dose limits defined by ICRP do not apply for patients who are undergoing radiotherapy, because in radiation therapy the aim is to suppress malignant cells, and if some dose limit would be applied, the effectiveness of the treatment could be jeopardized [43]. However, there is a conscious need to consider the doses outside the treatment fields, as well as the associated cancer risks, especially for paediatric

patients [14,43,46], and their measurement is essential for assessing the development of second tumours [76]. On the one hand, the specific dosimetric verification for patients who perform IMRT, represents the variation between the planned and measured doses within the target volume and not the dose outside this volume [76]. On the other hand, as stated above, TPS tend not to accurately predict the dose when it is calculated a few centimetres beyond the penumbra, where stochastic effects are a relevant risk [76]. Thus, modelling and simulation by MC methods allow the accurate calculation of the dose due to scattered radiation in the patient [15,76]. It is strongly recommended that each institute/clinic carries out its own measurements of out-of-field doses and use these measurements to make clinical decisions [43].

For radioprotection purposes, the most relevant dose range is 0-1 Gy, the analysis of atomic bomb survivors is usually focused on this range. With increasing survival rates, estimates of the risk of developing tumours at doses higher than 1Gy have become more important for patients undergoing radiotherapy [89]. Risk models should only be used carefully to estimate risk in radiotherapy, provided they are developed exclusively for low doses [89].

# CHAPTER 3 – CONFORMAL RADIOTHERAPY PHYSICS, TREATMENT PLANNING AND CLINICAL ASPECTS

## 3.1. MEDICAL LINEAR ACCELERATOR

LINACs are used in radiotherapy to accelerate electrons to kinetic energies to millions of electrons-volt (MeV), using voltages between 4 and 25 MV, before colliding with the target, namely. To do this, intermediate acceleration steps are used between the production of the electrons and their collision with the target [2,61]. The process consists of accelerating electrons subject to an electric field while moving through a structure consisting of metal rings (electrodes) connected to a radiofrequency source (Klystron or Magnetron). A vacuum system provides low pressure for the electron emitter, accelerator structure and beam deflection magnet [61].

Therefore, LINACs allow, through acceleration and collimation mechanisms, to obtain directed beams of electrons or photons of high energy. They are the most common equipment in external radiotherapy and usually operate at two photon energies, used for deep seated tumours, and at several electron energies used to irradiate more superficial tumour volumes [56]. LINACs are mounted isocentrically to allow the irradiation according to several incidence directions, which the central axes, intersect at the same point of space (isocenter), normally located 100 cm from the target (where the patient is positioned). Besides the sophisticated systems of production, collimation and control of the radiation, LINACs are also equipped with systems for positioning the patient and for locating and checking the radiation fields to be used during the radiotherapy treatments. Patient positioning is performed on a specific treatment table with the aid of a laser system [61].

Inside the LINAC, electrons are accelerated in straight paths in waveguides, using microwave technology. After being accelerated, the electrons collide with a high atomic number target (typically tungsten, detailed below) and produce X-rays. Conventionally, the radiation beam passes through a FF (detailed below), aiming at producing a flat beam profile. More recently, FF-free LINACs have been manufactured, the removal of the FF resulting in an increase in the dose rate, a reduction in the average energy of the particle and in the lateral dispersion of the beams. These characteristics are advantageous in special treatment procedures [2]. The X-ray beam is administered by

a part of the accelerator named gantry, which rotates around the patient lying in a table, delivering radiation in various directions [2,56].

The spatial conformation of the photon beam is achieved using devices incorporated in the collimator. The primary collimator (described in the sequence) defines a circular field, reduced by an adjustable collimator, referred to as secondary collimator (detailed in the sequence) consisting of an independent jaw system, that allows to obtain rectangular and square fields [61]. There is also the MLC (described in the sequence), which allows a higher degree of beam conformation and replaces the need of lead protection blocks. Each leaf is moved and controlled individually. To check the position of the leaves, additional quality controls are required in order to assess the penumbra and radiation transmission between the leaves[2].

### 3.1.1. LINAC COMPONENTS

LINACs components can be divided into five major categories [61], as can be seen in Figure 10, namely, gantry, stand, modulator, treatment table and console.

Commercially available LINAC models for use in radiotherapy differ according to the manufacturers [61].

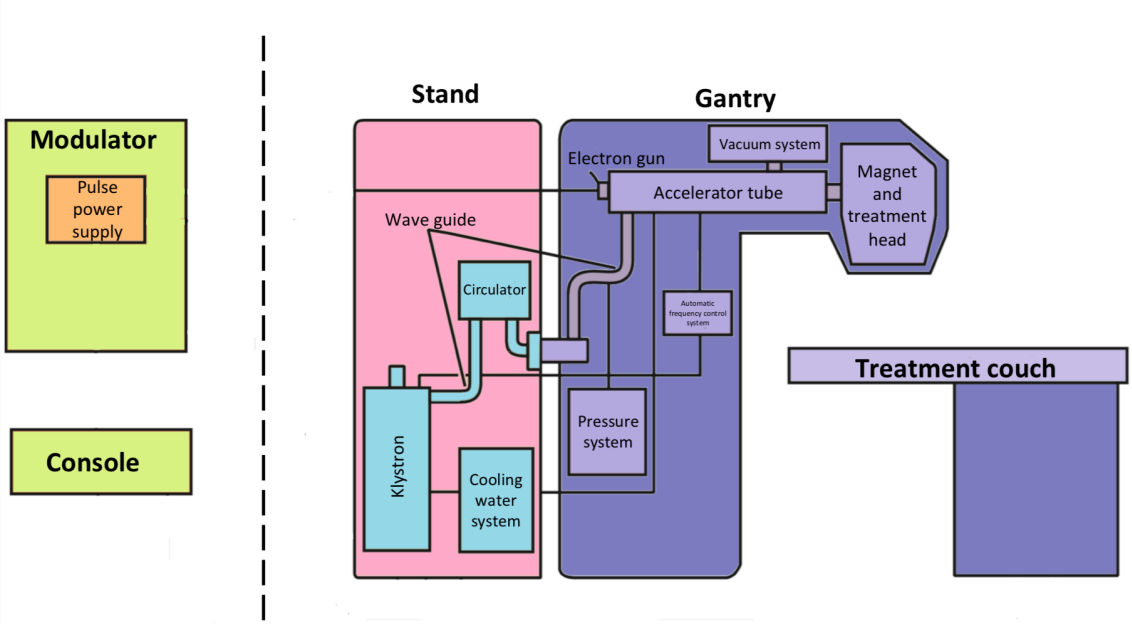


**Figure 10 -** Scheme of a medical LINAC (adapted from [2]).

The console is the control center of the accelerator. It makes possible to control the administration of the treatment, to check the positioning of the patient through the

imaging systems, and to monitor the patient during the treatment through video surveillance cameras [61,90].

The treatment couch movements are controlled by couch buttons or from the treatment console. Most treatment couches allow vertical, lateral, longitudinal and rotational movements around the isocenter [2,90].

In LINACs there is also a portal imaging system. This is an image verification system that uses X-rays with energy in the order of MV or kilovoltage (kV). It has a panel with amorphous silicon detectors for patient´s image acquisition. The verification is performed from the bony structures segmented in the digitally reconstructed radiography, presented in the system located in the console [2].

Nowadays most LINACs have a CBCT system that allows the acquisition of a planar or volumetric image of the patient, enabling the verification of the patient's positioning [2].

The main beam generation components are grouped into six systems [61]: (1) Injection system; (2) Radiofrequency (RF) power generation system; (3) Accelerating wave guide; (4) Auxiliary system; (5) Beam transport system; (6) Beam collimation and beam monitoring system.

#### 3.1.1.1. Injection System

In a LINAC, the injection system is basically a simple electrostatic accelerator called “electron gun”. The heating of a filament by the passage of electric current, similar to that of an incandescent lamp, makes the electrons of the material have enough energy to escape from its orbits. The emitting material (cathode) becomes positively charged by the emission of electrons and in order that the electrons are not attracted back, the application of a conveniently directed electric field is necessary [61,90]. The electric field is obtained through the application of a voltage, called extraction voltage, between the cathode (emitter) and the anode (electron gun structure). The extraction voltage of radiotherapy linear accelerators varies typically from 40 to 100 kV. The heating of the emitter material (cathode) can be performed by direct or indirect heating. The direct heating of the cathode uses a high electrical resistance wire in which a voltage is applied to raise the temperature between 1000 and 2000ºC. For indirect cathode heating, a heater is mounted close to the emitter material to raise the wire temperature to the desired temperature. With this process it is possible to obtain much higher electronic currents [56,90].

#### 3.1.1.2. RF Power Generation System

Electrons are accelerated in the waveguide of a RF generator, consisting of two main components [56]: (1) The RF source: it can be a magnetron or a klystron in combination with a lower power RF oscillator. Both systems use the acceleration and deceleration of electrons in vacuum to produce high RF fields. The magnetron is a high-power oscillator generating microwave pulses with frequencies in the order of 3000 MHz Microwaves can also be supplied by the klystron. The klystron is a microwave amplifier and should be used in conjunction with a low power source. (2) The pulsed modulator: the main purpose is to produce a high voltage pulse to be applied to the magnetron or klystron, and in most accelerators this pulse is also applied on the electron gun to give the first acceleration to the electrons.

#### 3.1.1.3. Accelerating Wave Guide

The electrons are accelerated in the acceleration waveguide using a high-power RF field produced by the RF power generator. The acceleration waveguide encompasses circular holes, all equidistant from each other, which allow the acceleration of electrons [56].

#### 3.1.1.4. Auxiliary System

The auxiliary system consists in several components that allow the LINAC to be clinically operational, including shielding, air-pressure system, water-cooling system and vacuum-pumping system [56]. The vacuum system produces a vacuum pressure of ~$10^{-6}$ torr in the RF generator and in the waveguide. The water-cooling system is used to cool the circulator, RF generator, target and waveguide. The air-pressure system is used for pneumatic motions of the target and other beam setting components. Finally the shielding is used to attenuate leakage radiation [61].

#### 3.1.1.5. Beam Transport System

In low energy LINACs there is no beam transport between the waveguide and the target, because the target is inserted in the waveguide. In LINACs with energies higher than 6 MeV bending magnets are used because the waveguides must be too long to

be mounted in a straight line. There are three beam bending systems [56,61]: (1) 90° bending; (2) 270° bending; (3) 112.5° bending.

The beam transport system drives the high energy electron beam to the target in x-ray mode or to the scattering foil in electron mode [56].

#### 3.1.1.6. Beam Collimation and Beam Monitoring System

Beam monitoring and beam collimation systems ensure that the dose is administered according to the clinical prescription with high accuracy. In order to do this, the monitoring system includes ionization chambers within the LINAC, whilst the collimators define the area to be irradiated [56].

The first ionization chamber measures the MUs. The second ionization chamber acts as a protective element, in case of any defect with the first ionization chamber. The ionization chambers are used to monitor the dose rate, the symmetry of the beam, the total dose and to warn to turn off the radiation beam after completing the prescribed dose [61,90].

### 3.1.2. TREATMENT HEAD

The LINAC head has numerous constituents that affect the creation, contour, positioning and monitoring of the clinical beam of electrons and photons, namely [56,61]: (i) X-ray production target; (ii) FF and electron scattering foils; (iii) Primary and secondary collimators; (iv) Ionization chambers; (v) Field light and range finder; (vi) Wedges (optional); (vii) MLC (optional). Figure 11 shows the layout of the photon beam path in the head of the LINAC.

#### 3.1.2.1. X-ray Production Target

To produce a photon beam, the electron beam impinges on a metal disc which constituent material has a high melting point and specific characteristics depending on the range of energies of the photons that are intended to generate. Mainly the bremsstrahlung process generates photons when electrons are decelerated in the target material. Usually, tungsten is the material chosen for the LINACs target (Figure 11). Its high atomic number (74) and high density (around 19.3) allows to maximize the efficiency of photon production. In addition, tungsten has a high melting point which

minimizes the damage produced to the target by the beam and is thick enough to absorb most of the incident electrons [61,90].

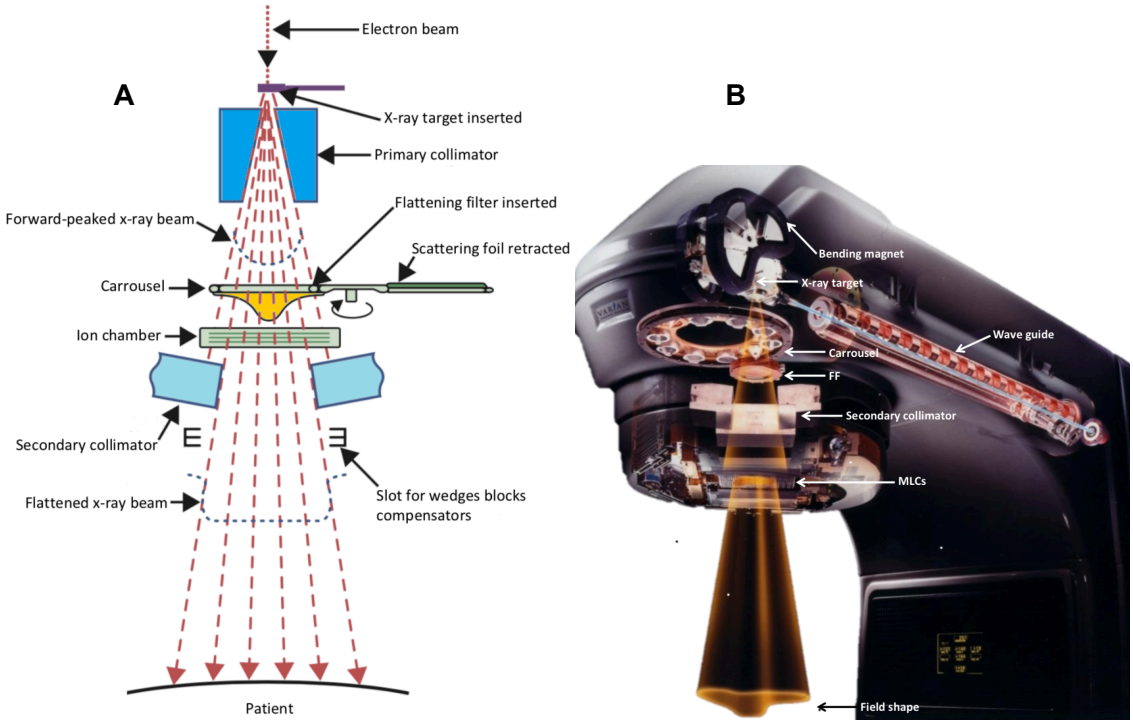


**Figure 11 -** Scheme of a X-ray beam path (A) and Varian Linac head (B) (adapted from [2,4]).

### 3.1.2.2. Flattening Filter (FF)

The focus of the electron beam, by the bending magnet, will determine the photon flux produced by bremsstrahlung. The higher energy photons are concentrated in the central part of the photon beam. The photon beam is made to intercept the FF that by its geometrical design introduces a higher attenuation in the central region of the photon beam, making the irradiation field spatially homogeneous (Figure 11). This filter is built using a low atomic number material such as aluminium or copper [90].

### 3.1.2.3. Primary Collimators

The primary collimators delimit the maximum irradiation field (Figure 11). They have a conical orifice that is aligned with the isocenter. These collimators, manufactured using lead or tungsten, are fixed and attenuate the photon beam intensity by a factor of approximately 1,000 relative to its intensity in central axis [61,90].

### 3.1.2.4. Secondary Collimators

The secondary collimators consist of mobile components and are designed to delimit the irradiation field size up to 40 x 40 $cm^2$at a source-surface distance (SSD) of 100 cm. These collimators are made in tungsten and depending on the equipment, this system may have asymmetrical displacement with the individualized displacement of the field edge (Figure 11). The advantage of using these components is the ability of defining fields outside the central axis and a faster definition of the irradiation field, decreasing the time that the patient has to remain in the treatment room [56,90].

### 3.1.2.5. Multi-Leaf Collimators (MLC)

The MLC system is the tertiary collimation system of a LINAC. MLC allow to shape the irradiation field more accurately [61], as detailed in Figure 12 [91]. Depending on the manufacturer, MLC can be formed by 52, 80 or 120 leaves that move at a maximum speed 3-4 $cm.s^{-1}$ [92] and are individually controlled by motors through a computerized system.

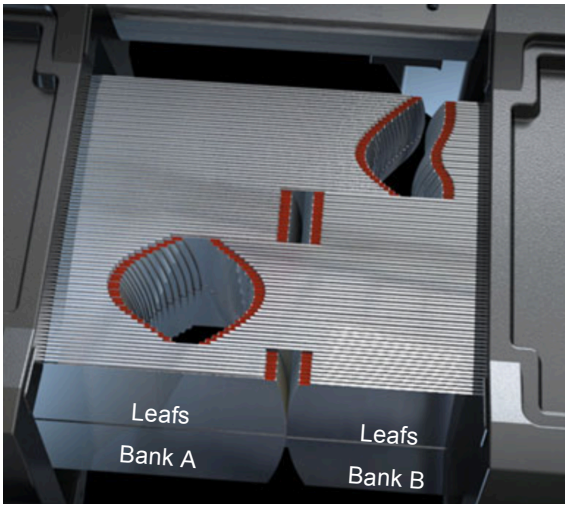


**Figure 12 –** Scheme of a LINAC MLC (adapted from [92]).

### 3.1.2.6. Ionization Chambers

Ionization chambers are also incorporated in the LINACs to allow continuous dose monitoring during patient treatment, as well as for quality assurance & quality control (Figure 11). Dose delivery is expressed in MU. A MU is an output measure of the

LINAC allowing to properly calibrate and ensure the intended dose value is administered in each treatment. One MU is equal to a specific dose of radiation at a given depth in a water phantom, for a given energy beam, with a specific field size and a distance to the target [2].

### 3.1.3. BEAM PRODUCTION

The waveguides are based on the acceleration in a progressive wave tube. The electron is accelerated along the tube, from left to right [56,90]. A potential difference is established between the various electrodes along the tube and through the momentary inversion of the electric field the electrons are accelerated. The distance of the electrodes is progressively increased, as the electron increases its speed, allowing in this way the synchronism in the electron acceleration is not lost [90]. The microwave pulses, generated by the microwave source, typically at a frequency of 3GHz, establish the potential difference needed for the acceleration of the electrons in the waveguide [56,61].

The microwave pulses are generated by the application of high voltage pulses, with approximately 50 kV, generated by the modulator, to the microwave source, which is usually a magnetron or, in higher energy accelerators, a klystron. The magnetron is generally used for electron energies up to 15 MeV and the klystron for higher energies [2,56].

#### 3.1.3.1. Photon Beam

The electron beam accelerated to a given kinetic energy in the waveguide impinges in the target, where approximately 10% of the kinetic energy of the electrons is transformed into bremsstrahlung photons (x-rays). The x-ray beams used for radiotherapy treatment purposes are produced after crossing the FF, in the LINAC head, that causes the flattening of the beam [56,90].

In modern LINACs (Figure 11), the collimation of a photon beam is achieved with the primary collimator, the secondary collimator and the tertiary collimation, performed by the MLC. The primary collimator defines a circular field. The secondary collimator consists of two upper independent jaws and two lower independent jaws, which allows to define rectangular or square fields up to a maximum of 40 x 40 $cm^2$ at the isocenter, at 100 cm from the x-ray target. MLCs have emerged since the 1990s and allow

irregular treatment fields. This collimation system consists, in the most modern models, up to 120 leaves (60 pairs), and each leaf works independently of the others, controlled by its own motor [56,61].

#### 3.1.3.2. Electron Beam

Electron radiotherapy treatments have been performed since the early 1950s, and sometimes provide the only clinical option for the treatment of superficial tumours. Modern LINACs can operate at various electron energies between 4 MeV to 25 MeV. These beams are produced in the LINAC head by retracting the target and FF and introducing the scattering foil into the electron beam path [56,61], as shown in Figure 13. In addition, applicators are used to collimate the electron beam.

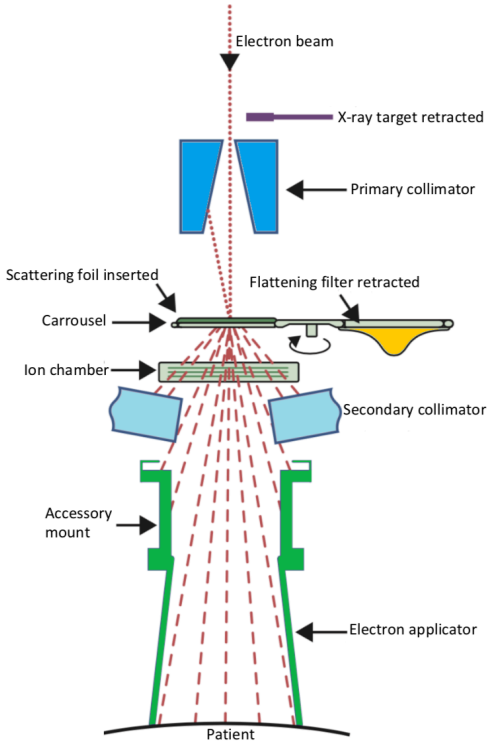


**Figure 13 –** Scheme of an electron beam path (adapted from [2]).

### 3.1.4. Dosimetric Parameters and Measurements

The most relevant dosimetric parameters measured clinically during the LINAC commissioning and data acquisition for TPS are presented in the sequence. These parameters should then be regularly measured and checked for quality assurance and quality control purposes, during the clinical use of the equipment to assess their reliability. The measurements are normally performed in a water phantom using

ionization chambers. Water phantoms are ideal for measuring dose distributions that vary in space and for fixed source geometries relative to the phantom. Ionization chambers have good long-term stability, high sensitivity and low energy dependence in response to photon beams [2,56].

#### 3.1.4.1. Ionization Chambers

Ionization chambers are among the oldest metrological instruments and their operating principle is based on measurement by ionization of a gas. They are simple, practical, relatively low cost and precise instruments for exposure and absorbed dose measurements and are therefore among the most widely used equipment in radiotherapy [61]. Their use is associated with a measuring device, the electrometer. There are several types of ionization chambers, varying in shape, size, constitution, but in general they have similar properties. The ionization chambers are consisting of a central electrode, the anode, and the wall of the chamber, which is coated with a conductive material, the cathode. The space enclosed by the wall of the chamber constitutes the sensitive volume of the detector and is no more than a cavity filled with a gas, or a mixture of gases, at a relatively low pressure. A potential difference is established between the anode and the cathode in order to separate the ion pairs produced by the ionization and excitation processes from the molecules making up the gas, creating an ion flow which produces an extremely low electric current, measured by an electrometer, in the order of $10^{-9}$ A or less [61].

In this study, cylindrical ionization chambers were used, namely the 0.125 $cm^3$ semiflex chamber type 31010 from PTW. There are several types of cylindrical ionization chambers, produced by various types of manufacturers, with active volumes ranging from 0.1 to 1 $cm^3$. They normally have an internal diameter of less than 7 mm and an internal length of 25 mm or less [93]. The central electrode is made of aluminium, 21 cm long and 1 cm thick, and the outer wall is made of low atomic material (equivalent to air or tissue) with a density of less than 0.1 $g/cm^3$ [61].

The ionization chambers used in this study (Figure 14) are flexible to be easily placed in the water phantom. They have an ionization volume of 0.125 $cm^3$ and are used for high precision absolute measurements. These ionization chambers have a sensitive wall volume of 0.55 mm polymethylmethacrylate (PMMA) (1.19 $g/cm^3$), 0.15 mm graphite (0.82 $g/cm^3$); a density of the total wall area of 78 $mg/cm^2$; sensitive volume

dimensions 2.75 mm - radius and length 6.5 mm; central electrode made up of Al 99.98 with a diameter of 1.1 mm and build up cap of PMMA with a thickness of 3 mm [94].

**Figure 14 –** PTW ionization chamber semiflex type 31010 (adapted from [94]).

### 3.1.4.2. Water Phantoms

The ionization chambers are placed in water phantoms or other type of materials that mimic the human body [56]. Water phantoms are fundamental for radiotherapy measurements [56,61].

This study used the water phantom MP3-M from PTW, as can be seen in Figure 15. This phantom is a 3D phantom for dose measurements in radiotherapy. It carries out vertical, horizontal and arbitrary absolute dose measurements for fields up to 40 cm X 40 cm. It integrates the MEPHYSTO® $mc^2$ software also from PTW, allowing the acquisition and analysis of data in TPS [95].

**Figure 15 –** PTW water phantom MP3-M (adapted from [94]).

### 3.1.4.3. Percentage Depth Dose

Percentage depth dose (PDD) s the dose, measured longitudinally along the central axis, at a certain depth d inside the waster phantom relative to the maximum value measured at depth $d_0$, as shown in Figure 16. This is expressed, in percentage, as the

quotient of the absorbed dose in the central axis at depth *d* and the absorbed dose at a given reference point *d0*:

$$PDD = \frac{D_d}{D_{d0}} .100\ (\%) \quad (3.1)$$

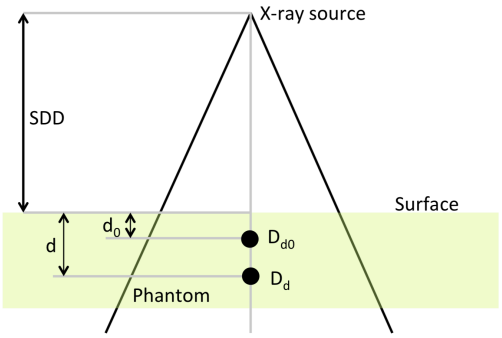


**Figure 16 –** PDD scheme.

PDD curves allow to infer about the variation of dose with the depth and their accurate measurement is a crucial step to ensure that the appropriate dose is delivered to the patient during the course of the treatment. The PDD depends on several factors, such as the distances d and d0, the field size, SSD and the energy of the radiation beam or beam quality. The photon beam PDD increases with increasing energy, SSD and field size [2,56]. Figure 17 shows different PDD curves for x-ray and electron beams of different energies.

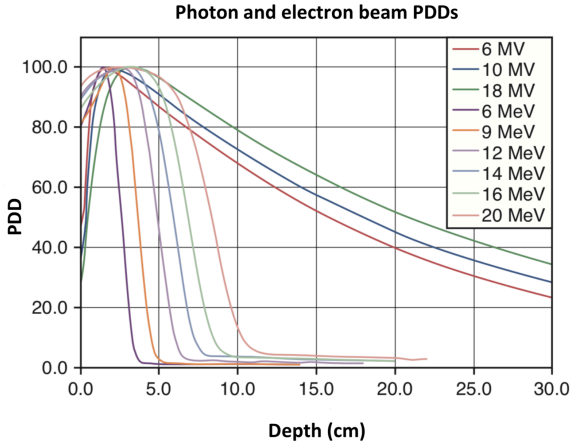


**Figure 17 –** Different photon and electron beam PDDs (adapted from [2]).

#### 3.1.4.4. Dose Profile

A dose profile is a representation of the dose in an irradiated volume as a function of the spatial position along a line (Figure 18) in a direction transverse to the beam axis. From the measurements of the dose profile, it is possible to obtain information about the symmetry and homogeneity of the beam as well as the penumbra. The data are presented as standardised dose doses in the central axis [2,56].

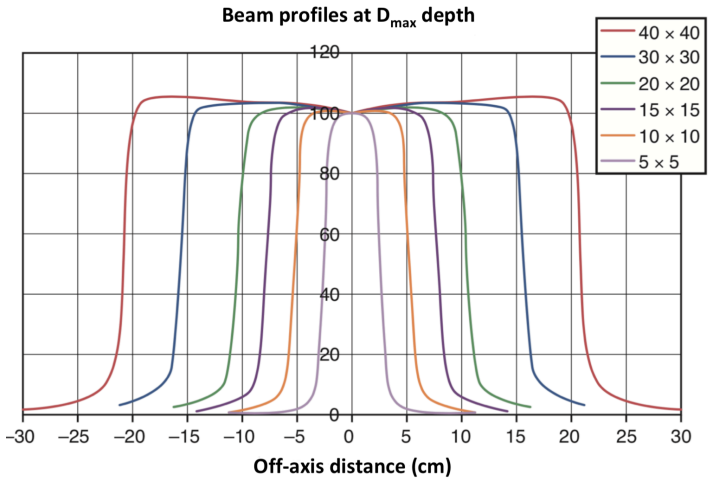


**Figure 18 –** Dose profiles for an 18 MV x-ray beam of diferente dimensions (adapted from [2]).

The dose profiles can be measured in air or in a water phantom at various depths. Measurements in air only consider variations in the intensity of the primary beam, whereas measurements in water show the effect of scattering on the phantom.

The accurate measurement of the dose profile curves is of cornerstone importance to ensure that the appropriate dose is delivered to the patient during the course of the treatment.

### 3.2. RADIOTHERAPY TREATMENT PLANNING

The human body is a complex system with several types of cells. These cells form tissues and organs, which due to their chemical, physical and biological characteristics, respond to ionizing radiation in a different way. Some locations in the human body, such as the lungs, soft tissues and bones, due to their different densities, have properties of absorption and dispersion of radiation that differ from each other [96].

Developments in radiation dosimetry allowed the practice of treatment planning to begin in 1940, enabling physicists to measure isodose charts for any treatment field,

allowing 2D manual planning [97]. Until the 1970s, dose distributions calculations were carried out considering that the human body consisted only of water. A real breakthrough for radiotherapy was the introduction of computed tomography in the 1970s. This type of image allowed the detailed acquisition of anatomical information of the patient in 3D [97] and made it possible to obtain the electronic densities of each human tissue, allowing dose calculations and corrections of heterogeneity [96,98].

After the 1970s, it became feasible to conduct studies in order to find the best way to integrate density corrections in the calculation of dose distributions [97]. Computerized radiotherapy TPS were initially introduced in 1995, allowing the immediate effect of beam modifications on the calculated dose distribution to be visualized. This resulted in better quality dose plans as detailed in Figure 19 [97]. On the other hand, calculation algorithms were also developed for the correction of tissue heterogeneity [96]. Figure 19 shows higher dose conformability at the target volume in 3DCRT compared to 2D planning.

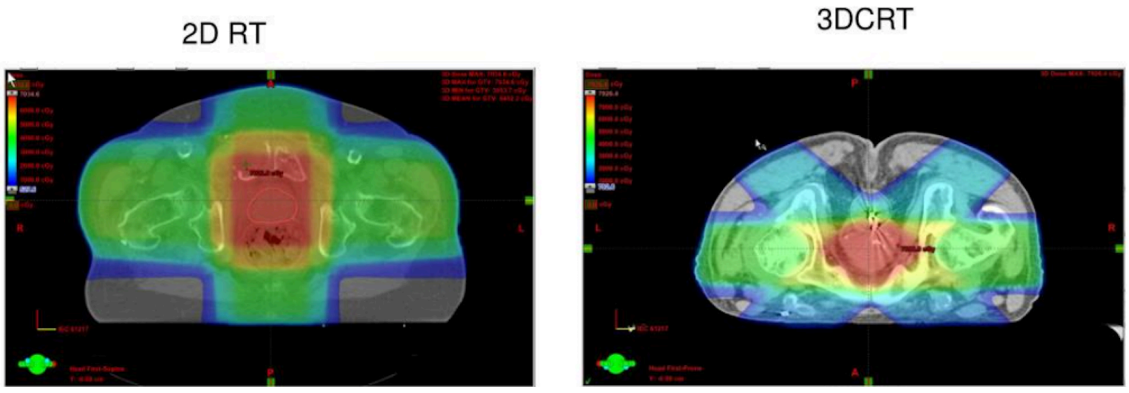


**Figure 19 -** Differences between 2D and 3DCRT dose distributions.

In a few years, computed tomography started to be routinely used in the radiotherapy planning process, resulting in a 3D view of the dose distribution [97]. Nowadays, computed tomography has become fundamental for radiotherapy planning. The acquired images of the patient are transferred to the TPS, which reconstructs in 3D the patient's body, namely the area to be irradiated, as well as the healthy tissues to be protected [96].

The aim in radiotherapy treatment planning is to determine a dose distribution as uniform as possible inside the target volume (the tumour), whilst minimizing the dose outside that volume [7,97]. In radiotherapy planning, beam quality, dimension, position,

orientation and relative contributions of fields are often modified. It is also possible to add certain structural components and accessories, such as wedge or blocks, to be considered irregularities on the patient's surface or to protect critical structures from radiation exposure [97].

### 3.2.1. PRESCRIPTION, REGISTRATION AND DOCUMENTATION IN RADIOTHERAPY

For several decades, the International Commission on Radiation Units and Measurements (ICRU), has devoted a considerable effort to harmonise the way radiation treatments are recorded and documented [40,99,100]. The use of a common language in defining terms and concepts has become crucial for an accurate and effective transfer of information and a requirement for the innovation and development of modern radiotherapy.

#### 3.2.1.1. ICRU Report 29

The concepts of volumes and margins in Radiotherapy were formally introduced by the ICRU Report 29 of 1978 entitled "*Dose Specification for Reporting External Beam Therapy with Photons and Electrons*" [101]. This report was the first to distinguish between target volume and tumour volume. In terms of specification and dose records, the Report 29 recommends that the prescribed dose be specified, whenever possible, for the intersection of the treatment field axis and preferably in the center of the target volume [101].

#### 3.2.1.2. ICRU Report 50 and ICRU Report 62

The ICRU Report 50 entitled "*Prescribing, Recording, and Reporting Photon Beam Therapy*" was published amidst the technological developments in medical imaging in the 1980s and 1990s, which made possible to redefine treatment volumes, OARs and dosimetry calculation for techniques with 3DCRT. In 1999, ICRU Report 62 was published as a supplement to ICRU 50, aimed at introducing and refining concepts and recommendations for the performance of advanced techniques, volumes and statistical margins based on clinical evidence. This supplement recognizes that linear addition of margins to compensate for all kinds of uncertainties usually introduces excessive margins for PTV, which can result in increased clinical consequences. Also in this report the concept of compliance index (CI), the functional biological categorisation of

risk organs and the recommendations necessary for dosimetry recording of patients and patient series were introduced [99].

ICRU report 62 also defined three levels of dose and volume assessment for registration based on the complexity of the technique, the technological development and research of new dosimetric models in external radiotherapy.

In this context the levels of evaluation and registration can be described as follows [99]:

- Level 1 - minimum safety and accuracy requirements to be ensured by all radiotherapy departments and for all patients. At this level it is assumed that the ICRU reference point can be determined exactly as well as the maximum and minimum dose in PTV. The minimum requirements imply a mastery of the clinical, physical and dosimetric component and the use of appropriate equipment.
- Level 2 - Dosimetry planning standards allow complete and relevant information to be shared between different departments. At this level it is assumed that Gross Tumour Volume (GTV), Clinical Target Volume (CTV), Planning Target Volume (PTV), OARs and Planning Organs at Risk Volumes (PRV), can be defined using safe data acquisition instruments and imaging techniques under trustworthy conditions (CT, MRI, PET). It is assumed that dosimetric distributions can be available in the various geometric planes, the use of dose volume histograms (DVH), and whenever necessary the application of heterogeneity correction. A quality control program covering the whole process must be associated to this evaluation and registration level.
- Level 3 - Includes the development and research of new techniques for which the evaluation and registration criteria have not yet been established. The techniques and technologies associated with this level may become level 2 with the consolidation of these new models accompanied by the development of new techniques and equipment.

For any of these three levels, the ICRU reference point and the best estimate of the maximum and minimum dose in PTV shall be reported. For dose records in external photon beam radiotherapy, the ICRU reports 50 and 62 recommend that the ICRU reference point comply with the following requirements [99,100]:

- The dose at ICRU point should be clinically relevant and representative of the dose distribution through the PTV;

- The reference point should be clearly defined and located where it can be easily determined;
- The reference point should be selected in a region where there is no high gradient of dose;
- The ICRU point should be selected for the centre of the PTV, or central region.

#### 3.2.1.3. ICRU Report 71

The recommendations of the ICRU Report 71 entitled "*Prescribing, recording, and Reporting Electron Beam Therapy*" are consistent with those present in ICRU Reports 50 and 62s; however, since the dose distribution of the electron beam is so different from that of photons, it became necessary to establish dosimetric recommendations more appropriate to this type of beam. In the case of electrons, the ICRU reference point should be specified for the maximum dose point preferably on the central axis of the electron field, when the beam is perpendicular to the irradiation surface. The percentage dose received for the reference isodose should be reported [102].

#### 3.2.1.4. ICRU Report 83

The ICRU Report 83, entitled "*Prescribing, Recording, and Reporting Intensity-Modulated Photon-Beam Therapy (IMRT)*" published in 2010 explores in its levels of complexity the dose-volume records, as well as the concepts of clinical and biological measurement in the tumour control probability (TCP), the normal tissue complication probability (NTCP) and the equivalent uniform dose (EUD). It stipulates that conformity index (CI) and homogeneity index (HI) as well as absorbed dose uncertainties should be reported at level 3 [40].

#### 3.2.1.5. Volumes Definition in Radiotherapy

A correct contouring of organs and treatment volumes, to which specific dose levels will be associated in the treatment planning procedures, is imperative for the adequacy of recommendations to clinical practice in prescribing, evaluating and recording doses. In this context it is important to review the concepts described in the ICRU Reports 29,50, 62 and 83 reports regarding the determination of volumes and safety margins in external beam radiation therapy [2].

In the definition of treatment volumes, the ICRU considers the concepts GTV and CTV purely oncologic and independent of any therapeutic approach. The safety margin that is added to the CTV is for planning purposes, PTV ensures that the geometric errors and uncertainties associated with therapy are taken into account. [99]. Figure 20 shows the evolution in the definition of volumes in the ICRU reports 29, 50 and 62.

GTV, is the palpable, visible or clinically demonstrable mass and extent of malignant growth. The GTV consists of the primary tumour (GTV-T), whether in the presence of nodes (GTV-N) or in metastatic disease (GTV-M). In GTV the cellular density is usually > 106/mm$^3$, so the prescribed dose, in radiotherapy, should always include its totality of volume. The complete and precise description of the GTV is essentially for [2,99,100]:

- The correct staging according to the classification systems (e.g. TNM)
- Adequacy of full volume dose for maximum tumour control - Evaluation of tumour regression
- Adjustment of volumes during the radiotherapy treatment

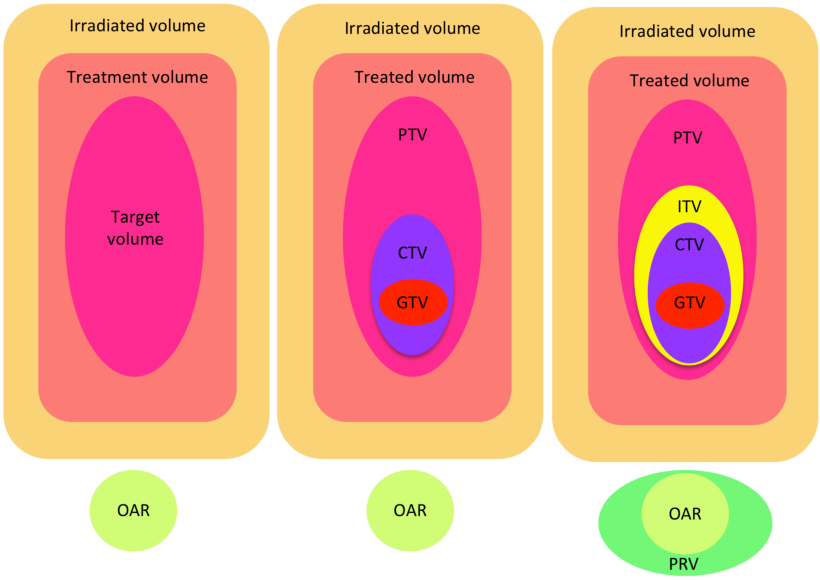


**Figure 20 -** Different volumes defined by ICRU: Left - ICRU Report 29, Middle - ICRU Report 50, Right - ICRU Report 62 (adapted from [2]).

The CTV is the volume that includes the GTV and surrounding tissues with the likelihood of subclinical malignancy. The CTV, as a clinical-anatomical volume, should be included in its entirety by the prescribed dose. Even if the cell density is less than 103/mm$^3$, the cells cannot be clinically detected and should be considered as subclinical volume. Relevant data to consider are the likelihood of microscopic

extension around the GTV and subclinical invasion of lymph nodes and other tissues [2,99,100].

The PTV, is the geometric concept introduced for planning purposes. It is used to select the appropriate technique and field size thus to ensure that the dose is given to the entire CTV. The PTV margin described in ICRU Report 62 makes a clear distinction between the two margins, which are responsible for considering the movement, shape and size of the CTV. The first is the internal margin that is usually added asymmetrically around the CTV, as it is closely related to the physiological movements of each patient. Its analysis and definition are generally based on 3D or 4D volumetric imaging studies. Its determination defines the concept of internal target volume (ITV). The other margin is the setup margin that includes the variations and uncertainties related to the location of treatment area [2,99,100].

The treated volume (TV) is defined as the volume involved by the selected isodose surface and specified as appropriate to achieve the therapeutic objective (e.g. 95% isodose curve). The irradiated volume (IV) is the volume of tissue that receives a dose considered significant in relation to the tolerance of normal tissues. The irradiated volume is closely related to the treatment technique [2,99].

The ICRU Report 83 introduced a new volume, the remaining volume at risk (RVR), defined by the difference between the body volume and the CTV/OARs on the images where these were delimited. RVR is important for the evaluation of treatment plans, in the detection of volumes outside the high-dose region that are receiving a significant dose in relation to the tolerance of normal tissues. RVR can be useful in estimating the risk of late side effects and the likelihood of carcinogenesis. The RVR delimitation is particularly important in young patients with a long life expectancy [2,40].

In carrying out the dosimetric planning it is of crucial importance to define the OARs associated with the anatomical location treated, and therefore they should be carefully segmented and preferably according to existing recommendations in the literature. The OARs are by definition normal anatomical structures exhibiting a radiosensitivity that can influence the planning and/or prescribed dose [100]. The OARs can be classified according to their morphological and functional structure into serial, parallel or serial-parallel organs, as detailed in Figure 21.

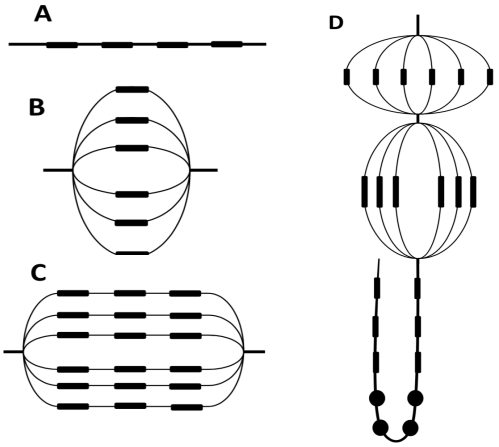


**Figure 21 -** Example of different tissue organization structures. (A) serial organ (B) parallel organ (C) serial-parallel organ (D) combination of serial and parallel organ (adapted from [99]).

Serial organs as the spinal cord or the vascular system have a continuous functional structure so that any subunit is closely related to the others, which indicates that doses above the specific tolerance, even at a reduced volume, may compromise all or part of the other body functionality. Parallel organs, like lung or liver have a functional structure in which the irradiation of a partial volume above tolerance will condition only the percentage of volume involved [40].

The serial-parallel organs, like the heart, work in an integrated way in which the excessive irradiation of sub-units of serial structures (e.g. coronary arteries) can determine the functioning of the sub-units that work in parallel (e.g. myocardium) and thus partially or totally condition the organ viability. The combined organs (e.g. nephrons) establish internal connections between sub functional organization in series and parallel, so depending on the percentage of volume-dose and location of the irradiated organ, a smaller or larger dysfunction may occur [40].

In ICRU Report 62, a margin was also determined around OARs, in parallel with what happens with the safety margin (PTV) added to the CTV. This analogous margin is also defined by the combination of the internal margin and the setup margin, which in the case of the OARs defines the concept of Planning Organ at Risk Volume (PRV). The PRV has a greater impact when it comes to serial organs in relation to OARs in parallel.

### 3.2.2. Dose Calculation Limitations in Commercial TPS

Many studies compared different treatment techniques with respect to peripheral doses in healthy surrounding organs, based on TPS calculations or even through point measurements [36]. Both approaches have their limitations: on the one hand, the TPS dose calculations are obtained/valid/accurate up to a few centimetres away from the field edge [36]. According to Cozzi and collaborators, the maximum distance that the TPS considers for taking into account the effect of the contamination electrons is related to an internal parameter of the system that represents the sigma value of the Gaussian distribution convoluted with the primary fluency of the photons [103]. On the other hand it is not possible to obtain volumetric dose information from point measurements [36].

#### 3.2.2.1. Dose Measurements versus Calculations, Models and Algorithms

Currently, it is almost impossible to obtain direct measurements and predictions of the 3D dose distributions in the patients. Thus, treatment planning should be based on calculation models [97]. Even if dose measurements in the patient are possible, it would be much more practical and convenient to perform the planning on calculation models. The dose provided by a calculation method should correspond to the dose actually absorbed by the patient or be as accurate as possible [97]. On the other hand, the dose received by the target volume should be as close as possible to the dose prescribed by the clinician. Several organs feature critical dose levels that should not be exceeded; otherwise, serious side effects may occur. More accurate dose calculations are also needed to improve the understanding of the biological response mechanisms in radiotherapy, as the dose calculation should be used in reports, so that tumour responses are later correlated with specific doses [97]. Moreover, the biological response of cells to radiation is not linear, and thus small errors in the calculated dose may lead to large uncertainties in predicting the biological response [104].

Methods based on empirical formulas were the first techniques developed to calculate the dose. In these methods, primary and scattered radiation are treated separately [97]. The component of primary radiation describes the distribution of energy deposited in the first photon interaction in the medium, while the component of scattered radiation describes the result of subsequent interactions leading to energy transfer or absorption outside the site of the first interaction [97]. In the method described by Cunningham, the dispersion is calculated with the aid of the scatter-air ratio (SAR), which is derived

from a measurement of the tissue-to-air ratio (TAR) and its extrapolation to a null beam [97]. The manipulation of irregularly shaped fields is usually based on the integration method developed by Clarkson, where the field near the calculation point is divided into several angular segments. The dose contribution of each segment is estimated from the scatter function, such as SAR, and the contributions are added together [97]. Later, more elaborated semi-empirical methods were developed using measurements of beam data. However, all empirical and semi-empirical methods feature difficulties and limitations to model the set-up of the beams in a generalized way [97].

Several methods have been developed, which consider the fact that the densities of the tissues are different from the density of water. Frequently, the dose distribution calculated for homogeneous situations is converted to heterogeneous situations by applying a correction factor point by point [97]. Most methods, such as the equivalent path method [104], or the Batho method, determine the correction factor through a direct tracing of the beam, from the source of primary radiation to the point of interest [97]. More sophisticated techniques, such as the equivalent TAR method, use the information of the electronic densities of CT images to determine the correction factors. The use of these correction factors can also lead to deviations of up to 10% in the measured dose, for certain types of geometries [97]. Dose calculation methods based on kernels or convolution/superposition methods are based on physical principles of radiation behaviour rather than direct beam measurements [104]. Methods based on kernels have proven to be more accurate than empirical methods, but still have limitations in modelling in situations of great lateral electronic disequilibrium, such as in cases of small fields with high energy beams inside the lung tissue [97]. A requirement of radiotherapy treatments is the administration of the dose to the target volume, with a high degree of accuracy [105,106], because an underdose may not eliminate all cancer cells and an overdose may damage the surrounding healthy tissues, causing serious side effects [107,108]. To achieve the aimed accuracy, the uncertainties at all stages of the radiotherapy process, from simulation to planning the dose distribution to be administered in treatment, should be as low as possible. For this reason, it is crucial to be aware of all the uncertainties associated with each stage of the process [105,107].

#### 3.2.2.2. From 2D to 3D and to Increasingly Complex Radiotherapy Techniques

The treatment planning dose calculation algorithms for photon dose distributions were changed from 2D to 3D algorithms, with some variety of small differences between

them [109]. Over the last decades, two different approaches were considered and implemented in planning systems:

- Clarkson-Cunningham integration methods: in this approach the beam is divided into a primary component and a dispersed component. The scattered component is calculated from the derivative of the dispersed function of the experimental ratios of the phantom. These types of calculation methods have been successfully implemented in commercial planning systems [109].
- Dose calculations of the scatter kernel: in this approach the dose is calculated as an overlap of dispersion contributions, created by kernels interacting with the tissue. In simple formalism, scatter kernels are unique pencil beams. Ideally the scatter kernels are 3D point spread, which would represent the interaction of the photon beam in each voxel [109].

The introduction of highly complex treatment techniques and the possibility of administering higher doses in radiotherapy treatments has reinforced the need for increasingly accurate calculation algorithms [105,110,111]. Historically, one of the fundamental limitations of TPS relates to the ability to predict the dose in the presence of heterogeneity, particularly in the case of the difficulty of TPS to perform the electrons calculation in the material [105,107,108,112]. This stems from the fact that simple calculation algorithms fail in accurately calculating the dose in heterogeneous tissues [105], since they use a very simplified model of electron transport along that surface. Indeed, large deviations can be observed, compared to actual measurements, especially in lung tissue [113,114].

#### 3.2.2.3. TPS Accuracy, Commissioning and Quality Control

Dose calculation algorithms play a key role in modern TPS. In 1976, the International Commission on Radiation Units and Measurements (ICRU) recommended that the dose administered should have an error of less than 5% [96,113,115,116] in order to achieve tumour control and minimize complications in healthy tissue [117]. However, it is believed that the accuracy between the calculated dose and the dose delivery to the patient is in the range 2-3% [96,115,117]. This requirement becomes extremely challenging when different tissue interfaces, such as lung and bone, are involved, as the algorithms used for dose calculation in commercial TPS are not optimized to account for electron transport with high accuracy [113].

Quality control of TPS is essential to ensure the accuracy of the calculation [118]. This concern has triggered the creation of documents describing procedures for quality control and commissioning of TPS, such as the IAEA Technical Report 430 [118], Report 55 published by the American Association of Physicists in Medicine (AAPM) and Booklet No. 7 published by the European Society for Radiotherapy and Oncology (ESTRO) [116]. In terms of quality control of TPS, several approaches have been used to investigate the accuracy of newly developed algorithms. To test the algorithms under homogeneous conditions, several authors have compared the calculated dose distributions with their own experimental measurements, or even compared them with Monte Carlo calculations [109,116].

Nowadays, it is commonly recognised that commercial TPS have limitations in their ability to account for the effects of transporting electrons [119]. Uncertainties in calculation of dose distributions often result in poor modelling in situations where there is no electronic equilibrium, particularly in the presence of heterogeneity [106,112,119], when using small fields [106,119], or in high energy beams [106]. The prediction of the dose near the air cavities is complicated and time consuming. Almost all new developments related to algorithms are concentrated in heterogeneous areas, but in the vast majority of clinical cases, with homogeneous tissues, simple calculation methods can be applied safely [112].

### 3.2.3. 3DCRT DOSIMETRIC TREATMENT PLANNING

Dosimetry planning starts with the segmentation, using CT images or other imaging methods such as magnetic resonance imaging and positron emission tomography, of the volumes of interest [120–122]. Then, the treatment fields are introduced in the TPS. The conformation of these fields is performed more frequently using MLC's. Less frequently metal alloy blocks can also be used. Treatment fields in 3DCRT show homogeneous dose fluency, contrary to field fluency in IMRT [120,121]. Beam modifiers, such as dynamic and physical wedges or even bolus, can also be used. After the conformation of the fields, the dose is calculated using the calculation algorithms inserted in conventional TPS [120,121]. Then the assessment of the dose distribution is performed based on the following parameters [99]: (1) The reference isodose curve should cover the entire PTV; (2) The dose distribution should be homogeneous; (3) There should be no hot spots, i.e. points outside PTV with more than 100% of the prescribed dose; (4) There should be no cold spots, i.e. points inside

PTV with less than 95% of the prescribed dose; (5) Using DVH the doses in the organs at risk are evaluated, based on the dose tolerance tables of the different organs at risk, as well as the maximum and average dose of each organ. The dose in the target volumes should also be evaluated considering:

- The minimum dose in PTV should not be less than 95% of the prescribed dose;
- The maximum dose at PTV should not exceed 107% of the prescribed dose;
- The average PTV dose should be about 100% of the prescribed dose.

If the evaluation of the dose distribution does not satisfy the parameters defined in ICRU reports 50 and 62 [99,100], it is necessary to perform the optimization of the dose distribution based on different parameters [40,120]: (1) Change of unit or energy used; (2) Contribution of the fields; (3) Change of the normalization point; (4) Change number, angulation and size of fields; (5) Introduction/change of beam modifiers.

### 3.2.4. IMRT DOSIMETRIC TREATMENT PLANNING

The concept of intensity fields created by inverse planning was first proposed by Brahme in 1998 [38]. Simple IMRT methods are based on conventional 3D treatment planning systems and conventional optimization methods. IMRT plans include two or more segments that are typically MLC conformed [123].

When the treatment is performed with IMRT sliding window, there are many possible sequences of dynamic movements of the leafs capable of producing the desired intensity pattern [37]. For a given intensity pattern, the ideal sequence pattern of the leaf is a compromise between an efficient dose administration, a minimization of the number of segments, the total number of MU, the distance travelled by the leafs and the total time of administration [37]. Since each pair of leafs should administer a different intensity profile, the speed of each leaf and its position, depending on the MU administered, should be individually controlled. In practice, a software, sometimes called leaf-sequencer, is used to translate the dose profiles into an IMRT beam in the so-called dMLC file, which contains the information on the position of the slides according to the MU.

The dose calculation for the dMLC technique should take into account the transmission of the leafs, the rounded edges of the leafs, the tongue-and-groove effect, the scatter inside the gantry and the leafs should slide smoothly over each other with a minimum distance between them to reduce the transmission and leakage radiation [30]. To reduce inter-leaf leakage, each leaf has a prolonged portion, called tongue, on one side that fits into a retracted portion, called groove, of the adjacent leaf [41], as can be seen in Figure 22. Each leaf has a tongue on one side and a groove on the opposite side and its precise manufacture, in independent and extremely small leafs, is an exact process [37]. While this tongue-and-groove design reduces the leakage radiation, it also complicates the dose calculations of the treatment planning, because the transmission on any slide depends on the passage of the beam through the tongue, the center, or the groove of the leaf. If adjacent leafs are placed in the same position, this is not a problem, because transmission through the tongue of one leaf plus transmission through the adjacent leaf groove is close to transmission through the center of the leaf. However, when two adjacent slides have different degrees of extension, the tongue portion of the longer slide produces an underdose region near the edge of the leaf [37]. The solution to the tongue-and-groove problem in the context of dMLC was initially developed in 1996 by Van Santvoort and Heijmen, who proposed a modification in the trajectory of the leafs, segment by segment, to make a smaller gap of the leafs inside the larger one. This will cause a direct exposure under the tongue-and-groove equal to the lowest direct exposure of the two adjacent pairs of leafs [41]

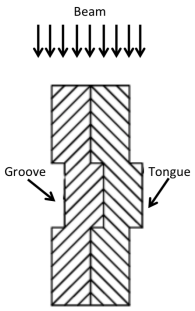


**Figure 22 -** Tongue-and-groove effect.

There are restrictions on leaf movement that affect the accuracy and efficiency of IMRT dose administration. These restrictions are detailed in Figure 23 and include the minimum gap distance from opposite leaf in order to prevent the leaves from hitting each other (A); another restriction is the design that does not allow interdigitation that occurs when one end of the leaf extends beyond the ends of its two neighbouring leaves (B); other restriction is the distance of each leaf can travel beyond the midline of the field (over travel distance), which affects the maximum IMRT field size, which is always smaller maximum static MLC field size (C) [37,124].

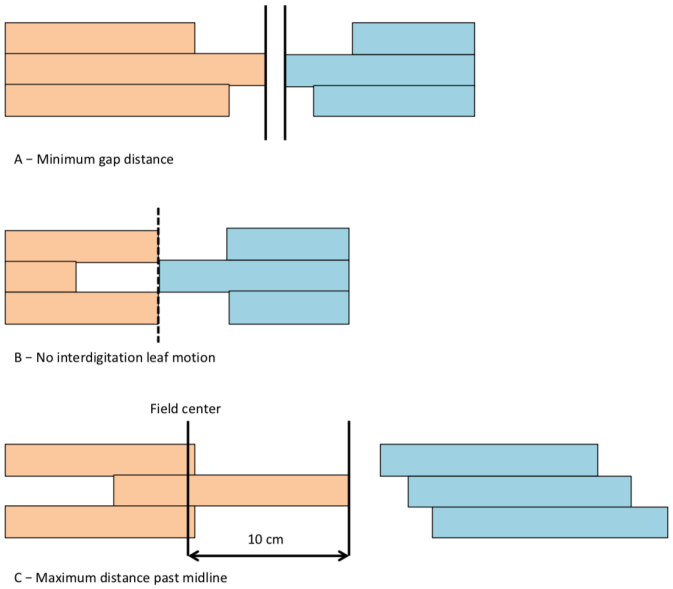


**Figure 23 -** MLC movement restrictions. (A) Minimum gap distance; (B) No interdigitation leaf motion; (C) Maximum distance past midline (adapted from [124]).

IMRT treatment planning is usually performed using the inverse planning algorithms as opposed to conventional planning, which means that the treatment planning team does not specify the contributions of each field, filter angles, beam modifiers, among other parameters, nor do they have direct control over these at any point in the planning process [37,40]. However, the energy, the number and direction of the beams, continue to be chosen by the users in a conventional way. As soon as the beams are specified, the system assumes complete control over all other properties of the beams, namely MU, contributions of each field, MLC movements, among others, and designs an ideal intensity pattern to best meet the dose-volume constraints specified for PTV and normal tissues. In other words, the user must define the desired dose distribution and the system calculates the contribution of the fields, the modelling of the intensity and the movement of the MLC, which most closely approximates the production of the

requested dose distribution. Obviously, a key to the whole process is the specification of the objectives, that is, the minimum and maximum doses that should be applied to PTV, as well as the tolerance of healthy tissue, that is, the dose volume restrictions, which should be physically achievable and realistic [37].

The IMRT normally incorporates a computerized iteration as opposed to manual optimization procedures used in conventional planning. With inverse planning, the system performs thousands of iterations and in each iteration there is an adjustment of thousands of individual rectangular bixels, so the system can model the fluence intensity within each radiation input port [37]. The selection of the beams is based on a combination of experience, standard protocols and patient specific anatomy. For some tumour locations, such as the prostate, the small variations between patients in anatomical detail allow the use of standard templates for the initial parameters, such as beam directions and dose-volume restrictions [37,40].

To specify realistic dose constraints, users need to learn the relationship between these constraints and the resulting dose distributions for the specific inverse planning system they use. They should also have some familiarity with basic dosimetric concepts. Once the user has gained experience, it becomes possible to develop disease-specific models, which can be used as a starting point for dose restrictions for the treatment of frequently localized tumours such as prostate, nasopharynx and oropharynx. The anatomical variations of each patient limit the use of standard dose restrictions, but these can be a good starting point [37].

From mathematical algorithms, the inverse planning system performs the optimization of treatment planning, modifying the intensity of the beam in each segment of each field, according to previously defined doses [40]. This process offers a better dose adequacy to tumour volumes, with a higher protection of normal critical structures, even compared to 3DCRT [37]. The optimization process compares the various dose distribution constraints. However, it should be emphasized that the parameters specifying the relative dose limits, the critical structures and the overlap regions should be selected to efficiently conduct the optimization algorithm towards a desirable dose distribution [38].

The success of any optimization scheme is the specification of an objective or cost function. The objective function includes parameters of healthy tissue as well as PTV, and is normally a weighted sum between the two [125]. Objective functions can be based on biological criteria or more often on dose-based criteria and dose-volume

effects are usually incorporated in objective functions [37]. In defining the objective functions for IMRT, the choice of the objectives of the plan should be made with the knowledge of the effects of the dose calculation accuracy on the outcome of the optimization [40,125,126].

Most inverse planning algorithms allow the user to define multiple points on a tissue, with different priorities set for each point. Histogram type dose volume restrictions instead of a single dose limit can also be set for PTV if desired [37]. If the system cannot find an intensity profile that exactly matches the set dose constraint, then the system tries to perform a suboptimal plan, bringing the dose constraint values closer to the values initially set. For this, the user must set penalty values or relative priorities, quantifying the relative importance of the match of the dose constraint set for each organ. The choice of priority factors is a subjective decision by the user [37]. With inverse planning, changes in planning and adjustment of dose distributions can only be achieved by changing dose-volume restrictions and/or priorities [37,40]. The assessment should be carried out by placing the dose distribution in some representative plans, including three mutual orthogonal plans through the isocenter (transverse, coronal and sagittal). A volumetric dose calculation is created by regions of interest to determine the histogram dose volume [38].

# CHAPTER 4 – MONTE CARLO SIMULATION METHODS AND ANTHROPOMORPHIC VOXEL PHANTOMS

## 4.1. MONTE CARLO SIMULATION METHODS IN PARTICLE TRANSPORT

### 4.1.1. GENERAL CONCEPTS

The name comes from Monte Carlo, Monaco, where the game is popular and refers to the random nature of this type of activity [127]. MC methods use pseudo-random numbers to sample particle track lengths, energies, angles, multiplicities, among others, allowing an efficient and effective simulation of the particle interactions at the microscopic level.

The application of MC methods emerged during World War II at Los Alamos National Laboratory in the framework of the development of the atomic bomb and associated needs to model and simulate neutron induced interactions when they travel across nuclear materials. In the years after the World War II, MC simulation software packages started to be developed mainly associated to nuclear weapons research and development. A few decades later, starting in the 1970s, with the advent of modern computers and afterwards during the 1980s with modern processor architectures, the use of MC methods to simulate the interaction of particles in heterogeneous materials, such as the human body [128] as well as for many other applications such as high energy particle and nuclear physics experiments, medical applications, radiological protection and dosimetry for endless applications of radiation sources and radioactive substances, etc.).

MC simulation programs use pseudo-random numbers to determine the position, direction, energy, type of interactions and therefore the path of a particle crossing a certain material, using the available cross-section data (probabilities of interaction) for each geometric region of interest [128,129]. This process is repeated for many particles. Relative uncertainties of the level of a few percent require the simulation of a large number of particles (in some cases in excess of $10^9$). The simulation of a large number of particles allows to score quantities such as deposited energies and absorbed doses inside volumes, particle fluencies in surfaces, among others [128,129]. MC methods are therefore appropriate for dosimetry, radiation protection and safety calculations in radiotherapy.

#### 4.1.1.1. Pseudo Random Number Generators

A fundamental requirement in MC simulations is the generation of sequences of pseudo random numbers, by computer and numerical algorithms specifically developed and duly tested.

In theory, a random number cannot be predicted or calculated. Nevertheless, the most common approach in computer simulations is to use a program to obtain sequences of randomly distributed numbers. These pseudo-random numbers are calculated from previous numbers, which implies thus, starting two simulations with the same initial value (often referred to as “seed”) will produce the same simulated results, ensuring the reproducibility of simulations [127]. Moreover, since the simulations are performed on digital machines using numbers limited to a known range (2 byte, 4 byte, 8 bytes, etc.) there is always a possibility that a random number sampled during the simulation is equal to the initial value. It can be shown that for a given algorithm, the same sequence of generated pseudo-random numbers will be periodically repeated, therefore raising the issue of the independence of generated histories (initial particles). The repetition of the sequence of pseudo-random numbers generated may have serious consequences for the accuracy of the results [127]. State-of-the-art MC programs must therefore use algorithms with an extremely high period to avoid these problems.

### 4.1.2. Application of Monte Carlo Methods in Radiotherapy

During the last decades, MC techniques became increasingly used in medical physics applications [130]. MC methods are generally classified as the most accurate methods available for dose calculation because they model the interaction of each beam particle (photon, electron, others) in the patient [97]. However, it is considered impractical to use MC algorithms in real time clinical situations, due to its long-time of calculation [114], not allowing its full implementation in the routine of radiotherapy services [109]. Figure 24 shows time to solution and complexity for MC versus deterministic/analytic methods. When the complexity of problems increases, MC methods are more advantageous, however, the time required to achieve the solution may be a disadvantage for MC methods [131].

Dose calculation should be fast so that the treatment planning process can be completed in clinically acceptable time [110,112], i.e. depending on the type of treatment it can range from  hours to a few days. The result of the dose calculation must be sufficiently accurate so that the established correlations between the dose delivered and the clinical effects are reliable and meaningful. The conflict between high speed and accuracy is one of the crucial challenges for the development of modern dose calculation algorithms [112].

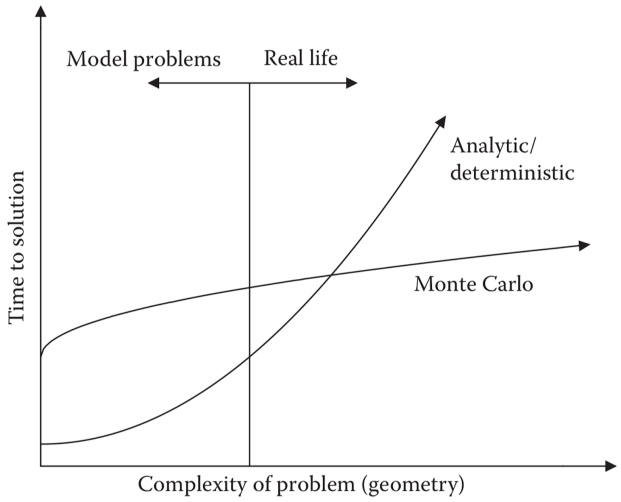


**Figure 24 -** Problem complexity and time to solution for MC and analytic/deterministic methods (adapted from [132]).

Currently, in electron and photon radiotherapy MC simulations using state-of-the-art computer programs are the most accurate methods to perform 3D transport and dose calculations [106,107,133,108–112,115,116,132]. Simulations using MC methods consider the scattering in high density materials, such as bone, as well as dose heterogeneities, generated through air cavities, more accurately than any other available method of dose calculation [130,134]. Due to the difficulties associated with the complexity of geometries in experimental measurements, many researchers are now using MC simulation methods and techniques to assess and evaluate the accuracy of planning systems´ algorithms for 3D conformational radiotherapy [117,135].

The simulation encompasses the modelling of the geometry, e.g. the linear accelerator geometry, based on the technical specifications and/or the patient anatomy provided by CT images [136]. It also considers the properties of the materials. For the primary photon, the distance should be sampled based on the cross-section of the

corresponding media. At the interaction site, the type of interaction should be sampled. All parameters of the secondary particles, such as their energies and scattering angles, are determined using differential cross sections and the corresponding probability distribution functions. These steps are repeated until the primary and secondary particles leave the geometry or the particle´s energy is below a pre-set value (sometimes referred to as “energy cut” [136] or are absorbed.

As a consequence, only a reduced number of studies were/are undertaken involving Monte Carlo simulation methods for treatment planning with IMRT [137]. This type of methods are not being used in realistic clinical situations because they are very time consumption for dose calculation purposes [114].

#### 4.1.2.1. Simulation of Out-of-Field Doses in Radiotherapy

In recent decades, several studies investigating and assessing the doses outside the irradiation field have been performed. Most of these studies involved out-of-field dose measurements, however, others performed the calculation of these doses using MC simulations for radiation transport [15,43]. The MC LINAC models for leakage and scattered radiation are fundamental for evaluating the dose outside the treatment fields up to 60 cm away from the isocenter [7].

Although there is a good agreement between the measured and the calculated dose using MC programs in several studies, the dose outside the treatment fields is often ignored. Some groups have used MC methods to simulate dose distributions outside the treatment fields from a LINAC [7]. Kry *et al.* described a method to model and validate 6 and 18MV beams of a LINAC for studies of doses outside the treatment fields with MC [138]. Another study performed by Lehmann *et al*. compared measurements and MC simulations for out-of-field doses for distances shorter than 15cm from the central axis of the beam [139]. However, the authors only modelled the components that the primary beam crossed, ignoring the influence of secondary shielding. Both studies did not analyse techniques to reduce the dose outside the treatment fields. Moreover, these studies did not use patient anthropomorphic computational phantoms for the MC calculations.

To accurately quantify the dose in organs/tissues outside the treatment fields, it is necessary to combine LINAC modelling with whole body computational phantoms. This has been successfully achieved in the studies report in this Thesis.

#### 4.1.2.2. The MCNP Computer Program

One of the Monte Carlo computer programs often used in radiotherapy is the Monte Carlo N-Particle code (acronym MCNP). In its current version, MCNP allows the simulation of the physics and interactions of photons, electrons and neutrons, as well as of protons, alpha particles, tritons, and several other charged particles, with the material [43,58,85,114,131]. Concerning photon interactions, MCNP has the ability to simulate various types of interactions (scattering, fluorescent emission after photoelectric absorption, pair production with local emission of annihilation of photons and bremsstrahlung radiation, photoneutrons production) and secondary radiation created from interactions of one type of radiation with a particular material [127]. The MCNP code also features the computational capability to use real patient anatomic data obtained from tomographic images. It can be easily interfaced (produce results to or use input data from) commercial treatment planning systems [140].

The first version of MCNP was released in 1977. In 1990, in its fourth version the possibility of carrying out the transport of electrons [131] was implemented.

The main features of the currently available and used version of MCNP, written in Fortran 90 programming language, encompass:

- The simulation the transport of neutrons, photons, electrons or neutron/photon/electron coupled transport, as well as the transport of charged particles such as protons, alpha particles, tritons, etc., over a wide energy range.
- The implementation of an arbitrary three-dimensional configuration of materials in cell geometry [128].
- Powerful source definition and specification features, namely criticality source, surface source, volumetric source, directional source, etc.
- A set of sophisticated tallies, including mesh tallies, allowing the easy manipulations, recording, plotting and representation of output results and data.
- A rich variety set of variance reduction techniques [128].

Concerning the simulation of photons and electrons, the two main particles considered in this study, photons are transported in the energy range between 1 keV to 100 GeV, electron transport is performed between 1 keV to 1 GeV [141].

*4.1.2.2.1. Input File Structure*

The input file created by the user contains information and specifications of:

- The geometry of the system to be modelled;
- The material description and assignment of materials to volumes (“cells”);
- The cross-sections data to be used, for the different particles, types of interaction, materials, energies, etc.;
- The source term characteristics (energies and angles of radioactive source emitted particles, energy and spatial distributions of beam particles, surface or volume distributions in materials, etc.);
- The physics processes to be simulated (types of interactions to be considered cut-offs for tracking of particles, etc.);
- Variance reduction techniques to be used to speedup and improve the calculation efficiency;
- The type of tallies,

as can be seen in Figure 25.

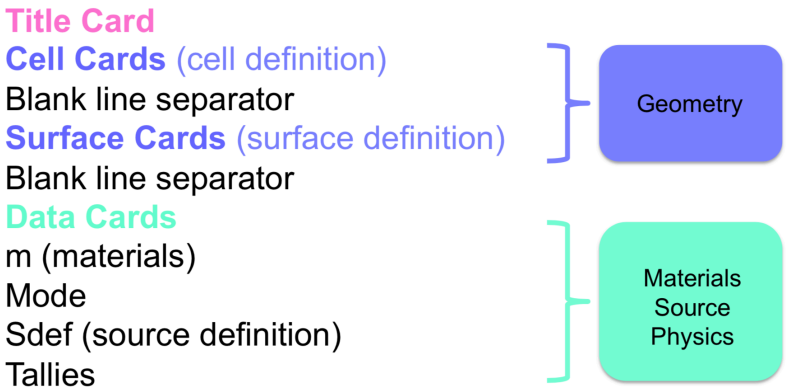


**Figure 25 -** MCNP input file structure.

*4.1.2.2.2. Cell and Surface Cards*

Boolean operators, like intersections, unions of geometric shapes such as cylinders, cones, spheres, flat hyperboloids and others define the cells (to be understood as volumes or sub-volumes constituent of a major volume). It is also possible to use complementarity and repetition operators, containing user-defined materials [141].

The surfaces are referenced in Cartesian coordinates and each surface has a positive side and a negative side. Surfaces such as planes, spheres, cylinders and cones, among others, can be defined by equations, described in the user's manual [141]. It is also possible to define surfaces as macrobodies. The surface of the macrobody is decomposed internally into surface equations. The space inside a macrobody is negative with respect to its surface [141].

*4.1.2.2.3. Data Cards*

The specification of the materials that fill the cells involves the following elements: (a) the definition of individual elements, (b) the elemental composition of compounds and mixtures and (c) the effective section tables to be used. The MCNP identifies the isotopes and elements by the so-called ZAID. The elements are identified by a ZAID of 100 x Z (atomic number) by adding the atomic mass, A, in the isotopes (ZAID = 100 x Z + A) [141].

The MODE command specifies which particles in the problem should be created and tracked, as follows: MODE = P for photon transport and E for electron or positron transport [141].

MCNP allows the specification of a wide variety of source conditions, with specification of probability distributions for the source particles´ variables: energy, time, position and angles (directions) and for other parameters such as cells or starting surfaces from which particles are generated. It also allows the specification of the geometric extension of the source. The source and type of radiation particles are specified through the source definition (SDEF) command, containing the variables and characteristics of all sources in the problem. Generally, it is defined as follows:

SDEF variable source = specification.

The specification of a source variable is usually an explicit value or a distribution number. Only one particle type is allowed in an SDEF source [141].

MCNP records and registers aspects of the average behaviour of particles, such as fluency and energy deposition, on tallies. The different types of tallies available in MCNP are described in Table 1 [141].

**Table 1 -** Types of tallies available in mcnp6 (adapted from [141]).

| Mnemonic | Tally Description | $F_n$ units | $*F_n$ units |
|---|---|---|---|
| F1 | Current integrated over a surface | particles | MeV |
| F2 | Flux average over a surface | particles/cm$^2$ | MeV/cm$^2$ |
| F4 | Flux average over a cell | particles/cm$^2$ | MeV/cm$^2$ |
| F5a | Flux at a point or ring detector | particles/cm$^2$ | MeV/cm$^2$ |
| FIP5 | Array of point detectors for pinhole flux image | particles/cm$^2$ | MeV/cm$^2$ |
| FIR5 | Array of point detectors for planar radiograph flux image | particles/cm$^2$ | MeV/cm$^2$ |
| FIC5 | Array of point detectors for cylindrical radiograph flux image | particles/cm$^2$ | MeV/cm$^2$ |
| F6 | Energy deposition averaged over a cell | MeV/g | jerks/g |
| +F6 | Collision heating | MeV/g | N/A |
| F7 | Fission energy deposition averaged over a cell | MeV/g | jerks/g |
| F8 | Energy distribution of pulses created in a detector by radiation | pulses | MeV |
| +F8 | Charge deposition | charge | N/A |

Tallies F1, F2, F4 and F5 are respectively surface current tallies (F1), average flux on a surface (F2), average flux in a cell (F4) and flux in a point or ring (F5). Tallies F6 and F7 give the energy deposition in a cell. Tally F8 is a pulse-height tally, allowing to simulate, inter alia, the pulse distribution in a detector, but offers many other options. The tallies are normalised to a particle emitted by the source. By adding an asterisk (*Fn) the units are changed in an energy tally.

In addition to the types of tallies shown in Table 1, MCNP also allows the use of mesh tallies. These are an important feature offered by MCNP, allowing the graphical display of particle fluencies, fluxes, energy deposition, dose or other quantities in a user-specified rectangular, cylindrical or spherical grid, superimposed on the problem geometry. The particles are followed through the independent mesh as part of the normal transport of the problem [141].

#### *4.1.2.2.4. Calculation of the Absorbed Dose with MCNP*

MCNP usually calculates the absorbed dose assuming the kerma approach, i.e. assuming that the kinetic energy transferred to the medium is absorbed (deposited) locally. This condition is satisfied when the equilibrium of charged particles is assured. In this condition MCNP can calculate the absorbed dose using tally F6, or even F4 and F5 tallies, if the flux-to-dose conversion functions provided in the literature are used [141].

When the equilibrium of charged particles cannot be guaranteed, the absorbed dose should be determined using tally *F8. This tally counts the energy deposited in a volume *dV* of mass *m* by subtracting the energy of the outgoing particles from the energy of the incoming particles, in volume *dV* [141], as shown in Figure 26. To obtain the value of the absorbed dose the result provided by tally *F8 must be divided by the mass *m* of volume *dV*.

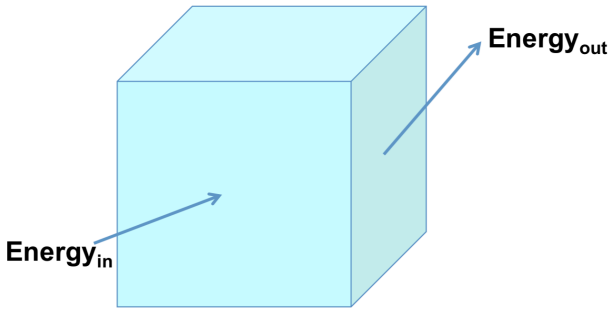


**Figure 26 -** Representation of the energy deposited by the mcnp tally *F8.

#### *4.1.2.2.5. Variance Reduction*

The challenge of using MC methods, such as MCNP, is to minimise the calculation time required to obtain an acceptable statistical uncertainty. Since a direct simulation may require the simulation of a very high number ($10^8$-$10^9$) of histories to obtain acceptable (statistically significant, with low uncertainties as required in radiotherapy) results, it is useful to use techniques either to reduce the uncertainty of the tallied values (or its variance) or to reduce the computing time to achieve the aimed relative uncertainty [131].

Variance reduction techniques include:

- Truncation methods and

- Population control methods.

Truncation methods refer to techniques for simplifying the model geometry and physics used for simulating the transport of particles, allowing the reduction of the computational time required to simulate each particle history. Energy cut-off is a truncation method that allows the specification of a minimum energy below which the particle is killed, decreasing the time per history. However, it can only be used when it is known that low energy particles have zero or close to zero importance [142].

Population control methods are examples of non-analog simulations when the simulated process is modified making certain events more or less likely than what would occur in nature. In population control methods, the number of particles in regions of high/low importance is artificially increased/reduced [142]. The importance of the cell (IMP) can be used to (1) end the history of the particle when it enters a cell of zero importance; (2) to control the population of particles in a cell by geometry splitting and Russian roulette; (3) for scaling the cut-offs.

Examples of population control methods implemented in MCNP are geometry splitting and Russian roulette (IMP) and weight window generator (WWG). In geometry splitting, importances are assigned to each cell (volume). Normally, cells near the tally region should have higher importance than cells further away. When a particle with weight w leaves a cell with importance I1 and enters a cell with higher importance I2, the particle is split (Splitting) into I2/I1 particles, each with weight (probability) I1/I2. Otherwise, if I2 is smaller than I1, the particle is killed (Russian roulette) with a given probability [141,142].

The importance of the cells should be pre-set and adjusted to keep the particle population in the cells relatively constant from the source to the tally region. On the other hand, the importance of the adjacent cells should not be too different. As a rule, the ratio between the adjacent cells should not exceed a factor of 6 to 8 [141].

With the WWG it is possible to increase the particle importance in the areas of interest, which are the areas where particles contribute to the tally result, and decrease the particle importance in the undesired areas, therefore this method optimises the sampling of particles in the areas of interest.

In the WWG variance reduction technique, the particle weights are adjusted as their energy is modified and they move through the various cells of the problem geometry. In each cell, a minimum (wmin) and maximum (wmax) weight is specified, defined as a multiple of the minimum weight. When a particle enters or is generated in the cell with a

weight above the upper limit, it is divided in such a way that all the daughter particles are inside the windows of weights. Similarly, if a particle has a weight below the minimum specified for the cell, Russian roulette is used to increase the weight of the particle until it is inside the windows of weight or until the particle is killed [141,143].

#### *4.1.2.2.6. Relative Error and Figure Of Merit (FOM)*

In variance reduction methods the simulation is changed so that the *p(x)* distribution produces fewer counts at zero and becomes more concentrated around $\bar{x}$ , the mean value of the random variable *x*. Thus, the variance of the mean $\sigma_{\bar{x}}^2$ will be lower than that of the *p(x)* analog distribution and the estimate of the most accurate mean [141].

In addition to the mean value for each tally, MCNP also determines the relative uncertainty, R, and the figure of merit, FOM. R is defined as [141]:

$$R \equiv \frac{\sigma_{\bar{x}}}{\bar{x}} \quad (4.1)$$

The value of R must be less than 0.1 to be significant. The FOM is defined by [141]:

$$FOM \equiv \frac{1}{R^2 T} \quad (4.2)$$

where T is the simulation time, proportional to the number N of simulated particles. For different simulations of the same problem, it is preferable the simulation with higher FOM, since it requires less time to obtain a given statistical error [141].

## 4.2. HUMAN PHANTOMS

In radiological protection and dosimetry, the term “phantom” refers to an anatomical model that can be either physical or computational. Physical phantoms have constituent materials that have elemental composition comparable or similar to human tissues and anthropomorphic computational phantoms are mathematical representations of organs or tissues, of a biological system of the human body [128,129,144]. On the other hand, the term phantom can be also used to refer to an object designed to be irradiated experimentally, with the objective of performing measurements of physical quantities using radiation detectors placed on or inside the object [145].

### 4.2.1. PHYSICAL PHANTOMS

Physical phantoms can be polymethyl methacrylate (PMMA) or water phantoms constructed of solid materials with composition equivalent to human tissue without having a specific human shape or size [128,129,144]. As the human body consists essentially of water, homogeneous plastic or water phantoms are widely used for the calibration of radiation detectors and treatment systems [129].

On the other hand, anthropomorphic phantoms (described in the next sub-section) have shapes and densities equivalent to human organs and tissues, allowing a more realistic representation of the human body [128,129,144]. They are divided into several sections, and in each one there are small cavities for the placement of dosimeters [128,129].

Measurements using physical phantoms, are often used for the benchmarking and validation of MC simulation results and calculations [129].

#### 4.2.1.1. Anthropomorphic Phantoms

Currently there are three versions of anthropomorphic phantoms commercially available for medical physics in radiotherapy [144]. One is the Alderson Rando phantom for radiotherapy - "Alderson Radiation Therapy phantom". This phantom is a modified version of its original version [144]. Another body phantom is the RANDO® phantom which is very similar to the original Alderson Rando phantom. Finally, the third group of body phantoms are the "ATOM® Dosimetry Phantoms", available in different sizes and ages, from newborn to adult [144].

The Alderson Radiation Therapy phantom is a model based on a man, 175 cm in height and 73.5 kg, matching the physical dimensions of the adult male model recommended by ICRP report 89. The female version is based on a woman of 155 cm in height and 50 kg. Both are made of 2.5 cm thick transverse slices and tissue-equivalent materials recommended by ICRU report 44 to represent the lungs and soft tissue [144]. Figure 27 shows the two different versions of the Alderson Radiation Therapy phantom.

**Figure 27 -** Female and male versions of Alderson Radiation Therapy phantom (adapted from [144]).

On each slice of these phantoms there are several holes for positioning thermoluminescent dosimeters (TLDs) or optically stimulated dosimeters in order to measure the radiation dose on specific points. Although it does not contain representations of all the organs and tissues of the human body, this phantom can be used as a basic physical model for building custom voxel computational phantoms [144]. This phantom has had some improvements since its original version, namely the replacement of the skeleton. This substitution has allowed the skeleton to be reproduced more realistically. On the other hand, it is also possible to couple various breast sizes to the female phantom [144].

In contrast to the Alderson Radiation Therapy phantom, each RANDO® phantom has a human skeleton that provides asymmetry in the bone structure, as well as alterations in the joints, typical of a patient. Just like the previous phantom, in the female version of RANDO® it is possible to couple 5 different breast sizes [144,146].

There are six different types of ATOM® phantoms, as shown in Figure 28, as well as their characteristics in Table 2 [144].

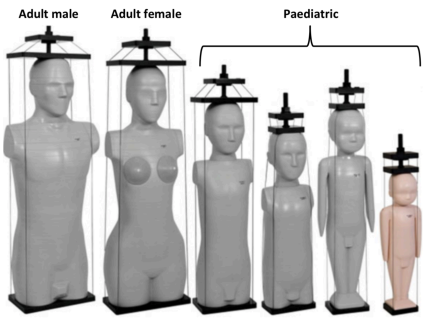


**Figure 28 -** ATOM® phantoms (adapted from [144]).

**Table 2 -** Characteristics of ATOM® phantoms.

| Phantom | Height (cm) | Weight (kg) |
|---|---|---|
| Adult male | 173 | 73 |
| Adult female | 160 | 55 |
| Paediatric 10 years | 140 | 32 |
| Paediatric 5 years | 110 | 19 |
| Paediatric 1 year | 75 | 10 |
| Paediatric newborn | 51 | 3.5 |

They are the only commercially available paediatric body phantoms. They also feature the possibility of coupling arms and legs in the adult phantoms, as well as in the paediatric phantoms of 10 and 5 years. The material equivalent to the bone tissue is homogeneous and its density varies according to the age of the phantom, being 1.41 g/cm$^3$ for the newborn and 1.6 g/cm$^3$ for the adults. Each cross sectional slice has 2.5 cm and it is possible to place radiation detectors, on average, in 21 radiosensitive organs [144].

### 4.2.2. ANTHROPOMORPHIC COMPUTATIONAL PHANTOMS

Anthropomorphic computational phantoms are computational models of human anatomy and a mathematical or voxel representation of the external form of the human body together with the limits of internal organs and tissues [128,129,145]. The volumes that define organs and tissues are filled with a material with elemental composition and density very close to that of the tissues tabulated in reference ICRU reports and ICRP publications [145,147]. The conceptual basis behind the development of computational phantoms is to mimic in the most accurate way the anatomy, composition and density of an organ or body region or even of an entire human body [128,129,148]. These phantoms allow reproducing through MC simulations the absorbed and equivalent doses received by organs and tissues under different types of exposure to ionizing

radiation. This will allow a better understanding of how radiation interacts with tissues [129,148].

Anthropomorphic computational phantoms and models have been widely used with MC computer programs for radiological protection and dosimetry purposes, namely to estimate the doses in the organs for radiotherapy treatment planning [8,145,149].

Computational phantoms existing until now can be classified in three categories according to the technique used in their construction: stylized (or mathematical) phantoms, voxel (or tomographic) phantoms and BREP (Boundary REPresentation) phantoms [128,129]. Figure 29 shows the evolution of human computational phantoms. In the late 1950's the human body was modelled as a sphere with small spherical organs [148].

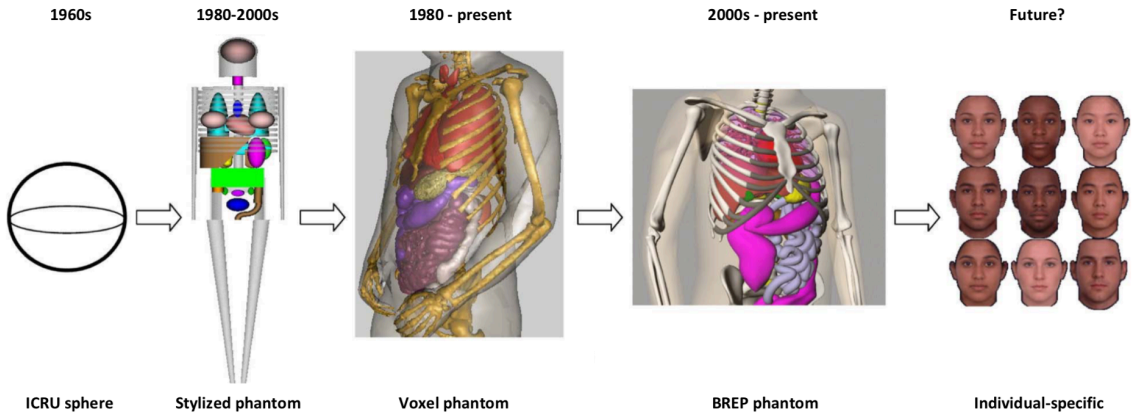


**Figure 29 -** Evolution of human computational phantoms (adapted from [148]).

#### 4.2.2.1. Mathematical or Stylized Phantoms

Anthropomorphic mathematical phantoms were the first type of computational phantoms developed. They are simple structures where body size and shape, as well as organs and tissues, are delimited by combinations and intersections of planes, circular and elliptical cylinders, spheres, and cones [128,129,144] which mathematical expressions are well known and parameters can be adjusted to match a specific organ volume or shape. Since these phantoms do not satisfactorily represent the human anatomy, and consequently generate approximate dosimetric results, they were used mostly for internal dosimetry purposes and studies [144].

One of the first anthropomorphic mathematical phantoms was described by Snyder *et al.* [150] at the Oak Ridge National Laboratory of the U.S. Department of Energy. This

phantom was composed of three different regions: skeleton, lungs and soft tissue with three different constituent materials, becoming known as Medical Internal Radiation Dose (MIRD-5) phantom.

In 1978, Snyder and colleagues published a revised form of MIRD-5 phantom with an elliptical head, legs, male genitals, improved skeletal structure and gastrointestinal tract [128]. The series of phantoms developed by Cristy at Oak Ridge National Laboratory, included a newborn phantom, as well as children 1, 5, 10 and 15 years old and an adult.

The 15-year-old phantom of the model was modified to represent both a 15-year-old individual and an adult female, after noting that the body weight and dimensions of an ICRP 23 reference adult woman were approximately the same as those of a 15 years-old individual. The remaining phantoms are hermaphrodites [129,144].

Kramer and colleagues introduced the adult female (EVA) and male phantoms (ADAM) as shown in Figure 30 [151].

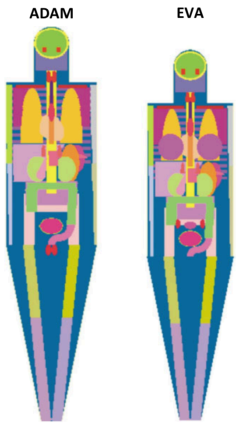


**Figure 30 -** Adult stylized MIRD-5 phantoms (adapted from [151]).

More recent studies [152–154] reviewed the simplified organ models of mathematical phantom models, comparing them with the actual human anatomy and improving the models of some organs. These models were incorporated in new phantoms [155] and currently constitute the most advanced and sophisticated series of mathematical phantoms [156].

#### 4.2.2.2. Anthropomorfic Voxel Phantoms

The rapid advance in medical imaging technology, specifically in computed tomography and magnetic resonance imaging, has provided the ability to produce high resolution transverse digital images of the human internal anatomy [145,148]. The pixels of these images, when extended to the third dimension, become cubic volume elements called voxels [145]. These data can be used to create a three-dimensional digital representation of the shape, volume and composition of human organs. Each voxel is defined in such a way that it contains a uniform shape and is assigned an index that identifies it as belonging to a particular organ or tissue [145]. These computational models have also been called tomographic models, voxel models and voxel phantoms. Voxels have typical volumes of $mm^3$ and a few million voxels are required for a complete and accurate representation of the human body anatomy.

Voxel models constitute a very detailed representation of human anatomy and are currently available to perform Monte Carlo modelling and simulation studies of relevance for radiation protection, dosimetry and, of special interest to this thesis, in radiotherapy related calculations. These models are representations of reference individuals since the masses and volume of organs and tissues do not necessarily match those of a particular individual [145].

The ICRP publication 89 states that the analysis and calculations of retrospective dosimetry for individuals and specific situations should use appropriate values for the individuals involved, when this information is available [145,157]. Thus, the greater the number of reference voxel phantoms (as a function of age, gender, ethnicity, size, height and even weight), the greater the correspondence between the reference phantom and the actual patient.

In terms of geometric spatial representation, tomographic models are, in essence, different from stylized models, in the sense that 3D anatomical images consist of a digital description of anatomy [148,158]. The information from computed tomography is composed of several sections, each one presenting a two-dimensional map of the anatomy [129]. The three-dimensional volume of the voxel is measured by multiplying the pixel size by the thickness of an image slice [129]. Therefore, the voxel model contains a large number of voxels connected together to describe individual anatomical structures and organs, i.e., the object is represented by volume matrices or voxel dimensional matrices [148].

The development of anthropomorphic voxel phantoms from various imaging modalities, such as computer tomography, faces some technical challenges: (1) Whole-body models are often required, but for radioprotection reasons, the series of images are usually executed at a limited anatomic region of the human body [129,148,149]; (2) Organs/tissues must be manually segmented by or with help of experienced professionals (radiologists), or automatically through dedicated software [129,148]; (3) The number of voxels and the number of images of the whole body tomographic model can be too large to be worked with some MC codes [148], or even for a processor to handle [129].

#### *4.2.2.2.1. Existing Anthropomorphic Voxel Phantoms*

In 1984, the first voxel phantom representing a head and trunk of a tomography examination of a female cadaver was reported, and it was used to calculate the effective dose of a dental radiograph [129,145]. Excluding this initial model, in 2004, there were about 21 voxelized phantoms, partial or whole body reported in the literature [145] and in 2007 there were 38 [129]. Zankl *et al*. in the late 1980s decided to use three-dimensional CT images in healthy volunteers to develop a family of 12 voxel phantoms, including BABY, CHILD, DONNA, FRANK, HELGA, IRENE, GOLEM, GODWIN, VISIBLE HUMAN, LAURA, KLARA and KATJA. Initially, male adult phantoms were developed, followed by female adults, paediatrics and pregnant women [128,129]. The LAURA and GOLEM phantoms were reviewed and the REX and REGINA phantoms were obtained, published as the ICRP adult, male and female reference phantoms [129,147,157], as can be seen in Figure 31.

**Figure 31 -** Rex and Regina phantoms (adapted from [129]).

Voxel Man was developed in 1994 by Zubal and collaborators, based on computer tomography images, consisting of head and trunk. Initially, this phantom was used to optimize images in nuclear medicine [128,129,135]. Additionally, improvements were made in the phantom with brain magnetic resonance imaging, becoming known as the Zubal phantom [128,129]. Later, this phantom gave rise to MANTISSUE3-6 and VOXTISS8 phantoms, in which the upper and lower limbs were introduced in two different positions [128,129]. From the published information, in 2003 Kramer and collaborators developed an adult male phantom called MAX and in 2004 an adult female, the FAX phantom. Both phantoms were adjusted to the reference values of height and mass of the organs according to ICRP publication 89 [129,149]. In 2006, Kramer *et al.* reviewed these phantoms in order to improve their compatibility with the recommendations of ICRP publication 103 [60,129]. They became known as the MAX06 and FAX06 phantoms [129].

In 1996, Dimbylow developed an adult male phantom known as NORMAN from magnetic resonance imaging. In 1997, Jones used NORMAN to estimate doses in organs from internal and external photon sources. In 2005, Dimbylow, also from magnetic resonance imaging developed an adult female phantom known as NAOMI, however it is only used in non-ionizing radiation calculations [128,129]. In the same year, NORMAN-5 was created in Italy to obtain external photon source dose data. In 2006, Dimbylow merged NOAMI with stylized fetal phantoms, creating a series of phantoms of a pregnant woman [128,129].

In 1999, from the tomographic images of a 14-years-old girl, the trunk phantom ADELAIDE was created and for some time it was the only non-adult voxelized phantom. The VIP-Man voxel phantom, implemented in the MCNP code, was created from cross-sectional photographic images of a 39-year-old cadaver with 103 kg [129]. The digital photographs were captured with a pixel resolution of 0.33 mm x 0.33 mm. This phantom consists of more than 3.7 billion pixels. Since the phantom was created from a cadaver, the lungs are smaller compared to a living individual. This phantom has been used in numerous studies in the field of medical physics [29,128,129]. The VISIBLE HUMAN phantom was created from tomographic images of the same individual with a resolution between 2 to 4mm [128,129].

In Japan in 2001, an adult male model called OTOKO and an adult female phantom known as ONAGO were developed. Between 2007 and 2008 Sato and colleagues developed the JM, JM2 and JF phantoms, mainly used in dosimetric applications. Another Japanese group reported the development of 2 phantoms known as TARO

and HANAKO created from magnetic resonance imaging for studies of non-ionizing radiation [128,129].

Also in Korea, several Korean phantoms have been developing at Hanyang University: Korean male (KORMAN), typical Korean male (KTMAN-1, KTMAN-2), Korean high-definition reference (HDRK) and Korean female (KORWOMAN) [156].

Other Asian voxel phantoms have been developed in China. For example, the Chinese Man (CNMAN) constructed from colour photographs of cadavers by the Chinese Institute for Radiological Protection, the Visible Chinese Human (VCH) also produced from colour photographs of cadavers by the Huzhong University of Science and Technology and the Chinese Voxel Phantom (CVP) produced from magnetic resonance imaging by Tsinghua University [129,144,156].

*4.2.2.2.2. Paediatric Voxel Phantoms*

There is a need for paediatric anthropomorphic computational phantoms. However, such phantoms cannot be obtained by sizing an adult phantom, because there are differences in organs, namely in their position, size and composition according to the individual age [29]. Nipper and collaborators in 2002 constructed two paediatric phantoms from CT images. One phantom is female of a 6-day old newborn with a 512 x 512 x 485 matrix and the other a male phantom of approximately 2 months old with a matrix of 512 x 512 x 438 [159]. Between 2002 and 2006, Choonik Lee and colleagues in University of Florida (UF) developed a series of voxelized paediatric phantoms, representing children between 0 and 15 years of age. With the intention of creating a reference library of paediatric phantoms to evaluate organ doses, these phantoms were divided into 2 series [128,129,160,161]. Serie A involved a female and male voxel phantom of a newborn, 1 year, 5 years, 10 years and 15 years of age, for which the stature, weight and mass of individual organs vary only in 1% of the reference values of the ICRP publication 89. Serie B is made up of phantoms constructed by sizing the phantoms of Serie A, in order to obtain phantoms with 1 year difference among all phantoms of Serie A [128,129,160,161]. Thus, 5 voxel phantoms of 9 months, 4, 8, 11 and 14 years were created with resolutions between 0.43 x 0.43 x 3.0 $mm^3$ and 0.625 x 0.625 x 6.00 $mm^3$. The interpolation of ages took into account organ masses, heights, changes in geometry and material composition according to age and gender, as mentioned in ICRP references [161]. These phantoms can be seen in Figure 32.

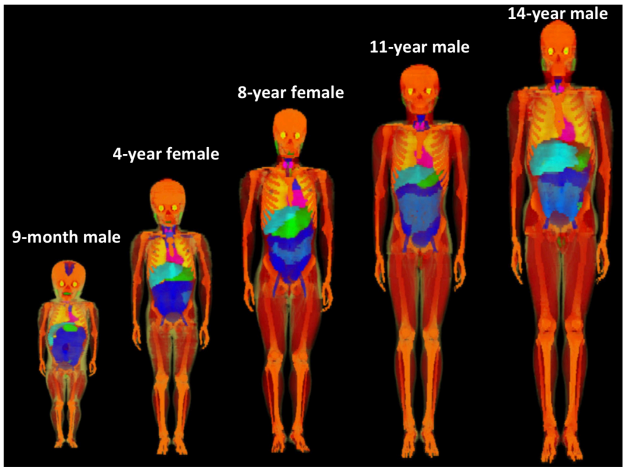


**Figure 32 -** UF Series B of paediatric computational phantoms (adapted from [161]).

In 2009, Taddei and collaborators developed a voxel phantom in the MCNPX code to evaluate the doses administered in paediatric patients with proton beams [129]. Also in 2009, a French group built 4 full body computational phantoms to be used in radiotherapy, from computed tomography images, and also used IMAgo and ISOgray software to model the phantoms. The phantoms included a 27-year-old male adult, a 52-year-old female adult and 2 children with 3-year-old, one in prone position and the other in supine position [128,129,149]. Also in 2009, Alziar developed a tool in which it is possible to adjust the phantom values to the anatomical data of the patient in order to obtain a greater correspondence with each individual [128,129,149]. Becker and colleagues in 2007 developed the software VolumeChange that allows editing segmented voxel models, i.e., we can change the volume, shape and location of each organ [149].

#### *4.2.2.2.3. ICRP Reference Voxel Phantoms*

The previously mentioned LAURA and GOLEM phantoms were reviewed and the REX and REGINA phantoms were obtained, published as the ICRP adult, male and female reference phantoms [129,147,157] , as can be seen in Figure 31.

In order to develop the reference phantoms of ICRP, several processes were considered [128,129]: (1) CT images of individuals with values of height and weight close to the reference man and woman were necessary; (2) Segmentation of the

structures was performed; (3) Heights were adjusted to the reference values by sizing the pixels; (4) Bone masses were adjusted to the reference values; (5) The organs were adjusted to the reference values through the addition and subtraction of pixels.

Although these phantoms fill a gap in radiological protection, they exhibit a considerable thickness (up to 8 mm) when compared to later developed phantoms [128,129]. With these voxel dimensions, smaller organs cannot be realistically defined and the skin as well as the organ walls contain small holes. To address this issue, a Korean group developed in 2013 a new version of the ICRP reference man, converting the voxels into polygon-surface volumes [129]. Table 3 shows the main characteristics of adult female and male reference computational phantoms.

**Table 3 -** Main characteristics of adult female and male reference computational phantoms.

| Property | Female | Male |
|---|---|---|
| **Height (m)** | 1.63 | 1.76 |
| **Mass (kg)** | 60.0 | 73.0 |
| **Number of tissue voxels** | 3,886,020 | 1,936,375 |
| **Slice thickness (voxel height, mm)** | 4.84 | 8.0 |
| **Voxel in-plane resolution (mm)** | 1.775 | 2.137 |
| **Voxel volume ($mm^3$)** | 15.25 | 36.54 |
| **Number of columns** | 299 | 254 |
| **Number of rows** | 137 | 127 |
| **Number of slices** | 348 | 222 |

*4.2.2.2.4. Voxel Phantoms Construction*

For the development of a voxel-based model, four major phases should be followed [129,148]: (1) Acquisition of a computed tomography or high definition magnetic resonance imaging data set; (2) Classification and segmentation of the various tissues and organs by assigning an identification number to each pixel; (3) Identification of the type of biological tissue and organs, their elementary compositions and respective densities, using, for example, tissue characteristics [129] from ICRU report 46 and ICRP publication 89 [145,148]; (4) Implementation of the computational model in the MC computer program to simulate radiation transport and calculate quantities of interest for the task under consideration (e.g., simulation of a medical image, dosimetry calculation system, among others).

The construction of tomographic models requires the identification of the boundaries between the different organs and tissues that are displayed in the medical image. All pixels belonging to an organ or tissue are assigned an organ identification number that replaces its original value on a grey scale [145]. In this way, each pixel belonging to an organ or tissue can be identified and distinguished from pixels belonging to other organs [145,148]. This process is known as segmentation, since the image is divided into smaller segments [145].

Segmentation is a very time-consuming process, because there are a large number of boundaries and a large number of cuts to process. With CT images, it is difficult to visualize the ovaries, pancreas, oesophagus and distinguish adrenal glands from the kidneys [145]. Moreover, the walls of hollow organs, such as the intestines, are not always perceptible from their contents. Consequently, manual manipulation of images using processing software and considerable anatomical knowledge is necessary [145].

*4.2.2.2.5. Drawbacks and Limitations of Voxel Models*

The characterization of 3D volumes from voxel models has produced more realistic representations of human anatomy compared to mathematical models. However, one of the main issues with voxel models is the voxel size. Although some authors reported that voxel resolution of 2 x 2 x 2 $mm^3$ in x, y and z can accurately represent human anatomy, there are some small and radiosensitive organs that can not be delineated using voxels of this size (e.g. bone marrow) [129]. For this reason, the length of one side of the pixel defines skin thickness and this can result in a very large value for skin thickness. To a certain extent this gap can be overcome during dosimetric calculations

by coding the radiation transport to assign only the deposited dose to the first 1.5 mm of voxel [129,145]. Additionally, a surface composed of voxels has an irregular shape instead of a smooth surface. This will have an effect of overestimating the surface area of an organ, which is particularly relevant in organs with spherical shapes. Some studies indicated that the effect of the dose on an organ is not very large [145]. Voxel models with smaller voxel sizes have improved anatomical realism. Nevertheless, the number of voxels has to be much higher to represent the whole body, thus greatly increasing computational effort during MC simulations [129].

Furthermore in voxel phantoms, body dimensions can be modified by changing the voxel resolution, which entails a proportional modification to the size of all organs and tissues in the body, which is anatomically inaccurate [145,162]. For example, creating an individual who does not fall in the $50^{th}$ percentile morphometric (height and weight) from an individual at the $50^{th}$ percentile (reference individual) cannot be realistically performed, because the subcutaneous distribution of fat tissue may be intrinsic to each patient [29]. Therefore, voxel models are too specific for an individual and they are difficult to personalize for each specific patient [129].

#### 4.2.2.3. BREP Computational Phantoms

The development of BREP (Boundary Representation) phantoms began in the early 2000s. Software tools for 3D image manipulation (erosion, dilatation, combination, among others) already existed before their use in the construction and manipulation of BREP computational phantoms. These graphic softwares were mainly used in 3D animations and industrial design. There are two main techniques of representing bodies in BREP modeling: Non-Uniform Rational Basis Spline (NURBS) and Polygon Mesh (PM). The Polygon Mesh geometries allow the construction of models with a higher level of detail but can present difficulties in cases that require simulations of motion and movements. On the other hand, NURBS modeling is usually computationally more efficient in motion simulation, but can present loss of detail in organs with more complex geometries [144].

However, most of the particle transport codes are not yet adapted to directly use the BREP phantoms [144]. Thus, after manipulations, the BREP phantom must be voxelized so that it can be interfaced with and used in MC codes for dosimetric calculations. In addition, the images used in the generation of BREP models (CT and

MR) are voxelized images, since they are composed of pixels arranged in cross-sections on the z-axis [144].

The first phantom of this type to be described in the literature was NCAT, developed from the set of computerized tomography images of Visible Human. The 3D anatomy was later extended to a 4D representation, by modeling the heart and respiratory movements and creating the XCAT family of phantoms [129].

In 2007, Xu and collaborators developed a series of phantoms of a pregnant woman and fetus in various gestational stages (3, 6 and 9 months), designated as RPI-3, RPI-6 and RPI-9 [129,144]. In 2010, Lee and collaborators at The University of Florida's developed a series of hybrid phantoms consisting of female and male models of newborns, 1 year, 5 years, 10 years, 15 years and adults. These models are based on the University of Florida B-series phantoms and the organ and tissue masses were adjusted according to the values published in ICRP 89 [129,163]. These phantoms are considered by ICRP as reference and there is currently a draft of an ICRP report entitled Paediatric Reference Computational Phantoms, which summarizes the methods, and procedures used to create the paediatric phantom group. This phantom family can be seen in Figure 33.

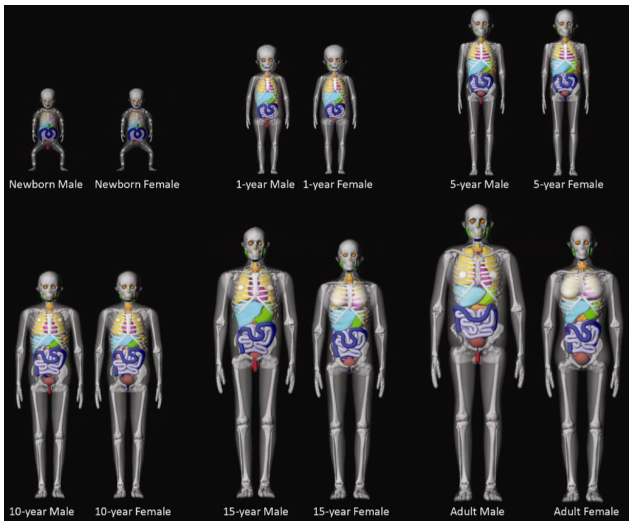


**Figure 33 -** UF phantom family [163].

In 2014, a nine-month-old female hybrid phantom and fetus were developed for studies in nuclear medicine. The phantoms were constructed based on a set of MRI images of the pelvis of a pregnant woman, and the data were combined with the adult female

ICRP phantom using polygonal mesh modeling and techniques. The phantom organs were resized to match the mass of the ICRP publication. The fetus contains 20 different organs [164].

Two adult phantom models, the male Rensselaer Polytechnic Institute Adult Male (RPI-AM), and the female Rensselaer Polytechnic Institute Adult Female (RPI-AF), produced by Zhang and collaborators were the first mesh phantoms developed. Their 3D objects were obtained from the internet and are adjusted according to the reference man of ICRP 89 [165].

The Female Adult mesh (FASH) and Male Adult mesh (MASH) phantoms (shown in Figure 34) were developed by Cassola and collaborators in 2010 and adjusted to represent reference adults from ICRP 89 in orthostatic position. Some organs used in the models were obtained in websites and others developed using free 3D modeling software [166].

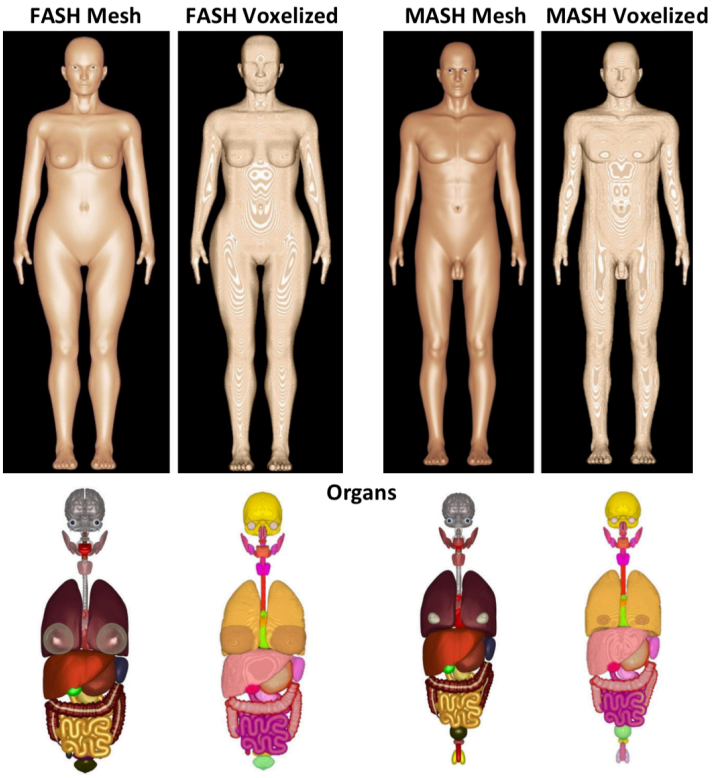


**Figure 34 -** FASH and MASH phantoms (adapted from [166]).

Two mesh phantom couples representing children of 5 and 10 years were developed in 2011 and are show in Figure 35 [167]. The published values for 5- and 10-years old children from ICRP 89 were the parameters used to adjust the mass of organs and tissues. They used polygonal mesh modeling for the body contour and shape of organs and tissues from anatomical information [167].

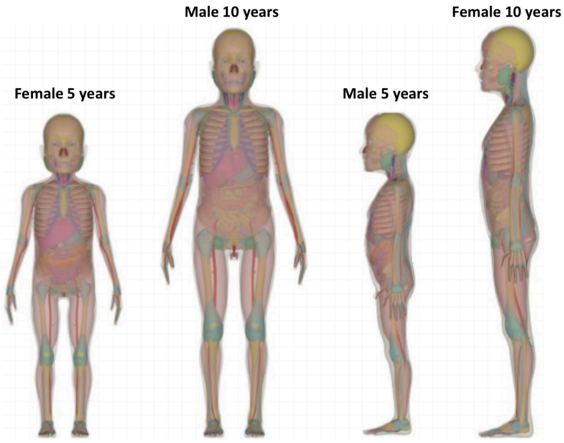


**Figure 35 -** Mesh phantoms (adapted from [167]).

In 2013, Cassola and collaborators built two reference phantoms, one of a newborn and another of a 1-year-old child [168]. The anatomical descriptions for the construction of the phantoms were taken from atlases, books and images provided by the Department of Anatomy of the Federal University of Pernambuco. Figure 43 shows the paediatric mesh phantoms developed.

In 2017 a Swiss group developed 1100 female and male phantoms with 10th, 25th, 50th, 75th and 90th body morphometries, from newborn phantoms and children of 1, 2, 5, 10 and 15 years old [169]. The development of numerous phantoms allows complete dosimetric calculations and risk assessment for the paediatric population in various age groups, as well as various anthropometric parameters.

In 2020, Choi *et al.* developed a body size dependent phantom library constructed from ICRP mesh-type reference computational phantoms. This library consists of 104 female adult phantoms and 108 male adult phantoms with different heights and body weights, representing Asian and Caucasian populations [170].

Compared to voxel models, the main advantages of BREP modeling are the possibility of more accurately representing detailed body structures and the ability of deforming organ surfaces (to easily manipulate phantom anatomy). Furthermore, the body position of BREP phantoms can be adjusted and some even allow 4D modelling (e.g. motion of lungs and heart over time) [129,170].

However, the application of BREP phantoms in current MC programs is not trivial and very computationally demanding, manly due to the very detailed modulation of complex anatomical structures [129].

Hybrid phantoms have been developed by combining voxel and BREP modelling [171]. They can represent detailed anatomical structures using polygon mesh surfaces and bigger organs (which should be very heavy computationally in polygon mesh) can be represented using voxels. In these phantoms, it is possible to adjust the organ surfaces to the desired shape and volume, using specific images of the patients and deformable image processing [29]. The interest in hybrid phantoms has greatly increased over the last decades, mainly because they combine the advantages of voxel and BREP phantoms [129,169].

### 4.2.3. Monte Carlo Methods and Computational Phantoms

Full-body computational phantoms can be a very powerful tool when combined with MC simulations [21,29,128]. The available computational phantoms listed in this chapter provide the necessary geometries for assessing several physical quantities to organs and tissues in the phantoms.

The geometry defining tools in most widely used MC computer programs are able to model very complex geometries and every type of material and thus replicate almost every possible radiation scenario. The application of computational phantoms in these geometries allow MC computer programs to predict the radiation transport of particles in the human body and tally various physical quantities (e.g. fluency, deposited energy, absorbed dose) [129,141]. The application of this method to the medical field allows for the replication of wide variety of medical scenarios and assessment of possible health risks due to radiation exposure of patients and professionals. Namely computational phantoms and MC computer programs can be used to calculate particle tracks and predict the outcome in situations [21] that could not be assessed in a clinical scenario, such as out-of-field doses.

One of the main drawbacks of MC methods is that the modelling of very complex geometries an the applications of computational phantoms with a very high number of voxels can be very computationally demanding [128,129].

# SECTION III – METHODS AND RESULTS

# CHAPTER 5 – OUT-OF-FIELD AND IN-FIELD MODELING AND VALIDATION OF 6 MV LINAC

## 5.1. MOTIVATION

LINACs are highly technological complex machines, used to treat cancer with high-energy (MeV) radiation beams [172]. In radiotherapy, MC methods have been often used to create a virtual models of LINACs [132,173,174] and radiation sources [132]. In order to perform Monte Carlo simulations of a 6 MV photon beam of a given LINAC, it is necessary to characterize and model both the electron and photon beams (from the point of view of particles´ fluencies and doses, spatial, energy and angular distributions) and the LINAC (from the point of view of the structural components, their geometry, material compositions, etc.). Therefore, it is fundamental to have access to the details of the composition, density, position and geometry (dimensions and shapes) of all components of the LINAC head. The most important components are the target, FF, the secondary collimators, MLC and wedges [132,175], described in a previous Chapter. The primary electron beam is accelerated to a certain nominal energy and features a spatial distribution. It reaches the target which normally consists of material with a high atomic number [176] which allows the production of bremsstrahlung photons [132]. Subsequently a primary collimator blocks the bremsstrahlung photons and the FF attenuates the fluency in order to produce a reasonably flat dose distribution at a given depth. The target and the FFs are the main sources of electron contamination, when a wedge is not present. The next component to be considered is the ionization chamber, however it is often omitted in MC studies, since it features low

photon beam attenuation [132]. Then the beam is dimensioned, modelled and geometrically shaped by secondary collimators (jaws), MLCs or even wedges [132]. MLCs consist of a set of tungsten leafs that allow to spatially define and shape the fields used with IMRT. They are the most challenging components to model, using MC simulation methods, in a LINAC, as they can have very complex shapes and can move during IMRT treatment delivery [132].

The fine-tuning of the beam and LINAC model is performed comparing clinical radiometric and dosimetric measurements using physical phantoms with MC simulation results using computational (sometimes anthropomorphic) phantoms of, *inter alia*, lateral and depth profiles, for different setups [177].

In order to be able to assess the out-of-field doses, using MC methods, it is first necessary to model the LINAC used and then to validate this modelling. The main aim of this chapter is to describe the steps and methodology leading to the development of a model and the validation, for the first time, of the 6 MV in-field and out-of-field beams of Varian Clinac 2100 CD coupled to a Millenium™ 120-leaf MLC, using experimental measurements and MCNP-MC calculations.

## 5.2. CLINICAL MEASUREMENTS

All measurements were performed in the Radiotherapy Service of Instituto Português de Oncologia de Lisboa Francisco Gentil (IPOLFG).

### 5.2.1. MILLENIUM™ 120-LEAF MLC

The Millennium™ 120-leaf MLC measurements were performed on a Varian Clinac 2100 CD operated at a nominal photon beam of 6 MV, using a 100 cm source to surface distance (SSD) in a 30 x 30 x 30 $cm^3$ PTW™ water phantom with a 0.125 $cm^3$ PTW™ Semiflex Chamber Type 31010 detector at 5 cm depth. The MLC transmission and the dosimetric leaf separation (DLS) were assessed. The transmission with the two banks of leafs closed ($MLC_{closed}$) measured for a 10 x 10 $cm^2$ field was defined by the jaws, for 1000 MU, a source-phantom distance of 100 cm and at 5 cm depth. First it was measured with the bank A of leaves closed and then with the bank B of leaves closed. Then the average of the two was determined.

Afterwards, the transmission with the two banks of leafs open ($MLC_{open}$) was measured for a 10 x 10 $cm^2$ field defined by the jaws, for 200 MU, a source-phantom distance of

100 cm and at 5 cm depth. The MLC transmission ($MLC_{TR}$) was calculate as follows [178],

$$MLC_{TR} = \left[\frac{\frac{MLC_{closed}}{5}}{MLC_{open}} * 100\right] \quad \text{(Eq. 5.1)}$$

Where $MLC_{close}$ and $MLC_{open}$ are the readings/calculations of the IC charge in nC, and 5 is the factor between 200 and 1000 MU.

The measurements of the DLS were performed for 200 MU, a 10x10 $cm^2$ field, a source-phantom distance of 100 cm and at 5 cm depth, for different gap sizes ($Gap_{size}$): 0.5, 1, 5, 10 and 20 mm. The DLS was determined according to the equation 5.2 [178], where *a*, is the slope of linear regression between the corrected readings and the gap sizes.

$$DLS = \frac{Corrected_{Reading} - (a * Gap_{size})}{a} \quad \text{(Eq. 5.2)}$$

The $Corrected_{Reading}$ was calculated through the following equation:

$$Corrected_{Reading} = Reading - Correction\ factor \quad \text{(Eq. 5.3)}$$

where the $Reading$ is in nC and is the value obtained directly from the electrometer. The $Correction\ factor$ is given by the following equation:

$$Correction\ factor = \left(\frac{MLC_{closed}}{5}\right) \times \left(1 - \left(\frac{Gap_{size}}{120}\right)\right) \quad \text{(Eq. 5.4)}$$

According to the manufacturer's information, a model of the Millennium™ 120-leaf MLC was developed using the state-of-the-art MC program MCNP6™ (version 1.0, Los Alamos National Laboratory, Los Alamos, NM) [141], divided into 2 banks, each one with 60 leaves, as can be seen in Figure 36. The leaves´ thickness closest to the

isocenter is 0.5 cm and the leaves´ thickness farthest from the isocenter is 1 cm. The MLC is composed of a tungsten alloy consisting of $^{74}W$ (90%), $^{28}Ni$ (6%), $^{29}Cu$ (2.5%) and $^{26}Fe$ (1,5%), with a density of 17.5 g $cm^{-3}$ [179].

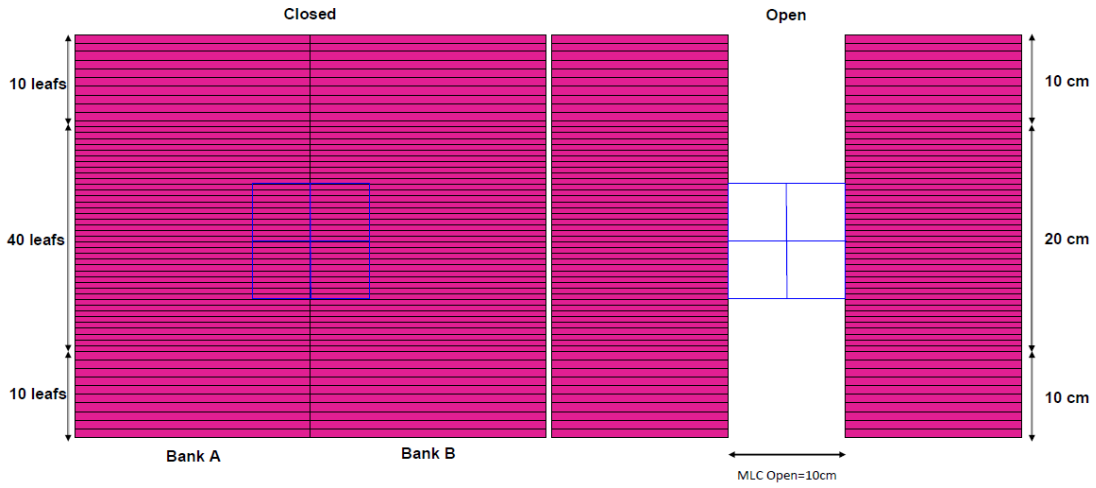


**Figure 36 -** MLC geometry used to calculate the transmission.

It was defined that the MLC transmission should be about 1.6% and for the DLS the tolerance should be below 0.2 mm [180,181].

### 5.2.2. Measurements of the Beam Profiles and PDD Curves using a Clinac Varian 2100 CD Operated at 6 MV

Measurements to verify the accuracy of the MC model, which will be described later in this chapter, were performed in the Linac operated at 6 MV. Beam profiles and Percentage Depth Dose (PDD) curves were measured at a 100 cm SSD in a 30 x 30 x 30 $cm^3$ PTW™ water phantom using a 0.125 $cm^3$ PTW™ Semiflex Chamber Type 31010 ionization chamber, under the same clinical conditions used in the radiotherapy department routine, namely the depth and field sizes of the measurements A PTW™ Tandem Dual-Channel Electrometer and the PTW™ Mephysto software were used to perform, record and analyse the measurements. The PTW™ Mephysto software not only acquires the plots at the time of measurement, but also allows access to a .txt file with all the information of the measurements that will be used for data analysis.

For in-field doses, values for determining the PDD curves and dose profiles were measured. PDD curves were obtained from 5 x 5 $cm^2$ and 10 x 10 $cm^2$ field sizes. The beam profiles were acquired in square fields sizes of 10 x 10 $cm^2$ and 30 x 30$cm^2$. For out-of-field measurements, square field sizes of 5 x 5 $cm^2$ and 10 x 10 $cm^2$ were defined. The values were measured outside the field for distances 5 cm to 17 cm away from the central axis, for the 5 x 5 $cm^2$ field size. For 10 x 10 $cm^2$ field size the values were measured outside the field for distances 10 cm to 17 cm away from the central axis. All beam profiles were measured at 10 cm depth (Figure 37).

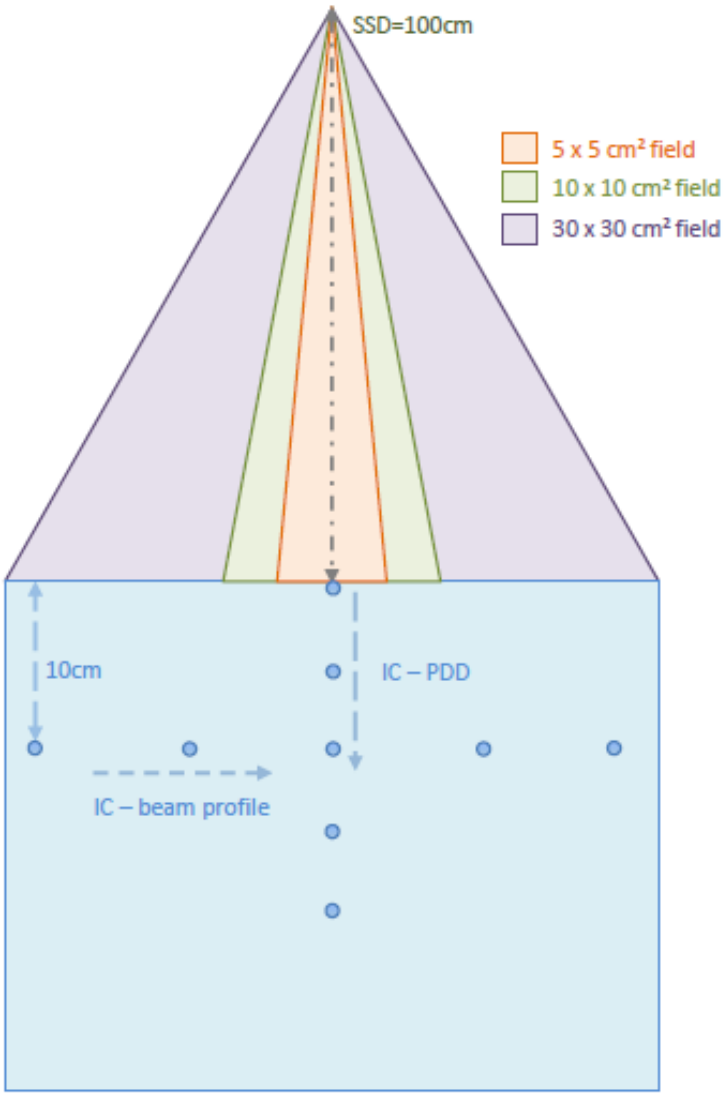


**Figure 37 -** Schematic representation of in and out-of-field validation performing measurements in a water phantom.

The IC (Semiflex Chamber Type 31010 detector from PTW™) used in this study had a sensitive volume of 0.125 $cm^3$, and was modelled assuming a length and radius dimensions of 6.5 mm and 2.75 mm, respectively, as per the manufacturer´s specifications. For the calculation of the PDDs and dose profiles, various positions of the IC were modelled, as described in Table 4. These positions were selected from the positions where the measurements were carried out. The total number of positions where measurements were performed varied according to the size of the irradiation fields.

**Table 4 -** In-field and out-of-field geometry.

| | | Depth dose profiles | | Lateral Profiles | |
|---|---|---|---|---|---|
| In-field geometry | Field size | 5 x 5 $cm^2$ | 10 x 10 $cm^2$ | 10 x 10 $cm^2$ | 30 x 30 $cm^2$ |
| | Number of positions | 37 | 42 | 27 | 29 |
| Out-of-field geometry | Field size | --- | --- | 5 x 5 $cm^2$ | 10 x 10 $cm^2$ |
| | Number of positions | --- | --- | 45 | 28 |

## 5.3. MC MODELLING AND SIMULATIONS

All simulations were performed individually for each position of the ionization chamber with the gantry positioned at 0°.

### 5.3.1. INNOVATIVE MODEL OF THE LINAC COMPONENTS COUPLED TO THE 120-LEAF MLC

The model of the Linac head was created using MCNP6™ (version 1.0, Los Alamos National Laboratory, Los Alamos, NM) [141] based on the geometry kindly provided by Bryan Bednarz [7] and the data provided by the manufacturer. The components included in the model were the accelerator tube, bending magnet, target, primary collimators, flattening filter, secondary collimators and secondary shielding [7]. In this

computational study, the modelling of the Millennium™ 120-leaf MLC coupled with the Varian Clinac 2100 CD LINAC head was for the first time undertaken in MCNP6. The materials used were tungsten, iron, lead, copper, tin and aluminium, as previously described. In accordance with the latest data releases of the manufacturer, some parameters of the initial model [7] were modified, such as materials and densities of FF and target. To couple the MLCs to the LINAC model it was necessary to run the MLCs using the coordinate transformations of the MCNP6.

Considering a setup with the patient positioned in supine position, the positive x-axis expands from the isocenter to the right side of the patient. The positive y-axis expands from the isocenter to the patient head and the positive z-axis expands from the target to the isocenter. The developed and implemented model of the Linac head with the MLC model is shown in Figure 38.

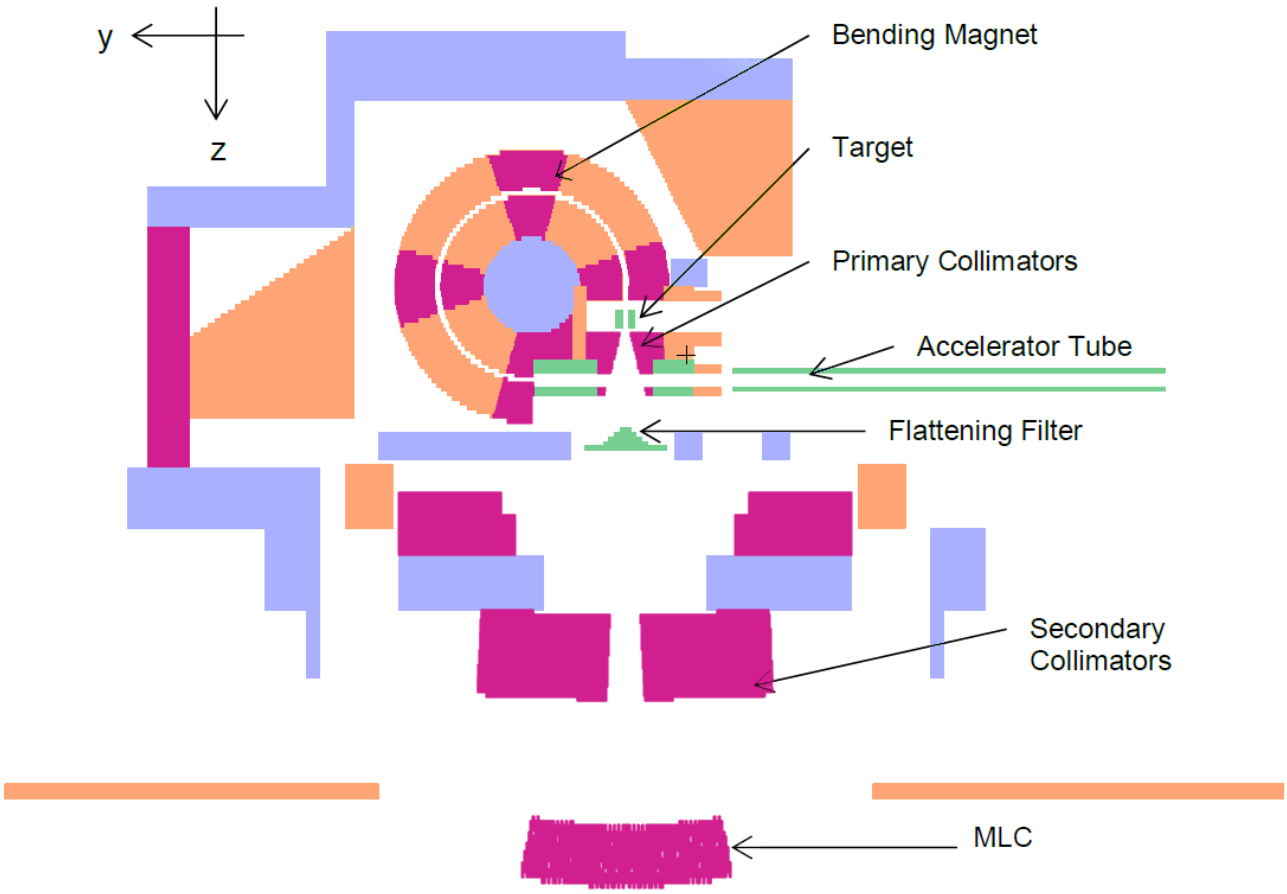


**Figure 38 -** MCNP6 model of Varian Clinac 2100 CD head with main componentes and secondary shielding.

To model the 6 MV energy photon beam a fine-tuning process was performed, in order to adjust the parameters previously described in other studies [7,176,182–185], such as the primary electron energy and the full width half maximum (FWHM) of the Gaussian beam intensity distribution. MC simulations were performed for different values of the primary electron energy and different values of FWHM. By comparing the measured and calculated deph dose profiles and beam profiles [179,186–189], the electron beam's energy and the FWHM were selected. Differences between the measured and calculated values of the dose profiles and depth profile were considered to be less than 2% [178].

#### 5.3.1.1. MCNP Modeling of the Water Phantom

In addition to the LINAC model, a model of a water phantom was created in MCNP6™ with dimensions of 30 x 30 x 30 $cm^3$ and a target-to-phantom distance of 100 cm.

Figures 39 and 40 show examples of the water phantom model for the PDD and dose profiles.

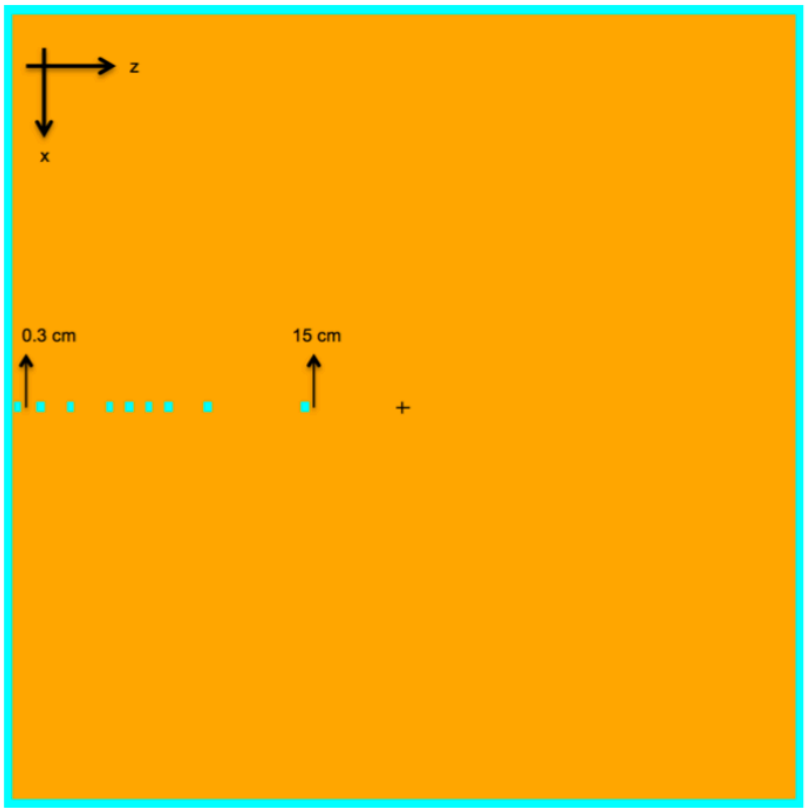


**Figure 39 -** MCNP6 water phantom model with some positions of the ionizing chamber for PDDs.

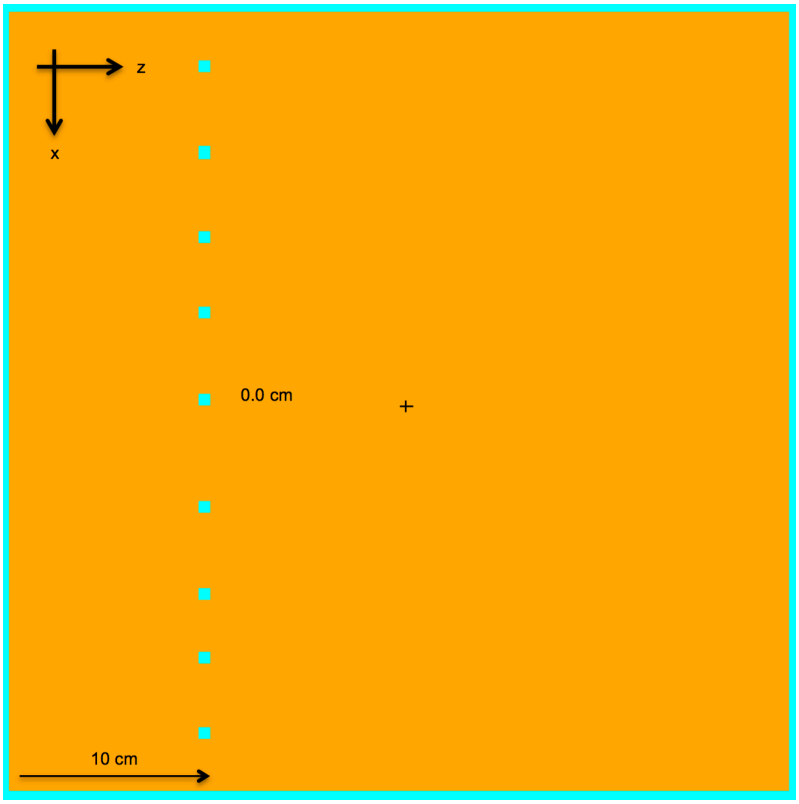


**Figure 40 -** MCNP6 water phantom model with some positions of the ionizing chamber for dose profiles.

In order to perform a preliminary evaluation of the LINAC head geometry and the water phantom, a mesh tally type 3 plot was implemented to visualize the energy deposited from the source to the water phantom. The mesh tally type 3 is a tally that scores energy deposited per unit volume and its units are expressed in MeV/cm$^3$/source particle [141].

Through f2 tally, the electron and photon average flux in the water phantom was assessed. The f2 tally scores the average flux across a surface and its units are expressed in particles/cm$^2$ [141].

#### 5.3.1.2. MCNP6 MC Simulations of the Transmission and DLS

For the MC simulations of the MLC transmission and the DLS, the measurement conditions previously defined were used. For each simulation 2 x 10$^9$ primary/source

particles were generated and simulated in photon and electron mode, in order to achieve a statistical uncertainty below 2%. In order to measure the charge deposition a +F8 tally was used [178].

#### 5.3.1.3. MCNP6 MC Simulations of the Full Model (LINAC coupled to MLC)

For each simulation, $2x10^9$ source particles were simulated. The simulations ran on a cluster with 17 Intel processors of 2.7 GHz CPU. Each simulation took about 23 days (elapsed time). The electron and photon cut off energies was assumed 0.1 MeV and 0.01 MeV, respectively. The "Russian roulette" variance reduction technique was implemented for all Monte Carlo calculations in order to improve the efficiency of the calculations [178]. The tally *F8 was selected and after the values were obtained, they were converted to relative values for comparison with the measured values [141]. For the purposes of this work, the tally *F8 values were considered acceptable when the statistical uncertainty was lower than 10%.

## 5.4. RESULTS

### 5.4.1. PRELIMINARY RESULTS OF THE LINAC HEAD GEOMETRY ASSESSMENT

Figure 41 depicts a mesh tally plot, showing the geometry of the Linac head and its components and of the water phantom. The defined mesh creates a (virtual) spatial grid that is used to delimit small volumes at the LINAC head, in air and at different depths in the phantom, inside which the energy deposition is calculated (results displayed in MeV/$cm^3$/source particle). In addition, Figure 41 allows the evaluation of the direction of the beam, mainly in z-axis, that is, if the beam has been well defined and aligned in the correct position along the z-axis. As can be seen in Figure 41, there is less energy deposited in the air than in the superficial region of the phantom.

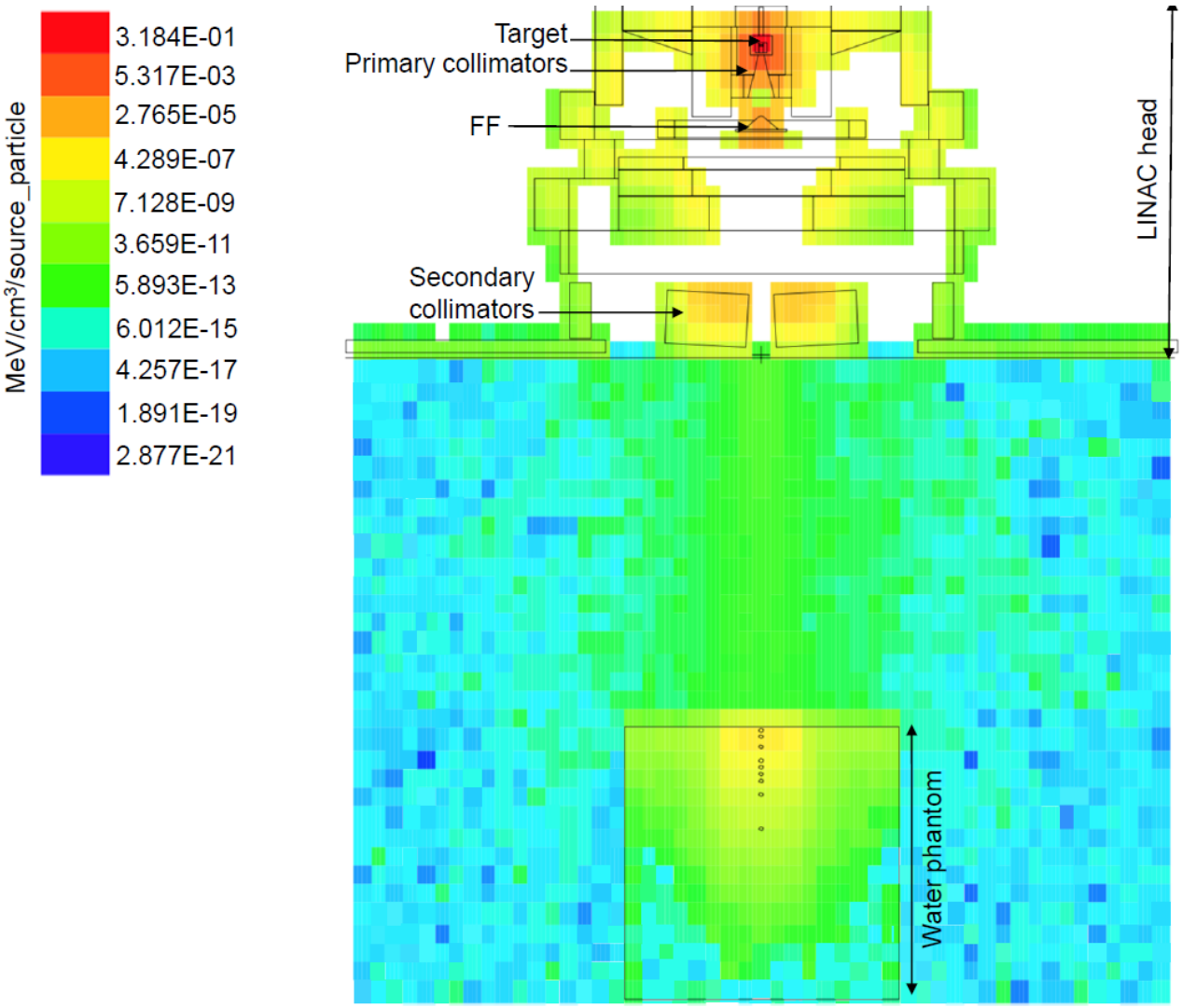


**Figure 41 -** Energy deposition calculated using a mesh tally type 3 plot (units: MeV/cm3/source_particle).

In order to evaluate the correct modelling of the water phantom as well as the photon beam, tally F2 was used to calculate the electron and photon average flux along the z-axis. Figure 42 shows a decrease in electron and photon flux along the depth in the water phantom, as would be expected.

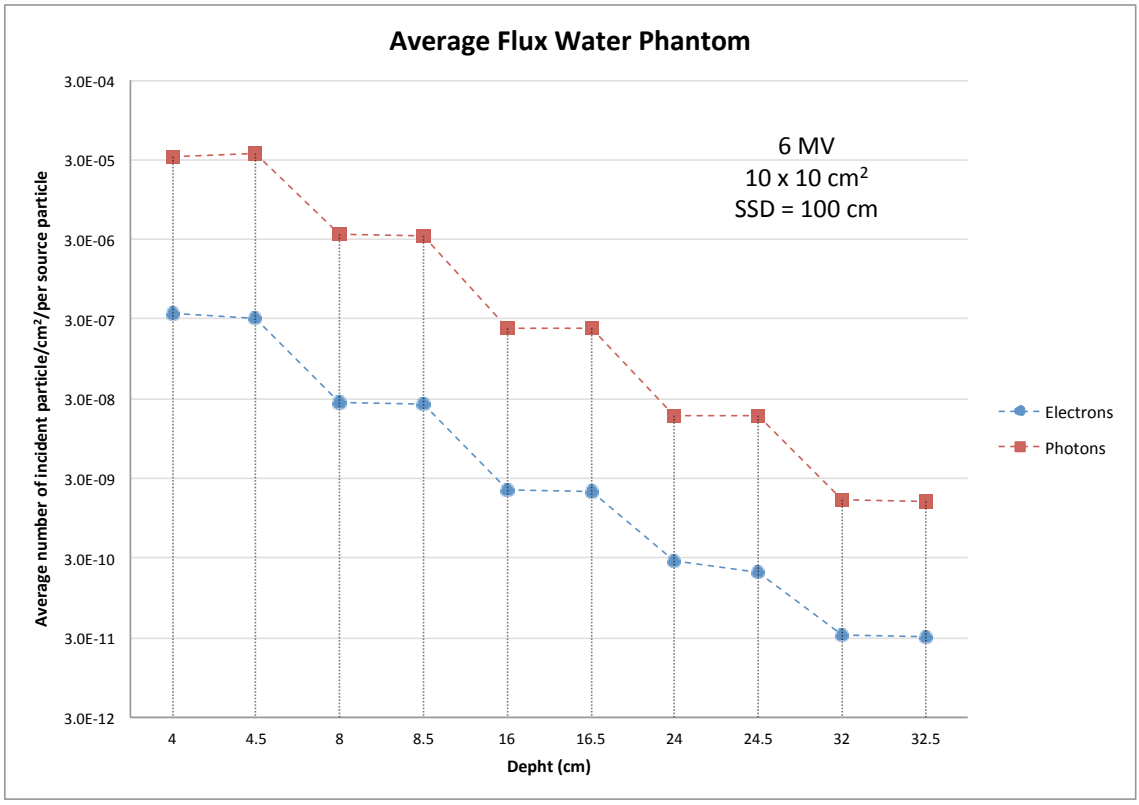


**Figure 42 -** Average photon and electron flux as a function of depth in the water phantom, normalized to the number of generated/source particles.

### 5.4.2. MILLENNIUM™ 120-LEAF MLC VALIDATION

The validation of the Millenium™ 120-leaf MLC model (namely the implemented geometry of the leaves) was performed comparing the measured and calculated MLC transmissions, as well as the measured and calculated DLS for different gap sizes. Regarding the measured MLC transmission at 6 MV a value of 1.44% was obtained with an overall uncertainty below 5%, mainly due to the uncertainties associated to the measurements using the IC and to its calibration (mainly uncertainties in the operating gas pressure and temperature). The calculated MLC transmission was 1.49% with an uncertainty below 2%. Figure 43 displays the measured values and the MCNP simulated values of the DLS for 0.5, 1-, 5-, 10- and 20-mm gap sizes. Figure 43 also depicts the linear regression curves for measured and MCNP simulated values, as well as DLS values, which were calculated from the regression curve parameters. In this

Figure the difference between the measured and calculated values is lower than 0.20 mm, which is an accepted tolerance between DLS values.

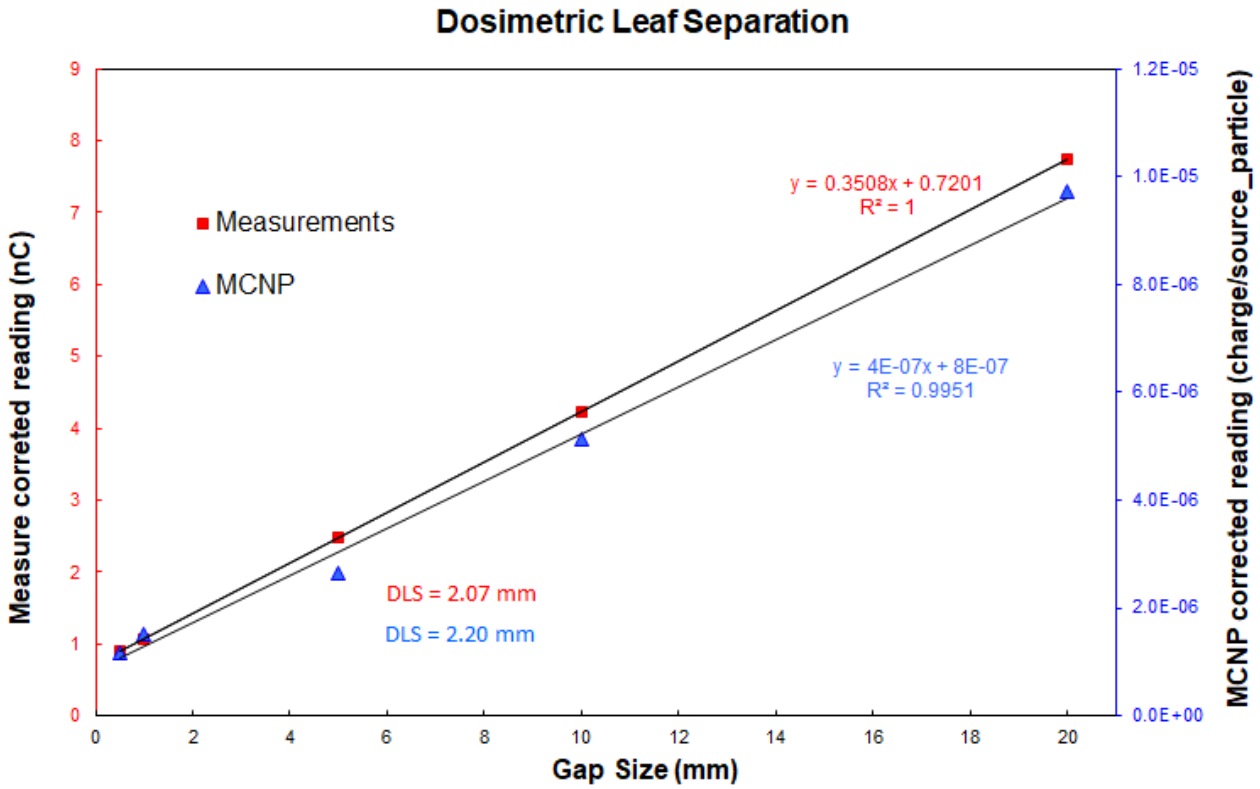


**Figure 43 -** Measurements and MCNP simulations of the DLS for 0.5, 1-, 5-, 10- and 20-mm gap sizes.

### 5.4.3. VARIAN CLINAC 2100 CD HEAD OPERATED AT 6 MV VALIDATION

Considering electron beam modeling, the best fit between the MC calculations and the measurements was obtained for the incident electron energy of 6.2 MeV and a Gaussian intensity profile with a full width at half maximum (FWHM) of 1.2 mm.

Initially, the plots of the measurements of the PDDs and dose profiles for different field dimensions were visually obtained by PTW™ Mephysto software. As an example in Figure 44, a plot of the beam profile measurement on the x-axis with the 6MV energy beam and for 5 x 5 $cm^2$ field size can be seen.

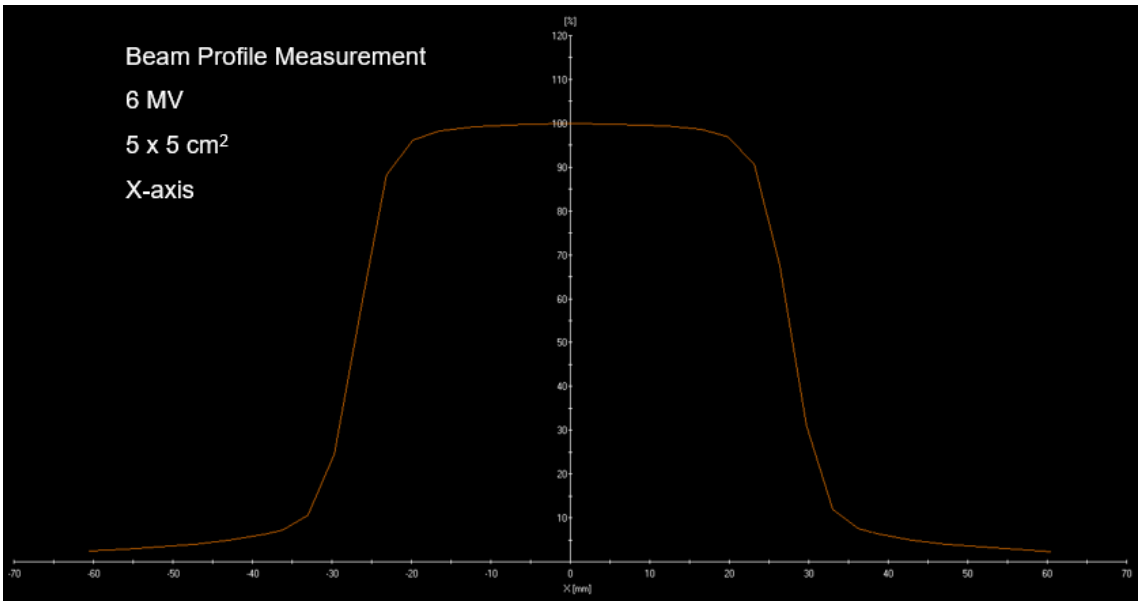


**Figure 44 -** Beam profile measurement obtained by PTW™ Mephysto software.

To validate the LINAC head model, a comparison was performed between the measured and calculated PDD and beam profiles, considering different field sizes, both in-field and out-of-field.

#### 5.4.3.1. Comparison of PDD Curves

For in-field, a good agreement was observed, between the measured and calculated values of PDD curves for different field sizes, as can be seen in Figures 45 and 46.

The average statistical uncertainty of the values calculated by MCNP is 6.50% for a 5 x 5 $cm^2$ field and 5.48% for a 10 x 10 $cm^2$ field.

The average relative difference between measured and simulated data is 2.69% for a 5 x 5 $cm^2$ field and 2.53% for a 10 x 10 $cm^2$ field.

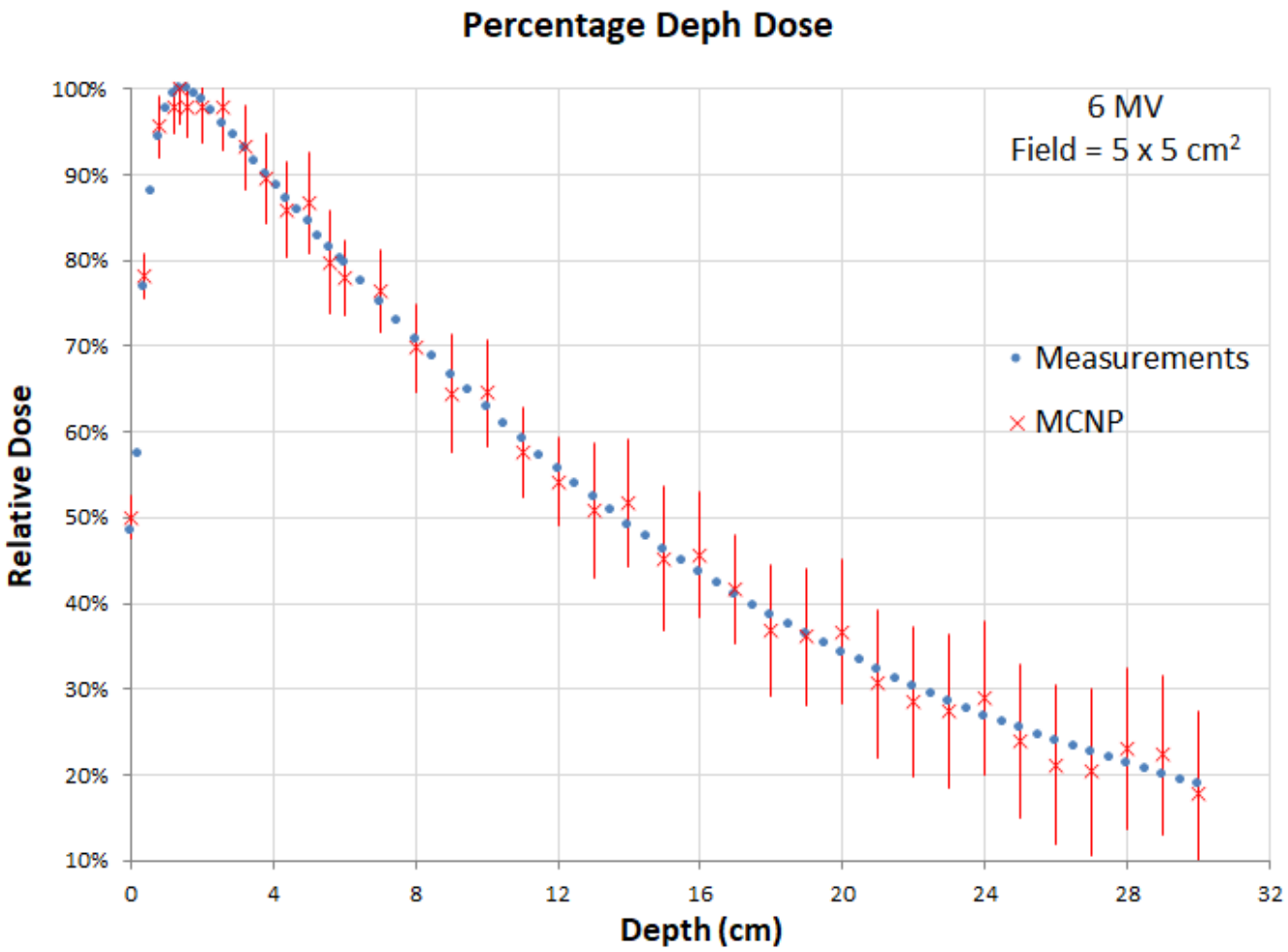


**Figure 45 -** In-field comparison of measured and calculated PDDs for a 5 x 5 $cm^2$ field. The average relative difference between measured and calculated values is 2.69% and the maximum relative difference is 11.58%. The average statistical uncertainty of the values calculated by MCNP is 6.50%.

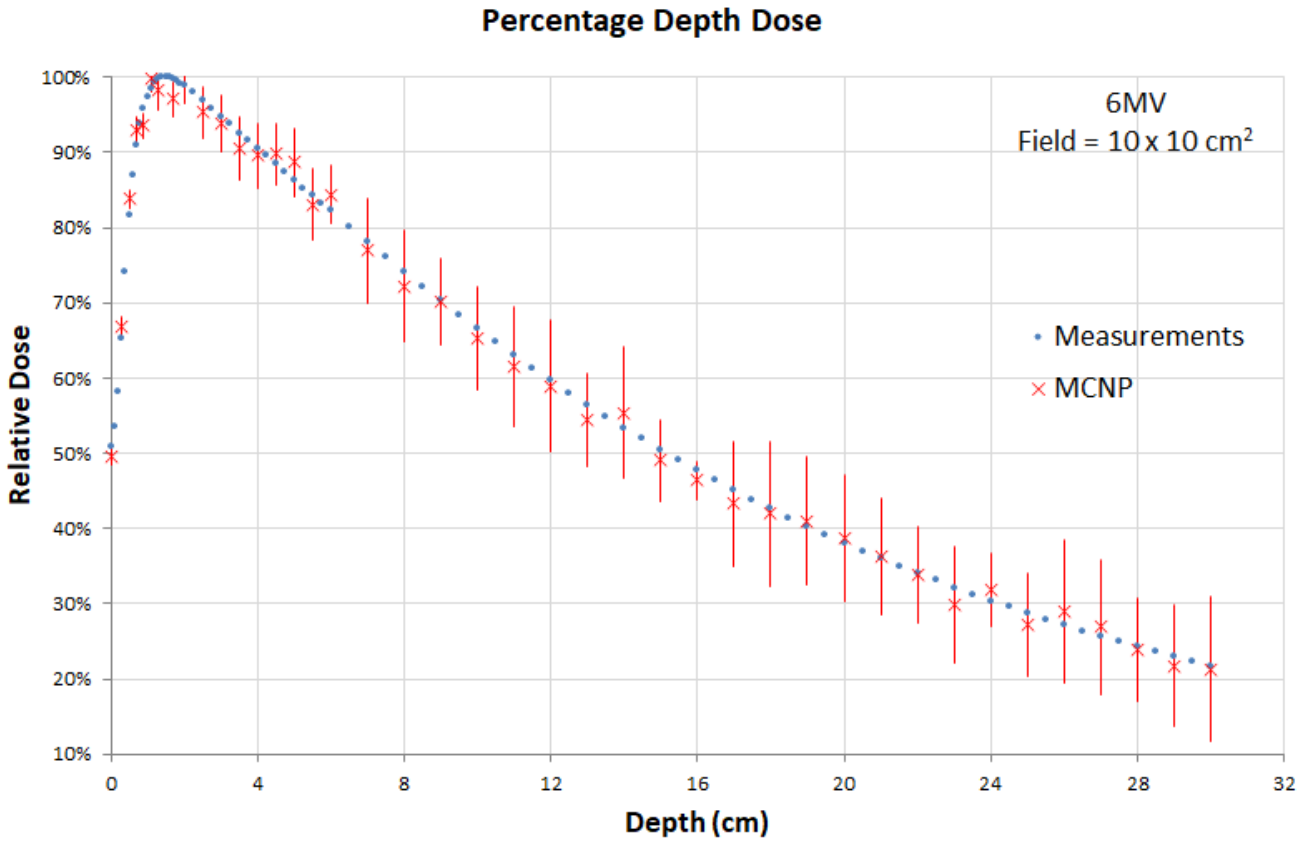


**Figure 46 -** In-field comparison of measured and calculated PDDs for a 10 x 10 $cm^2$ field. The average relative difference between measured and calculated values is 2.53% and the maximum relative difference of 7.17%. The average statistical uncertainty of the values calculated by MCNP is 5.48%.

### 5.4.3.2. Comparison of Dose Profile Curves

Figures 47 and 48 shows the in-field comparison between the measurements and the MC simulated values of the dose profile for a 6MV beam at a depth of 10 cm for 10 x 10 $cm^2$ and 30 x 30 $cm^2$ fields. The average statistical uncertainty of the values calculated by MCNP is 5.50% for a 10 x 10 $cm^2$ field and 5.51% for a 30 x 30 $cm^2$ field.

The average relative difference between the measured and simulated data is 2.79% for a 10 x 10 $cm^2$ field and 2.54% for a 30 x 30 $cm^2$ field, showing a good agreement between the measured and calculated values.

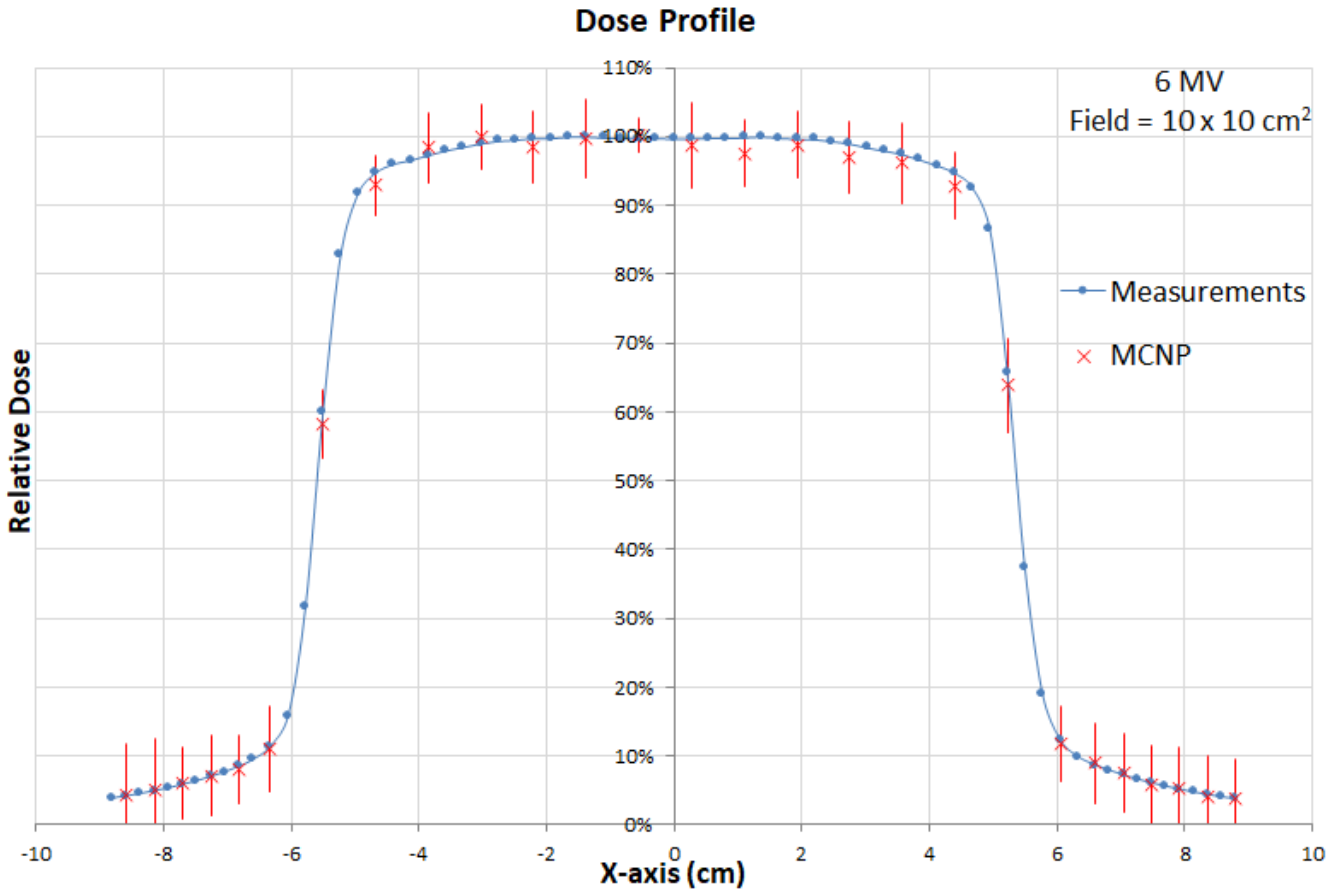


**Figure 47 -** In-field comparison of measured and calculated dose profiles for a 10 x 10 $cm^2$ field. The average relative difference between measured and calculated values is 2.79% and the maximum relative difference is 5.84%. The average statistical uncertainty of the values calculated by MCNP is 5.50%.

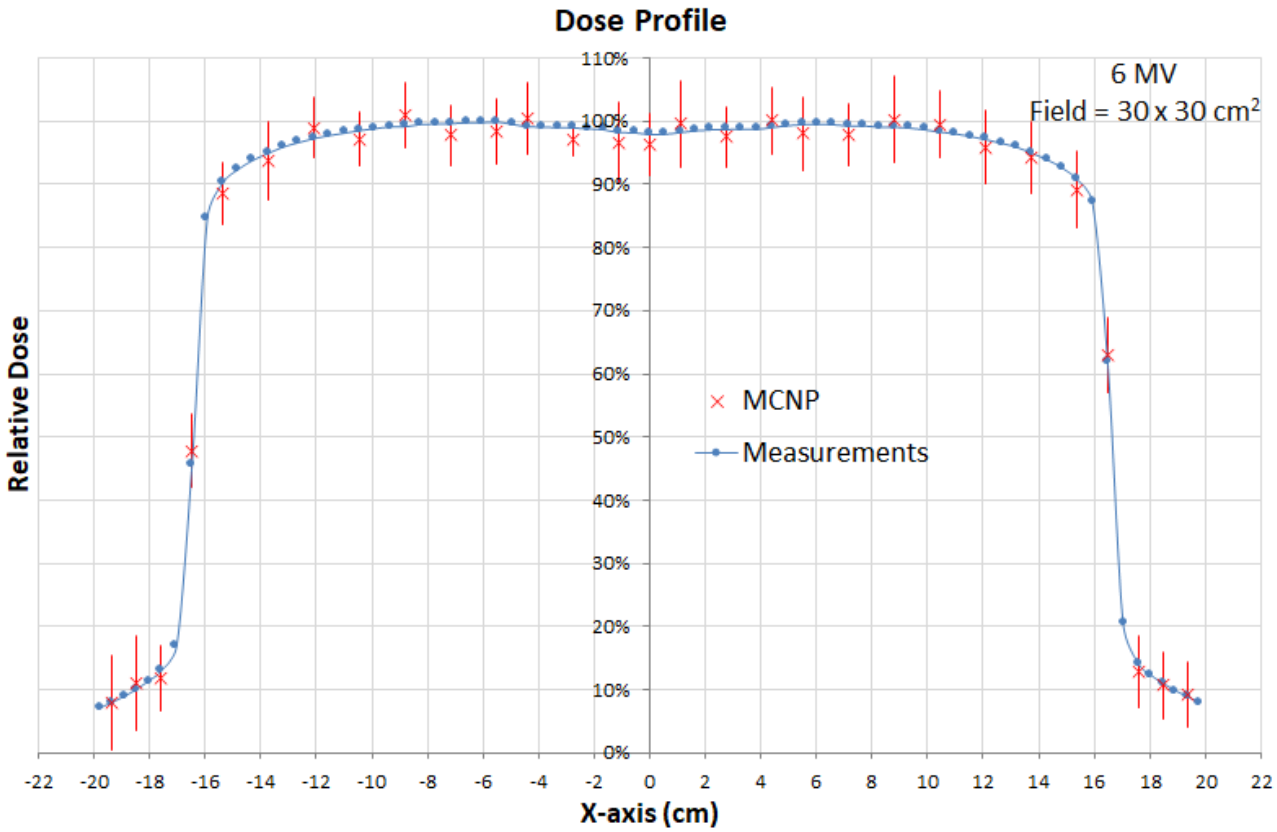


**Figure 48 -** In-field comparison of measured and calculated dose profiles for a 30 x 30 $cm^2$ field. The average relative difference between measured and calculated values is 2.54% and the maximum relative difference is 9.53%. The average statistical uncertainty of the values calculated by MCNP is 5.51%.

The out-of-field dose profiles for 5 x 5 $cm^2$ and 10 x 10 $cm^2$ field sizes are shown in Figures 49 and 50, respectively.

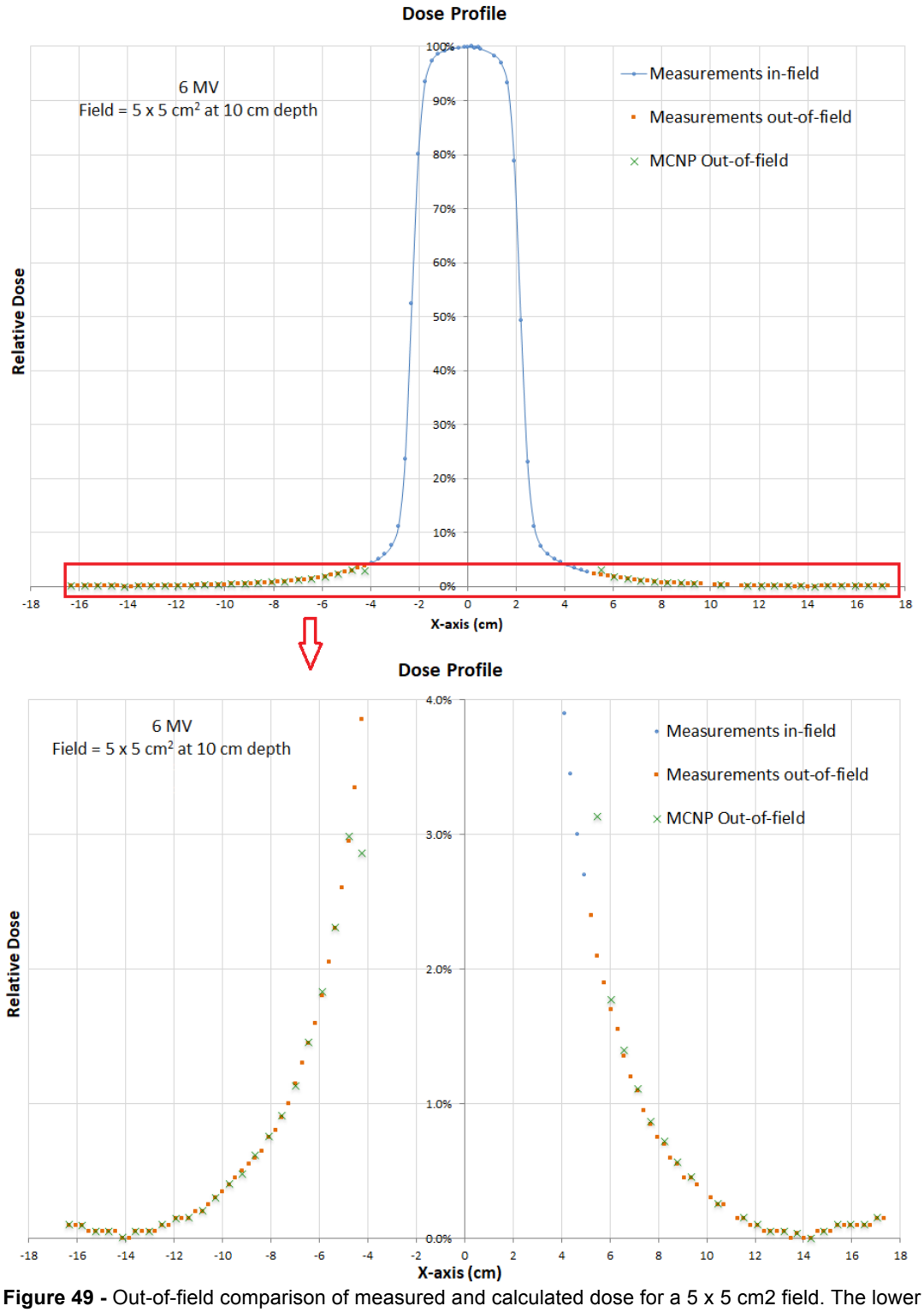


**Figure 49 -** Out-of-field comparison of measured and calculated dose for a 5 x 5 cm2 field. The lower graph is a zoom of the rectangular area of the upper graph. The average relative difference between measured and calculated values is 2.45% and the maximum relative difference is 5.93%. The average statistical uncertainty of the values calculated by MCNP is 5.30.

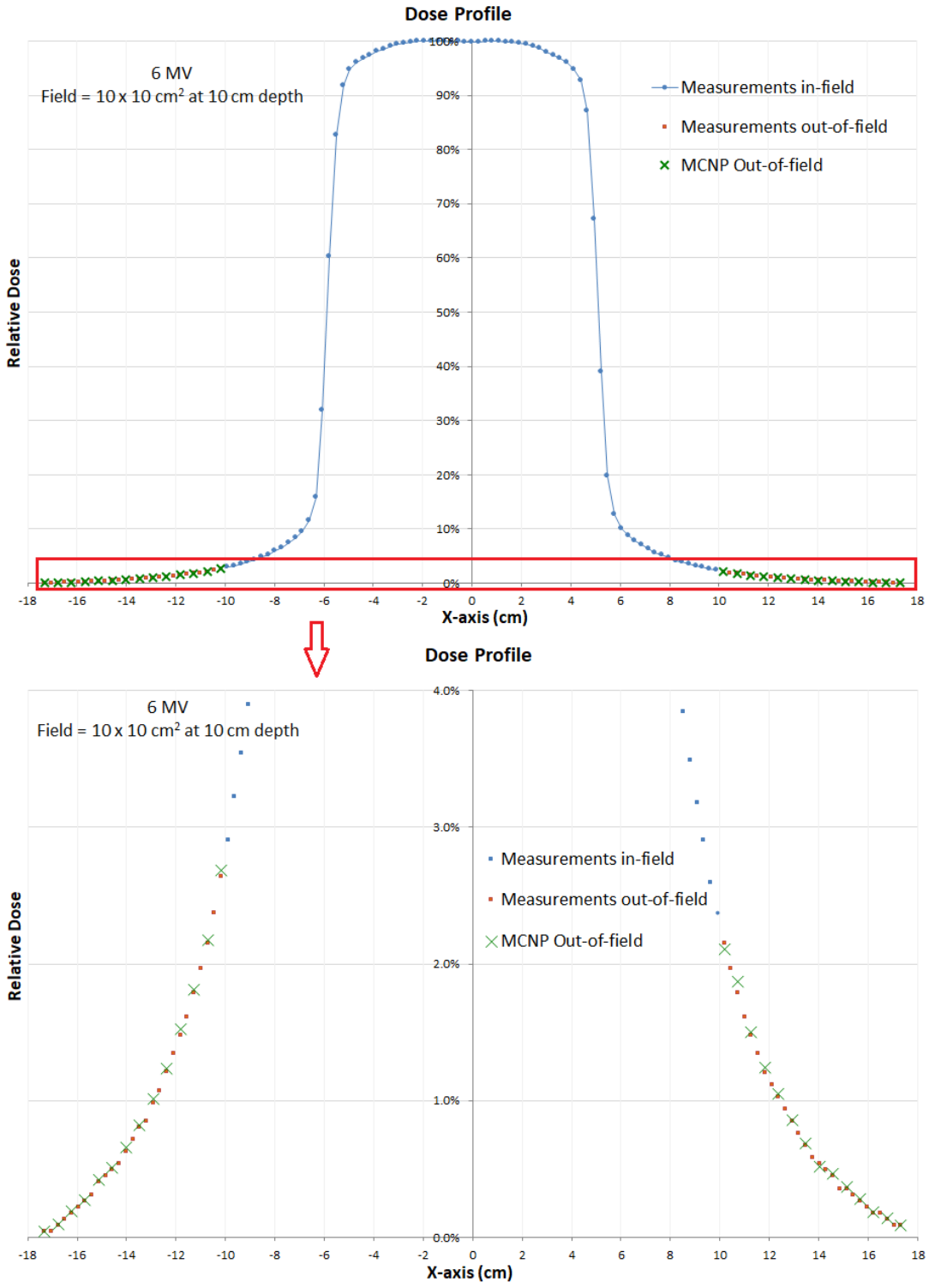


**Figure 50 -** Out-of-field comparison of measured and calculated dose for a 10 x 10 $cm^2$ field. The lower graph is a zoom of the rectangular area of the upper graph. The average relative difference between measured and calculated values is 2.94% and the maximum relative difference is 5.37%. The average statistical uncertainty of the values calculated by MCNP is 5.21%.

In Figure 49 the out-of-field doses are shown for the intervals from -5 cm (field edge) to -17.5 cm and from 5 cm (field edge) to 17.5 cm, in steps of 0.275 cm. In Figure 50 doses outside the field are shown for the intervals from -10 cm (field edge) to -17.5 cm and from 10 cm (field edge) to 17.5 cm, in steps of 0.275 cm.

The average statistical uncertainty of the values calculated by MCNP is 5.30% for a 5 x 5 $cm^2$ field and 5.21% for a 10 x 10 $cm^2$ field.

The average relative difference between the calculated and measured values is 2.45 % for a 5x5 $cm^2$ field and 2.94 % for a 10 x 10 $cm^2$ field.

## 5.5. DISCUSSION

This work reports a good agreement between measurements with ionization chamber and MCNP calculations for MC LINAC model validation, which made it possible to find the best fit for primary electron parameters.

Although the simulation process is time-consuming, once the MC simulation results are validated by the measurements, they allow to assess the validity of the implemented LINAC model and to be confident that accurate dose predictions can be obtained by the simulations, particularly in situations where there is irregular geometry and heterogeneity of materials such as the body of patients.

### 5.5.1. ELECTRON BEAM MODELING

Information about the nominal parameters of the electron beam (the radiation source for modelling and simulation purposes) namely the energy and the radius of the electron beam incident on the target is scarce and manufacturers of the equipment have some reluctance to make it available. In most cases the nominal energy value must be adjusted, by successive iterations until the discrepancies between dosimetric measurements and MC calculations are minimized [190–192]. However, this process is time-consuming, lengthy and requires many resources [5,193].

Regarding the electron beam spatial distribution (namely the radius), most manufacturers do not provide detailed information. However, this parameter has a high influence in MC calculations and its determination is fundamental for the implementation of an accurate LINAC model [190]. Zarza-Moreno *et al.* [187] assessed

the same LINAC and energy beam and they obtained an nominal energy value very close to the one determined in this thesis. However, the incident electron beam radius on the target was 1.5 mm and in our study 1.2 mm. This difference is due to our fine-tuning process in order to achieve the best match between our measurements and MC calculations. Jaffray *et al*. also achieved a FWHM of 1.2 mm for a 6 MV beam in a Varian Clinac 2100 C [188].

### 5.5.2. MODELING OF THE MILLENIUM™ 120-LEAF MLC

Regarding the MLC validation, the differences between the measured and calculated DLS values in our study allowed to determine that the nominal parameters used in our computational model deviates less than 0.20 mm from the real parameters, which is an accepted tolerance [180,181]. For the transmission differences between measured and calculated values less than 0.05% were obtained. As in the study by Borges *et al.* the transmission values are 1.44%, considering the density of MLC of 17.5 g $cm^{-3}$ [179].

### 5.5.3. MODELING OF THE VARIAN CLINAC 2100 CD

Most studies validating LINAC models with MC methods, only consider LINAC components from the target. However, MC simulations of LINACs are strictly dependent on the accurate geometrical description of the LINAC head [194].

This study includes an accurate and detailed model of Varian Clinac 2100 CD, and the obtained results exhibit a level of uncertainty that enable to obtain accurate dosimetric result, as will be shown in a following Chapter. In a recent study, with a different LINAC, the authors also validated a in-field MC LINAC model through measurements with water phantom and ionization chambers with differences between the calculated and measured values were less than 2% [192]. Other studies using MC methods in the validation of LINAC models also display a percentage difference between in-field measured and calculated values below 2-3% [7,195–197]. For in-field, this work also shows relative average differences less than 3%.

Considering the in-field measurements, the statistical uncertainty of the MCNP results is tendentionally higher at greater distances from the source (Figure 45 and 46). This is probably because there is a lower number of particles being transported and suffering collisions farther from the source (as can be seen in Figure 42), increasing the statistical uncertainty.

In this study, was also assessed the out-of-field dose up to 12 cm from the field edge and determined that the average relative difference between the measurements and the MC simulations is less than 3%. The obtained results therefore follow and comply to the recommendations of the AAPM publication TG 158, which states that a good agreement can be reached on the measured and calculated values up to 15 cm [198] or 14 cm from the field edge [175]. According to Kry *et al.* [138], the out-of-field calculated doses are generally overestimated when compared with measurements. Other published works reported higher differences (> 20%) between calculated and measured doses [7,138,175]. However, these studies assess the out-of-field doses at very large distances from the field edge. Another study that evaluated the out-of-field doses up to 60 cm from the isocenter, obtained an average relative difference of 14.2% between measurements and calculations in MCNP for 10 x 10 $cm^2$ fields. Similarly, the results presented in this study show an average relative difference between the calculated and measured values of 2.94% for 10 x 10 $cm^2$ fields.

According to Bryan Bednarz et al. [7], for out-of-field doses the statistical uncertainty of the MC calculations decreases with increasing field size because there is a high photon fluency in the out-of-field region from larger field sizes. This study also shows a lower statistical uncertainty in 10 x 10 $cm^2$ fields (5.21%) compared to the statistical uncertainty in 5 x 5 $cm^2$ fields (5.30%).

The LINAC model developed in this study can be adjusted to a newer LINAC, such as a Varian TrueBeam, since it has great similarities with the Varian Clinac 2100 [194].

## 5.6. CONCLUSIONS

For the first time, a detailed model of the LINAC 2100 CD and the Millennium™ 120-leaf MLC was implemented and validated in MCNP6, using measurements in clinical settings. In this chapter, a Varian Clinac 2100 CD was modelled based on manufacturer information and on geometry details provided in [7]. By comparing measured and MCNP6 calculated doses, the validation of the Varian Clinac 2100 CD head model was performed for a 6 MV beam. A good agreement between measured and calculated values for PDD curves and beam profiles was obtained, both for in-field and out-of-field doses. This study provides a Linac and ancillary equipment model, never before implemented in MCNP6, that could be used in clinical research, namely for dose evaluation outside the treatment fields, which is scarce in the literature. This implemented and validated model is particularly relevant, especially in paediatric

patients, for studying new radiotherapy treatment techniques, since it can be used to obtain dosimetric data feeding state-of-the-art cancer incidence and risk models, to estimate the development of secondary cancers.

# CHAPTER 6 – DEVELOPMENT AND IMPLEMENTATION OF A PAEDIATRIC COMPUTATIONAL PHANTOM

## 6.1. MOTIVATION

For a few decades, MC calculations became of paramount importance for dose calculation in radiation therapy, to accurately model and simulate the transport of photons and electrons in materials [130,176,199,200], particularly in heterogeneous tissues and structures. As detailed in a previous Chapter the development of computational phantoms emerged since the end of the 1960s and since the 1990s voxel phantoms developed from computed tomography images [201], allowed the implementation of very accurate and realistic representations of the human body anatomy and constituent organs and tissues. These allowed unprecedentedly accurate MC simulations to be undertaken eaten in support of dosimetry calculations. However, such methods are not yet being used in clinical situations due to the vey high computing times required for dose calculation [97]. On the other hand, for research, MC methods and anatomically realistic computational anthropomorphic phantoms can be used to assess organ doses [202–207].

In this Chapter, the steps leading to the development and implementation of a paediatric anthropomorphic computational phantom used for the specific objectives of this study are detailed.

## 6.2. MATERIALS AND METHODS

### 6.2.1. ACQUISITION OF CT IMAGES OF A PAEDIATRIC PHANTOM

A 5 years old ATOM® anthropomorphic phantom (Figure 51) manufactured by CIRS (ATOM 705-D; CIRS, Norfolk, VA) was placed in supine position inside the CT gantry, as can be seen in Figure 52. The brain protocol was defined as the imaging protocol and the phantom was anatomically aligned with the aid of three lasers. The longitudinal laser coincided with the midline and the axial and coronal lasers crossed in the tragus.

CT images of the phantom were acquired using a Siemens scanner (SOMATOM Definition AS; Siemens Healthcare), with 2.0 mm slice thickness. The acquired CT

images of the phantom were used to construct its computational voxel phantom for MC modelling and simulation purposes. The tube current and exposure time (mAs) product and peak voltage (kVp) used scanning protocol for paediatric patients at the Radiotherapy Service of IPOLFG is 180 mAs and 100 $kV_p$, respectively.

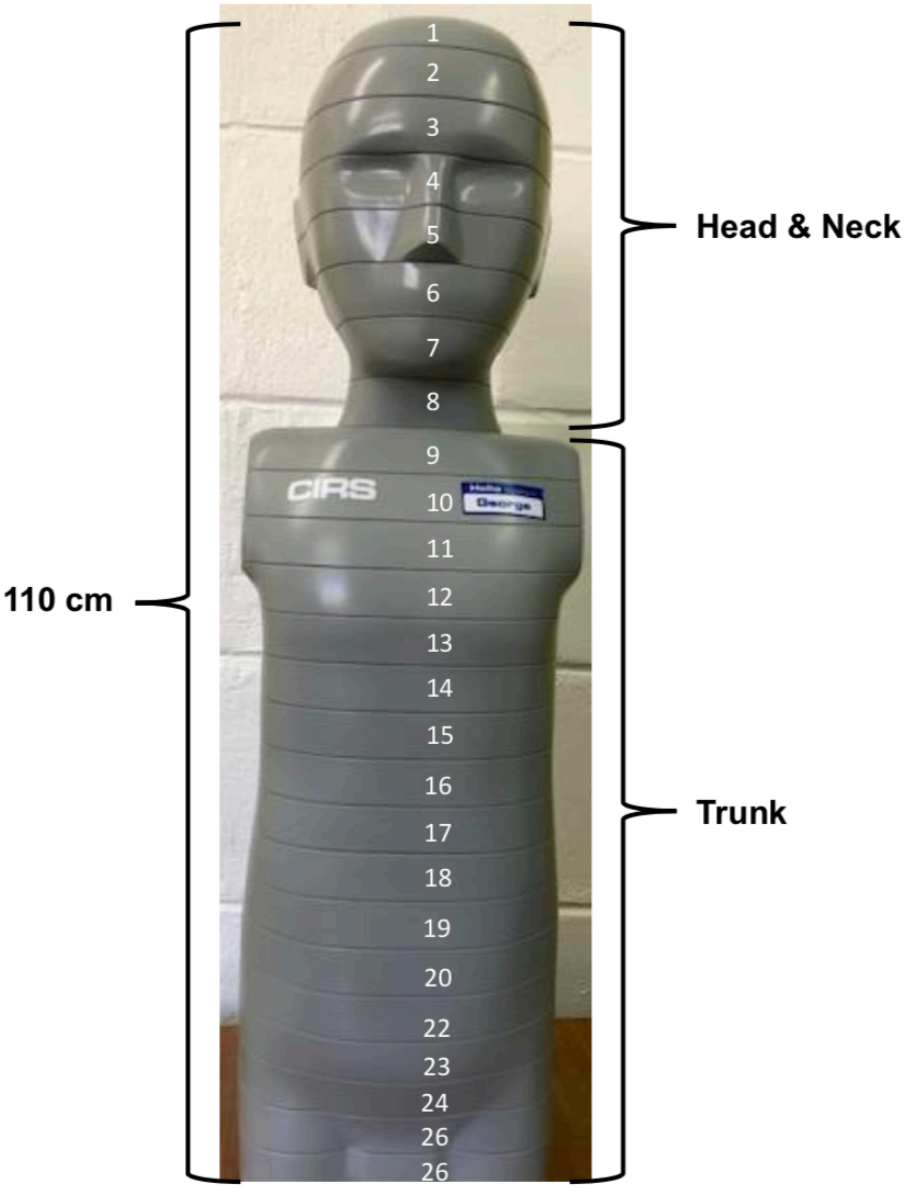


**Figure 51 -** 5 years old ATOM 705-D anthropomorfic phantom from CIRS.

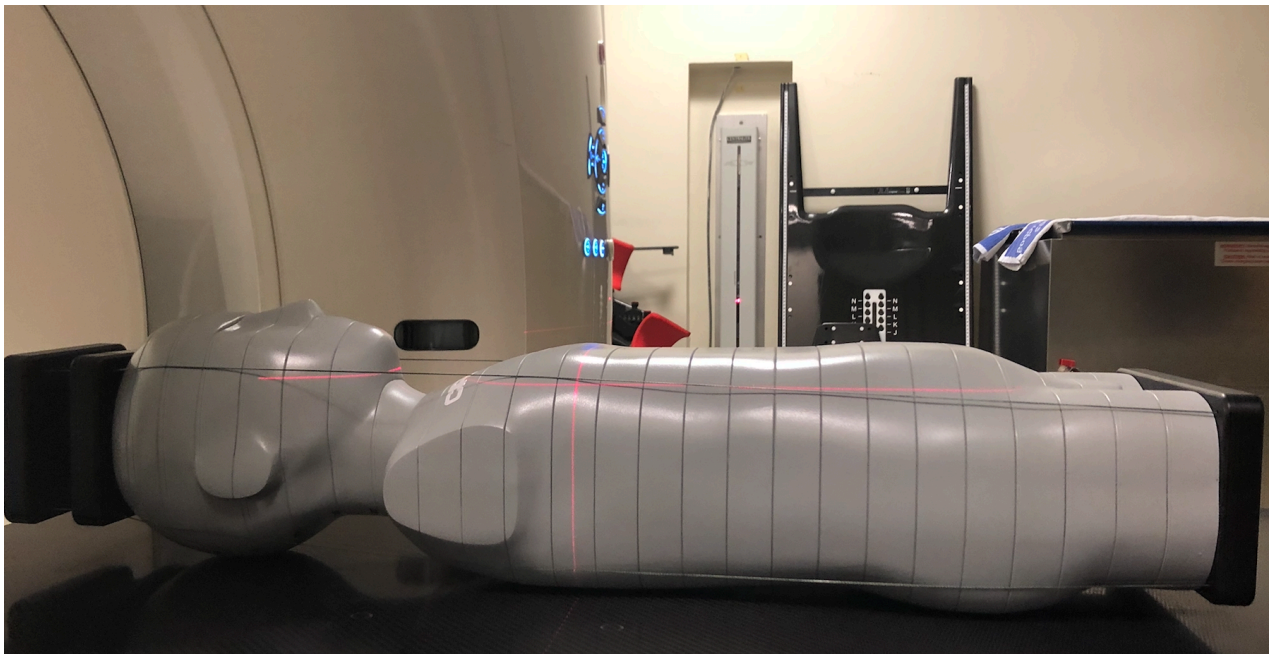

**Figure 52 -** Computed tomography scanner with paediatric phantom in supine position inside the gantry.

Figure 50 represents in detail the anthropomorphic phantom used in this study. The phantom is divided into 26 numbered sections, each one 25,4 mm thick and has several holes with 5 mm diameter into which TLDs can be placed for organ dosimetry [208,209]. The head and neck region is between section 1 and 8 and the trunk region between section 9 and 26. This phantom has some specific characteristics, namely a height of 110 cm, thorax dimensions of 14 x 17 cm and 1.52 g/cc of bone tissue density. This phantom consists of four different tissue-equivalent materials: lung, bone, brain and soft tissue [208,209].

The alignment of the phantom with the three lasers allows defining three points, one at nasion and one in each tragus. Before acquiring the images, three radiopaque markers are placed at the crossing of the lasers to define the reference slice that will later be mentioned in the dosimetric planning. Initially, the scout view was performed to evaluate the correct alignment and positioning of the phantom. Then the images were acquired in the different planes.

### 6.2.2. DEVELOPMENT AND IMPLEMENTATION OF THE PAEDIATRIC VOXEL PHANTOM

In order to create the voxel phantom the ImageJ program [210–212] was used. From the original 397 CT images of the phantom, 180 images were selected, covering the anatomic regions from the skull to the end of the lungs. These 180 images were divided into 6 stacks, each with 30 images. Using the image processing and analysis tools of ImageJ software, the images were converted to 8-bit grayscale with pixel values between 0-255 [213]. All images were imported into the ImageJ program. Initially the brightness and contrast were automatically adjusted on all images. Then, unwanted objects in the images, such as the phantom supports, as well as the CT table, were eliminated.

The whole body has been defined, and for this it is necessary to create the binary image and define everything within the body in black, as can be seen in Figure 53.

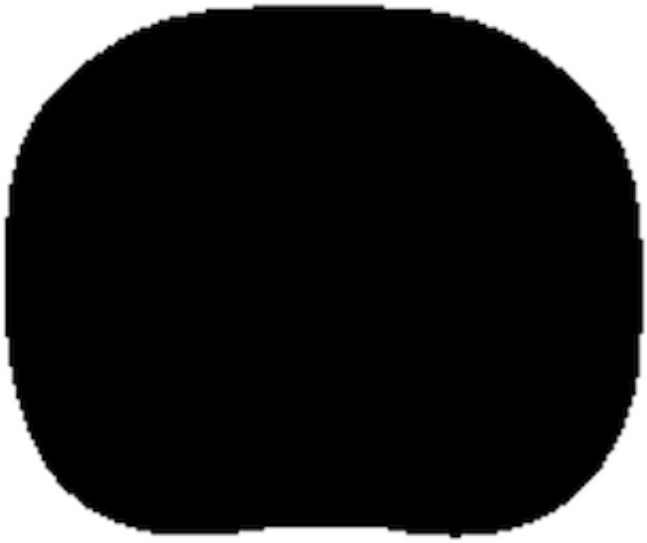

**Figure 53 -** Whole body definition in a thoracic axial slice.

For the definition of the skin, the binary image was created and only the skin became visible in each image, as shown in Figure 54.

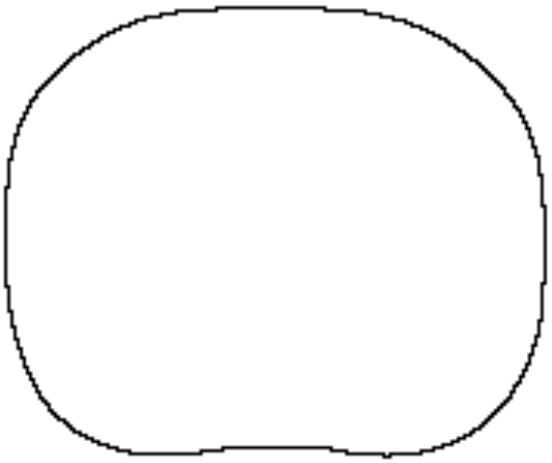

**Figure 54 -** Skin definition in a thoracic axial slice.

The skin was then removed from all the images of the phantom through the subtraction operation (Figure 55).

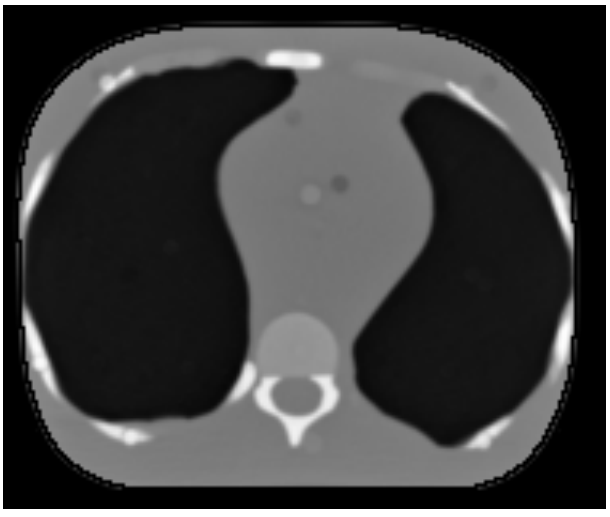

**Figure 55 -** Removal of skin in a thoracic axial slice.

In order to define the lungs, they were manually segmented, slice by slice and then the binary image of them was created, as can be seen in Figure 56.

**Figure 56 -** Lungs definition in a thoracic axial slice.

Subsequently the lungs were removed from the phantom images, as shown in Figure 57.

**Figure 57 -** Removal of lungs in a thoracic axial slice.

Later the bones were defined by setting threshold values for bone tissue and creating the binary image, as seen in Figure 58.

**Figure 58 -** Bone's definition in a head axial slice.

Similarly, to the other structures, the bones have been removed from the phantom images, as can be seen in Figure 59.

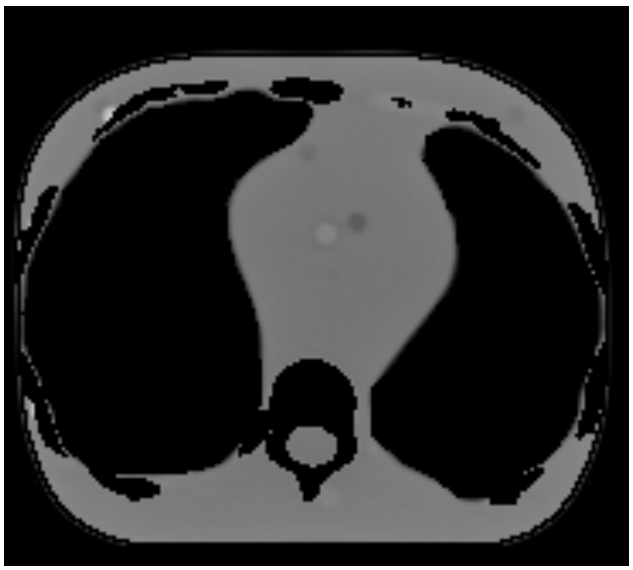

**Figure 59 -** Removal of bones in a thoracic axial slice.

The heart, spine, c-spine, brain, right and left eyes, thyroid and PTV were all manually segmented, slice by slice and for each one the binary image was created. The PTV is located on the right side of the brain and on the frontal lobe. Like the other structures, each of these structures was also removed from the phantom images.

In order to segment the soft tissue, it was defined by threshold values for soft tissue and then the binary image of it was created. The soft tissue was then removed from all images of the phantom.

Therefore, after the removal of all structures we obtained an image like the one shown in Figure 60.

**Figure 60 -** Thoracic axial slice after removing all structures.

For each volume of interest an identification number has been assigned. First, it was necessary to open each stack of images of each volume of interest. Then, using the ImageJ's image processing tool, each volume of interest was divided by 255. In an 8-bit image each pixel is represented by one byte. This means that each pixel has 256 possible numerical values, from 0-255 [212].

Thereafter each volume of interest was multiplied by *n*, where *n* is:

i. $n_{Whole_body}=100$
ii. $n_{Skin}=110$
iii. $n_{Brain}=115$
iv. $n_{Lungs}=120$

v. $n_{PTV}$=125
vi. $n_{Bones}$=130
vii. $n_{Right_eye}$=135
viii. $n_{Heart}$=140
ix. $n_{Left_eye}$=145
x. $n_{Spinal}$=150
xi. $n_{C\text{-}spine}$=155
xii. $n_{Thyroid}$=160
xiii. $n_{Soft_tissue}$=170

Subsequently it was necessary to place all segmented volumes of interest together in the whole body, as can be seen in Figure 61. To this end, all volumes of interest were combined, adding to the skin the rest of the volumes of interest, one by one. From the image resulting from the previous step the "*Max*" mathematical operation present in the ImageJ tools is performed, together with the whole-body image previously defined.

**Figure 61 -** Thoracic axial slice of the voxel phantom.

In short, the volumes of interest such as skin, whole body, bones, heart, brain, PTV, eyes, soft tissue, lungs, thyroid, spine and c-spine were manually segmented in all axial slices. From the original CT images, all volumes of interest were extracted. These volumes were saved as binary images´ stacks. The corresponding identification numbers were assigned to each volume and then, all images were combined in a

single stack shown in Figure 62. The voxelized version of the paediatric phantom yields an anthropomorphic computational phantom consisting of 47.185.920 voxels, each with

dimensions x=0.09766 cm, y=0.09766 cm and z=0.3 cm.

**Figure 62 -** Voxelized phantom in ImageJ 3D volume viewer. Left: Front view Right: Lateral view.

The input file for MCNP was created using the voxel phantom tool for ImageJ software developed by J. M. Gómez-Ros from CIEMAT, Spain [214]. “Voxel Phantom Tools.txt” is an ImageJ toolset to create the MCNP input file related to a voxel phantom stored as an 8-bit segmented images´ stack. This toolset has two macros: “Change Organs ID.txt” and “Create VX Phantom.txt”. The first macro allows to change the organ identification numbers in a given voxel phantom. The second macro creates the MCNP

input file for a given voxel phantom [214]. The two macros can be edited for different purposes, for example, in this study, the materials added were defined based on the body composition and density used in the 4-year phantom published by Choonsik Lee *et al.* [160].

After implementing the phantom in MCNP6, the phantom was visualized in the XQuartz© plot window. The viewing of the phantom allowed an evaluation of the position of the phantom in different planes. It was necessary to rotate the phantom using the coordinate transformations of MCNP6.

## 6.3. RESULTS

### 6.3.1. PAEDIATRIC PHANTOM CT IMAGES

CT images were obtained in different planes, namely axial, coronal and sagittal. Figure 63 shows the reference slice in an axial view with the radiopaque markers.

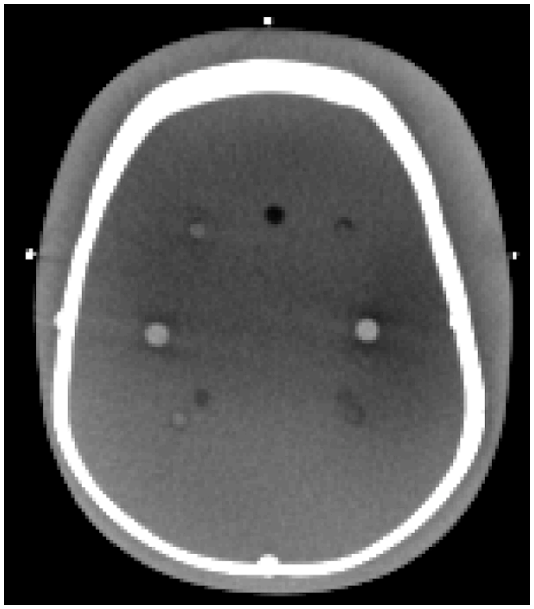

**Figure 63 -** Reference slice with radiopaque markers.

As previously mentioned, 397 images were acquired, however only 180 images were used. These 180 images range from the skull to the end of the lungs, since this region covers all the volumes of interest for the study.

### 6.3.2. PAEDIATRIC VOXEL PHANTOM

Figures 64, 65 and 66 shows the voxelized phantom in different planes.

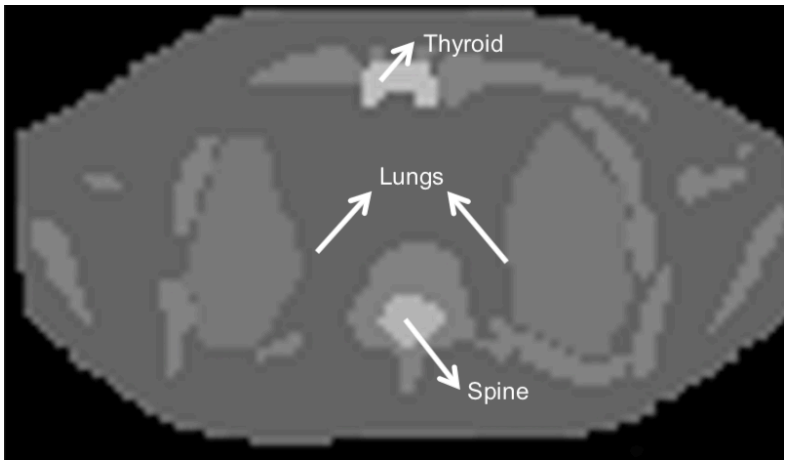


**Figure 64 -** Axial view of the voxelized phantom in ImageJ software.

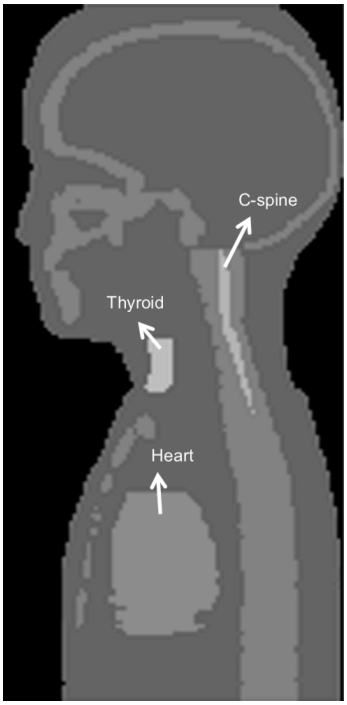


**Figure 65 -** Sagittal view of the voxelized phantom in ImageJ software.

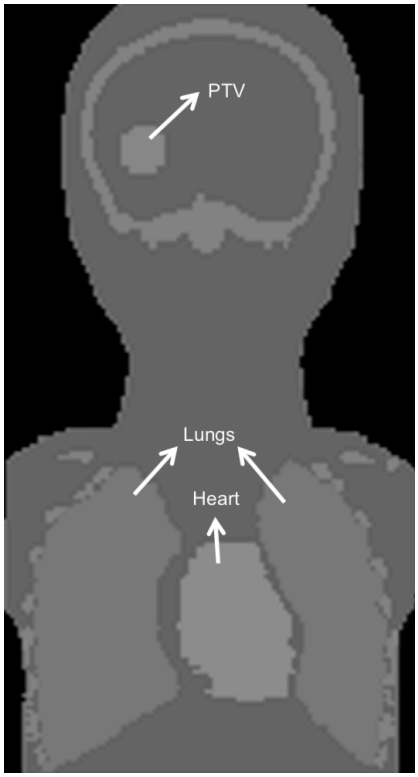


**Figure 66 -** Coronal view of the voxelized phantom in ImageJ software.

Figures 67, 68 and 69 illustrate the MCNP voxel phantom created from the original paediatric phantom. The colours shown in the Figure are described in the Table 5.

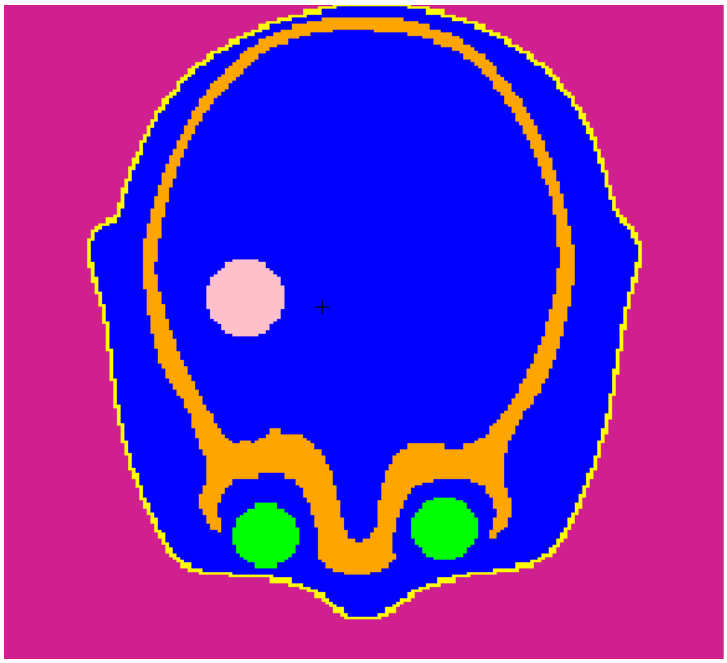

**Figure 67 -** Axial view of the voxel phantom implemented in MCNP6.

**Figure 68 -** Sagittal view of the voxel phantom implemented in MCNP6.

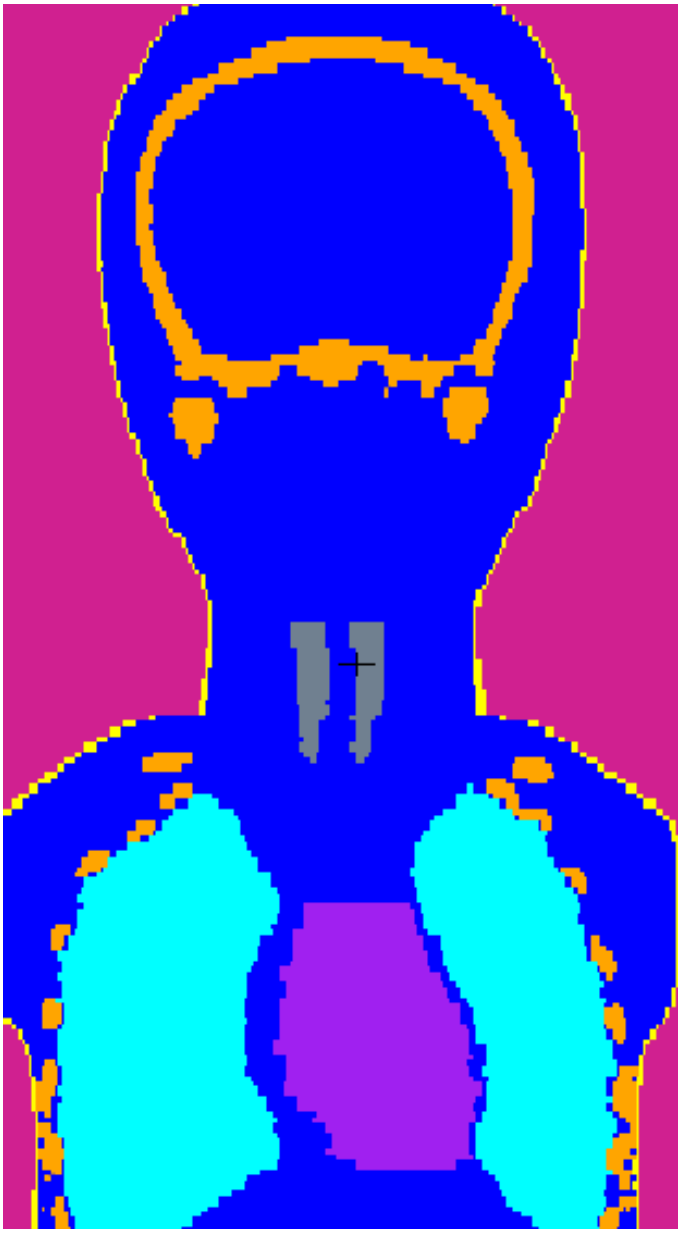

**Figure 69 –** Coronal view of the voxel phantom implemented in MCNP6.

**Table 5 -** Description of the phantom colours.

| Volumes | Colours |
|---|---|
| Air | Pink |
| Skin | Yellow |
| Eyes | Green |
| Bones | Orange |
| PTV | Beige |
| Spine | Red |
| Thyroid | Gray |
| Heart | Purple |
| Lungs | Light blue |
| Soft tissue | Dark blue |

## 6.4. DISCUSSION

In this study, a paediatric voxel phantom was developed and implemented using the ImageJ software and interfaced with MCNP6, aiming at computing and evaluating the doses in volumes of interest outside the treatment fields. Considering that it is a very time-consuming work requiring enormous computational resources, an anthropomorphic 5-year-old phantom, representative of a reference 5 years-old child was selected.

Segmentation is a very time-consuming process, because there is a large number of boundaries and a large number of slices to process. With CT images, it is difficult to visualize organs like ovaries, pancreas, oesophagus and distinguish adrenal glands from the kidneys [145]. Moreover, the walls of hollow organs, such as the intestines,

are not always perceptible from their contents. Consequently, manual manipulation of images using processing software and considerable anatomical knowledge is necessary [145]. In this study, a radiation oncologist reviewed the segmentations of all volumes of interest.

Choi SH *et al*. developed a voxel phantom, representative of male radiation workers with 29.602.950 voxels with 1.981 mm x 1.981 mm x 2.085 mm [215]. The same authors segmented 22 volumes of interest from CT and MRI images of a cadaver. For the manual segmentation of the volumes they used Photoshop 7.0™ and automatic segmentation the IDL 5.6 software [215]. Our phantom has more than double the voxels used in the Choi study, enabling more accurate modeling and definition of smaller volumes of interest. In another study, Dimbylow [216], developed a female voxel phantom, named NAOMI from MRI data with 41 different tissue types. The computational paediatric phantom developed in this study, based on a physical anthropomorphic phantom, enables the evaluation of 9 different types of tissues. It allows accurate dosimetric calculations and the comparison of the 3DCRT and IMRT techniques, which will be presented in the following chapter.

In voxel phantoms, body dimensions can only be modified by changing the voxel resolution, which limits the modification to a uniform scale. For example, creating an individual whose morphometry is not at the 50th percentile from an individual representative of the 50th percentile cannot be realistically performed, because the subcutaneous distribution of fat tissue may be patient-dependent [29]. To overcome these limitations, the information from the pixels can be combined with surface equations to develop hybrid computational phantoms. In these phantoms it is possible to adjust the organ to the desired shape and volume, using specific images of the patients and deformable image processing [29]. Other studies such as the work of Borbinha *et al.* use the ICRP reference phantoms and through a FORTRAN-based program modified the volumetric information of organs to specific individuals, obtaining personalized patient dosimetry [162].

On the one hand through the voxel phantoms, it is possible to evaluate the dose in the organs but voxel size constrains the accuracy of the results. Small volumes, like the lens of the eye, skin and micron-thick tissue present in the digestive and respiratory tract can not be segmented properly [217]. However, the work reported in this thesis does not aim at delivering a detailed dose assessment in small organs.

Contrary to this study in which the images of an anthropomorphic phantom were used, Gallagher *et al.* [5] in 2018 developed a method to supplement the anatomy of patients. Considering the anatomical limitation of CTs for radiotherapy, Gallagher *et al.* supplemented the missing anatomy of these patients. To this end, they relied on tomographic images of patients of the same age, height and gender and performed a rigid fusion of the images in order to evaluate the dose outside the treatment fields [5].

In a recent study Lee *et al.* [218] assessed the dosimetric impact of voxel resolutions of computational human phantoms for external photon exposure and they conclude that the existing voxel phantoms can offer adequate dosimetric accuracy in external photon exposures from 0.1 to 10 MeV [218].

## 6.5. CONCLUSIONS

In this chapter a paediatric computational phantom with voxel dimensions 0.09766 cm x 0.09766 cm x 0.3 cm was successfully developed and implemented, from a physical anthropomorphic phantom. 13 volumes of interest were segmented, namely whole body, skin, bones, heart, eyes, brain, PTV, soft tissue, lungs, thyroid, spine and c-spine.

The development of this computational phantom aims at evaluating the doses outside the treatment fields, compared with measurements performed in clinical environment, for two radiotherapy modalities (3DCRT and IMRT). The results are detailed in the next Chapter.

# CHAPTER 7 – ASSESSMENT OF OUT-OF-FIELD DOSES IN PAEDIATRIC PATIENTS

## 7.1. MOTIVATION

On the one hand, out-of-field doses are a concern in the field of radiotherapy, where absorbed doses less than 3 Gy or doses below 5% of the total prescribed dose to the target volume, are considered low doses [198]. Most of the time, these doses (< 3Gy or 5% of the prescribed dose) are frequently ignored in radiotherapy treatment planning [198], because the main aim in radiotherapy is the treatment of tumour volume, with the lowest dose in the surrounding healthy tissues.

On the other hand, while out-of-field doses are low compared to the doses of the primary field, they are of clinical and radiobiological interest and relevance because they are potentially administered to a considerable volume of the healthy organs and tissues and may therefore lead to new tumours induced by ionizing radiation [15,43]. Radio-carcinogenesis is the most severe side effect that may be caused by out-of-field doses [43], their assessment being therefore of paramount importance [76], particularly in paediatric patients [14,43] due to the manifold times higher radiosensitivity of their organs and tissues and to the corresponding potential detrimental effects of ionizing radiation, compared to adult individuals. There is an on-going debate within the scientific communities to ascertain if the increased used of IMRT will lead to an increased risk of developing second tumours, as it implies doses administration to large volumes of tissue outside the fields [47].

The main objective of this Chapter was to assess out-of-field doses in 3DCRT and IMRT treatments of paediatric patients, using the MC model of the LINAC head described and validated in Chapter 5 coupled to the developed and implemented voxelized version of a physical paediatric phantom detailed in Chapter 6.

## 7.2. MATERIALS AND METHODS

### 7.2.1. TREATMENT PLANNING

A treatment planning was initially performed using the 3DCRT technique and later it was performed with the IMRT technique, for a 6 MV photon beam in both cases. In both cases the same segmentations of volumes of interest were used, as well as the same total dose and dose per fraction. The total prescribed dose to the PTV was 54 Gy, with a dose per fraction of 1.8 Gy. The treatment plans were performed by the Eclipse TPS from Varian (Varian Medical Systems, Palo Alto, CA), Version 13.0. The version 13.6.23 of the Analytical Anisotropic Algorithm (AAA) dose calculation algorithm incorporated in the Eclipse TPS was used.

#### 7.2.1.1. Definition of the Origin of Dosimetric Planning

The dosimetric planning starts with the import of CT images into the TPS. Then it is important to define the point of origin of the dosimetric planning. The origin is the point of coordinates (0,0,0) from which the TPS will be able to calculate the location of all other points of interest and allows it to calculate all necessary deviations throughout the treatment. Coincident with the crossing of the three radiopaque markers previously placed at CT, an orthogonal referential was defined, as seen in Figure 70. The intersection of the axis represents the origin of treatment planning.

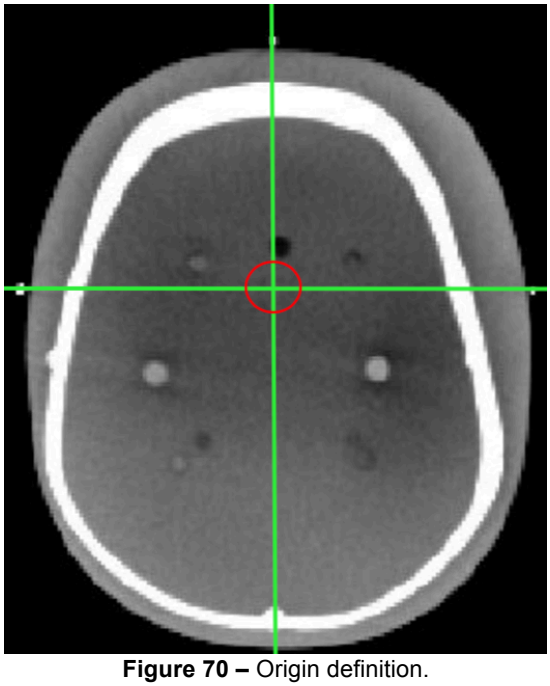

**Figure 70 –** Origin definition.

#### 7.2.1.2. Volumes of Interest Segmentation

It is important to carry out the segmentation of the volumes of interest, namely the PTV and the OARs to be assessed in this study. Only after the segmentation of those structures is it possible to evaluate the dose in each volume by DVH analysis. In this study, a radiation oncologist confirmed all the segmented volumes.

##### *7.2.1.2.1. External Contouring*

The outer contour is often known as “body”. It is important to segment this volume, so that the TPS identifies that from this volume, the photon beam stops interacting with air and starts to interact within the patient´s organs and tissues. To perform this segmentation, an automatic contouring tool is used, which allows the 3D segmentation of the entire contour of the phantom.

##### *7.2.1.2.2. PTV Definition*

Considering that the phantom does not contain a tumour volume, a PTV was defined. This volume is located on the right side of the brain and extends over 13 slices. A manual segmentation tool with the shape of a circle was selected. To create the PTV, seven circles were defined in consecutive slices with 2.5 cm of diameter, four circles with a diameter of 2.0 cm and two slices with a diameter of 1.5 cm, as can be seen in Figure 71, in order to define an elliptical volume, resembling a real PTV. The PTV was defined as a volume with 9.8 $cm^3$ elliptically shaped.

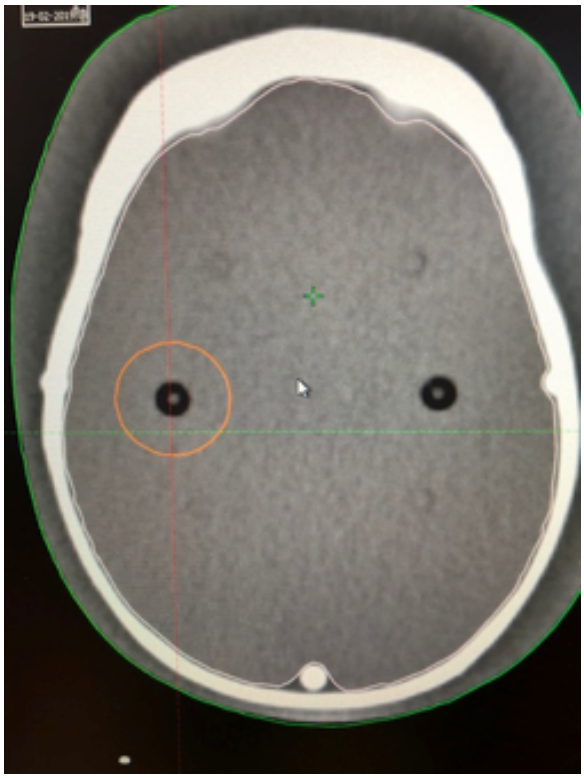

**Figure 71 –** PTV definiton. PTV: Orange; Brain: Light pink; Body: green.

*7.2.1.2.3. OAR*

The OARs segmented were the:

- Lungs (right and left);
- Thyroid;
- Heart;
- C-spine and
- Eyes (right and left).

The lungs were semi-automatically segmented, i.e., in each slice the lungs were filled, allowing an automatic 2D segmentation. As the process occurred in all slices, a 3D segmentation was obtained. The thyroid and heart were manually segmented, i.e., slice by slice with the manual delineation tool, based on the paediatric phantom manual.

Figure 72 displays an axial slice of the phantom in which it is possible to observe the right and left lung, body and the heart.

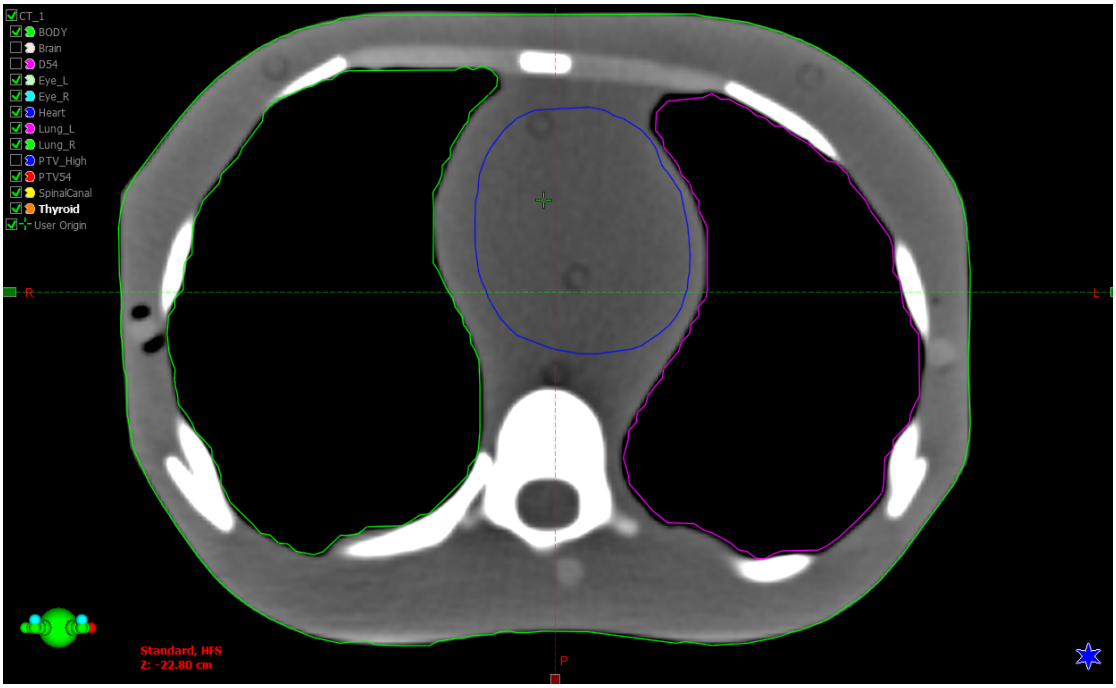


**Figure 72 –** Axial slice of the phantom. Right lung: green; Left lung: pink; Body: green.

The C-spine and eyes were also manually segmented, slice-by-slice, according to the anatomy of the phantom. Figure 73 shows the volumetric reconstruction of the segmented volumes in the TPS.

### 7.2.1.3. 3DCRT Planning

Initially in 3DCRT planning the treatment fields were defined, followed by dose calculation, dose evaluation and dose optimization. Whenever an optimization was carried out, i.e. when any planning parameter was changed, a new dose calculation and a new dose distribution assessment were performed.

#### *7.2.1.3.1. Fields*

The 3DCRT treatment plan was created using six non-coplanar brain fields. The treatment field details are displayed in Table 6 and the positions of the MLC leaves of the treatment fields in the Table 7.

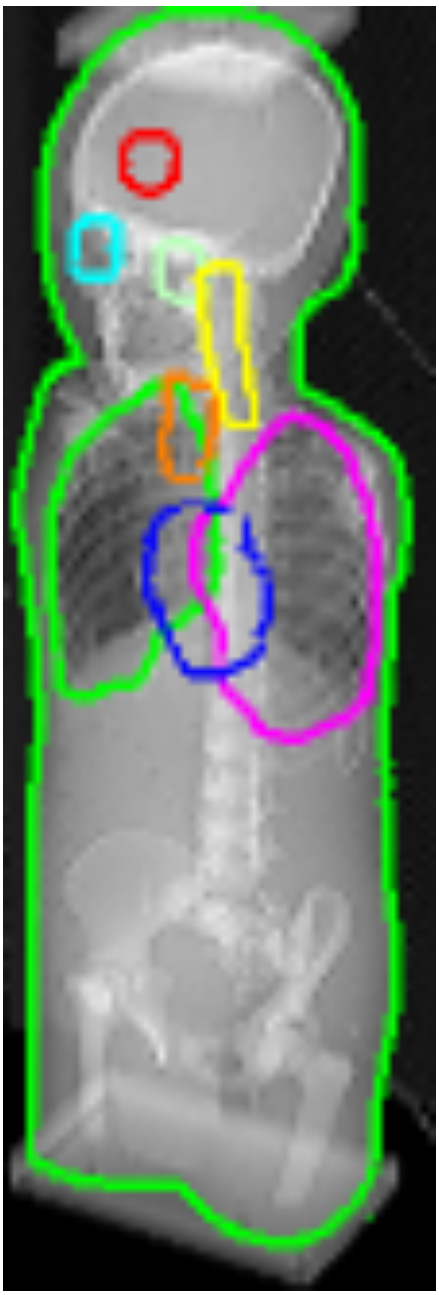

**Figure 73 –** Volumetric reconstruction of the segmented volumes. Body: green; PTV: red; Right eye: light blue; Left eye: light green; C-spine: yellow; Thyroid: orange; Right lung: green; Left lung: pink; Heart: dark blue.

**Table 6 -** 3DCRT planning dose parameters.

| Field ID | Gantry (deg) | Collimator (deg) | Couch (deg) | Field X (cm) | X1 (cm) | X2 (cm) | Field Y (cm) | Y1 (cm) | Y2 (cm) | Field weight | SSD (cm) | MU |
|---|---|---|---|---|---|---|---|---|---|---|---|---|
| **1** | 320.0 | 0.0 | 0.0 | 3.2 | +1.6 | +1.6 | 3.2 | +1.6 | +1.6 | 0.70 | 95.1 | 32 |
| **2** | 270.0 | 0.0 | 0.0 | 3.2 | +1.6 | +1.6 | 3.2 | +1.6 | +1.6 | 0.70 | 96.5 | 30 |
| **3** | 235.0 | 0.0 | 15.0 | 3.4 | +1.7 | +1.7 | 3.4 | +1.7 | +1.7 | 0.70 | 95.9 | 31 |
| **4** | 40.0 | 0.0 | 50.0 | 3.4 | +1.7 | +1.7 | 3.4 | +1.7 | +1.7 | 1.10 | 90.1 | 63 |
| **5** | 155.0 | 0.0 | 345.0 | 3.4 | +1.7 | +1.7 | 3.4 | +1.7 | +1.7 | 1.00 | 91.5 | 53 |
| **6** | 60.0 | 309.0 | 30.0 | 3.4 | +1.7 | +1.7 | 3.5 | +1.7 | +1.8 | 1.00 | 89.3 | 60 |

Non-coplanar fields were used by rotating the treatment couch so that the fields would not pass through volumes of interest like the eyes.

**Table 7 -** MLC leaf positions.

| Field ID | | Leaf pair | | | | | | | | | |
|---|---|---|---|---|---|---|---|---|---|---|---|
| | | 26 | 27 | 28 | 29 | 30 | 31 | 32 | 33 | 34 | 35 |
| **1** | **Field size (cm)** | 0.000 | 1.240 | 2.320 | 3.000 | 3.075 | 3.080 | 3.010 | 2.320 | 1.330 | 0.000 |
| | **Bank A (cm)** | -0.000 | +0.620 | +1.160 | +1.505 | +1.538 | +1.547 | +1.515 | +1.160 | +0.620 | -0.000 |
| | **Bank B (cm)** | +0.000 | +0.620 | +1.160 | +1.495 | +1.537 | +1.533 | +1.495 | +1.160 | +0.710 | +0.000 |
| **2** | **Field size (cm)** | 0.000 | 1.060 | 2.320 | 3.000 | 3.093 | 3.091 | 3.020 | 2.340 | 1.130 | 0.000 |
| | **Bank A (cm)** | -0.000 | +0.500 | +1.180 | +1.515 | +1.553 | +1.557 | +1.515 | +1.180 | +0.545 | -0.000 |
| | **Bank B (cm)** | +0.000 | +0.560 | +1.140 | +1.485 | +1.539 | +1.534 | +1.505 | +1.160 | +0.585 | +0.000 |
| **3** | **Field size (cm)** | 0.000 | 1.120 | 2.285 | 2.888 | 3.130 | 3.132 | 2.897 | 2.245 | 1.150 | 0.000 |

| | | | | | | | | | | | |
|---|---|---|---|---|---|---|---|---|---|---|---|
| | **Bank A (cm)** | -0.000 | +0.640 | +1.105 | +1.459 | +1.537 | +1.604 | +1.449 | +1.160 | 0.480 | -0.000 |
| | **Bank B (cm)** | +0.000 | +0.480 | +1.180 | +1.429 | +1.593 | +1.528 | +1.448 | +1.085 | +0.640 | +0.000 |
| **4** | **Field size (cm)** | 0.000 | 1.140 | 2.140 | 2.965 | 3.303 | 3.348 | 2.938 | 2.100 | 1.130 | 0.000 |
| | **Bank A (cm)** | -0.000 | +0.610 | +1.180 | +1.545 | +1.675 | +1.656 | +1.405 | +0.960 | +0.520 | -0.000 |
| | **Bank B (cm)** | +0.000 | +0.530 | +0.960 | +1.420 | +1.628 | +1.692 | +1.533 | +1.140 | +0.610 | +0.000 |
| | **Field size (cm)** | 0.000 | 0.880 | 2.215 | 2.909 | 3.204 | 3.198 | 2.919 | 2.200 | 0.905 | 0.000 |
| **5** | **Bank A (cm)** | -0.000 | +0.200 | +1.160 | +1.493 | +1.656 | +1.542 | +1.407 | +1.040 | +0.670 | -0.000 |
| | **Bank B (cm)** | +0.000 | +0.680 | +1.055 | +1.416 | +1.548 | +1.656 | +1.512 | +1.160 | +0.235 | +0.000 |
| | **Field size (cm)** | 0.000 | 1.070 | 2.160 | 2.900 | 3.304 | 3.293 | 2.910 | 2.180 | 0.950 | 0.000 |
| **6** | **Bank A (cm)** | -0.000 | +0.430 | +1.000 | +1.365 | +1.651 | +1.653 | +1.535 | +1.160 | +0.520 | -0.000 |
| | **Bank B (cm)** | +0.000 | +0.640 | +1.160 | +1.535 | +1.653 | +1.640 | +1.375 | +1.020 | +0.430 | +0.000 |

The dose normalization has been carried out for the geometric centre of PTV. Figure 74 shows the fields arrangement of the 3DCRT plan.

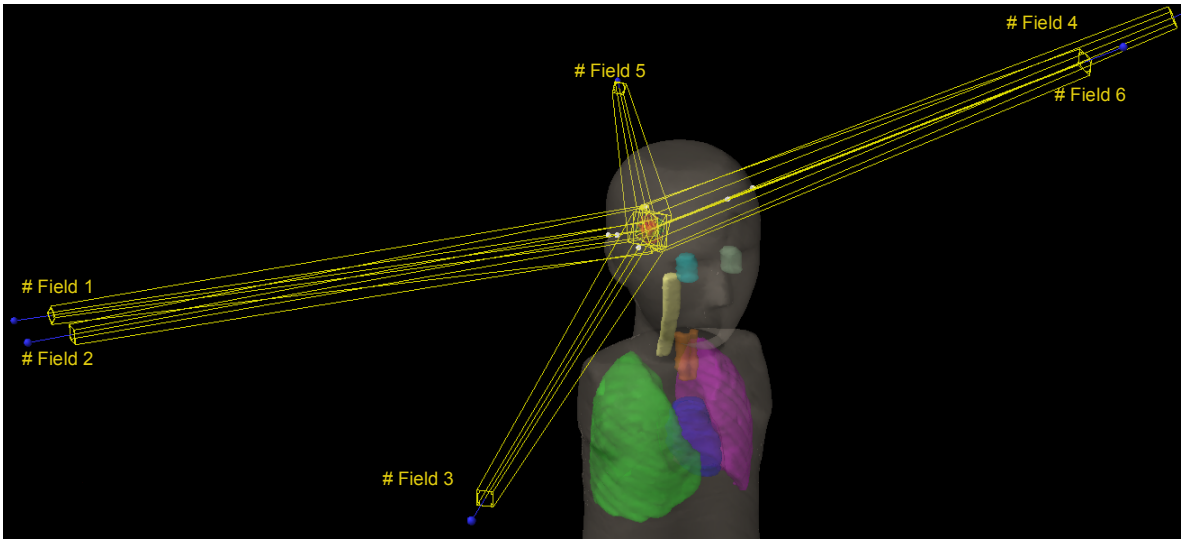


**Figure 74 –** Field arrangement for 3DCRT plan.

*7.2.1.3.2. Dose Distribution Assessment*

The evaluation of the dose distribution was carried out, after the dose calculation, in two different ways: a qualitative and a quantitative evaluation were made. In the qualitative assessment, it was verified whether the reference isodose curve, 95% of the prescribed dose, i.e. 51.3 Gy included the entire PTV. This evaluation was carried out slice by slice, as can be seen in Figure 75.

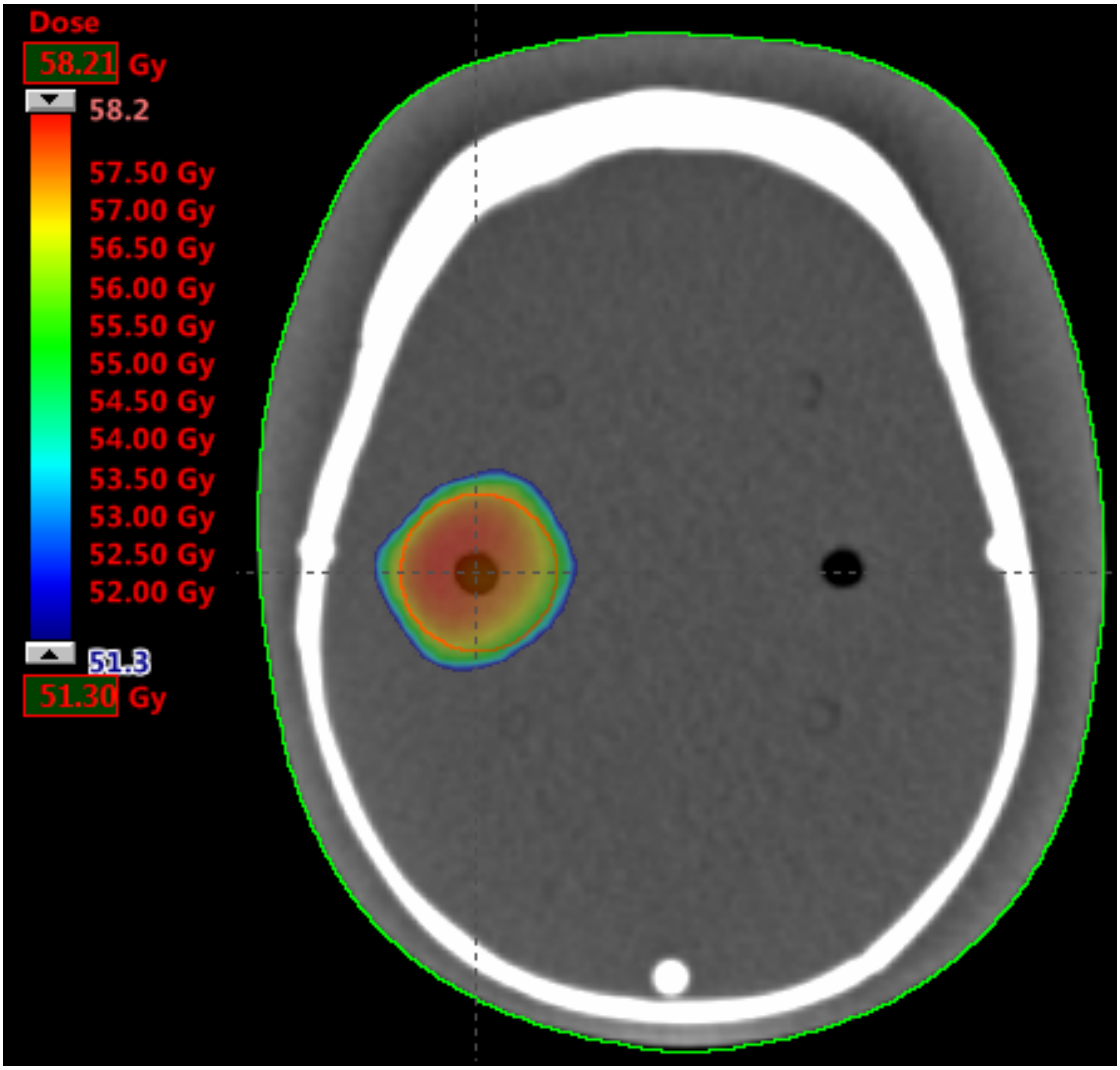


**Figure 75 –** Assessment of 95% of prescribed dose in PTV.

The homogeneity of the dose distribution was also evaluated, as well as the presence of hot spots and cold spots.

The quantitative evaluation was carried out using the DVH and aimed to evaluate PTV, and the OAR, as detailed in Figure 76. Through the analysis of DVH, for PTV the minimum dose, average dose and maximum dose were evaluated. For the OAR of this study, the QUANTEC tables were used, as can be seen in Table 8 [219–223].

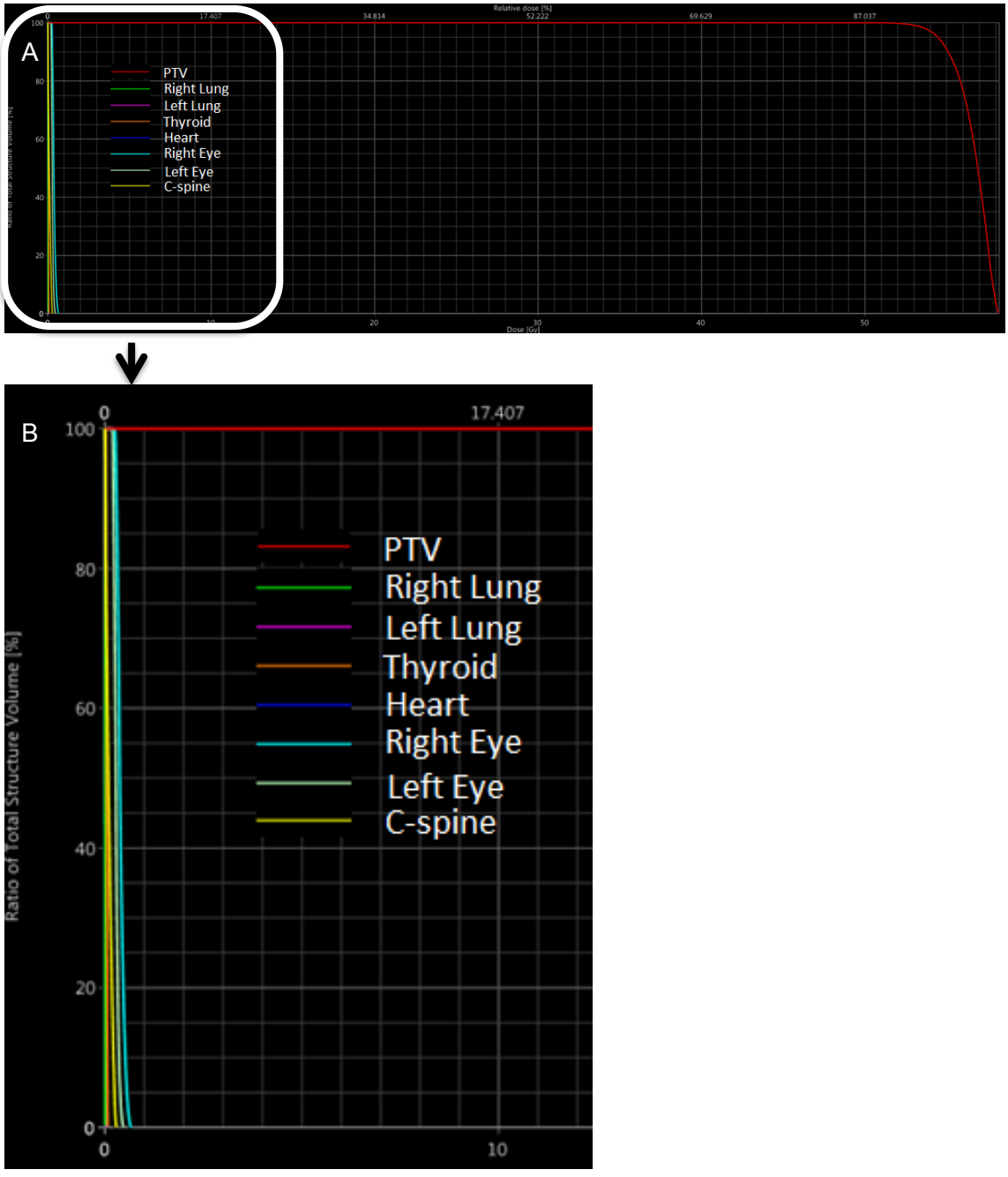


**Figure 76 –** DVH of the 3DCRT plan. A: Overview of the DVH; B: Detail of the OAR.

**Table 8 -** Normal tissue tolerance for standard fractionation [219–223].

| Organ | $D_{max}$ (Gy) | $D_{mean}$(Gy) | Dose-volume parameter | Rate (%) | Endpoint |
|---|---|---|---|---|---|
| **Eye** | < 45-50 | -- | -- | < 1 | Blindness |
| **Spine cord** | 50 | | | < 1 | Myelopathy |
| **Lung** | | 7 | V5 < 42% | 5 | Pneumonitis |
| | | | V20 < 22% | | |
| | | 13 | V20 < 31% | 10 | |
| | | 20 | V20 < 40% | 20 | |
| | | 24 | | 30 | |
| | | 27 | | 40 | |
| **Heart** | | < 26 | V30 < 46% | < 15% | Pericarditis |
| | | | V25< 10% | < 1% | Long-term cardiac mortality |
| **Thyroid** | | < 45 | V30 < 60% | | Hypothyroidism |

*7.2.1.3.3. Dose Distribution Optimization*

Whenever an evaluation of the dose distribution did not follow all the criteria defined by ICRU reports 50 and 62 [99,100], an optimization of the dose distribution was performed. In this study, weight, angulation and MLC shape of the treatment fields were changed until a satisfactory dose distribution was obtained, i.e., a compromise between correct irradiation of the PTV with the minimum possible dose in OAR and healthy tissue.

#### 7.2.1.4. IMRT Planning

Initially in IMRT planning the number of fields and their gantry angle were selected for each field. Then, the initial objectives of the dose planning were defined. After several dose calculations, the final dose distribution was obtained.

##### *7.2.1.4.1. Fields*

IMRT treatment plan was created using seven coplanar brain fields. The treatment field details are displayed in Table 9 and the field arrangement in Figure 77. For MLC, the dynamic mode was used.

**Table 9 -** IMRT planning dose parameters.

| Field ID | Gantry (deg) | Collimator (deg) | Couch (deg) | Field X (cm) | X1 (cm) | X2 (cm) | Field Y (cm) | Y1 (cm) | Y2 (cm) | Field weight | SSD (cm) | MU |
|---|---|---|---|---|---|---|---|---|---|---|---|---|
| **1** | 340.0 | 0.0 | 0.0 | 5.0 | +2.5 | +2.5 | 3.6 | +1.8 | +1.8 | 1.00 | 93.5 | 51 |
| **2** | 314.0 | 0.0 | 0.0 | 5.0 | +2.5 | +2.5 | 3.6 | +1.8 | +1.8 | 1.00 | 95.4 | 47 |
| **3** | 266.0 | 0.0 | 0.0 | 5.0 | +2.5 | +2.5 | 3.6 | +1.8 | +1.8 | 1.00 | 96.5 | 43 |
| **4** | 228.0 | 0.0 | 0.0 | 5.0 | +2.5 | +2.5 | 3.6 | +1.8 | +1.8 | 1.00 | 95.8 | 43 |
| **5** | 197.0 | 0.0 | 0.0 | 5.0 | +2.5 | +2.5 | 3.6 | +1.8 | +1.8 | 1.00 | 94.2 | 47 |
| **6** | 173.0 | 0.0 | 0.0 | 5.0 | +2.5 | +2.5 | 3.6 | +1.8 | +1.8 | 1.00 | 92.7 | 50 |
| **7** | 154.0 | 0.0 | 0.0 | 5.0 | +2.5 | +2.5 | 3.6 | +1.8 | +1.8 | 1.00 | 91.5 | 53 |

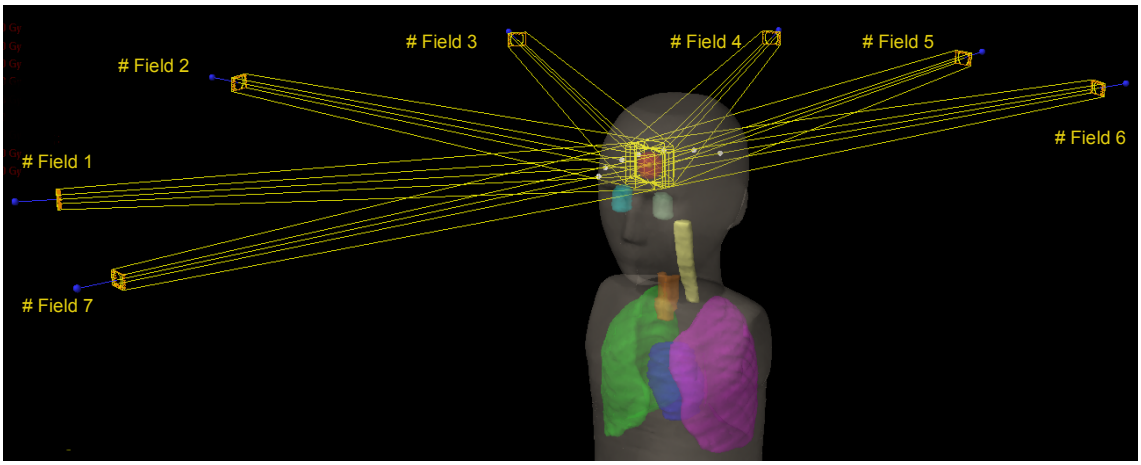


**Figure 77 –** IMRT field arrangement.

*7.2.1.4.2. Dose Objectives*

In inverse planning, in order to perform the dose calculation, it was necessary to establish the optimization objectives. Considering a brain irradiation and the previously segmented volumes, it was decided to define the dose objectives for the eyes, since they are the volumes of risk closest to PTV and in clinical environment only these would be considered as OAR in radiotherapy planning, as shown in Table 10.

**Table 10 -** Optimization objectives for inverse planning.

| Structure | Limit | Volume (%) | Dose (Gy) | Priority |
|---|---|---|---|---|
| **Left Eye** | Upper | 0.0 | 5.0 | 60 |
| | Upper | 5.0 | 3.0 | 60 |
| **Right Eye** | Upper | 0.0 | 8.0 | 70 |
| | Upper | 5.0 | 6.0 | 70 |
| **PTV** | Upper | 0.0 | 55.1 | 220 |
| | Lower | 99.0 | 54.3 | 280 |
| | Lower | 100.0 | 53.7 | 280 |
| | Lower | 100.0 | 54.00 | 280 |

The upper limits are related to the OAR, so that a certain dose/volume is not exceeded. The lower limits are more related to PTV, so that a given dose/volume is not lower than the values set. The priority serves so that the TPS, in the dose calculation, tries to achieve the objectives with the highest priority first, compared to the objectives with the lowest priority. In this case, higher priorities (220-280) were given to the PTV and lower priorities were given to the eyes (60-70. However, the right eye had a higher priority (70) than the left eye (60), since PTV is in the right hemisphere of the brain.

*7.2.1.4.3. Dose Distribution Assessment*

To assess the dose distribution of the IMRT plan, it was initially checked whether the reference isodose curve of 95% of the prescribed dose involved the entire PTV. This was done by selecting only the corresponding isodose curve in order to check slice by slice. Subsequently, the HI and CI of the dosimetry plan were evaluated. The HI was evaluated on the basis of the ICRU report 83 [40], as can be seen in the following equation,

$$HI = \frac{D_{2\%} - D_{98\%}}{D_{50\%}} \quad \text{Eq. 7.1}$$

where $D_{2\%}$ is the calculated dose in 2% of the PTV volume, $D_{98\%}$ is the calculated dose in 98% of the PTV volume and $D_{50\%}$, is the calculated dose in 50% of the PTV volume.

The CI was assessed on the basis of the following equation [224],

$$CI = \frac{V_{95\%\, isodose}}{PTV_{volume}} \quad \text{Eq. 7.2}$$

where $V_{95\%\, isodose}$ is the target volume covered by the 95% isodose and the $PTV_{volume}$ is the volume of the PTV.

Later, the doses in the OAR and PTV were evaluated with the aid of DVH, as shown in Figure 78. This assessment was based on tolerance dose tables with conventional

fractionation [219–221], i.e., between 1.8 and 2 Gy per fraction, as can be seen in Table 8.

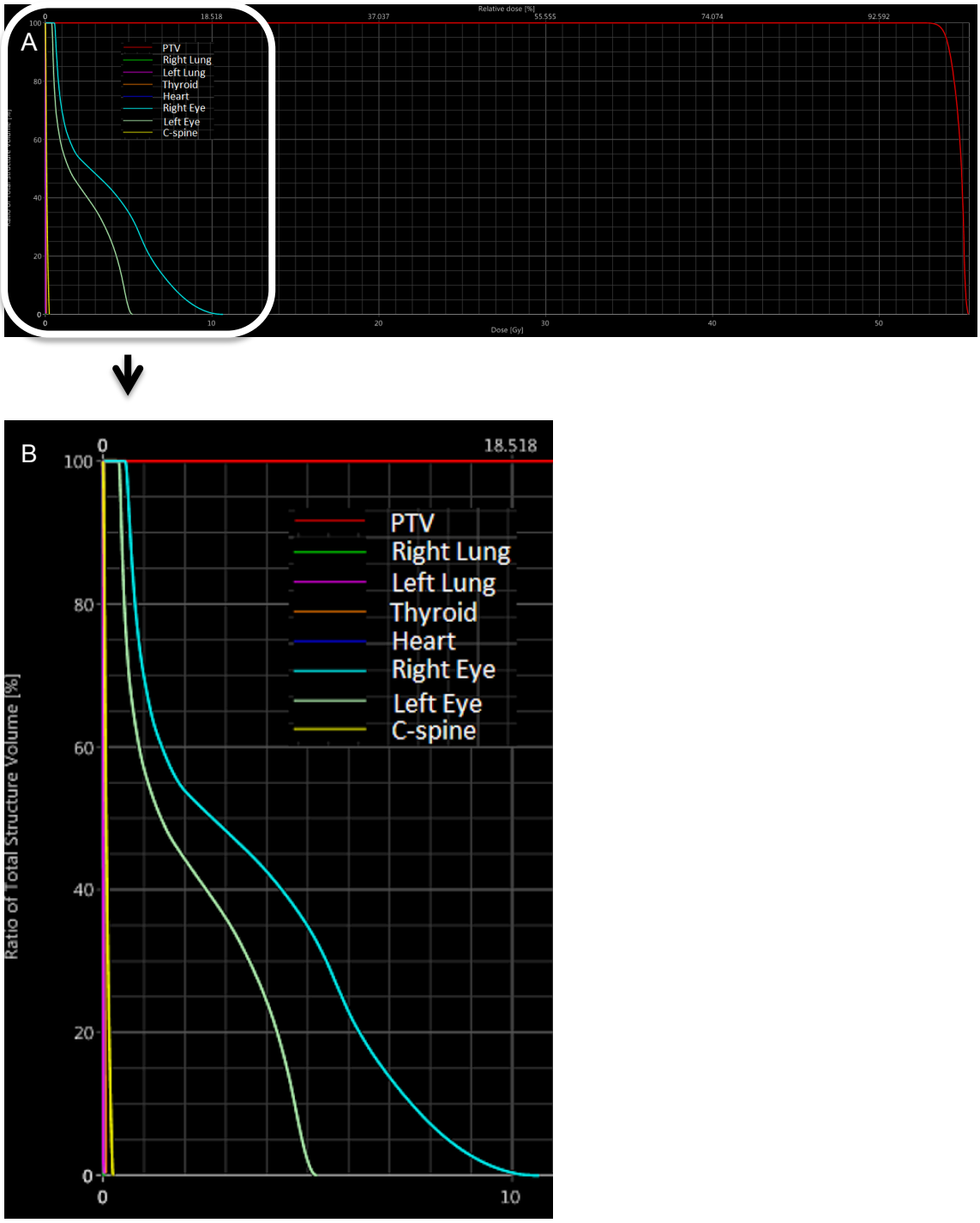


**Figure 78 –** DVH of the IMRT plan. A: Overview of the DVH; B: Detail of the OAR.

*7.2.1.4.4. Dose Distribution Optimization*

Throughout the optimization of the dose distribution, it was necessary to set more optimization goals, which is, two more goals were added for PTV and one more for each eye. There was also a change in priorities for each of the optimization objectives.

### 7.2.2. TLD Measurements Using a Paediatric Phantom

In this work, LiF:Mg,Cu,P (TLD-100H) Harshaw Ext-Rad TLD were placed in the physical paediatric phantom to assess the out-of-field doses, namely in organs such as the eyes (right and left), C-spine, thyroid, heart and lungs. A total of 76 round detectors, divided into two groups of 38 detectors, were used. The first group of detectors was irradiated with the 3DCRT technique and the second group of detectors was irradiated with the IMRT technique. Each detector has a diameter of 5 mm and for each group one detector was placed in the right eye, one for the left eye, two for the c-spine, four for the thyroid, two for the heart, 12 for the right lung and 16 for the left lung.

Examples of TLDs placed in the phantom can be seen in Figure 79. Figure 79A shows section 8 of the phantom where two TLDs are placed in the thyroid and one TLD in the C-spine. In Figure 79B there are two TLDs placed in the thyroid in section 9. Figure 79C shows section 13 where 5 TLDs are placed in the right lung and 3 TLDs in the left lung.

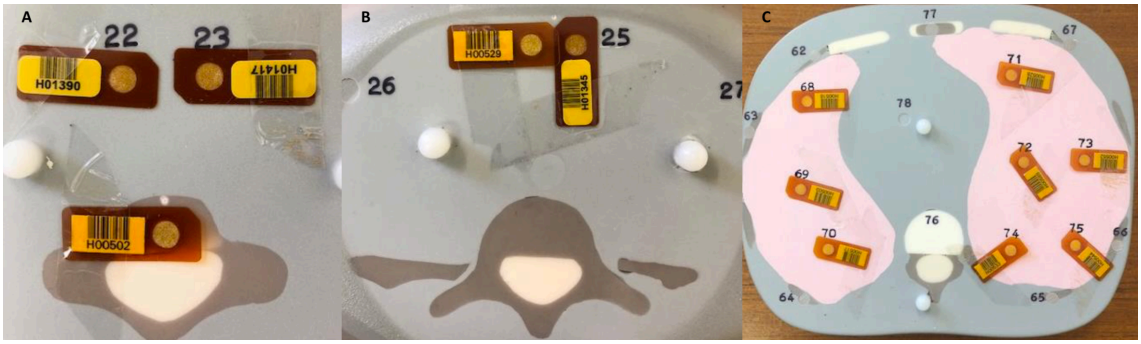


**Figure 79 –** Example of TLDs placement in the phantom. Left (A): dosimeters placed in section 8; Center (B): dosimeters placed in section 9; Right (C): dosimeters placed in section 13.

A more accurate description of the placement of TLDs in the phantom is displayed in Table 11. This table shows in detail the position of the TLD placement in the phantom.

**Table 11 -** TLDs placement in different sections and location numbers of the phantom**.**

| Organ | Section number (Location number) |
|---|---|
| **Right eye** | 4 (15) |
| **Left eye** | 4 (16) |
| **C-spine** | 6 (20); 8 (21) |
| **Thyroid** | 8 (22-23); 9 (24-25) |
| **Heart** | 12 (61); 13 (78) |
| **Right lung** | 10 (28); 11 (46-47); 12 (52-54); 13 (68-70); 14 (79-81) |
| **Left lung** | 10 (29); 11 (48-49); 12 (55-57); 13 (71-75); 14 (82-86) |

The LiF detectors family is widely used in different areas due to their advantages like the low effective number (Zeff = 8.14), different shapes, size and sensitivity [225]. The TLD dosimeters were previously calibrated in terms of air kerma using a Cs-137 source.

The TLD dosimeters were reset on the day before the irradiation and the readouts were performed on the day after irradiation using a Harshaw 6600 reader with a pre-defined time-temperature profile to avoid any contribution of the non-dosimetric peaks [226]. Transit detectors were also used; however, background subtraction was not performed due to their negligible value.

The Kerma in air ($K_{air}$) was calculated using the following equation [227]:

$$K_{air} = \frac{RD \times Ecc}{RCF} \times f(Q) \times f(fad) \times f(E) \times f(\alpha) \qquad \text{Eq. 7.3}$$

For each TLD, the Raw Data $(RD)$ is multiplied by the Efficiency Correction Coefficient $(Ecc)$, the correction factors of reader stability $(f(Q))$, fading effect $(f(fad))$, energy dependency $(f(E))$, angular dependency $(f(\alpha))$ and divided by the Reader Calibration Factor $(RCF)$.

Considering that the quality control did not show any variations, the $f(Q)$ was equal to one. The interval between the reset and the readout was negligible and for this reason the correction due to the fading effect was not considered. Since the irradiation conditions were well known, the energy and angular dependence correction factors were considered equal to one.

The final dose value assessed at each position of the TLD in the paediatric phantom was obtained based on the following equation [227], assuming that the electronic equilibrium condition is observed:

$$D_{organ} = K_{air} \times \frac{(\mu_{en}/\rho)_{tissue}}{(\mu_{en}/\rho)_{air}} \quad \text{Eq. 7.4}$$

where $K_{air}$ was previously defined, $(\mu_{en}/\rho)_{tissue}$ is the mass energy-absorption coeficiente for each organ and $(\mu_{en}/\rho)_{air}$ is the mass energy-absorption coefficient for air at an average energy of the spectrum of 6 MeV. The mass energy-absorption coefficients for air and tissues were obtained through a web-based National Institute of Standards and Technology (NIST) [228] as can be seen in Table 12.

**Table 12 -** Organ characteristics assessed in phantom.

| Organ | $\mu_{en}/\rho$ (cm$^2$/g) @ 6 MeV | Nr. of phantom sections | Nr. of TLDs |
|---|---|---|---|
| **Right eye** | 0.0179 | 1 | 1 |
| **Left eye** | 0.0179 | 1 | 1 |
| **C-spine** | 0.0179 | 2 | 2 |
| **Thyroid** | 0.0194 | 2 | 4 |
| **Heart** | 0.0179 | 2 | 2 |
| **Right lung** | 0.0179 | 5 | 12 |
| **Left lung** | 0.0179 | 5 | 16 |

The final uncertainty of the measurements was ≈16% (k=1), calculated using the law of propagation of uncertainties, as the square root of the sum of the uncertainties squared [229] from the following contributions: (1) detector efficiency - 3.0%, (2) stability of the quality control correction factor – 3.8%, (3) reader calibration factor – 15.0% and (4) energy dependence - 1.4%. The contribution from the reader calibration factor takes into account the uncertainty reported by the metrology laboratory and the results for the calibration factors of the last years. To the energy dependence contribution, only high energies were considered. The phantom irradiation was performed on the same LINAC with an energy of 6 MV under the conditions previously described in Tables 4 and 6, for the two techniques.

### 7.2.3. MCNP6 MONTE CARLO SIMULATIONS OF OUT-OF-FIELD DOSES

For both 3DCRT and IMRT techniques, all MC simulations of out-of-field doses in the organs were performed using MCNP6 and the developed paediatric voxel phantom and the implemented and validated LINAC head model. Each simulation ran in parallel processing mode with 10 x $10^9$ photons produced in the target and the electron and photon energy cut off were 0.1 MeV and 0.01 MeV, respectively. The tally *F8 was used and a statistical relative uncertainty of less than 5% for the computational results was achieved.

For the 3DCRT technique, MC simulations were made for the six fields with the MLC positions described in Table 7.

For the MC simulations with IMRT the position of the MLCs was obtained through the MLC log file of each field extracted from the Varian TPS Eclipse system. Each log file contains information for about 100 MLC positions for each field. For the IMRT planning considering seven fields, there are about 700 MLC positions. In order to minimize the computational effort, 20 MLC positions were selected for each field, making a total of 140 simulations. As in 3DCRT (Table 7), the movement of the leaves in IMRT appears only between the pair 27 and 34. Based on the log files and for each IMRT field the indexes 5, 10, 15, 20, 25, 30, 35, 40, 45, 50, 55, 60, 65, 70, 75, 80, 85, 90, 95 and 100 were selected. An average of these same values was obtained.

In the MCNP computer program, in order to change the position of the leaves it was necessary to use the cell coordinate transformation (TRCL) card, which allows, together with the surface coordinate transformation (TR) card, to create the rotation of the leaves, obtaining different MLC positions based on the different secondary

collimators. The *TR and *TRCL input cards were used to specify that the entries in the rotation matrices were in degrees and not in cosines of the angles [141].

The results in MCNP6 are normalized per source particle. To obtain the absolute dose in mGy a conversion factor (CF) was calculated. According to Frank Verhaegen [132], it is possible to obtain a CF for each beam energy produced by the LINAC. For data normalization the maximum dose values were considered, as presented in the following equation [178]:

$$CF = \frac{Measured\ Dose^{dmax}}{Calculated\ Dose^{dmax}} \Leftrightarrow \frac{mGy}{\frac{mGy}{Particle}} \quad \text{Eq. 7.5}$$

where $Measured\ Dose^{dmax}$ and $Calculated\ Dose^{dmax}$ are the measured and calculated dose at the depth of the maximum radiation dose. These values were measured and calculated considering the SSD of 100 cm between the source and the water phantom in the central axis of the beam, under the reference conditions, i.e. 10 x 10 $cm^2$ field size with the MLC retracted.

Considering that the results are presented in MeV / source particle, it is necessary to convert them to mGy [178].

$$Tally * F8 = \frac{MeV}{Particle} \rightarrow \frac{J}{Particle} \rightarrow \frac{\frac{J}{Kg}}{Particle} \rightarrow \frac{mGy}{Particle} \quad \text{Eq. 7.6}$$

Thereby, the absolute doses are achieved by multiplying the tally *F8 value by the CF [178]:

$$Normalization = Tally * F8 \times FC \rightarrow \frac{mGy}{Particle} \times \frac{mGy}{\frac{mGy}{Particle}} = mGy \quad \text{Eq. 7.7}$$

All values obtained with the tally *F8 in MCNP for organs were multiplied by the FC.

## 7.3. RESULTS

The results will be divided into three parts for both techniques. Initially, the results of the dose calculation in the TPS will be presented. Then, the measurements performed on the paediatric physical phantom using a Varian Clinac 2100 will be shown. Finally, MC calculations using the LINAC computational model as well as the paediatric computational phantom will be displayed.

### 7.3.1. TPS DOSE CALCULATION

After the dose calculation performed by the TPS it was found that for the 3DCRT technique, the PTV was covered by the isodose curve of 95% of the prescribed dose, i.e. 51.3 Gy almost in all axial slices. It was also found that there were no hot spots and cold spots in the dose distribution.

For the IMRT technique, the PTV was also covered by the 95% isodose curve of the prescribed dose, with HI=0.027 and CI = 1.35. In both techniques, the OARs are all within the tolerance values, namely the eyes have values of maximum dose ($D_{max}$) < 50 Gy.

Table 13 shows the detailed results of the dose calculation in the TPS for 3DCRT and IMRT, namely the minimum dose ($D_{min}$), mean dose ($D_{mean}$) and $D_{max}$, as well as the distance of the structures from the PTV.

**Table 13 -** Volumes of interest doses calculated by TPS for 3DCRT and IMRT.

| | | | **$TPS_{3DCRT}$** | | | **$TPS_{IMRT}$** | | |
|---|---|---|---|---|---|---|---|---|
| **Structure** | **Distance from $PTV_{center}$ to $organ_{center}$** (cm) | **Volume** ($cm^3$) | **$D_{min}$** (mGy) | **$D_{max}$** (mGy) | **$D_{mean}$** (mGy) | **$D_{min}$** (mGy) | **$D_{max}$** (mGy) | **$D_{mean}$** (mGy) |
| $PTV_{54}$ | 0.0 | 9.8 | 50948.0 | 58210.0 | 54591.0 | 52499.0 | 55391.0 | 54789.0 |
| Right eye | 6.2 | 7.1 | 247.0 | 695.0 | 395.0 | 538.0 | 10706.0 | 3512.0 |
| Left eye | 8.4 | 7.0 | 181.0 | 503.0 | 282.0 | 372.0 | 5257.0 | 2166.0 |

| | | | | | | | | |
|---|---|---|---|---|---|---|---|---|
| C-spine | 11.1 | 14.3 | 0.0 | 300.0 | 103.0 | 0.0 | 250.0 | 91.0 |
| Thyroid | 13.1 | 8.7 | 7.0 | 81.0 | 44.0 | 0.0 | 69.0 | 37.0 |
| Right Lung | 21.7 | 652.7 | 0.0 | 25.0 | 2.0 | 0.0 | 50.0 | 2.0 |
| Heart | 22.2 | 123.7 | 0.0 | 8.0 | 2.0 | 0.0 | 4.0 | 2.0 |
| Left lung | 23.3 | 518.5 | 0.0 | 42.0 | 3.0 | 0.0 | 44.0 | 3.0 |

From the analysis of Table 13, it can be seen that in general, with the TPS there is a decrease in the dose as the distance from the target volume increases. Organs outside the treatment fields receive higher doses when they are closer to the field edge. Considering that the target volume is in the right hemisphere, the right eye is exposed to a higher dose when compared to the left eye. However, the same is not true for the lungs. For the IMRT technique, only the $D_{max}$ in the right lung is higher that the corresponding value of the left lung.

To compare the different treatment techniques in each structure, a graphical analysis of each one was performed in Figure 80. Figure 80 A shows that the TPS calculations for the PTV with the 3DCRT technique presents a $D_{max}$ higher than with the IMRT technique. For the $D_{mean}$ and $D_{min}$ the IMRT yields higher values than the 3DCRT technique. In Figure 80 B and C, it is observed that in the eyes, the IMRT technique features higher values in $D_{min}$, $D_{mean}$ and $D_{max}$ than the 3DCRT technique. Figure 80 D shows that for the C-spine the 3DCRT technique have higher values than the IMRT technique for $D_{mean}$ and $D_{max}$. The $D_{min}$ has values of zero for both techniques. In the thyroid (Figure 80 E) the 3DCRT technique yields higher values than the IMRT technique for $D_{min}$, $D_{mean}$ and $D_{max}$. The $D_{min}$ with the IMRT technique has a value of zero. For the heart (Figure 80 G), it is observed that the $D_{min}$ is zero for both techniques. The $D_{mean}$ also has an equal value for both techniques, but the $D_{max}$ obtained with the 3DCRT technique, doubles the one obtained with the IMRT technique. In the right lung (Figure 80 F) and left lung (Figure 80 H) the IMRT technique leads to higher values for Dmax, compared to the 3DCRT technique; however, equal values are obtained for both techniques for Dmean and Dmin, zero for the latter.

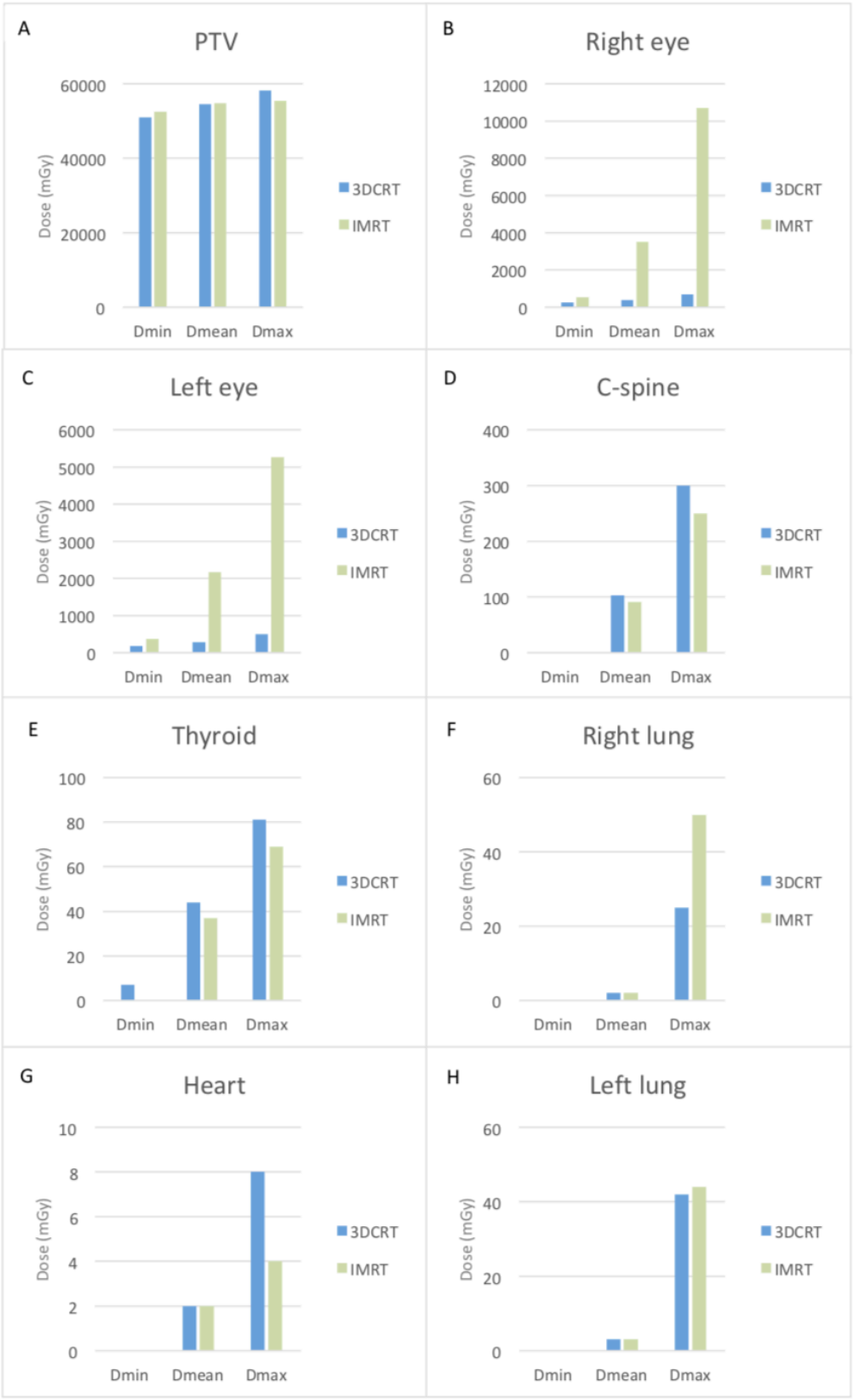


**Figure 80 –** Doses calculated by the TPS for all structures. A: PTV, B: Right eye, C: Left eye, D: C-spine, E: Thyroid, F: Right lung, G: Heart, H: Left lung.

### 7.3.2. Out-of-Field Doses in Paediatric Phantom Measurements with TLDs – Physical Paediatric Phantom

Applying equations 7.3 for $K_{air}$ and 7.4 for $D_{organ}$, the dose values obtained using the TLDs, for the 3DCRT and IMRT techniques, are detailed in Table 14.

**Table 14 –** Out-of-field organ doses measured by TLDs for 3DCRT and IMRT treatments.

| | | **$TLD_{3DCRT}$** | **$TLD_{IMRT}$** |
|---|---|---|---|
| **Structure** | **Distance from $PTV_{center}$ to $organ_{center}$** (cm) | **$D_{organ}$** (mGy) 30 fractions | **$D_{organ}$** (mGy) 30 fractions |
| Right eye | 6.2 | 593.0 ± 94.9 | 13040.6 ± 2086.5 |
| Left eye | 8.4 | 475.2 ± 76.0 | 6525.3 ± 1044.1 |
| C-spine | 11.1 | 180.9 ± 28.9 | 182.3 ± 29.2 |
| Thyroid | 13.1 | 69.7 ± 11.2 | 79.4 ± 12.7 |
| Right Lung | 21.7 | 28.0 ± 4.5 | 37.4 ± 6.0 |
| Heart | 22.2 | 25.1 ± 4.0 | 30.6 ± 4.9 |
| Left lung | 23.3 | 19.8 ± 3.2 | 27.1 ± 4.3 |

Table 11 shows that the TLD measurements with IMRT yields higher values in all organs outside the treatment fields when compared to the TLD measurements with 3DCRT technique.

The TLD doses in each organ outside the treatment fields and the associated uncertainties for both radiotherapy techniques all treatment are displayed in Figure 81. Figure 81 A shows that TLD dose measurements with IMRT has dose values in the right eye about 22 times higher than the 3DCRT technique. The dose in the left eye with the IMRT technique is about 14 times higher than the 3DCRT technique (Figure 81 B). In the C-spine the dose values are very similar between the two techniques, however, IMRT presents about 1 mGy more compared to the 3DCRT technique (Figure 81 C). In Figure 81 D, it can be seen that in the thyroid the 3DCRT technique presents

values lower by about 10 mGy compared to the IMRT technique. Regarding the lungs, it is observed that the right lung presents a higher dose compared to the left lung and in both lungs the IMRT technique has higher values compared to the 3DCRT technique, namely, about 9 mGy for the right lung (Figure 81 E) and about 7 mGy for the left lung (Figure 81 G). Finally, The heart is an organ about 22 cm from the center of the PTV and it is observed that at the end of the 30 fractions of treatment the IMRT technique has higher dose values than the 3DCRT technique (Figure 81 F).

Although there is a trend pinpointing that IMRT yields higher organ dose values than 3DCRT, for all out-of-field organs except the eyes the differences between the dose's values obtained by both techniques are statistically compatible considering the associated uncertainty.

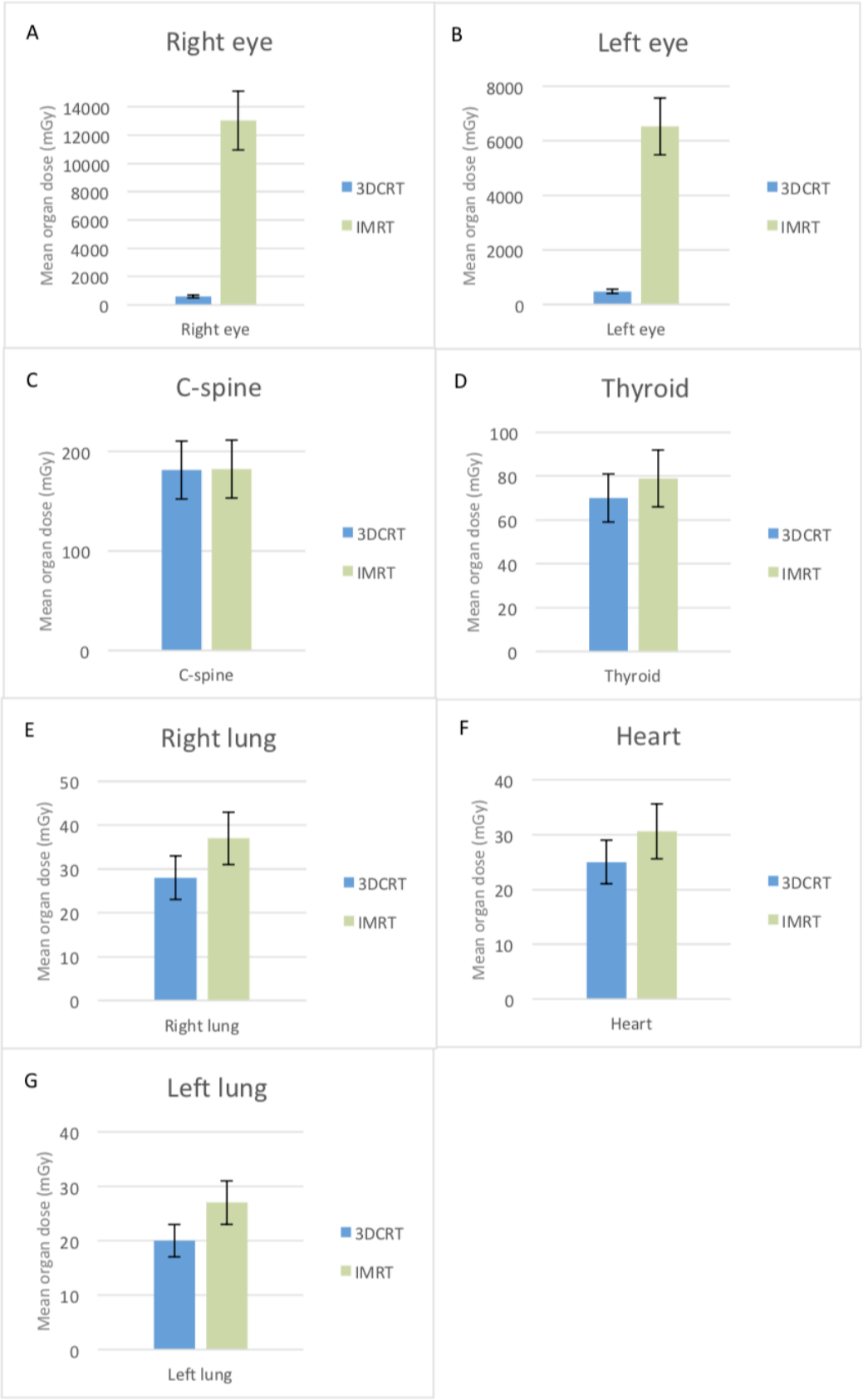


**Figure 81 –** Out-of-field mean organ doses measured by TLDs for the 3DCRT and IMRT techniques.

### 7.3.3. Out-of-Field Doses in Paediatric Phantom Calculations With MCNP – Computational Paediatric Phantom

The MC simulations using MCNP6 and the developed, implemented and validated computational models of the LINAC and the paediatric phantom, for the 3DCRT and IMRT techniques with the radiation beams previously described, are shown in Table 15 All results have a tally statistical uncertainty of less than 10%.

**Table 15 -** Out-of-field organ doses calculated by MCNP6 for 3DCRT and IMRT techniques.

| | | **$MCNP6_{3DCRT}$** | **$MCNP6_{IMRT}$** |
|---|---|---|---|
| **Structure** | **Distance from $PTV_{center}$ to $organ_{center}$** (cm) | **$D_{organ}$** (mGy) 30 fractions | **$D_{organ}$** (mGy) 30 fractions |
| Right eye | 6.2 | 636.0 ± 9.5 | 11940.3 ± 322.4 |
| Left eye | 8.4 | 416.2 ± 7.1 | 7236.3 ± 10.1 |
| C-spine | 11.1 | 153.6 ± 3.2 | 215.9 ± 5.6 |
| Thyroid | 13.1 | 59.5 ± 1.4 | 89.5 ± 3.8 |
| Right Lung | 21.7 | 32.4 ± 1.7 | 42.5 ± 2.1 |
| Heart | 22.2 | 30.4 ± 0.8 | 34.9 ± 1.0 |
| Left lung | 23.3 | 22.7 ± 1.3 | 31.1 ± 1.2 |

Through the analysis of Table 15, it can be seen that dose calculations with MCNP6 show that the mean dose in organs outside the treatment fields is always higher for the IMRT technique when compared to the 3DCRT technique.

Figure 82 shows the results of the dose calculations in MCNP6 for each of the techniques for the different organs outside the treatment fields. Figure 82 A shows that MCNP6 dose calculations with IMRT yields dose values in the right eye approximately 19 times higher than those obtained for the 3DCRT technique. The dose in the left eye

with the IMRT technique is approximately 17 times higher than the ones obtained with the 3DCRT technique (Figure 82 B). In the C-spine the dose values for the 3DCRT technique are about 62 mGy lower than the calculated dose using the IMRT technique (Figure 82 C). In Figure 82 D, it can be seen that in the thyroid the 3DCRT technique results in a dose value 30 mGy lower than the calculated dose value using the IMRT technique. In the right lung the IMRT technique yields a value about 10 mGy higher compared to the calculated dose with the 3DCRT technique (Figure 82 E). Figure 82 F shows that the dose calculation in the heart for the IMRT technique presents a value about 5 mGy higher than the 3DCRT technique. Finally, in the left lung (Figure 82 G), a higher dose (about 8 mGy) is observed for the IMRT technique.

It should be noticed that for the eyes, C-spine and thyroid the difference between the obtained computational values for both techniques are not compatible with their statistical uncertainty.

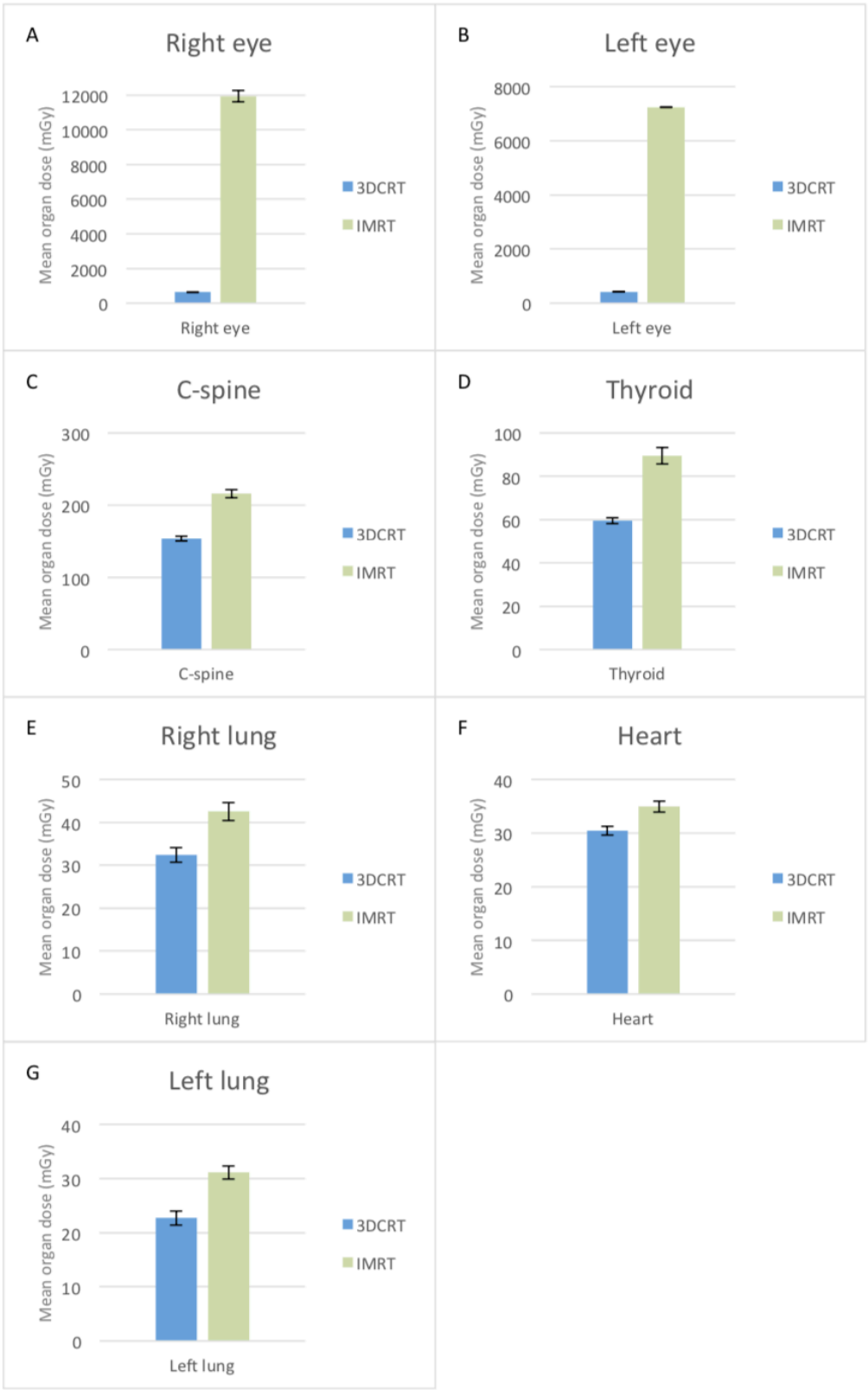


**Figure 82 –** Out-of-field organ doses calculated by MC simulations using MCNP6.

### 7.3.4. Comparison Between TLD Measurements, TPS ans MCNP Calculations

Analysing the results provided by the TPS it was possible to compare the dose distributions obtained with the 3DCRT and the IMRT techniques. Figures 83 and 84 show the dose distributions for 3DCRT (A, B and C) and IMRT (D, E and F) techniques, up to a minimum dose (selected in the TPS by the user) of 500 mGy and 10000 mGy respectively, for 30 daily fractions.

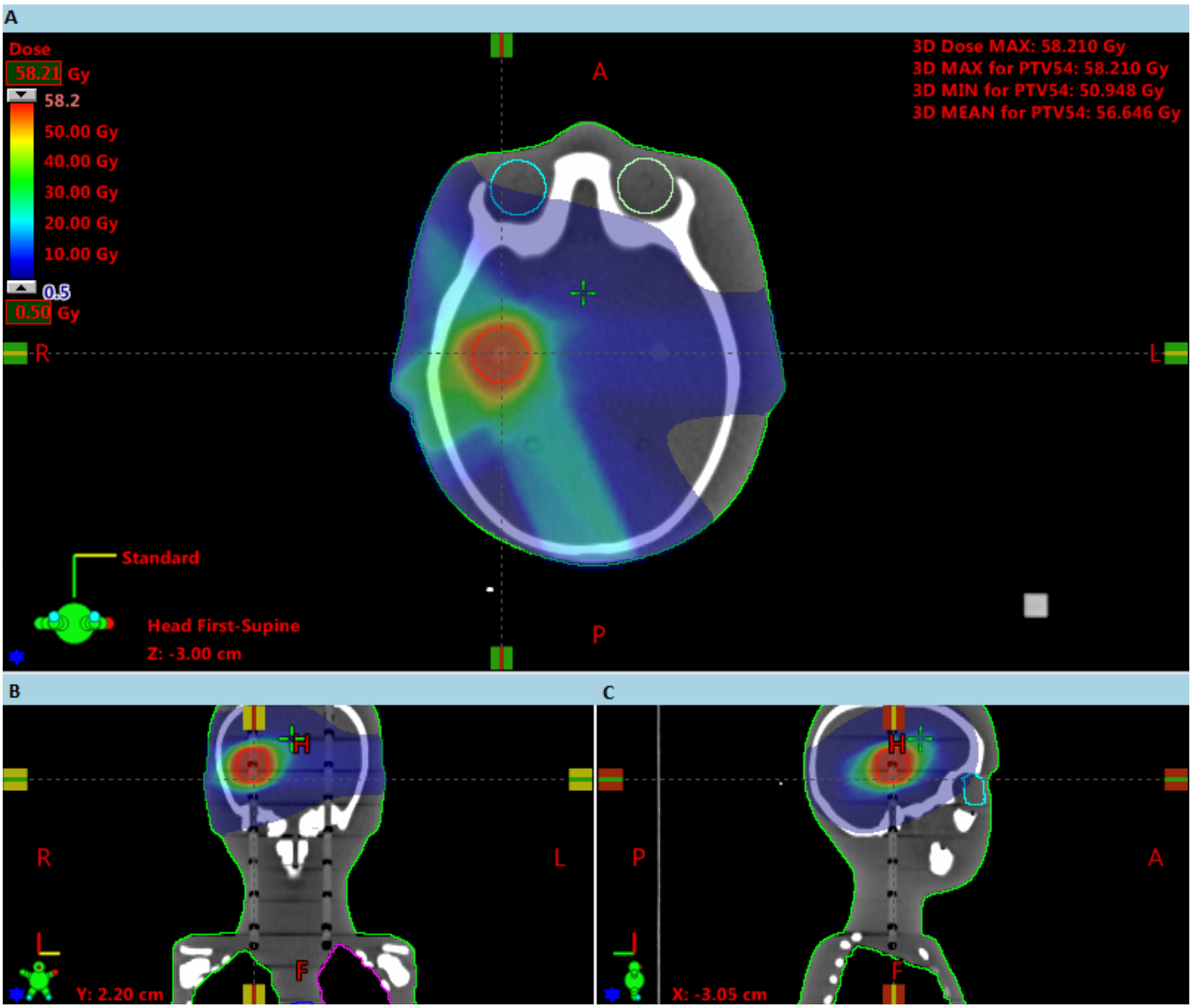

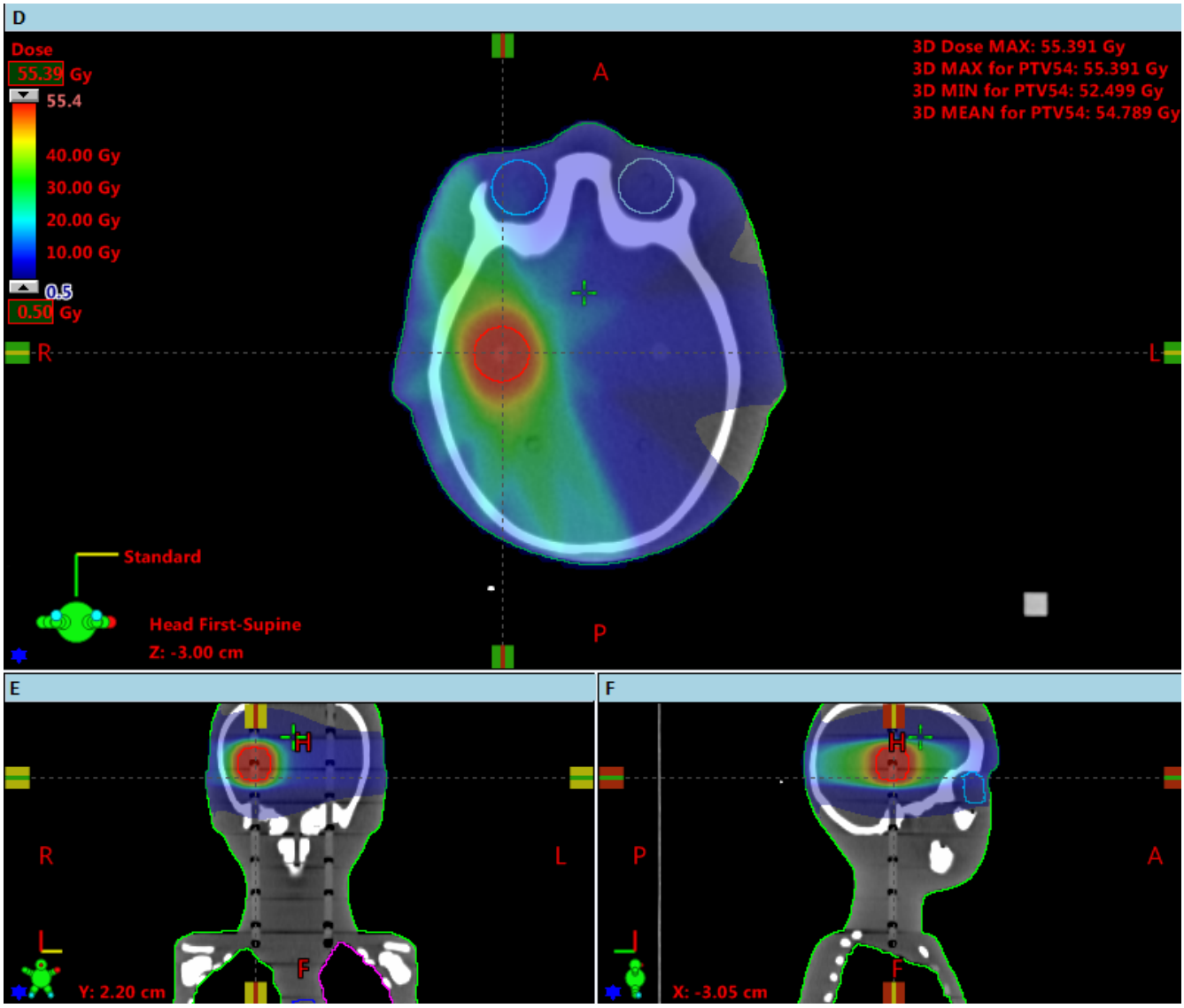


**Figure 83 –** Comparison of dose distributions between the 3DCRT and IMRT techniques up to a minimum dose of 500 mGy. A: 3DCRT axial view; B: 3DCRT coronal view; C: 3DCRT sagittal view; D: IMRT axial view; E: IMRT coronal view; F: IMRT sagital view.

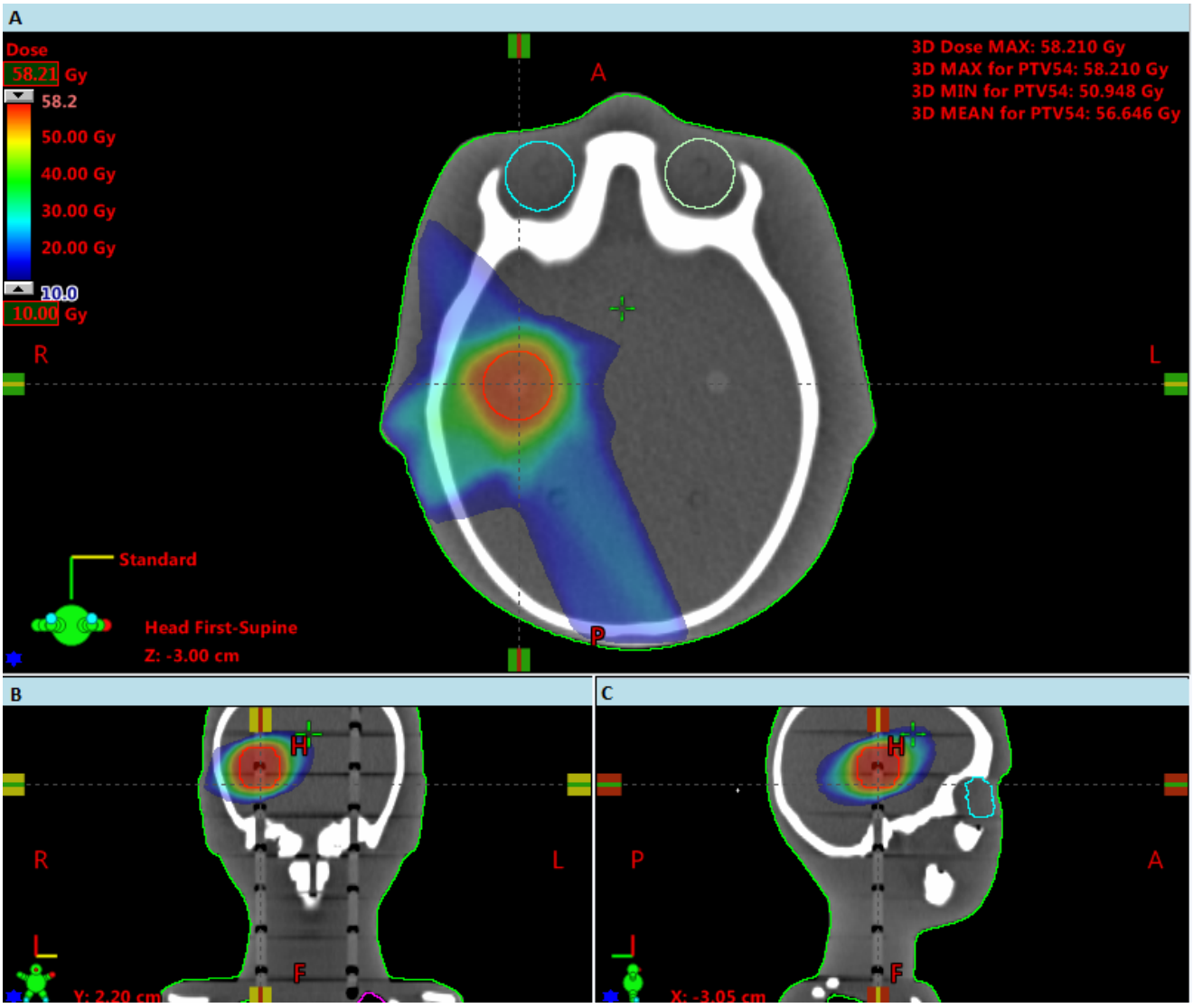
A
Dose
58.21 Gy
58.2
50.00 Gy
40.00 Gy
30.00 Gy
20.00 Gy
10.0
10.00 Gy
3D Dose MAX: 58.210 Gy
3D MAX for PTV54: 58.210 Gy
3D MIN for PTV54: 50.948 Gy
3D MEAN for PTV54: 56.646 Gy
A
R
L
P
Standard
Head First-Supine
Z: -3.00 cm
B
H
R
L
F
Y: 2.20 cm
C
H
P
A
F
X: -3.05 cm

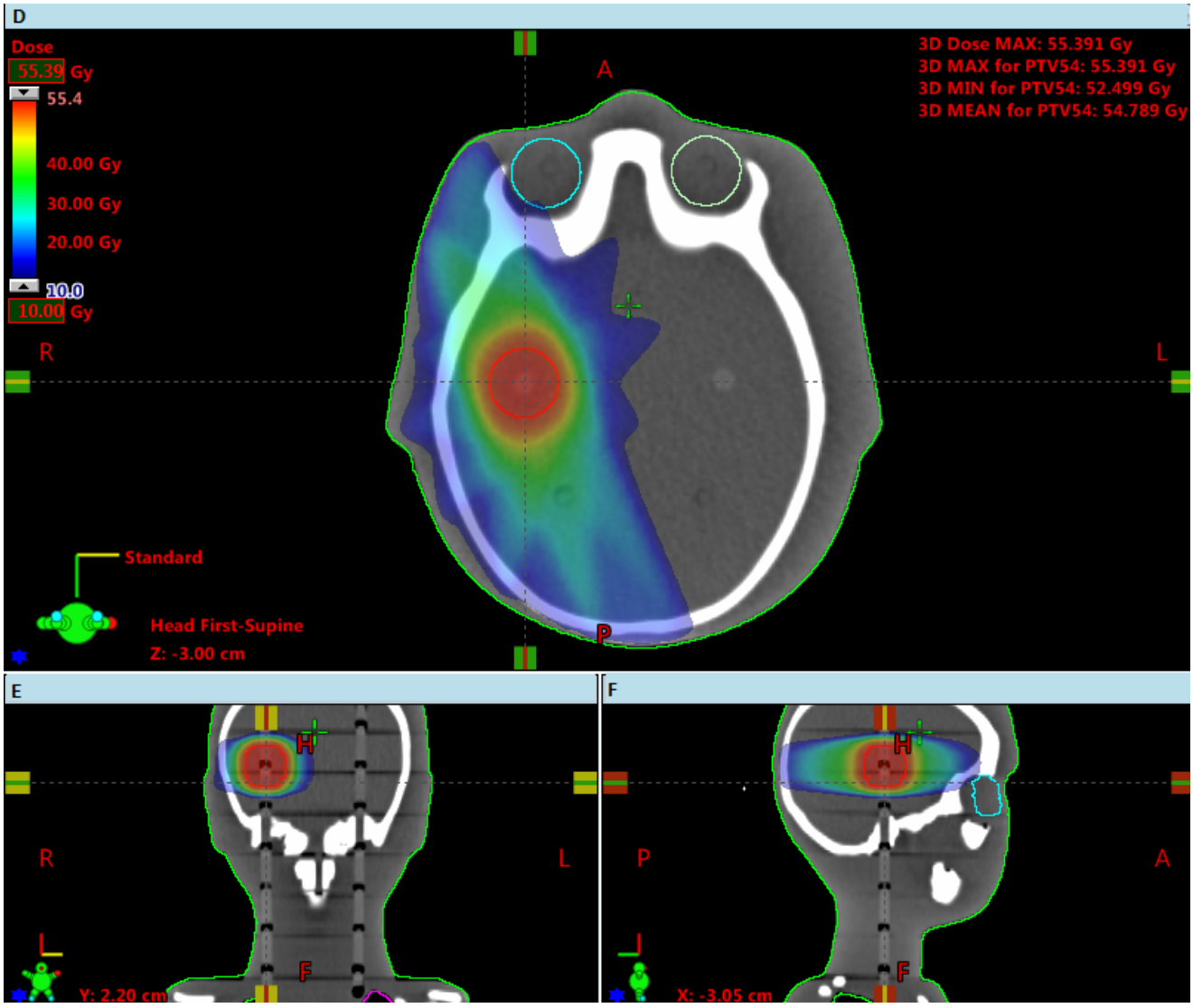


**Figure 84 –** Comparison of dose distributions between 3DCRT and IMRT techniques up to a minimum dose of 10000 mGy. A: 3DCRT axial view; B: 3DCRT coronal view; C: 3DCRT sagittal view; D: IMRT axial view; E: IMRT coronal view; F: IMRT sagital view.

In Figures 83 and 84, it is observed that the IMRT technique (D, E and F) yields a “bath” of lower doses when compared to the 3DCRT technique (A, B and C). Figure 83 show that the 500 mGy isodose curve in the IMRT technique includes both eyes. Similarly, with the IMRT technique, the isodose curves between 20000 and 40000 mGy

include more brain tissue than the 3DCRT technique. In Figure 84 it is evident that the IMRT technique covers more brain area for the isodose curves between 10000 and 40000 mGy.

In order to compare the results, Figure 85, 86, 87 and 88 shows the out-of-field doses in different OAR, obtained by the TPS calculations, the TLD measurements and the MCNP6 simulations, for the 3DCRT and IMRT techniques.

The comparison between the dose calculations with the TPS and the doses measured with TLDs shows that the out-of-field dose values are always higher for the TLDs (Figure 85 and 87). On the other hand, the doses outside the treatment fields are significantly higher with IMRT than with 3DCRT (Figure 85 and 87). From Figures 85 and 87, it can be seen that as the distance from the out-of-field organs to the centre of PTV increases, the relative difference between the dose calculation using the TPS and the dose measured by the TLDs also increases.

When comparing the MCNP dose calculations with the TLD dose measurements (Figures 86 and 88), a better agreement (meaning, lower differences) between the out-of-field doses obtained by the two methods can be observed. For both TLD measurements and MCNP6 calculations, there is significant increase in dose using the IMRT technique when compared to the 3DCRT technique, as can be observed in Figures 86 and 88).

Figure 85 compares the out-of-field doses with the TPS calculations and the measured doses with the TLDs for the 3DCRT technique and it is found that the TPS has lower values in all organs. The dose values with the TLDs are about 1.5, 1.7, 1.8, 1.6, 14, 13 and 6.7 times higher for the right eye, left eye, C-spine, thyroid, right lung, heart and left lung, respectively.

The doses outside the treatment fields calculated with the TPS and the doses measured with the TLDs for the IMRT technique are shown in Figure 86. It is observed that TPS yields lower dose values in all organs. The doses measured with the TLDs are about 3.7, 3.0, 2.0, 2.1, 18.5, 15.5 and 9.0 times higher for the right eye, left eye, C-spine, thyroid, right lung, heart and left lung, respectively.

Figure 87 compares the doses outside the calculated treatment fields with the MCNP6 and the measured doses with the TLDs for the 3DCRT technique. The dose values calculated with MCNP6 are about 1.1, 1.1, 1.2 and 1.2 times higher for the right eye, right lung, heart and left lung, respectively. The doses measured with the TLDs are about 1.1, 1.2 and 1.2 times for the left eye, C-spine and thyroid, respectively.

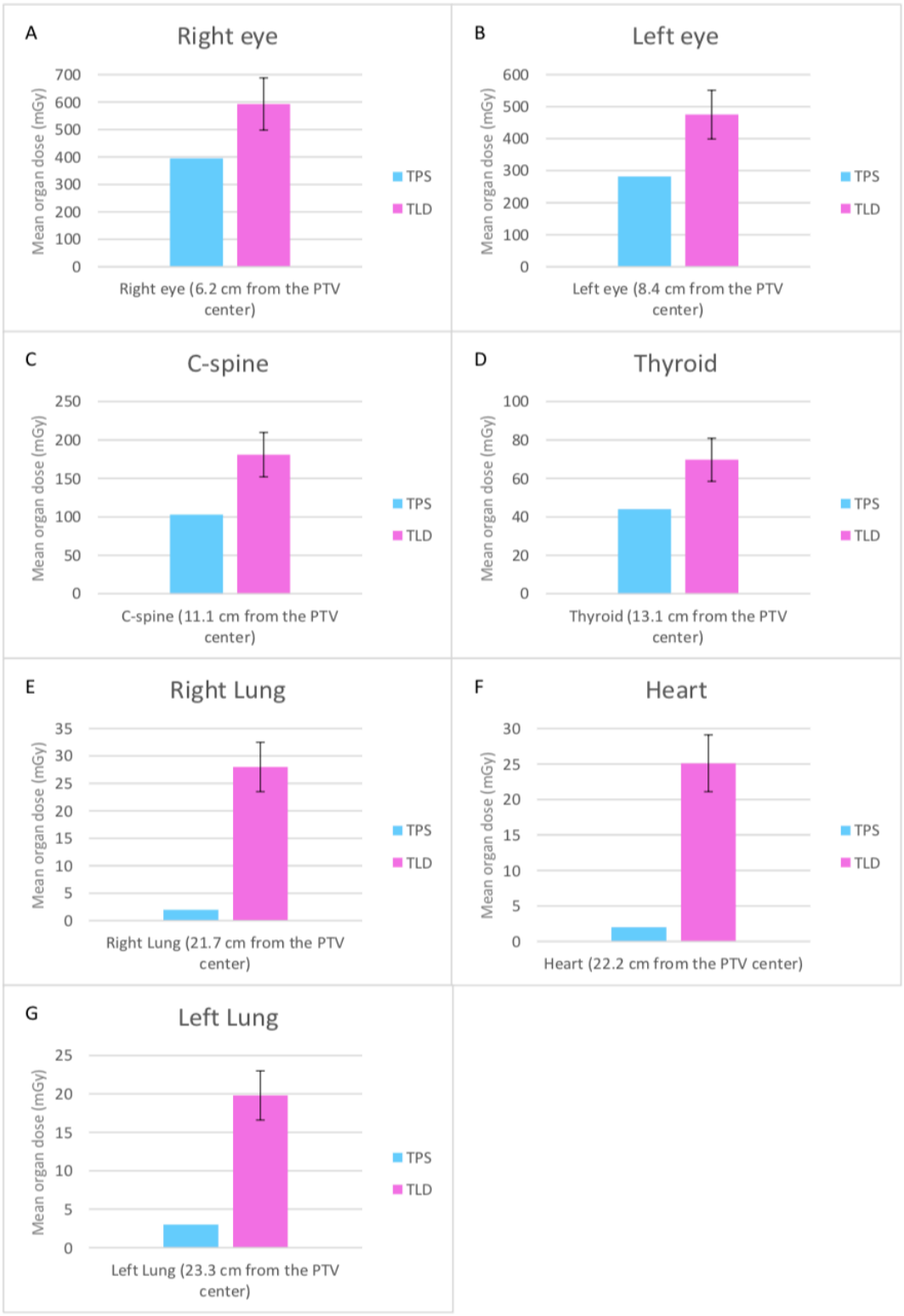


**Figure 85 –** Comparison between doses outside the treatment fields obtained by TPS vs TLD for 3DCRT.

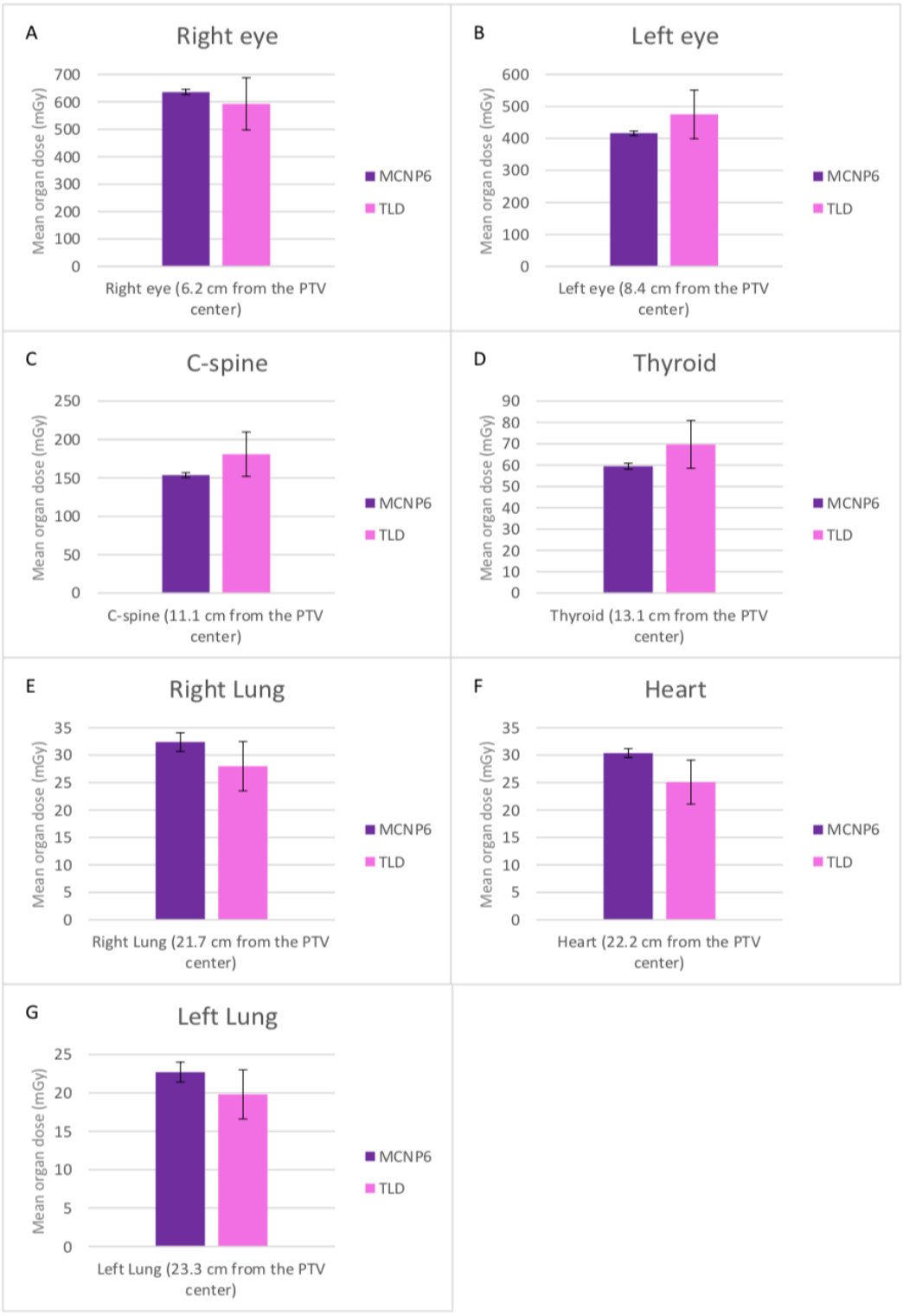


**Figure 86 –** Comparison between doses outside the treatment fields obtained by MCNP6 vs TLD for 3DCRT.

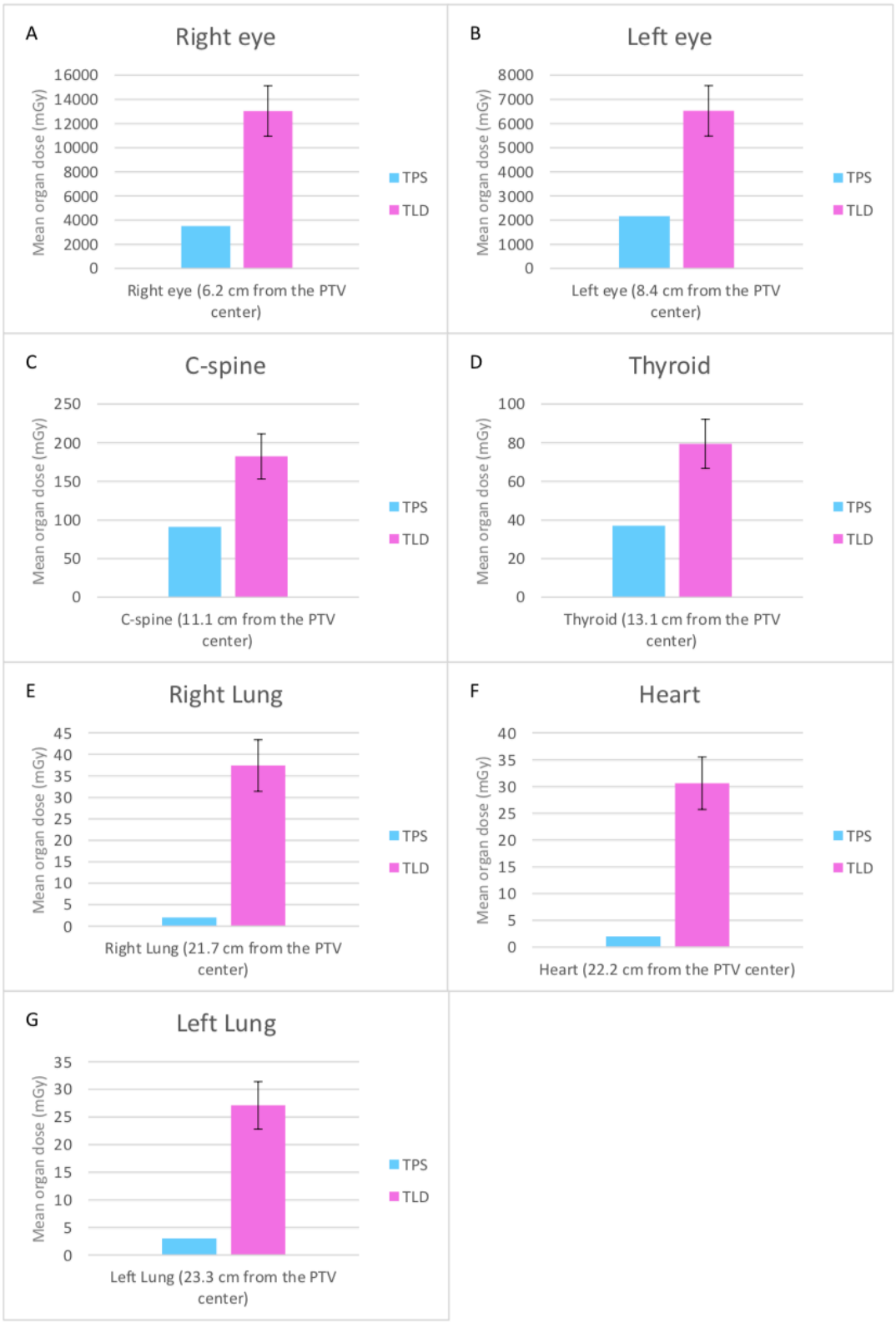


**Figure 87 –** Comparison between doses outside the treatment fields obtained by TPS vs TLD for IMRT.

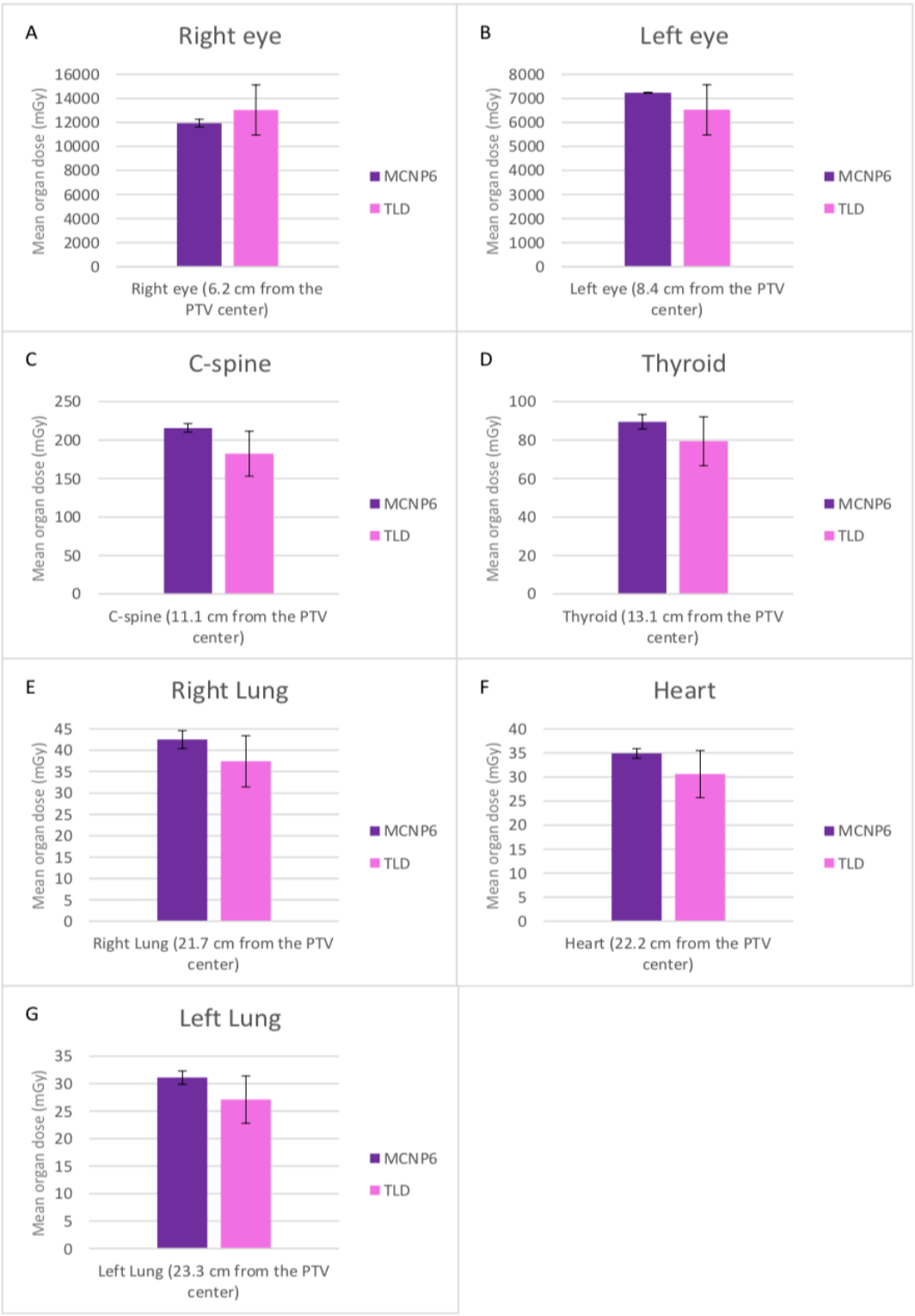


**Figure 88 –** Comparison between doses outside the treatment fields obtained by MCNP6 vs TLD for IMRT.

Figure 88 compares the out-of-field doses with calculations in MCNP6 and measured doses with TLDs for the IMRT technique. It is observed that doses are about 1.1, 1.2, 1.1, 1.2, 1.1 and 1.1 higher with MCNP6 calculations for left eye, C-spine, thyroid, right lung, heart and left lung, respectively. For the right eye, a higher dose was found with the TLDs in about 1.1 times.

In short, for the 3DCRT technique, the dose differences between TLD measurements and MCNP6 calculations are lower than the dose differences between TLD measurements and TPS calculated dose values. For the IMRT technique, the dose differences between TLD measurements and MCNP6 calculations are also lower than the dose differences between TLD measurements and TPS calculated values.

The organs closest to the PTV (up to ~ 13 cm), such as thyroid, c-spine and eyes show a TLD and MCNP6 lower relative difference, when compared with TLD and TPS dose differences. These dose differences are generally accentuated when the organs are further (up to 23.3) from the centre of PTV, such as lungs and heart.

## 7.4. DISCUSSION

This work reported in this thesis was undertaken in clinical environment, in the Radiotherapy Service of a major oncology Hospital in Portugal - IPOLFG. As abundantly documented in the literature dose measurements in clinical settings provide more realistic and insightful information about organ doses [230] in radiotherapy treatments. Additionally, they allow the benchmarking and validation of MC simulated and TPS calculated doses.

This study provides a better understanding of the out-of-field organ doses in paediatric patients that are scarse in the literature. Additionally, this study combines in a unique way MC simulations, TLD measurements and TPS calculations, using a paediatric computational phantom voxelized from the original anthropomorphic phantom CT images and a developed model of the LINAC including the MLC when IMRT is considered. Although in radiotherapy planning, doses outside the treatment fields in the order of cGy or higher can be neglected, for radiological protection and safety purposes these doses cannot be ignored [43], because they can cause radiation-induced tumours in healthy organs and tissues.

### 7.4.1. UNCERTAINTIES OF TLDS MEASUREMENTS, TPS AND MCNP6 CALCULATIONS

The final uncertainty of the TLDs measurements was 15.8% (k=1), as mentioned above, calculated from the detector efficiency, stability of the quality control correction factor, reader calibration factor and energy dependence. Another factor that could contribute to the uncertainty of the TLD measurements is the existence of minor deviations in TLD placement during the measurements.

Regarding the model validation measurements the uncertainty of the ionization chamber can be taken into account (2-2.5%) [231].

Besides the statistical uncertainty reported in this work (< 10%), the results obtained using MCNP6 could be influenced by other systematic sources of uncertainty:

1. Uncertainty of transport algorithms and materials cross-sections libraries used in MCNP6;
2. Uncertainty of the MCNP6 due to the application of the energy cut-off to electrons and photons;
3. Uncertainty of the LINAC model used in this work (e.g. accurate modulation of the LINAC components, uncertainty of the electron spectrum);
4. Uncertainty related to the creation of the computational phantom (e.g. uncertainty from the segmentation of the volumes present in the CT images of the physical phantom and uncertainty in the conversion of CT data to density and material composition).

There are several uncertainties related to TPS [232]:

1. Uncertainty of dose calculation limitations (e.g. accuracy varies according to circumstances, calculation grid dimensions and point kernels size affect accuracy, deviations tend to be systematic, algorithms provide a approximate solution to the problem);
2. Uncertainty of beam parameters and target volumes (e.g. intra- and inter observer variability in volumes segmentation);
3. Uncertainty of individual patient data (e.g. different imaging modalities of the same patient, intra- and inter fraction organ motion, set-up reproducibility);
4. Uncertainty of data transfer (e.g. from CT images to TPS, from TPS to LINAC);

5. Uncertainty of plan evaluation limitations (e.g. DVH accuracy is affected by the location and number of points used for DVH calculation, DVH is influenced by the accuracy of the doses and/or volumes);
6. Uncertainty of input and output devices (e.g. CT density assumptions, image resolution);
7. Uncertainty of essential beam data (e.g. detector reproducibility, resolution and sensitivity).

All dose calculations performed by Varian Medical Systems' TPS Eclipse AAA algorithm have an uncertainty of less than 5% [133,233].

### 7.4.2. TPS DOSE CALCULATIONS

For the 3DCRT treatment plan, the obtained results indicate that PTV was covered by the isodose curve of 95% of the prescribed dose, with no hot or cold spots, $D_{min}$ equals 50.95 Gy (94.4% of the prescribed dose) and a $D_{max}$ value of 58.21 Gy (107.8% of the prescribed dose). According to the ICRU 62 report the minimum dose should be at least 95% of the prescribed dose and the maximum dose about 107% of the prescribed dose [99]. Despite the slight differences, the radiation oncologist approved the treatment plan.

For the IMRT treatment plan, the results showed a CI of 1.35. According to Freuvret *et al*., a CI equal to one indicates that the dose distribution obtained corresponds to the ideal dose conformation to the tumour volume. As this value is very difficult to obtain, it is well known that when the value is greater than one the irradiated volume is greater than PTV and includes healthy tissues [224]. On the other hand, if the value of the CI is between one and two, treatment is considered to be as planned [224], as corroborated by this study (CI = 1.35).

Regarding the value of the HI, it should be zero so that the dose distribution is almost homogeneous [40]. In this thesis, an HI value of 0.027 was obtained and therefore the dose distribution can be considered homogeneous throughout the tumour volume.

The available literature pinpoints that commercial TPS are not adequate for accurately assessing and characterizing the dose in out-of-field regions, where the dose is less than 5% of the total prescribed dose [16,48,50,234,235]. The findings reported in this thesis agree with previous studies, in which the TPS systematically underestimates

doses outside the treatment fields, when compared with TLD measurements and MC calculations. Both this study and the findings of Beierholm *et al.* demonstrated that the TPS always calculates lower doses than both TLD measurements and MC simulations [236].

Huang *et al*. were the first to evaluate the accuracy of the dose calculation outside the treatment fields using the Pinnacle$^3$ TPS for the IMRT technique [16]. They calculated the dose distributions using the superposition convolution collapsed algorithm implemented in the Pinnacle$^3$ system and found that the calculation significantly underestimated the out-of-field doses for the evaluated step-and-shoot IMRT plans by an average of 50% [16]. According to the authors there is no information available in the literature that evaluates the effectiveness of any commercial TPS regarding the out-of-field dose for dynamic IMRT and Volumetric Modulated Arc Therapy (VMAT) techniques in real cases, although the results are expected to be similar to step-and-shoot IMRT administration [16]. The results reported in this thesis indicate that out-of-field doses with dynamic IMRT and the TPS underestimate the actual dose administered. However, we should consider that (i) the dynamic IMRT treatment used is different (ii) the different TPS and (iii) the different calculation algorithm. On the other hand, Howell *et al*. quantified the accuracy of out-of-field dose calculations with the AAA algorithm for a simple field and found that the TPS underestimated out-of-field doses (average value of 40%) and as the distance to the field boundary increases the underestimation of the dose by the TPS also increases (up to 55%) by 11.25 cm [235]. Shine *et al*. identified in their study an average underestimation of TPS doses by about 45% to a maximum of 20 cm from the off-axis distance, compared to calculations performed in a PENELOPE-based MC program for a LINAC Varian TrueBeam, also with the same Eclipse TPS [237]. In a study undertaken by Wang *et al*. the authors verified that for all the energies studied (6, 10 and 15 MV) the TPS Eclipse consistently underestimated the out-of-field doses by 30 to 50% compared with MC methods [238]. In the results reported in this thesis, it was observed an underestimation of the out-of-field doses calculated by TPS, within a maximum of 23.3 cm from PTV to the center of the out-of-field organs.

The results of this thesis show that the mean dose calculated by the TPS in the organs more distant from PTV (lungs and heart) is approximately the same for both techniques. In out-of-field organs closest to the PTV center, such as the eyes, the dose calculated by TPS shows higher values for the IMRT technique. This may be related to the lack of accuracy of the TPS calculation in organs outside and farther away from the

treatment fields. This is probably due to the simplification of the AAA algorithm, which makes it faster and feasible in routine radiotherapy treatments.

The in findings reported in this thesis were obtained used the AAA as a dose calculation algorithm for out-of-field doses. However, MC based algorithms and Acuros XB are commercially available and lead to more accurate results in out-of-field doses calculation. Commercial algorithms based on MC methods are more accurate in assessing the out-of-field doses, followed in accuracy by the Acuros XB and AAA [239]. Other study reports that Acuros XB predicts higher out-of-field doses when compared to AAA [240]. Both, AAA and Acuros XB underestimated the dose outside the treatment fields [241], however, the Acuros XB showed lower average errors when compared to the measurements [241].

### 7.4.3. TLD MEASUREMENTS

According to AAPM Task Group 158, any MC model that assesses the dose outside the treatment fields should be validated against out-of-field measurements [198]. TLDs can be used to evaluate the out-of-field doses in radiotherapy [242,243].

Roger Harrison [244] points out that the out-of-field doses vary in a wide range, between 10 mGy to 60 Gy. This study reports out-of-field doses from 19.8 mGy to 593 mGy for TLD measurements for 3DCRT and from 27 mGy to 13041 mGy for IMRT. This result should be taken into account as it relates to paediatric doses and to a maximum distance from the PTV of 23.3 cm. The out-of-field measurements reported in this thesis were performed using a physical anthropomorphic paediatric phantom using TLDs and have a relative uncertainty of approximately 16% (k=1).

In both radiation therapy techniques evaluated, the doses measured by the TLDs decrease as the distance between the PTV and the organ outside the treatment field's increases.

### 7.4.4. COMPARISON BETWEEN TLD MEASUREMENTS, TPS AND MC CALCULATIONS

Some studies available in the literature performed measurements of out-of-field doses and compared them with doses calculated by TPS. Other researchers also used MC calculations to evaluate the out-of-field doses provided by the TPS software [43,48]. The findings of these studies vary and depend on the treatment modality and on the anatomical location of the target volumes [48]. Joosten *et al.* found that in the first 10

cm outside the treatment fields, the MC dose calculations are more accurate than those the dose calculations of commercial TPS [50]. This study shows that up to about 23 cm from the center of the target volume the MC-based dose calculations produce more accurate results than the doses calculated by commercially available TPS. The highest differences between phantom measurements and dose calculations were 20% for MC calculations and 179% for TPS calculations [50]. In the results reported in this thesis there is a large discrepancy between the dose calculation with the TPS and the dose measurement with the TLD. On the other hand, there are small discrepancies between dose calculation with MCNP6 and dose measurement with the TLDs. Additionally, it is observed that the discrepancies are greater for out-of-field organs more distant from the PTV center. Peripheral dose variability tends to increase as a function of the distance from the central axis of the beam, with the decrease in field dimensions and with the number of collimators considered [50].

A study by Majer *et al.* [230] measured organ doses outside the treatment fields using the same phantom with a 3DCRT and IMRT techniques and compared with TPS calculated doses, but in opposition to this study, Majer *et al.* did not evaluated organ doses for lungs and heart.

Contrary to the results reported in this thesis, the results of Majer et al. show higher doses in C-spine and thyroid for the 3DCRT technique when compared to the IMRT technique, both for measurements with TLDs and for dose calculations with TPS [230]. In general, for 2 Gy per fraction, out-of-field doses are higher in Majer *et al.* study for all organs except the right eye, where the dose was measured with TLD for the IMRT technique.

The differences between the results obtained by Majer *et al.* and the results of this thesis can be explained by: (1) different PTV size and location considered; (2) different planning dose protocols used; (3) different versions of the same TPS, which translates into different calculation algorithms; (4) The uncertainty of this study TLD measurements was approximately 16%; (5) Majer *et al*. calculated doses independently for each TLD localization, while in this study the average dose for all TLD localizations in each considered organ was calculated, which can introduce considerable errors.

Another study [236] assessed the thyroid as an organ outside the treatment fields in a paediatric phantom and reported a value of 103.4 mGy for a PTV smaller than 2 cm with VMAT and our results indicate 69.7 mGy received by the thyroid for a whole

treatment with 3DCRT and 79 mGy for IMRT. The difference between the values can be explained by the use of different irradiation techniques and LINACs. The study reported in this thesis assesses the out-of-field doses for 3DCRT and IMRT techniques and according to the literature, the doses outside of the treatment field are higher using IMRT [21,44]. In this thesis, the doses obtained outside the treatment fields for 3DCRT ranged from 20 to 590 mGy and for IMRT from 27 to 13040 mGy.

Out-of-field doses are of concern because according to Paganetti about 50% of all second tumours seem to develop with doses delivered in tissues below 2500 mGy [15] and the results of this thesis show that the IMRT technique for the right eye yields doses about 13040 mGy and for the left eye about 6525 mGy. These results may raise some concerns as the dose tolerance tables for OAR only mention that the eyes should have a Dmax below 45-50 Gy [222,223].

## 7.5. CONCLUSIONS

The TPS are not commissioned to evaluate dose outside the treatment fields and we verified an underestimation of the out-of-field doses, which tends to increase as the distance from the field edge increases. The organs closest to the PTV show relative differences lower than the organs far away from the PTV. In organs closest to PTV such as the eyes, the TPS calculated the dose with the IMRT technique in an order of magnitude higher than the 3DCRT technique.

In the 3DCRT technique, in the measurements performed with TLD, doses of about 20 mGy are observed in organs such as the lungs with a distance of 23 cm from PTV to doses of 395 mGy in the eyes at a distance of 6 cm from PTV. In the IMRT technique, measurements with TLDs show doses of about 27 mGy in the lungs up to doses of 13041 mGy in the eyes.

In an unparalleled way, this study provides, TLD measurements, TPS and MC calculations of a manually voxelized paediatric computational phantom. Prospectively, this model could be used to build a database of out-of-field doses for adults and children. Thus, it will be possible to identify the dosimetric characteristics of treatment plans that may lead to higher doses outside the treatment fields, allowing a significant improvement in radiotherapy treatment planning.

# SECTION IV – CONCLUSIONS

## CHAPTER 8 – CONCLUSIONS AND FUTURE WORK

In this thesis, the doses in organs and tissues outside the treatment fields for paediatric patients submitted to radiotherapy were evaluated, comparing the 3DCRT and IMRT techniques.

To achieve this objective the out-of-field doses in paediatric patients were investigated, performing:

- Dose measurements in a paediatric physical phantom usingTLDs,
- Dose calculations in a Treatment Planning System, and
- Modelling and simulations in Monte Carlo, using the state-of-art computer program MCNP6 and an anthropomorphic computational phantom representative of a pediatric patient.

This was performed in order to achieve a detailed and accurate evaluation, as well as a characterization, of the 3DCRT and IMRT techniques used in clinical practice in the radiotherapy department of IPOLFG.

In order to achieve these goals, detailed modeling and simulations, of the Varian Clinac 2100 CD combined with the Millenium™ 120-leaf MLC in MCNP6 were undertaken for the first time. All this paved the way to evaluate the dose outside the fields of treatment for paediatric patients, enabling comparison between 3DCRT and IMRT techniques.

Throughout the thesis, several innovative scientific and technical results were obtained, of potential interest to the medical and radiological protection communities and experts and some of them with high societal impact.

The findings of this study, undertaken in the framework of a Doctoral thesis work, may be used to support, but do not intend to replace, the clinical decisions about the type of treatment to be described, that always rest with medical doctors and the medical team.

## 8.1. SUMMARY AND CONCLUSIONS

### 8.1.1. OUT-OF-FIELD AND IN-FIELD VALIDATION OF THE COMPUTATIONAL MODEL OF THE LINAC HEAD FOR A 6 MV PHOTON BEAM

In a first step, several dosimetric measurements were performed inside and outside the treatment fields of a Varian Clinac 2100 CD in the radiotherapy department of IPOLFG. These measurements were performed with a 6 MV photon beam, using a water phantom and ionization chambers.

Besides, a detailed computational model of the LINAC head was developed and implemented using the state-of-the-art Monte Carlo program MCNP6, mimicking the LINAC head used in the measurements. This model, implemented and validated for the first time using MCNP6, includes more components than to the majority of other medical Linac computational models found in the literature, such as the electron accelerator tube and the bending magnet. This allowed to obtain a more detailed and accurate model of the LINAC head.

Afterwards, the water phantom and the ionization chambers used in the measurement were also implemented in the developed computational model.

The 6 MV beam was modelled and validated through adjustments in parameters such as FWHM and primary electron energy, comparing measurements and MCNP6 simulation results. As a result, the obtained values for the FWMH and electron energy were1.2 mm and 6.2 MeV, respectively.

A computational model of the Millenium™ 120-leaf MLC was also created and successfully validated, comparing:

i. the measured and calculated values (using MCNP6) of the transmission,
ii. the measured and calculated (using MCNP6) values of the DLS for different gap sizes.

The validation of the innovative Varian Clinac 2100 CD computational model coupled with the Millenium™ 120-leaf MLC operating at 6 MV photon beam was successfully

achieved with mean relative differences between measurements and MC simulations smaller than 3%.

### 8.1.2. PAEDIATRIC COMPUTATIONAL VOXEL PHANTOM

A paediatric computational phantom was developed from original CT images of a 5-year-old anthropomorphic ATOM phantom™ from CIRS. Initially, a CT scan was performed on the physical phantom and the 397 acquired images were imported into the imageJ software™. Of these images, only 180 were selected because they encompassed the area of interest, i.e., from the brain to the end of the lungs, in order to obtain a reduction in the calculation time udring the Monte Carlo simulations. These images were processed and each volume of interest was segmented individually. ImageJ's manual, automatic and semi-automatic segmentation tools were used to segment the following volumes: whole body, skin, lungs, bones, heart, spinal canal, c-spine, brain, PTV, eyes, thyroid and soft tissues. After individualized segmentation of all volumes of interest was achived, the volumes were combined, creating the voxelized paediatric phantom. With the aid of ImageJ's voxel phantom tool, the previously created paediatric voxel phantom input file for MCNP6 was created. The paediatric voxel phantom consists of 47.185.920 voxels, each with dimensions x=0.09766 cm, y=0.09766 cm and z=0.3 cm.

Furthermore, the aforemention anthropomorphic physical phantom was used to perform TLD measurements and the corresponding anthropomorphic computational voxel phantom was used in the TPS and Monte Carlo calculations, providing an unique detailed and accurate methodology and framework to evaluate the consistency of the out-of-field organ doses assessed in this work.

### 8.1.3. OUT-OF-FIELD DOSES ASSESSMENT

The computational models of the paediatric voxelized phantom and the Varian Clinac 2100 CD were combined in an unprecedented way with the Millenium 120-leaf MLC to calculate using MCNP6 the doses outside the treatment fields for the 3DCRT and IMRT techniques.

Using Varian Medical Systems' TPS Eclipse, two treatment plans were created, one with the 3DCRT technique and another with the IMRT technique. Both treatment plans were clinically validated and it was found that the doses in organs outside the treatment

fields closest to PTV, such as the right eye, would range from $D_{min}$ = 538 mGy to $D_{max}$ = 10706 mGy ($D_{mean}$ = 3512 mGy) with the IMRT technique compared to $D_{min}$ = 247 mGy, to $D_{max}$ = 695 mGy ($D_{mean}$ = 395 mGy) with the 3DCRT technique. From distances greater than 10 cm from the center of the PTV, 3DCRT technique shows higher dose values, probably due to the lack of accuracy of the TPS in the out-of-field dose calculations.

The doses outside the treatment fields were also measured using the TLDs placed in the paediatric physical phantom using the Varian Clinac 2100 CD in the radiotherapy department of IPOLFG. The out-of-field doses for both techniques were calculated for the first time, using MCNP6 and the paediatric computational voxel phantom combined with the Varian Clinac 2100 CD model. As with TLD measurements, the doses calculated with MCNP6 yielded higher doses for the IMRT technique.

The obtained results seem to indicate that out-of-field doses are significantly higher with IMRT, compared to 3DCRT. The dose measured by TLD for the different treatment techniques for the right eye were 593 mGy for 3DCRT and 13040.6 mGy for IMRT. The dose values for the c-spine presents were 180.9 mGy with 3DCRT and 182.3 with IMRT. Thyroid dose values of 69.7 mGy with 3DCRT and 79.4 mGy with IMRT were obtained. For the right lung the measured values were 28 mGy for 3DCRT and 37.4 mGy for IMRT.

Besides, the obtained results indicate that out-of-field doses may be severely underestimated by the TPS and that out-of-field organs and tissue doses assessed in this work are of concern as they may presumably increase the risk of development of second tumours [21]. It must be emphasize however that the decision on the type of radiotherapy treatment and modality should always be taken by the radiation oncologists, considering all the clinically relevant information about the patient.

### 8.2. FUTURE WORK

As future work it is considered necessary to carry out more computational dosimetric studies in order to expand the evaluation of doses outside the treatment fields to children of other ages or even adults, for example, validate de MC model up to a distance of 1 m. CT images and other types of images such as MRI of real patients will

also be considered, with the objective of producing more detailed computational phantoms.

It is suggested the development of computational models of proton therapy equipment, typically used in clinical situations of paediatric oncology or re-irradiation of patients. This dosimetric research is justified since this type of treatment is available today in several countries in the world and with the use of high energy there is a greater probability of neutron production. This leads to the need to accurately determine the doses given outside the treatment fields in order to increase the quality of life of the patient after the treatment, decreasing the side effects.

Paediatric patients are the types of patients most at risk of developing cancer after exposure to ionizing radiation due to their rapid cellular development and high life expectancy. Therefore, it is of utmost importance that a dosimetric evaluation similar to this thesis be performed for proton treatments.

The use of individualized computational phantoms may be an improvement in the evaluation of out-of-field doses and may be appropriate for prospective dosimetric evaluations, necessary for radiological protection of patients undergoing radiotherapy. Therefore, nowadays, there is a draft report of paediatric reference computational phantoms from ICRP of a 10 computational phantoms that could be used in future studies.

Furthermore, the methodology followed in this work, namely the MC simulations, combined with the Varian Clinac 2100 CD and paediatric phantom computational models, will allow the development of applications and tools that may benefit from individualized information, such as individualized dose assessment methodologies, retrospective dosimetric calculations for epidemiological studies and radiological risk estimation models to estimate the development of secondary cancers.

# REFERENCES


[1] Shahmohammadi Beni M, Ng CYP, Krstic D, Nikezic D, Yu KN. Conversion coefficients for determination of dispersed photon dose during radiotherapy: NRUrad input code for MCNP. PLoS One 2017;12:e0174836. doi:10.1371/journal.pone.0174836.

[2] Halperin E, Wazer D, Perez C, Brady L. Principles and Practice of Radiation Oncology. Six Editio. Philadelphia: Lippincott Williams & Wilkins; 2013.

[3] Holmes JA, Chera BS, Brenner DJ, Shuryak I, Wilson AK, Lehman-Davis M, et al. Estimating the excess lifetime risk of radiation induced secondary malignancy (SMN) in pediatric patients treated with craniospinal irradiation (CSI): Conventional radiation therapy versus helical intensity modulated radiation therapy. Pract Radiat Oncol 2017;7:35–41. doi:10.1016/j.prro.2016.07.002.

[4] Khan FM, Gibbons JP, Sperduto PW. Khan's treatment planning in radiation oncology. Wolters Kluwer; 2016.

[5] Gallagher KJ, Tannous J, Nabha R, Feghali JA, Ayoub Z, Jalbout W, et al. Supplemental computational phantoms to estimate out-of-field absorbed dose in photon radiotherapy. Phys Med Biol 2018;63:025021. doi:10.1088/1361-6560/aa9838.

[6] Vaz P. Radiation protection and dosimetry issues in the medical applications of ionizing radiation. Radiat Phys Chem 2014;104:23–30. doi:10.1016/j.radphyschem.2014.02.007.

[7] Bednarz B, Xu XG. Monte Carlo modeling of a 6 and 18 MV Varian Clinac medical accelerator for in-field and out-of-field dose calculations: development and validation. Phys Med Biol 2009;54:N43–57. doi:10.1088/0031-9155/54/4/N01.

[8] Mesbahi A, Seyednejad F, Gasemi-Jangjoo A. Estimation of organs doses and radiation-induced secondary cancer risk from scattered photons for conventional radiation therapy of nasopharynx: a Monte Carlo study. Jpn J Radiol 2010;28:398–403. doi:10.1007/s11604-010-0432-2.

[9] Steliarova-Foucher E, Fidler MM, Colombet M, Lacour B, Kaatsch P, Piñeros M, et al. Changing geographical patterns and trends in cancer incidence in children and adolescents in Europe, 1991–2010 (Automated Childhood Cancer Information System): a population-based study. Lancet Oncol 2018;19:1159–69. doi:10.1016/S1470-2045(18)30423-6.

[10] Olch AJ. Pediatric Radiotherapy: Planning and Treatment. Taylor and Francis; 2013.

[11] IAEA. RADIOTHERAPY IN CANCER CARE: FACING THE GLOBAL CHALLENGE. Vienna: International Atomic Energy Agency; 2017.

[12] International Agency for Research on Cancer WHO. Cancer Today 2020.

[13] Padovani L, André N, Constine LS, Muracciole X. Neurocognitive function after radiotherapy for paediatric brain tumours. Nat Rev Neurol 2012;8:578–88. doi:10.1038/nrneurol.2012.182.

[14] Kumar S. Second Malignant Neoplasms Following Radiotherapy. Int J Environ Res Public Health 2012;9:4744–59. doi:10.3390/ijerph9124744.

[15] Paganetti H, Athar BS, Moteabbed M, A Adams J, Schneider U, Yock TI. Assessment of radiation-induced second cancer risks in proton therapy and IMRT for organs inside the primary radiation field. Phys Med Biol 2012;57:6047–61. doi:10.1088/0031-9155/57/19/6047.

[16] Huang JY, Followill DS, Wang XA, Kry SF. Accuracy and sources of error of out-of field dose calculations by a commercial treatment planning system for intensity-modulated radiation therapy treatments. J Appl Clin Med Phys 2013;14:186–97. doi:10.1120/jacmp.v14i2.4139.

[17] Merchant TE, Kortmann R-D, editors. Pediatric Radiation Oncology. Cham: Springer International Publishing; 2018. doi:10.1007/978-3-319-43545-9.

[18] Brenner DJ, Hall EJ, Phil D. Computed Tomography — An Increasing Source of Radiation Exposure. N Engl J Med 2007;357:2277–84.

[19] Brenner D, Elliston C, Hall E, Berdon W. Estimated Risks of Radiation-Induced Fatal Cancer from Pediatric CT. Am J Roentgenol 2001;176:289–96.

[20] Andersson M, Eckerman K, Mattsson S. Lifetime attributable risk as an alternative to effective dose to describe the risk of cancer for patients in diagnostic and therapeutic nuclear medicine. Phys Med Biol 2017;62:9177–88. doi:10.1088/1361-6560/aa959c.

[21] Paganetti H. Assessment of the risk for developing a second malignancy from

scattered and secondary radiation in radiation therapy. Health Phys 2012;103:652–61. doi:10.1097/HP.0b013e318261113d.

[22] Radiation C on the BE of I. BEIR V: Health Effects of Exposure to Low Levels of Ionizing Radiation. Washington, DC: National Academy Press; 1990.

[23] UNSCEAR. Sources and Effects of Ionizing Radiation. New York: United Nations; 1988.

[24] ICRP. ICRP 60: 1990 Recommendations of the International Commission on Radiological Protection. Oxford: 1990.

[25] Armstrong GT. Long-term survivors of childhood central nervous system malignancies: the experience of the Childhood Cancer Survivor Study. Eur J Paediatr Neurol 2010;14:298–303. doi:10.1016/j.ejpn.2009.12.006.

[26] Ward ZJ, Yeh JM, Bhakta N, Frazier AL, Atun R. Estimating the total incidence of global childhood cancer: a simulation-based analysis. Lancet Oncol 2019;20:483–93. doi:10.1016/S1470-2045(18)30909-4.

[27] Schlegel W, Grosser K, Harring P, Rhein B. Beam Delivery in 3D Conformal Radiotherapy Using Multi-Leaf Collimators. In: Schlegel W, Bortfeld T, Grosu A, editors. New Technol. Radiat. Oncol., 2006, p. 257–66.

[28] Purdy JA. From New Frontiers to New Standards of Practice: Advances in Radiotherapy Planning and Delivery. In: Meyer JL, editor. IMRT, IGRT, SBRT - Adv. Treat. Plan. Deliv. Radiother., Karger; 2007, p. 18–39.

[29] Paganetti H. Applications to Secondary Radiation Dosimetry in External Beam Radiation Therapy. In: Xu XG, Eckerman KF, editors. Handb. Anat. Model. Radiat. Dosim., Taylor and Francis; 2010, p. 567–89.

[30] Webb S. Contemporary IMRT Developing Physics and Clinical Implementation. Inst Phys Publ Bristol Philadelphia 2005.

[31] Schlegel W. New Technologies in 3D Conformal Radiation Therapy: Introduction and Overview. In: Schlegel W, Bortfeld T, Grosu A-L, editors. New Technol. Radiat. Oncol., Springer; 2006, p. 1–6.

[32] Cashmore J, Ramtohul M, Ford D. Lowering whole-body radiation doses in pediatric intensity-modulated radiotherapy through the use of unflattened photon beams. Int J Radiat Oncol Biol Phys 2011;80:1220–7. doi:10.1016/j.ijrobp.2010.10.002.

[33] Ruben JD, Lancaster CM, Jones P, Smith RL. A comparison of out-of-field dose and its constituent components for intensity-modulated radiation therapy versus conformal radiation therapy: Implications for carcinogenesis. Int J Radiat Oncol Biol Phys 2011;81:1458–64. doi:10.1016/j.ijrobp.2010.08.008.

[34] White P, Chan KC, Cheng KW, Chan KY, Chau MC. Volumetric intensity-modulated arc therapy vs conventional intensity-modulated radiation therapy in nasopharyngeal carcinoma: a dosimetric study. J Radiat Res 2013;54:532–45. doi:10.1093/jrr/rrs111.

[35] Kry SF, Salehpour M, Titt U, White RA, Stovall M, Followill D. Monte Carlo study shows no significant difference in second cancer risk between 6- and 18-MV intensity-modulated radiation therapy. Radiother Oncol 2009;91:132–7. doi:10.1016/j.radonc.2008.11.020.

[36] Joosten A, Matzinger O, Jeanneret-Sozzi W, Bochud F, Moeckli R. Evaluation of

organ-specific peripheral doses after 2-dimensional, 3-dimensional and hybrid intensity modulated radiation therapy for breast cancer based on Monte Carlo and convolution/superposition algorithms: Implications for secondary cancer risk asses. Radiother Oncol 2013;106:33–41. doi:10.1016/j.radonc.2012.11.012.

[37] Amols H, Ling C, Leibel S. Overview of the IMRT Process. A Prat. Guid. to Intensity-Modulated Radiat. Ther., Madison: Medical Physics Publishing; 2003, p. 15–49.

[38] Burman C, Hunt M. Treatment Planning Considerations Using IMRT. A Prat. Guid. to Intensity-Modulated Radiat. Ther., Medical Physics Publishing; 2003, p. 103–21.

[39] Lee EK, Fox T, Crocker I. Simultaneous beam geometry and intensity map optimization in intensity-modulated radiation therapy. Int J Radiat Oncol 2006;64:301–20. doi:10.1016/j.ijrobp.2005.08.023.

[40] ICRU. ICRU Report 83 - Prescribing, Recordind, and Reporting Photon-Beam Intensity-Modulated Radiation Therapy (IMRT). 2010.

[41] Spirou S, Chio C. Delivery of Intensity-Modulated Beam Profiles with a Multileaf Collimator. A Prat. Guid. to Intensity-Modulated Radiat. Ther., Madison: Medical Physics Publishing; 2003, p. 71–81.

[42] White P, Chan KC, Cheng KW, Chan KY, Chau MC. Volumetric intensity-modulated arc therapy vs conventional intensity-modulated radiation therapy in nasopharyngeal carcinoma: a dosimetric study. J Radiat Res 2013;54:532–45. doi:10.1093/jrr/rrs111.

[43] Taylor M, Kron T. Consideration of the radiation dose delivered away from the treatment field to patients in radiotherapy. J Med Phys 2011;36:59. doi:10.4103/0971-6203.79686.

[44] Harrison RM. Introduction to dosimetry and risk estimation of second cancer induction following radiotherapy. Radiat Meas 2013;57:1–8. doi:10.1016/j.radmeas.2013.01.018.

[45] Eldesoky I, Attalla EM, Elshemey WM, Zaghloul MS. A comparison of three commercial IMRT treatment planning systems for selected paediatric cases. J Appl Clin Med Phys 2012;13:3742. doi:10.1120/jacmp.v13i2.3742.

[46] Athar BS, Paganetti H. Comparison of second cancer risk due to out-of-field doses from 6-MV IMRT and proton therapy based on 6 pediatric patient treatment plans. Radiother Oncol 2011;98:87–92. doi:10.1016/j.radonc.2010.11.003.

[47] Athar BS, Bednarz B, Seco J, Hancox C, Paganetti H. Comparison of out-of-field photon doses in 6 MV IMRT and neutron doses in proton therapy for adult and pediatric patients. Phys Med Biol 2010;55:2879–91. doi:10.1088/0031-9155/55/10/006.

[48] Wang L, Ding GX. The accuracy of the out-of-field dose calculations using a model based algorithm in a commercial treatment planning system. Phys Med Biol 2014;59:N113–28. doi:10.1088/0031-9155/59/13/N113.

[49] Mazonakis M, Berris T, Varveris C, Lyraraki E, Damilakis J. Out-of-field organ doses and associated radiogenic risks from para-aortic radiotherapy for testicular seminoma. Med Phys 2014;41:051702. doi:10.1118/1.4870376.

[50] Joosten a, Bochud F, Baechler S, Levi F, Mirimanoff R-O, Moeckli R. Variability of a peripheral dose among various linac geometries for second cancer risk assessment. Phys Med Biol 2011;56:5131–51. doi:10.1088/0031-9155/56/16/004.

[51] Committee to Assess Health Risks from Exposure to Low Levels of Ionizing Radiation - National Research Council. Health Risks from Exposure to Low Levels of Ionizing Radiation: BEIR VII – Phase 2. 2006.

[52] National Council on Radiation Protection and Measurements. Ionizing exposure of the population of the United States, Report No.160. Bethesda, Maryland USA: 2009.

[53] United Nations Scientific Committee on the Effects of Atomic Radiation (UNSCEAR). Effects of ionizing radiation, 2006 Report. Vienna: 2006.

[54] Holmberg O, Czarwinski R, Mettler F. The importance and unique aspects of radiation protection in medicine. Eur J Radiol 2010;76:6–10. doi:10.1016/j.ejrad.2010.06.031.

[55] Vetter RJ, Stoeva MS. Radiation Protection in Medical Imaging and Radiation Oncology. New York: CRC Press - Taylor and Francis Group; 2016.

[56] Podgorsak EB. Radiation Physics for Medical Physicists. Cham: Springer International Publishing; 2016. doi:10.1007/978-3-319-25382-4.

[57] E. MJ. Physics for Radiation Protection. Weinheim: Wiley; 2013.

[58] Stabin MG. Radiation Protection and Dosimetry: An Introduction to Health Physics. Nashville: Springer; 2007.

[59] Antoni R, Bourgois L. Applied Physics of External Radiation Exposure. Cham: Springer International Publishing; 2017. doi:10.1007/978-3-319-48660-4.

[60] ICRP. ICRP 103: The 2007 Recommendations of the International Commission on Radiological Protection. Ann ICRP 2007;37:330. doi:10.1016/j.icrp.2007.10.001.

[61] Podgorsak EB. Radiation Oncology Physics: A Handbook for Teachers and Students. Vienna: IAEA; 2005.

[62] ICRP. ICRP 44 - Protection of the patient in Radiation Therapy. Oxford: 1985.

[63] IAEA. Radiation protection of patients in radiotherapy 2016.

[64] ICRP. ICRP Publication 105 - Radiological Protection in Medicine. 2008.

[65] ARPANSA. Radiation Protection in Radiotherapy. Victoria: Australian Radiation Protection and Safety Agency; 2008.

[66] IAEA. IAEA Safety Standards for protecting people and the environment: Radiation Protection and Safety in Medical Uses of Ionizing Radiation. No. SSG-46. Vienna: IAEA; 2018.

[67] Lemoigne Y, Caner A. Radiation Protection in Medical Physics. Archamps: Springer; 2009.

[68] Shimura T, Yamaguchi I, Terada H, Okuda K, Svendsen ER, Kunugita N. Radiation occupational health interventions offered to radiation workers in response to the complex catastrophic disaster at the Fukushima Daiichi Nuclear Power Plant. J Radiat Res 2015;56:413–21. doi:10.1093/jrr/rru110.

[69] Cullings HM. Impact on the Japanese Atomic Bomb Survivors of Radiation Received From the Bombs. Health Phys 2014;106:281–93. doi:10.1097/HP.0000000000000009.

[70] Berris T, Mazonakis M, Kachris S, Damilakis J. Peripheral organ doses from radiotherapy for heterotopic ossification of non-hip joints: is there a risk for radiation-induced malignancies? Phys Med 2014;30:309–13. doi:10.1016/j.ejmp.2013.09.003.

[71] United Nations Scientific Committee on the Effects of Atomic Radiation. Effects of radiation exposure of children, 2013 Report, Volume 2. New York: 2013.

[72] Balter S, Hopewell JW, Miller DL, Wagner LK, Zelefsky MJ. Fluoroscopically Guided Interventional Procedures: A Review of Radiation Effects on Patients' Skin and Hair. Radiology 2010;254:326–41. doi:10.1148/radiol.2542082312.

[73] Darby SC, Cutter DJ, Boerma M, Constine LS, Fajardo LF, Kodama K, et al. Radiation-Related Heart Disease: Current Knowledge and Future Prospects. Int J Radiat Oncol 2010;76:656–65. doi:10.1016/j.ijrobp.2009.09.064.

[74] Takahashi I, Ohishi W, Mettler Jr FA, Ozasa K, Jacob P, Ban N, et al. A Report from the 2013 International Workshop: Radiation and Cardiovascular Disease, Hiroshima, Japan. J Radiol Prot 2013;33:869–80. doi:10.1088/0952-4746/33/4/869.

[75] Ainsbury EA, Bouffler SD, Dörr W, Graw J, Muirhead CR, Edwards AA, et al. Radiation Cataractogenesis: A Review of Recent Studies. Radiat Res 2009;172:1–9. doi:10.1667/RR1688.1.

[76] Kinhikar R, Gamre P, Kadam S, Biju G, Suryaprakash, Dhote D, et al. Peripheral dose measurements with diode and thermoluminescence dosimeters for intensity modulated radiotherapy delivered with conventional and un-conventional linear accelerator. J Med Phys 2013;38:4. doi:10.4103/0971-6203.106599.

[77] Lin SH. Thoracic Esophageal Cancer. In: Nishimura Y, Komaki R, editors. Intensity-Modulated Radiat. Ther. Clin. Evid. Tech., Tokyo: Springer Japan; 2015, p. 301–14. doi:10.1007/978-4-431-55486-8_16.

[78] Sharma SD, Upreti RR, Deshpande DD. Use of peripheral dose data from uniform dynamic multileaf collimation fields to estimate out-of-field organ dose in patients treated employing sliding window intensity-modulated radiotherapy. Phys Med Biol 2006;51:2987–95. doi:10.1088/0031-9155/51/11/020.

[79] Sharma DS, Animesh, Deshpande SS, Phurailatpam RD, Deshpande DD, Shrivastava SK, et al. Peripheral dose from uniform dynamic multileaf collimation fields: implications for sliding window intensity-modulated radiotherapy. Br J Radiol 2006;79:331–5. doi:10.1259/bjr/16208090.

[80] Klein E, Maserang B, Wood R, Mansur D. Peripheral doses from pediatric IMRT. Med Phys 2006;33:2525–31.

[81] Verellen D, Vanhavere F. Risk assessment of radiation-induced malignancies based on whole-body equivalent dose estimates for IMRT treatment in the head and neck region. Radiother Oncol 1999;53:199–203. doi:10.1016/S0167-8140(99)00079-1.

[82] Mazonakis M, Tzedakis A, Damilakis J, Varveris H, Kachris S, Gourtsoyiannis N. Scattered dose to thyroid from prophylactic cranial irradiation during childhood: a

Monte Carlo study. Phys Med Biol 2006;51:N139–45. doi:10.1088/0031-9155/51/8/N01.

[83] Fiandra C, Filippi A, Catuzzo P, Botticella A, Ciammella P, Franco P, et al. Different IMRT solutions vs. 3D-Conformal Radiotherapy in early stage Hodgkin's lymphoma: dosimetric comparison and clinical considerations. Radiat Oncol 2012;7:186. doi:10.1186/1748-717X-7-186.

[84] Diallo I, Haddy N, Adjadj E, Samand A, Quiniou E, Chavaudra J, et al. Frequency distribution of second solid cancer locations in relation to the irradiated volume among 115 patients treated for childhood cancer. Int J Radiat Oncol Biol Phys 2009;74:876–83. doi:10.1016/j.ijrobp.2009.01.040.

[85] Thalhofer JL, Rebello WF, Correa SA, Silva AX, Souza EM, Batista D V. Calculation of Dose in Healthy Organs, during Radiotherapy 4-Field Box 3D Conformal for Prostate Cancer, Simulation of the Linac 2300, Radiotherapy Room and MAX Phantom. Int J Med Physics, Clin Eng Radiat Oncol 2013;02:61–8. doi:10.4236/ijmpcero.2013.22009.

[86] Vanhavere F, Huyskens D, Struelens L. Peripheral neutron and gamma doses in radiotherapy with an 18 MV linear accelerator. Radiat Prot Dosimetry 2004;110:607–12. doi:10.1093/rpd/nch135.

[87] National Council on Radiation Protection and Measurements. Limitation of exposure to ionizing radiation : recommendations of the National Council on Radiation Protection and Measurements. 1993.

[88] UNSCEAR. UNSCEAR 2013 REPORT Vol. I: SOURCES, EFFECTS AND RISKS OF IONIZING RADIATION. 2013.

[89] Schneider U. Modeling the risk of secondary malignancies after radiotherapy. Genes (Basel) 2011;2:1033–49. doi:10.3390/genes2041033.

[90] Hanna S. RF Linear Accelerators for Medical and Industrial Applications. Norwood: ARTECH HOUSE; 2012.

[91] Lo SS, Teh BS, Lu JJ, Schefter TE, editors. Stereotactic Body Radiation Therapy. Berlin, Heidelberg: Springer Berlin Heidelberg; 2012. doi:10.1007/978-3-642-25605-9.

[92] Wijesooriya K, Bartee C, Siebers J V., Vedam SS, Keall PJ. Determination of maximum leaf velocity and acceleration of a dynamic multileaf collimator: Implications for 4D radiotherapy. Med Phys 2005;32:932–41. doi:10.1118/1.1876581.

[93] IAEA. Technical Reports Series No. 398, Absorbed Dose Determination in External Beam Radiotherapy. An International Code of Practice for Dosimetry Based on Standards of Absorbed Dose to Water. Vienna: 2000.

[94] PTW. Detectors - Including Codes of Practice. Ptw 2015:21. doi:10.1007/SpringerReference_174795.

[95] PTW. MP3 - M: 3D Water Scanning System n.d. https://www.ptwdosimetry.com/en/products/mp3-m-water-phantom-system/?type=3451&downloadfile=1282&cHash=fc2f3337c1aa263b81020ee5dfa1f0b4.

[96] Baptista CG. CORREÇÃO DE HETEROGENEIDADES PARA FEIXES DE FÓTONS DE 6 MeV : COMPARAÇÕES ENTRE ALGORITMOS DE CÁLCULO

E MEDIDAS COM TLD. Universidade Tecnológica Federal do Paraná, 2009.

[97] Korhonen L. Methods for dose calculation and beam characterization in external photon beam radiotherapy. Helsinki University of Technology, 2009.

[98] Aird EGA, Conway J. CT simulation for radiotherapy treatment planning. Br J Radiol 2002;75:937–49. doi:10.1259/bjr.75.900.750937.

[99] ICRU. ICRU Report 62 - Prescribing, Recording and Reporting Photon Beam Therapy (Supplement to ICRU Report 50). 1999.

[100] ICRU. ICRU Report 50 - Prescribing, Recording, and Reporting Photon Beam Therapy. 1993.

[101] ICRU. ICRU 29: Dose Specification for Reporting External Beam Therapy with Photons and Electrons. Bethesda, Maryland USA: 1978.

[102] ICRU. ICRU Report 71. Prescribing, recording and reporting electron beam therapy. Bethesda, Maryland USA: 2004.

[103] Cozzi L, Buffa FM, Fogliata A. Dosimetric features of linac head and phantom scattered radiation outside the clinical photon beam: Experimental measurements and comparison with treatment planning system calculations. Radiother Oncol 2001;58:193–200. doi:10.1016/S0167-8140(00)00317-0.

[104] Ahnesjö A, Aspradakis MM. Dose calculations for external photon beams in radiotherapy. Phys Med Biol 1999;44. doi:10.1088/0031-9155/44/11/201.

[105] Bragg CM, Conway J. Dosimetric verification of the anisotropic analytical algorithm for radiotherapy treatment planning. Radiother Oncol 2006;81:315–23. doi:10.1016/j.radonc.2006.10.020.

[106] Aarup LR, Nahum AE, Zacharatou C, Juhler-Nøttrup T, Knöös T, Nyström H, et al. The effect of different lung densities on the accuracy of various radiotherapy dose calculation methods: Implications for tumour coverage. Radiother Oncol 2009;91:405–14. doi:10.1016/j.radonc.2009.01.008.

[107] Josefsson A. Evaluation of the Anisotropic Analytic Algorithm (AAA) for 6 MV photon energy. Göteborg University, 2008.

[108] Nilsson E. Evaluation of the Analytical Anisotropic Algorithm ( AAA ) in lung tumours for 6 MV photon energy. Göteborg University, 2009.

[109] Van Esch A, Tillikainen L, Pyykkonen J, Tenhunen M, Helminen H, Siljamäki S, et al. Testing of the analytical anisotropic algorithm for photon dose calculation. Med Phys 2006;33:4130. doi:10.1118/1.2358333.

[110] Vanderstraeten B. Biologically conformal radiation therapy and Monte Carlo dose calculations in the clinic. Universiteit Gent, 2007.

[111] Sievinen J, Ulmer W, Kaissl W. AAA photon dose calculation model in Eclipse. Varian Med Syst 2005;Varian:1–23.

[112] Oelfke U, Scholz C. Dose Calculation Algorithms. In: Schlegel W, Bortfeld T, Grosu A-L, editors. New Technol. Radiat. Oncol., Berlin/Heidelberg: Springer-Verlag; 2006, p. 187–96. doi:10.1007/3-540-29999-8.

[113] Rønde HS, Hoffmann L. Validation of Varian's AAA algorithm with focus on lung treatments. Acta Oncol 2009;48:209–15. doi:10.1080/02841860802287108.

[114] Ono K, Endo S, Tanaka K, Hoshi M, Hirokawa Y. Dosimetric verification of the

anisotropic analytical algorithm in lung equivalent heterogeneities with and without bone equivalent heterogeneities. Med Phys 2010;37:4456–63. doi:10.1118/1.3464748.

[115] Hasenbalg F, Neuenschwander H, Mini R, Born EJ. Collapsed cone convolution and analytical anisotropic algorithm dose calculations compared to VMC++ Monte Carlo simulations in clinical cases. Phys Med Biol 2007;52:3679–91. doi:10.1088/1742-6596/74/1/021007.

[116] Silva LFO, Batista DVS, Fortes SS. Testes Dosimétricos do Algoritmo Analítico Anisotrópico Implementado no Sistema de Planejamento Eclipse / Varian. Rev Bras Física Médica 2010;4:31–5.

[117] Gagne IM, Zavgorodni S. Evaluation of the analytical anisotropic algorithm (AAA) in an extreme water-lung interface phantom using Monte Carlo dose calculations. J Appl Clin Med Phys 2006;8. doi:10.1120/jacmp.v8i1.2324.

[118] Healy B, Murry R. Testing of a treatment planning system with beam data from IAEA TECDOC 1540. J Med Phys 2011;36:107. doi:10.4103/0971-6203.79688.

[119] Bragg CM, Wingate K, Conway J. Clinical implications of the anisotropic analytical algorithm for IMRT treatment planning and verification. Radiother Oncol 2008;86:276–84. doi:10.1016/j.radonc.2008.01.011.

[120] Purdy JA, Michalski JM, Jeffrey B, Vijayakumar S, Perez CA, Levitt SH. Three-Dimensional Treatment Planning and Conformal Therapy. In: Levitt SH, Purdy JA, Perez CA, Vijayakumar S, editors. Tech. Basis Radiat. Ther. Prat. Clin. Appl. 4th Revise, Springer; 2006, p. 179–202.

[121] Barrett A, Dobbs J, Morris S, Roques T. Practical Radiotherapy Planning. Hodder Arnold; 2009.

[122] IAEA. Transition from 2-D Radiotherapy to 3-D Conformal and Intensity Modulated Radiotherapy. Austria: 2008.

[123] Mu X, Löfroth P-O, Karlsson M, Zackrisson B. The effect of fraction time in intensity modulated radiotherapy: theoretical and experimental evaluation of an optimisation problem. Radiother Oncol 2003;68:181–7. doi:10.1016/S0167-8140(03)00165-8.

[124] Hoppe R, Phillips T, Roach M. Leibel and Phillips Textbook of Radiation Oncology. 3rd ed. Philadelphia: Elsevier; 2010.

[125] Deasy JO, Alaly JR, Zakaryan K. Obstacles and Advances in Intensity-Modulated Radiation Therapy Treatment Planning. In: Meyer JL, editor. IMRT, IGRT, SBRT – Adv. Treat. Plan. Deliv. Radiother., Karger; 2007, p. 42–58.

[126] Schwarz M, Bos LJ, Mijnheer BJ, Lebesque J V, Damen EM. Importance of accurate dose calculations outside segment edges in intensity modulated radiotherapy treatment planning. Radiother Oncol 2003;69:305–14. doi:10.1016/j.radonc.2003.09.002.

[127] LJUNGBERG M. Simulation Techniques and Phantoms. Emiss. Tomogr., Elsevier; 2004, p. 551–63. doi:10.1016/B978-012744482-6.50028-4.

[128] Xu XG, Eckerman KF. Handbook of Anatomical Models for Radiation Dosimetry. 2010.

[129] Xu XG. An exponential growth of computational phantom research in radiation protection, imaging, and radiotherapy: a review of the fifty-year history. Phys

Med Biol 2014;59:R233–302. doi:10.1088/0031-9155/59/18/R233.

[130] Nedaie H, Mosleh-Shirazi M, Allahverdi M. Monte Carlo N Particle code - Dose distribution of clinical electron beams in inhomogeneous phantoms. J Med Phys 2013;38:15. doi:10.4103/0971-6203.106607.

[131] Bielajew AF. History of Monte Carlo. In: Seco J, Verhaegen F, editors. Monte Carlo Tech. Radiat. Ther., New York: CRC Press - Taylor and Francis Group; 2013, p. 3–16.

[132] Verhaegen F. Monte Carlo Modeling of External Photon Beams in Radiotherapy. Monte Carlo Tech. Radiat. Ther., 2013, p. 63–86.

[133] Breitman K, Rathee S, Newcomb C, Murray B, Robinson D, Field C, et al. Experimental validation of the Eclipse AAA algorithm. J Appl Clin Med Phys 2007;8:76–92.

[134] Seco J, Fragoso M. Patient Dose Calculation. Monte Carlo Tech. Radiat. Ther., 2013, p. 111–23.

[135] Abella V, Miró R, Juste B, Verdú G. 3D dose distribution calculation in a voxelized human phantom by means of Monte Carlo method. Appl Radiat Isot 2010;68:709–13. doi:10.1016/j.apradiso.2009.10.016.

[136] Fippel M. Basics of Monte Carlo Simulations. Monte Carlo Tech. Radiat. Ther., 2013, p. 17–28.

[137] Ottosson RO, Karlsson A, Behrens CF. Pareto front analysis of 6 and 15 MV dynamic IMRT for lung cancer using pencil beam, AAA and Monte Carlo. Phys Med Biol 2010;55:4521–33. doi:10.1088/0031-9155/55/16/S07.

[138] Kry SF, Titt U, Pönisch F, Followill D, Vassiliev ON, Allen White R, et al. A Monte Carlo model for calculating out-of-field dose from a Varian 6 MV beam. Med Phys 2006;33:4405–13. doi:10.1118/1.2360013.

[139] Lehmann J, Stern RL, Daly TP, Rocke DM, Schwietert CW, Jones GE, et al. Dosimetry for quantitative analysis of the effects of low-dose ionizing radiation in radiation therapy patients. Radiat Res 2006;165:240–7.

[140] Boia LS, Menezes AF, Cardoso MAC, da Rosa LAR, Batista DVS, Cardoso SC, et al. Application of digital image processing for the generation of voxels phantoms for Monte Carlo simulation. Appl Radiat Isot 2012;70:144–8. doi:10.1016/j.apradiso.2011.08.017.

[141] Pelowitz DB, Goorley JT, James MR, Booth TE, Brown FB, Bull JS, et al. MCNP6 USER ' S MANUAL. Los Alamos National Laboratory; 2013.

[142] Saidi P, Sadeghi M, Tenreiro C. Variance Reduction of Monte Carlo Simulation in Nuclear Engineering Field. Theory Appl. Monte Carlo Simulations, InTech; 2013. doi:10.5772/53384.

[143] Bielajew AF. History of Monte Carlo, 2015, p. 1–16.

[144] DeWerd LA, Kissick M. The Phantoms of Medical and Health Physics. New York, NY: Springer New York; 2014. doi:10.1007/978-1-4614-8304-5.

[145] Caon M. Voxel-based computational models of real human anatomy: A review. Radiat Environ Biophys 2004;42:229–35. doi:10.1007/s00411-003-0221-8.

[146] Abella V, Miró R, Juste B, Santos A, Verdú G. Monte Carlo model of the female RANDO phantom irradiation with an Elekta Precise linear accelerator. Nucl

Instruments Methods Phys Res Sect A Accel Spectrometers, Detect Assoc Equip 2010;619:230–3. doi:10.1016/j.nima.2009.10.129.

[147] ICRP. ICRP Publication 110: Adult Reference Computational Phantoms. vol. 39. 2010.

[148] Zaidi H, Tsui BMW. Review of computational anthropomorphic anatomical and physiological models. Proc IEEE 2009;97:1938–53. doi:10.1109/JPROC.2009.2032852.

[149] Alziar I, Bonniaud G, Couanet D, Ruaud JB, Vicente C, Giordana G, et al. Individual radiation therapy patient whole-body phantoms for peripheral dose evaluations: method and specific software. Phys Med Biol 2009;54:N375–83. doi:10.1088/0031-9155/54/17/N01.

[150] Snyder W, Fisher HJ, Ford M, GG W. Estimates of absorbed fractions for monoenergetic photon sources uniformly distributed in various organs of a heterogeneous phantom. J Nucl Med 1969;3:7–52.

[151] Kramer R, Vieira J, Khoury H, Lima F, Fuelle D. All about MAX: a male adult voxel phantom for Monte Carlo calculations in radiation protection dosimetry. Phys Med Biol 2003;48:1239–62.

[152] Farfán EB, Han EY, Bolch WE, Huh C, Huston TE, Bolch WE. A REVISED STYLIZED MODEL OF THE ADULT EXTRATHORACIC AND THORACIC AIRWAYS FOR USE WITH THE ICRP-66 HUMAN RESPIRATORY TRACT MODEL. Health Phys 2004;86:337–52. doi:10.1097/00004032-200404000-00002.

[153] Bouchet L, Bolch W, Weber D, Atkins H, Poston J. MIRD Pamphlet No. 15: Radionuclide S values in a revised dosimetric model of the adult head and brain. J Nucl Med 1999;40:62S-101S.

[154] Bouchet L, Bolch W, Blanco P, Wessels B, Siegel J, Rajon D. MIRD Pamphlet No. 19: Absorbed Fractions and Radionuclide S Values for Six Age-Dependent Multiregion Models of the Kidney. J Nucl Med 2003;44:1113–47.

[155] Han EY, Bolch WE, Eckerman KF. REVISIONS TO THE ORNL SERIES OF ADULT AND PEDIATRIC COMPUTATIONAL PHANTOMS FOR USE WITH THE MIRD SCHEMA. Health Phys 2006;90:337–56. doi:10.1097/01.HP.0000192318.13190.c4.

[156] CHOONSIK L, LEE J. COMPUTATIONAL ANTHROPOMORPHIC PHANTOMS FOR RADIATION PROTECTION DOSIMETRY: EVOLUTION AND PROSPECTS. Nucl Eng Technol 2006;38:239–50.

[157] ICRP. ICRP publication 89 - Basic anatomical and physiological data for use in radiological protection: reference values. Ann ICRP 2002;32:1–277.

[158] Ljungberg M. Application of Monte Carlo Methods to Radionuclide Therapy. In: Seco J, Verhaegen F, editors. Monte Carlo Tech. Radiat. Ther., CRC Press - Taylor and Francis Group; 2014, p. 223–32.

[159] Nipper J, Williams J, Bolch W. Creation of two tomographic voxel models of paediatric patients in the first year of life. Phys Med Biol 2002;47:3143–64.

[160] Lee C, Williams JL, Lee C, Bolch WE. The UF series of tomographic computational phantoms of pediatric patients. Med Phys 2005;32:3537. doi:10.1118/1.2107067.

[161] Lee C, Lee C, Williams JL, Bolch WE. Whole-body voxel phantoms of paediatric patients—UF Series B. Phys Med Biol 2006;51:4649–61. doi:10.1088/0031-9155/51/18/013.

[162] Borbinha J, Di Maria S, Madeira P, Belchior A, Baptista M, Vaz P. Increasing organ dose accuracy through voxel phantom organ matching with individual patient anatomy. Radiat Phys Chem 2019;159:35–46. doi:10.1016/j.radphyschem.2019.02.014.

[163] Lee C, Lodwick D, Hurtado J, Pafundi D, Williams JL, Bolch WE. The UF family of reference hybrid phantoms for computational radiation dosimetry. Phys Med Biol 2010;55:339–63. doi:10.1088/0031-9155/55/2/002.

[164] Hoseinian-Azghadi E, Rafat-Motavalli L, Miri-Hakimabad H. Development of a 9-months pregnant hybrid phantom and its internal dosimetry for thyroid agents. J Radiat Res 2014;55:730–47. doi:10.1093/jrr/rrt223.

[165] Zhang J, Na YH, Caracappa PF, Xu XG. RPI-AM and RPI-AF, a pair of mesh-based, size-adjustable adult male and female computational phantoms using ICRP-89 parameters and their calculations for organ doses from monoenergetic photon beams. Phys Med Biol 2009;54:5885–908. doi:10.1088/0031-9155/54/19/015.

[166] Cassola VF, de Melo Lima VJ, Kramer R, Khoury HJ. FASH and MASH: female and male adult human phantoms based on polygon mesh surfaces: I. Development of the anatomy. Phys Med Biol 2010;55:133–62. doi:10.1088/0031-9155/55/1/009.

[167] de Melo Lima VJ, Cassola VF, Kramer R, de Oliveira Lira CAB, Khoury HJ, Vieira JW. Development of 5- and 10-year-old pediatric phantoms based on polygon mesh surfaces. Med Phys 2011;38:4723–36. doi:10.1118/1.3615623.

[168] Cassola VF, Kramer R, de Melo Lima VJ, de Oliveira Lira CAB, Khoury HJ, Vieira JW, et al. Development of newborn and 1-year-old reference phantoms based on polygon mesh surfaces. J Radiol Prot 2013;33:669–91. doi:10.1088/0952-4746/33/3/669.

[169] Xie T, Kuster N, Zaidi H. Computational hybrid anthropometric paediatric phantom library for internal radiation dosimetry. Phys Med Biol 2017;62:3263–83. doi:10.1088/1361-6560/aa63d0.

[170] Choi C, Yeom YS, Lee H, Han H, Shin B, Nguyen TT, et al. Body-size-dependent phantom library constructed from ICRP mesh-type reference computational phantoms. Phys Med Biol 2020;65:125014. doi:10.1088/1361-6560/ab8ddc.

[171] Bolch W, Lee C, Wayson M, Johnson P. Hybrid computational phantoms for medical dose reconstruction. Radiat Environ Biophys 2010;49:155–68. doi:10.1007/s00411-009-0260-x.

[172] Anderson R, Lamey M, MacPherson M, Carlone M. Simulation of a medical linear accelerator for teaching purposes. J Appl Clin Med Phys 2015;16:359–77. doi:10.1120/jacmp.v16i3.5139.

[173] Fix MK, Keall PJ, Dawson K, Siebers J V. Monte Carlo source model for photon beam radiotherapy: photon source characteristics. Med Phys 2004;31:3106–21. doi:10.1118/1.1803431.

[174] Wang LLW, Leszczynski K. Estimation of the focal spot size and shape for a

medical linear accelerator by Monte Carlo simulation. Med Phys 2007;34:485–8. doi:10.1118/1.2426407.

[175] Kry SF, Titt U, Followill D, Pönisch F, Vassiliev ON, White RA, et al. A Monte Carlo model for out-of-field dose calculation from high-energy photon therapy. Med Phys 2007;34:3489–99. doi:10.1118/1.2756940.

[176] Sawkey DL, Faddegon BA. Determination of electron energy, spectral width, and beam divergence at the exit window for clinical megavoltage x-ray beams. Med Phys 2009;36:698–707. doi:10.1118/1.3070547.

[177] Ma CM. Characterization of computer simulated radiotherapy beams for Monte-Carlo treatment planning. Radiat Phys Chem 1998;53:329–44. doi:10.1016/S0969-806X(98)00113-3.

[178] Cravo Sá A, Barateiro A, Bednarz B, Borges C, Pereira J, Baptista M, et al. Assessment of out-of-field doses in radiotherapy treatments of paediatric patients using Monte Carlo methods and measurements. Phys Medica 2020;71:53–61. doi:10.1016/j.ejmp.2020.02.008.

[179] Borges C, Zarza-Moreno M, Heath E, Teixeira N, Vaz P. Monte Carlo modeling and simulations of the High Definition (HD120) micro MLC and validation against measurements for a 6 MV beam. Med Phys 2012;39:415–23. doi:10.1118/1.3671935.

[180] Klein EE, Hanley J, Bayouth J, Yin F-F, Simon W, Dresser S, et al. Task Group 142 report: Quality assurance of medical acceleratorsa). Med Phys 2009;36:4197–212. doi:10.1118/1.3190392.

[181] Varian Medical Systems. DMLC QA Test Patterns and Procedures Guide. 2014.

[182] Dössel O, Schlegel WC. Updated Beam Parameters for Monte Carlo Simulation of Five Varian Megavoltage, 2009, p. 1067–70.

[183] Cho SH, Vassiliev ON, Lee S, Liu HH, Ibbott GS, Mohan R. Reference photon dosimetry data and reference phase space data for the 6MV photon beam from Varian Clinac 2100 series linear accelerators. Med Phys 2004;32:137–48. doi:10.1118/1.1829172.

[184] Keall PJ, Siebers J V., Libby B, Mohan R. Determining the incident electron fluence for Monte Carlo-based photon treatment planning using a standard measured data set. Med Phys 2003;30:574–82. doi:10.1118/1.1561623.

[185] Sheikh-Bagheri D, Rogers DWO. Monte Carlo calculation of nine megavoltage photon beam spectra using the BEAM code. Med Phys 2002;29:391–402. doi:10.1118/1.1445413.

[186] Rogers DWO. AAPM Task Group Report No . 105 : Issues associated with clinical implementation of Monte Carlo - based photon and electron external beam treatment planning. Med Phys 2006:1–7.

[187] Zarza-Moreno M. Monte Carlo simulations for dosimetric verification in photon and electron beam radiotherapy. Universidade Nova Lisboa, 2012.

[188] Jaffray DA, Battista JJ, Fenster A, Munro P. X-ray sources of medical linear accelerators: Focal and extra-focal radiation. Med Phys 1993;20:1417–27. doi:10.1118/1.597106.

[189] Bencheikh M, Maghnouj A, Tajmouati J. Validation of Monte Carlo Simulation of 6 MV Photon Beam Produced by Varian Clinac 2100 Linear Accelerator Using

BEAMnrc Code and DOSXYZnrc Code 1 2017;14:780–7. doi:10.1134/S154747711705003X.

[190] Sheikh-Bagheri D, Rogers DWO. Sensitivity of megavoltage photon beam Monte Carlo simulations to electron beam and other parameters. Med Phys 2002;29:379–90. doi:10.1118/1.1446109.

[191] Pena J, González-Castaño DM, Gómez F, Sánchez-Doblado F, Hartmann GH. Automatic determination of primary electron beam parameters in Monte Carlo simulation. Med Phys 2007;34:1076–84. doi:10.1118/1.2514155.

[192] Sadrollahi A, Nuesken F, Licht N, Rübe C, Dzierma Y. Monte-Carlo simulation of the Siemens Artiste linear accelerator flat 6 MV and flattening-filter-free 7 MV beam line. PLoS One 2019;14:e0210069. doi:10.1371/journal.pone.0210069.

[193] Bacala AM. Linac photon beam fine-tuning in PRIMO using the gamma-index analysis toolkit. Radiat Oncol 2020;15:8. doi:10.1186/s13014-019-1455-1.

[194] Rodriguez M, Sempau J, Fogliata A, Cozzi L, Sauerwein W, Brualla L. A geometrical model for the Monte Carlo simulation of the TrueBeam linac. Phys Med Biol 2015;60:N219–29. doi:10.1088/0031-9155/60/11/N219.

[195] Quino LV, Hernandez C, Papanikolaou N. A Monte Carlo model for independent dose verification in IMRT and VMAT for the Varian Novalis TX with high definition MLC. Int J Cancer Ther Oncol 2015;3:3312. doi:10.14319/ijcto.33.12.

[196] Nedaie HA, Shariary M, Gharaati H. Monte Carlo study of electron dose distributions produced by the elekta precise linear accelerator. Reports Pract Oncol Radiother 2006;11:287–92. doi:10.1016/S1507-1367(06)71074-4.

[197] Ma C-M, Mok E, Kapur A, Pawlicki T, Findley D, Brain S, et al. Clinical implementation of a Monte Carlo treatment planning system. Med Phys 1999;26:2133–43. doi:10.1118/1.598729.

[198] Kry SF, Howell RM, Klein E, Xu XG. AAPM TG 158_ Measurement and calculation of doses outside the treated volume from external-beam radiation therapy - Kry - 2017 - Medical Physics - Wiley Online Library n.d.

[199] Sardari D, Maleki R, Samavat H, Esmaeeli A. Measurement of depth-dose of linear accelerator and simulation by use of Geant4 computer code. Reports Pract Oncol Radiother 2010;15:64–8. doi:10.1016/j.rpor.2010.03.001.

[200] El Naqa I, Pater P, Seuntjens J. Monte Carlo role in radiobiological modelling of radiotherapy outcomes. Phys Med Biol 2012;57. doi:10.1088/0031-9155/57/11/R75.

[201] Gao Y, Quinn B, Mahmood U, Long D, Erdi Y, St. Germain J, et al. A comparison of pediatric and adult CT organ dose estimation methods. BMC Med Imaging 2017;17:28. doi:10.1186/s12880-017-0199-3.

[202] Miglioretti DL, Johnson E, Williams A, Greenlee RT, Weinmann S, Solberg LI, et al. The Use of Computed Tomography in Pediatrics and the Associated Radiation Exposure and Estimated Cancer Risk. JAMA Pediatr 2013;167:700. doi:10.1001/jamapediatrics.2013.311.

[203] Pearce MS, Salotti JA, Little MP, McHugh K, Lee C, Kim KP, et al. Radiation exposure from CT scans in childhood and subsequent risk of leukaemia and brain tumours: a retrospective cohort study. Lancet 2012;380:499–505. doi:10.1016/S0140-6736(12)60815-0.

[204] Ding A, Gao Y, Liu H, Caracappa PF, Long DJ, Bolch WE, et al. VirtualDose : a software for reporting organ doses from CT for adult and pediatric patients. Phys Med Biol 2015;60:5601–25. doi:10.1088/0031-9155/60/14/5601.

[205] Tian X, Li X, Segars WP, Frush DP, Paulson EK, Samei E. Dose coefficients in pediatric and adult abdominopelvic CT based on 100 patient models. Phys Med Biol 2013;58:8755–68. doi:10.1088/0031-9155/58/24/8755.

[206] Lee C, Kim KP, Long DJ, Bolch WE. Organ doses for reference pediatric and adolescent patients undergoing computed tomography estimated by Monte Carlo simulation. Med Phys 2012;39:2129–46. doi:10.1118/1.3693052.

[207] Turner AC, Zhang D, Khatonabadi M, Zankl M, DeMarco JJ, Cagnon CH, et al. The feasibility of patient size-corrected, scanner-independent organ dose estimates for abdominal CT exams. Med Phys 2011;38:820–9. doi:10.1118/1.3533897.

[208] Kim S, Yoshizumi TT, Frush DP, Toncheva G, Yin F-F. Radiation Dose From Cone Beam CT in a Pediatric Phantom: Risk Estimation of Cancer Incidence. Am J Roentgenol 2010;194:186–90. doi:10.2214/AJR.08.2168.

[209] McDermott A, White RA, Mc-Nitt-Gray M, Angel E, Cody D. Pediatric organ dose measurements in axial and helical multislice CT. Med Phys 2009;36:1494–9. doi:10.1118/1.3101817.

[210] Abramoff M, Magalhaes P, Ram S. Image Processing with ImageJ. Biophotonics Int 2004;43:36–42.

[211] Schneider CA, Rasband WS, Eliceiri KW. NIH Image to ImageJ: 25 years of image analysis. Nat Methods 2012;9:671–5. doi:10.1038/nmeth.2089.

[212] Rasband WS. ImageJ. US Natl Institutes Heal n.d. https://imagej.nih.gov/ij/index.html.

[213] Varde P V., Prakash R V., Vinod G, editors. Reliability, Safety and Hazard Assessment for Risk-Based Technologies. Singapore: Springer Singapore; 2020. doi:10.1007/978-981-13-9008-1.

[214] Gómez-Ros JM. Implementing voxel phantom geometries for MCNP codes. Train. Course Appl. MC Methods Dosim. Ioniz. Radiat., Karlsruhe: 2018.

[215] Choi S, Lee C, Cho S, Chung M, Na S, Kim C. Construction of a high-definition 'Reference Korean' voxel phantom for organ and tissue radiation dose calculation. IFMBE Proc 2007;14:4204–7.

[216] Dimbylow P. Development of the female voxel phantom, NAOMI, and its application to calculations of induced current densities and electric fields from applied low frequency magnetic and electric fields. Phys Med Biol 2005;50:1047–70. doi:10.1088/0031-9155/50/6/002.

[217] Zankl M, Becker J, Lee C, Bolch WE, Yeom YS, Kim CH. Computational phantoms, ICRP/ICRU, and further developments. Ann ICRP 2018;47:35–44. doi:10.1177/0146645318756229.

[218] Lee C, Badal A, Yeom YS, Griffin KT, McMillan D. Dosimetric impact of voxel resolutions of computational human phantoms for external photon exposure. Biomed Phys Eng Express 2019;5:065002. doi:10.1088/2057-1976/ab2850.

[219] Emami B. Tolerance of Normal Tissue to Therapeutic Radiation. Reports Radiother Oncol 2013;1:35–48.

[220] Marks LB, Yorke ED, Jackson A, Ten Haken RK, Constine LS, Eisbruch A, et al. Use of Normal Tissue Complication Probability Models in the Clinic. Int J Radiat Oncol 2010;76:S10–9. doi:10.1016/j.ijrobp.2009.07.1754.

[221] Brodin NP, Tomé WA. Revisiting the dose constraints for head and neck OARs in the current era of IMRT. Oral Oncol 2018;86:8–18. doi:10.1016/j.oraloncology.2018.08.018.

[222] Yamazaki H, Shiomi H, Tsubokura T, Kodani N, Nishimura T, Aibe N, et al. Quantitative assessment of inter-observer variability in target volume delineation on stereotactic radiotherapy treatment for pituitary adenoma and meningioma near optic tract. Radiat Oncol 2011;6:10. doi:10.1186/1748-717X-6-10.

[223] Shaffer R, Nichol AM, Vollans E, Fong M, Nakano S, Moiseenko V, et al. A Comparison of Volumetric Modulated Arc Therapy and Conventional Intensity-Modulated Radiotherapy for Frontal and Temporal High-Grade Gliomas. Int J Radiat Oncol 2010;76:1177–84. doi:10.1016/j.ijrobp.2009.03.013.

[224] Feuvret L, Noël G, Mazeron J-J, Bey P. Conformity index: A review. Int J Radiat Oncol 2006;64:333–42. doi:10.1016/j.ijrobp.2005.09.028.

[225] McKeever SWS. Thermoluminescence of solids. Cambridge: Cambridge University Press; 1985. doi:10.1017/CBO9780511564994.

[226] Pereira J, Pereira MF, Rangel S, Saraiva M, Santos LM, Cardoso J V., et al. FADING EFFECT OF LiF:Mg,Ti AND LiF:Mg,Cu,P Ext-Rad AND WHOLE-BODY DETECTORS. Radiat Prot Dosimetry 2016;170:177–80. doi:10.1093/rpd/ncv445.

[227] Baptista M, Di Maria S, Vieira S, Pereira J, Pereira M, Vaz P. Organ dose measurements using an adult anthropomorphic phantom and risk estimation of cancer incidence from CBCT exposures. Radiat Phys Chem 2020;171:108715. doi:10.1016/j.radphyschem.2020.108715.

[228] Hubbell J, Seltzer S. X-Ray Mass Attenuation Coefficients. NIST 2004.

[229] JCGM. Evaluation of measurement data - Guide to expression of uncertainty in measurement. Sevres: 2008.

[230] Majer M, Stolarczyk L, De Saint-Hubert M, Kabat D, Knežević Ž, Miljanić S, et al. OUT-OF-FIELD DOSE MEASUREMENTS FOR 3D CONFORMAL AND INTENSITY MODULATED RADIOTHERAPY OF A PAEDIATRIC BRAIN TUMOUR. Radiat Prot Dosimetry 2017;176:331–40. doi:10.1093/rpd/ncx015.

[231] Borges C. Impact of using different radiation therapy techniques in breast cancer : contralateral breast dose. 2014.

[232] IAEA. Commissioning and quality assurance of computerized planning systems for radiation treatment of cancer. Tech Reports Ser 430 2004.

[233] IAEA. IAEA Human Health - Accuracy Requirements and Uncertainties in Radiotherapy. 2016.

[234] Yoon J, Heins D, Zhao X, Sanders M, Zhang R. Measurement and modeling of out-of-field doses from various advanced post-mastectomy radiotherapy techniques. Phys Med Biol 2017;62:9039–53. doi:10.1088/1361-6560/aa94b5.

[235] Howell RM, Scarboro SB, Kry SF, Yaldo DZ. Accuracy of out-of-field dose calculations by a commercial treatment planning system. Phys Med Biol 2010;55:6999–7008. doi:10.1088/0031-9155/55/23/S03.

[236] Beierholm AR, Nygaard DE, Juhl EL, Hansen R, Hansen J. Evaluating out-of-field doses during radiotherapy of paediatric brain tumours using lead shielding and flattening-filter free beams. Phys Medica 2019;60:1–6. doi:10.1016/j.ejmp.2019.03.008.

[237] Shine N, Paramu R, Gopinath M, Jaon Bos R, Jayadevan P. Out-of-field dose calculation by a commercial treatment planning system and comparison by monte carlo simulation for varian TrueBeam ®. J Med Phys 2019;44:156. doi:10.4103/jmp.JMP_82_18.

[238] Wang L, Ding GX. Estimating the uncertainty of calculated out-of-field organ dose from a commercial treatment planning system. J Appl Clin Med Phys 2018;19:319–24. doi:10.1002/acm2.12367.

[239] Chopra KL, Leo P, Kabat C, Rai DV, Avadhani JS, Kehwar TS, et al. Evaluation of dose calculation accuracy of treatment planning systems in the presence of tissue heterogeneities. Ther Radiol Oncol 2018;2:28–28. doi:10.21037/tro.2018.07.01.

[240] Kan MWK, Leung LHT, Yu PKN. Dosimetric Impact of Using the Acuros XB Algorithm for Intensity Modulated Radiation Therapy and RapidArc Planning in Nasopharyngeal Carcinomas. Int J Radiat Oncol 2013;85:e73–80. doi:10.1016/j.ijrobp.2012.08.031.

[241] Covington EL, Ritter TA, Moran JM, Owrangi AM, Prisciandaro JI. Technical Report: Evaluation of peripheral dose for flattening filter free photon beams. Med Phys 2016;43:4789–96. doi:10.1118/1.4958963.

[242] Mijnheer B, Beddar S, Izewska J, Reft C. In vivo dosimetry in external beam radiotherapy. Med Phys 2013;40:070903. doi:10.1118/1.4811216.

[243] Miljanić S, Bordy J-M, D'Errico F, Harrison R, Olko P. Out-of-field dose measurements in radiotherapy – An overview of activity of EURADOS Working Group 9: Radiation protection in medicine. Radiat Meas 2014;71:270–5. doi:10.1016/j.radmeas.2014.04.026.

[244] Harrison R. Out-of-field doses in radiotherapy: Input to epidemiological studies and dose-risk models. Phys Medica 2017;42:239–46. doi:10.1016/j.ejmp.2017.02.001.